UNIVERSITY TRANSPORTATION CENTER
FOR UNDERGROUND TRANSPORTATION INFRASTRUCTURE

Resilience Assessment Tool for Tunnels Exposed to Blast and Fire

FINAL PROJECT REPORT

By
Zheda Zhu
Qi Guo
Spencer Quiel
Clay Naito

Lehigh University

Sponsorship
(List UTC-UTI and cost matching external sponsors)

For

University Transportation Center for
Underground Transportation Infrastructure
(UTC-UTI)

February 22, 2020

COLORADO SCHOOL OF MINES
EARTH • ENERGY • ENVIRONMENT

Disclaimer

The contents of this report reflect the views of the authors, who are responsible for the facts and the accuracy of the information presented herein. This document is disseminated in the interest of information exchange. The report is funded, partially or entirely, by a grant from the U.S. Department of Transportation's University Transportation Centers Program. However, the U.S. Government assumes no liability for the contents or use thereof.

1. Report No.	2. Government Accession No.	3. Recipient's Catalog No.	
4. Title and Subtitle Resilience Assessment Tool for Tunnels Exposed to Blast and Fire		5. Report Date: 2/21/2020 6. Performing Organization Code	
7. Author(s) Zheda Zhu, Ph.D.; Qi Guo, Ph.D. Spencer Quiel, Ph.D., P.E.; Clay Naito, Ph.D., P.E.		8. Performing Organization Report No.	
9. Performing Organization Name and Address University Transportation Center for Underground Transportation Infrastructure (UTC-UTI) Tier 1 University Transportation Center Colorado School of Mines Coolbaugh 308, 1012 14th St., Golden, CO 80401		10. Work Unit No. (TRAIS) 11. Contract or Grant No.	
12. Sponsoring Agency Name and Address United States of America Department of Transportation Research and Innovative Technology Administration		13. Type of Report and Period Covered 14. Sponsoring Agency Code	
15. Supplementary Notes Report also available at: https://zenodo.org/communities/utc-uti			
16. Abstract This report proposes the framework to quantify the tunnel structural fire resilience and risk by considering the real thermal impact on tunnel liner result from vehicle fire hazards, the corresponding damage, the inspection, and repair process afterward, and tunnel traffic volume and composition. The fast-running computational tool Confined Discretized Solid Flame (CDSF) model is upgraded to adapt to the longitudinal ventilated situation. Together with the natural ventilated model, it provides heat flux distribution on the tunnel liner. The spalling behavior of concrete tunnel subjected to thermal impact is simulated with Matlab-SAFIR interactive method while the damage is classified according to repairing procedure. By considering the uncertainties of the thermal properties of the concrete liner, the damage classification map is developed through the stochastic approach and applied to quantify the time for repair efficiently. The resilience of the tunnel is then measured with the metric of tunnel functionality loss. Uncertainties associated with tunnel fire (i.e., combustion energy), tunnel condition (i.e., dimension, ventilation, and presence of Fixed Fire-Fighting System (FFFS)), and tunnel traffic (i.e., volume and composition) are included in this calculation process. The framework provides information for decision-making on tunnel fire safety in terms of the design, renovation, inspection, and repair of tunnels.			
17. Key Words Tunnel, fire, solid flame model, resilience quantification; risk assessment		18. Distribution Statement No restrictions.	
19. Security Classification (of this report): Unclassified	20. Security Classification (of this page): Unclassified	21. No of Pages: 233	22. Price NA

Table of Contents

Table of Contents 4

List of Figures 7

List of Tables 11

EXCUTIVE SUMMARY 13

CHAPTER 1 - INTRODUCTION 14

CHAPTER 2 – TUNNEL FIRE RESILIENCE ASSESSMENT FRAMWORK 17

2.1. Tunnel Resilience 17

2.2. Quantification framework 19

CHAPTER 3 – CONFINED DISCRETIZED SOLID FLAME MODEL (NATURAL VENTILATION) 22

3.1. Confined Discretized Solid Flame (CDSF) Model 22

3.1.2 Modeling Assumption 23

3.1.2. Solid Flame Geometry 24

3.1.3. Radiation Heat Transfer 27

3.1.4. Convective Heat Transfer 29

3.2. Computational Model Validation 33

3.2.1. Modeling the Memorial Tunnel Fire Tests 33

3.2.2. Modeling the Runehamar Tunnel Fire Test 37

3.3. Parametric Study 38

3.3.1 Tunnel Prototypes 39

3.3.2. Fire Scenarios 41

3.4. Comparison and Discussion 43

3.5. Summary 51

CHAPTER 4 - CONFINED DISCRETIZED SOLID FLAME MODEL (LONGITUDINAL VENTILATION) 53

4.1. CDSF model with longitudinal ventilation 53
4.1.1. Calculate critical velocity 56
4.1.2. Apply wind tilt to the initially unconfined solid flame model 56
4.1.3. Apply confinement to the wind-tilted solid flame model 62
4.1.4. Calculate radiative heat transfer 65
4.1.5. Calculate convective heat transfer 65
4.2. FDS model validation 66
4.2.1. MTFVTP Test 615B 67
4.2.2. CFD modeling approach 68
4.2.3. Validation results 72
4.3. Parametric study 76
4.3.1. Tunnel prototypes 76
4.3.2. Fire scenarios 77
4.3.3. Parametric results 77
4.4. Conclusions 87
CHAPTER 5 – CONCRETE LINER DAMAGE ANALYSIS AND CLASSIFICATION 90
5.1. Concrete spall modeling via FE method 90
5.2. Uncertainties of concrete thermal properties 93
5.3. Concrete liner damage classification 98
5.4. Stochastic analysis 100
5.5. Repair procedure for concrete liners post fire 104
5.6. Influence of convective coefficient 107
CHAPTER 6 – TUNNEL FUNCTIONALITY LOSS ASSESSMENT 110
6.1. Tunnel fire thermal impact calculation 110
6.2. Uncertainties associated with tunnel fire thermal impact 110
6.3. Quantification of functionality loss for specific tunnel fire 113

6.4. Resilience quantification metric-functionality loss 116
CHAPTER 7 – TUNNEL RESILIENCE ASSESSMENT APPLICATION 117
7.1. Prototype tunnel 117
7.2. Analysis Matrix 118
7.3. Results and Discussion 118
CHAPTER 8 – FIRE RISK ASSESSMENT FOR TUNNEL LINEINGS 122
8.1 Stochastic Analysis of Vehicle Fire Hazards in Tunnels 122
8.2 Case Study: Fort Pitt Tunnel 124
8.3 Results and Discussion 126
CHAPTER 9 – CONCLUSION AND FUTURE WORK 134
9.1 Conclusion 134
9.2 Future Work 136
REFERENCE 137
APPENDIX A – TECHNOLOGY TRANSFER ACTIVITIES 146
1. Accomplishments 146
2. Participants and Collaborating Organizations 146
3. Outputs 147
4. Outcomes 148
5. Impacts 148
APPENDIX B - DATA FROM THE PROJECT 150
B.1 Time History of Heat Flux (kW/m^2) measured in the Runehamar Tunnel Fire test and FDS(Figure 11) 150
B.2 Heat Flux Results Comparison for the Tunnel Prototypes and Fire Scenarios (Figure 21) 203

List of Figures

Figure 1 Typical concrete damage after heat exposure: spalling (Jansson 2013) (left) and strength reduction (American Concrete Institute 2014) (right) 15
Figure 2: Typical schematic representation of resilience 17
Figure 3: Functionality of tunnel subjected to fire hazard 18
Figure 4: Tunnel fire resilience analysis flowchart. 21
Figure 5 Illustrations of radiative (left) and convective (right) heat transfer for the CDSF model 23
Figure 6 Development of the CDSF footprint based on an HGV fire scenario 24
Figure 7 Schematic comparison of the free flame and confined flame models in the tunnel cross-section 27
Figure 8 Flowchart of the proposed CDSF framework 32
Figure 9 Section cut at the longitudinal center showing typical CDSF output (heat flux values in kW/m^2) 33
Figure 10 Mesh distributions for the FDS sensitivity study in the Memorial Tunnel 35
Figure 11 Comparison of ceiling measurements for the 50 MW Memorial Tunnel fire: (a) gas temperature after 3 min elapsed time (test (Bechtel/Parsons Brinckerhoff. and Bechtel/Parsons Brinckerhoff. 1995) vs. FDS), and (b) average steady state heat flux (FDS only) 36
Figure 12 Comparison of FDS ceiling temperature (meshing option (b)) and test data (Bechtel/Parsons Brinckerhoff. and Bechtel/Parsons Brinckerhoff. 1995) for the 20 MW and 50 MW Memorial Tunnel fires 36
Figure 13 Heat release rate and ceiling heat flux time histories for the 6 MW Runehamar Tunnel fire 38
Figure 14 Locations of heat flux measurement to compare the CDSF and FDS models 39
Figure 15 Accumulated number and length of tunnels from 1882 to 2015 (USDOT 2015) 40
Figure 16 Cross-sectional dimensions (in meters) for the horseshoe, larger horseshoe, and circular tunnel prototypes 41
Figure 17 Tunnel roadway width frequency for circular and horseshoe tunnel shapes (USDOT 2015) 41
Figure 18 Dimensions (in meters) of the actual vehicle footprint (dashed gray), equivalent diesel pool footprint (solid gray) for FDS, and equivalent elliptical footprint (solid red) for CDSF 42

Figure 19 Total heat flux time histories at the ceiling of Tunnel B directly above each fire 44
Figure 20 Comparison of thru-thickness temperature gradients at the ceiling of Tunnel B directly above each fire 46
Figure 21 Comparison of steady-state heat flux predicted by FDS and CDSF for fire scenario HGV-2..... 47
Figure 22 Comparison of $RMSE_{CDSF}$ and $RMSE_{BOUND}$ for all fire scenarios and tunnel prototypes 49
Figure 23 Comparison of radial cross-section heat fluxes for HGV-1 and HGV-2 in Tunnel B . 49
Figure 24 Comparison of raw error from the FDS mean for the longitudinal ceiling heat flux ... 51
Figure 25: Illustration of the proposed wind-tilted CDSF model..... 54
Figure 26: Flowchart for applying the proposed wind-tilted CDSF model..... 55
Figure 27: Step-by-step procedure for developing the geometry of the unconfined wind-tilted solid flame model..... 61
Figure 28: Schematic comparison of wind-tilted CDSF models with escalating levels of confinement within a tunnel..... 64
Figure 29: Illustration of radiative heat transfer from the wind-tilted CDSF model..... 65
Figure 30: Tunnel cross-section dimensions (in meters) for (a) the horseshoe-shaped Memorial tunnel (Bechtel/Parsons Brinckerhoff. and Bechtel/Parsons Brinckerhoff. 1995), (b) a prototype 2-lane circular tunnel, and (c) a prototype 3-lane circular tunnel 68
Figure 31: Plan view of fire location and jet fan arrangement for Test 615B in the Memorial Tunnel (Bechtel/Parsons Brinckerhoff. and Bechtel/Parsons Brinckerhoff. 1995) 68
Figure 32: FDS model for Test 615B 69
Figure 33: Screenshots of the Test 615B tunnel fire simulated in FDS 72
Figure 34: Time histories of data measured close to the tunnel ceiling from Test 615B and FDS simulation..... 72
Figure 35: Longitudinal air velocity profiles for MTFVTP Test 615B at steady state: (a) test results (KBwiki 2017) and (b) numerical FDS results 74
Figure 36: Comparison of ceiling temperatures for MTFVTP Test 615B at steady state: test results (KBwiki 2017) versus FDS results 74
Figure 37: Longitudinal temperature contours along the transverse centerline for MTFVTP Test 615B at steady state: (a) test results (KBwiki 2017) and (b) FDS mean 75

Figure 38: Comparisons of steady-state heat flux along the top-of-ceiling for Prototype A with fire HRR from 30-300 MW 79
Figure 39: Comparisons of steady-state heat flux for the 100MW fire scenario in Prototype A: (a) the top-of-ceiling, and on transverse cross-sections (b) at the fire center, (c) at $Lmax$ downstream from the fire center, and (d) at $(Lmax + Deff)$ downstream from the fire center. 80
Figure 40: Comparisons of steady-state heat flux for the 200MW fire scenario in Prototype A: (a) along the top-of-ceiling, and on transverse cross-sections (b) at the fire center, (c) at $Lmax$ downstream from the fire center, and (d) at $(Lmax + Deff)$ downstream from the fire center. 81
Figure 41: Comparisons of steady-state heat flux along the top-of-ceiling for Prototype B with fire HRR from 50-300 MW 82
Figure 42: Comparisons of steady-state heat flux for the 100MW fire scenario in Prototype B: (a) along the top-of-ceiling, and on transverse cross-sections (b) at the fire center, (c) at $Lmax$ downstream from the fire center, and (d) at $(Lmax + Deff)$ downstream from the fire center. 83
Figure 43: Comparisons of steady-state heat flux for the 200MW fire scenario in Prototype B: (a) along the top-of-ceiling, and on transverse cross-sections (b) at the fire center, (c) at $Lmax$ downstream from the fire center, and (d) at $(Lmax + Deff)$ downstream from the fire center. 84
Figure 44: Comparisons of steady-state heat flux along the top-of-ceiling for Prototype C with fire HRR from 50-300 MW 85
Figure 45: Comparisons of steady-state heat flux for the 100MW fire scenario in Prototype C: (a) the top-of-ceiling, and on transverse cross-sections (b) at the fire center, (c) at $Lmax$ downstream from the fire center, and (d) at $(Lmax + Deff)$ downstream from the fire center. 86
Figure 46: Comparisons of steady-state heat flux for the 200MW fire scenario in Prototype C: (a) along the top-of-ceiling, and on transverse cross-sections (b) at the fire center, (c) at $Lmax$ downstream from the fire center, and (d) at $(Lmax + Deff)$ downstream from the fire center. 87
Figure 47: FE method of simulating the concrete spalling with MATLAB/SAFIR interactive process 93
Figure 48: Probabilistic model for concrete at elevated temperature: mean value, 5%, and 95% quantiles and 20 randomly generated curves used as thermal analysis inputs 95
Figure 49: FHWA 2015 US Roadway Tunnel Inventory 96
Figure 50: ASCE/SEI 41 concrete strength by construction era assumptions 97
Figure 51: Tunnel concrete liner model in SAFIR 101

Figure 52: Damage of concrete panel as a function of heat flux and exposure duration 103
Figure 53: Further concrete removal depth of heavy damaged class and surface regression for prediction 104
Figure 54: Surface temperatures subjected to ASTM E1529 thermal demands 108
Figure 55: Data points and damage levels of the concrete panel with convective coefficient =35 W/m^2K 109
Figure 56: The combustion energy bound of vehicle fires with respect to HRR 111
Figure 57: Process of tunnel concrete liner damage assessment using the damage assessment curve 115
Figure 58: Circular tunnel cross-section 117
Figure 59: HRR probability distribution based on tunnel traffic 118
Figure 60: Functionality loss of tunnel subjected to fire hazard 120
Figure 61: Integral functionality loss of considering tunnel traffic 121
Figure 62 Frequency distribution of fire HRR (in MW) for (a-e) each vehicle type and (f) in total 126
Figure 63 Frequency distribution for (a) HRR and (b) maximum heat flux at the fire location 127
Figure 64 Concrete strength reduction at high temperature and residual after cooling for unstressed calcareous normal weight concrete per (American Concrete Institute 2014 p. 216) 129
Figure 65 Thru-thickness gradients of compressive strength during and after heating for exposure to the two milestone heat flux time histories (a) 60 and (b) 560 kW/m^2 131
Figure 66 Comparison of average residual compressive strength due to the milestone heat flux time histories and standard fire curve exposures 133

List of Tables

Table 1 List of Roadway Tunnel Fires in the US during 1949 - 2007 16
Table 2 Matrix for comparative parametric analyses in FDS and CDSF 43
Table 3:FDS input parameters for MTFVTP Test 615B 70
Table 4: Matrix of comparative parametric analyses via FDS and the wind-tilted CDSF model 77
Table 5: ASCE/SEI 41 to ASTM C642 via Abdul Kareem Void Percent by Strength Assignment 98
Table 6: Input parameter for concrete liner damage classification development 101
Table 7: Linear SVM coefficients for damage limit boundaries concrete liner 103
Table 8: Tunnel concrete liner repair process post fire 106
Table 9: Parameters of damage map and removal depth for convective coefficient = 35 W/m^2-K 109
Table 10: HRR reduction factor by FFFS 112
Table 11: Simulated tunnel condition and associated uncertainties 114
Table 12: Parameters for prototype tunnels 118
Table 13 Peak HRR and weighted fire rates (per Eq. 48) for common vehicle types in tunnels 123
Table 14 Input proportion based on fire frequencies of different vehicle types 124
Table 15 Average daily traffic and fire input for the Fort Pitt Tunnel 125
Table 16 Summary of input parameters for fire curve generation per (Ingason 2009) 128

List of Abbreviations

CDSF: Confined Discretized Solid Flame

HRR: Heat Release Rate

HGV: Heavy Goods Vehicle

EXCUTIVE SUMMARY

Overview:

Fire resistant design of both structural and non-structural components in road tunnels is predicated on the determination of fire demand intensity. Recent vehicular fires in concrete-lined tunnels have demonstrated the vulnerability of the liner to heat-induced spalling and cracking damage. Current practice typically uses a conservative, deterministic fire curve that does not necessarily provide a representative evaluation of the spatial and temporal distribution of thermal demands in tunnels due to large vehicle fires. This project develops a tunnel-specific probabilistic framework for evaluating vehicle fire frequency and intensity based on tunnel geometry and traffic information. The framework leverages a fast-running computational tool called the Confined Discretized Solid Flame (CDSF) model that has been previously developed by the authors for the tunnel fire analysis. The CDSF model is able to calculate the spatial contour of total heat flux imparted to the tunnel liner due to an enclosed fire. The likelihood of a vehicular fire and the associated fire size distribution are used to generate probabilistic distributions of total fire exposure to the reinforced concrete tunnel liner. Critical heat flux values according to the probability distribution are then used to assess reductions in concrete material strength and resulting losses in structural performance of the system. A case study of the Fort Pitt Tunnel in Pittsburgh, PA is included for demonstration. The framework enables decision making regarding design and renovation of tunnels for fire as well as post-fire inspection by quantifying the risk of capacity reduction in the concrete liner due to a realistic range of fire hazard intensities.

Findings:

One goal of the work is technological transfer. The developed quantitative fire risk assessment of tunnel structure provides information for decision making of tunnel fire safety in terms of the design, renovation, inspection and repair of the fire protection system in tunnels. The stochastic analysis evaluates probability distribution of the fire hazard in tunnels to let tunnel owners determine the level of protection based on the risk of explicit consequence such as tunnel structure damage repair and tunnel closure. The fast-running CDSF model provides compatibility for stochastic and parametric study and capability to accurately predict tunnel-specific fire-induced heat flux on tunnel liners. The tool runs on MATLAB and includes visualization with Rhino and Grasshopper.

CHAPTER 1 - INTRODUCTION

Tunnels are vitally important to the transportation of goods and people by providing efficient passage through difficult terrain and under waterways and urban areas. According to the *Tunnel Operation, Maintenance, Inspection, and Evaluation (TOMIE) Manual* (Bergeson and Ernst 2015), an initial tunnel inventory has been conducted by both the Federal Highway Administration (FHWA) and the Federal Transit Administration (FTA). The inventory identified more than 350 highway tunnels in the United States, in which 40% of them exceed 50 years of service. While a tunnel is generally not the preferred form of transportation structure due to high economic costs and construction time, it several advantages over above ground transportation structures such as improved earthquake resistance (Kolymbas 2005), shorter routes under topography or waterways, and benefits to urban planning by passing under dense urban environments. With the continued improvements in tunnel boring technology, further expansion of U.S. tunnel networks is expected.

The large amount of traffic going through a tunnel with combustible materials such as vehicle fuel and flammable cargo poses threats to the fire safety of the tunnel structures. Flame energy and hot gases generated from vehicle fires in the confined tunnel environment can induce severe damage to the tunnel, which will ultimately lead to significant economic losses due to repair and disruption of tunnel functionality. Currently, the most common material for tunnel liners is reinforced concrete, which could be in the form of precast concrete segments, cast-in-place concrete, or shotcrete. Concrete has been long regarded for its inherent fire resistance due to its low thermal conductivity, high thermal capacity, and high cross-sectional mass. However, exposure to elevated temperature will result in concrete strength reduction both during heating and in its residual post-fire condition. Fire-induced spalling is also a major concern because of concrete's sensitivity to changes in moisture and the magnitude of internal stress developed in the hydrated material because of pore pressure increases and variations in the thermal expansion (Figure 1).

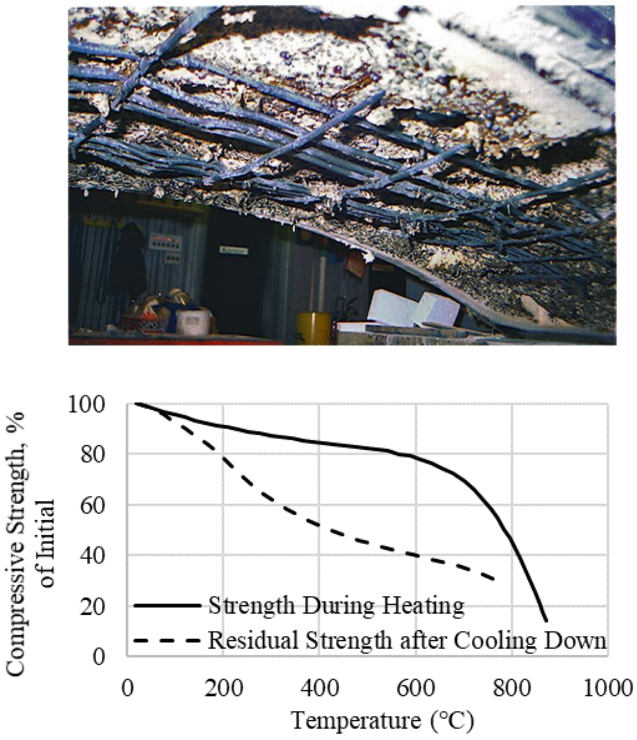

Figure 1 Typical concrete damage after heat exposure: spalling (Jansson 2013) (left) and strength reduction (American Concrete Institute 2014) (right)

Roadway tunnels have an extensive history of fire events which have resulted in damage severities ranging from limited non-structural effects to significant structural damage, including some partial collapses (Maevski 2011). For example, a severe fire from a 2008 cargo train accident inside the Channel Tunnel between the UK and France inflicted damage over a 750-m length of the concrete tunnel lining (BEA-TT and RAIB 2010). According to the technical investigation of that event, the concrete liner spalled to various depths and breached through the section at some locations. This ultimately led to a reduction of the structure's load bearing capacity and increased the risk of progressive collapse. The fire event was followed by 5 months of repair at an estimated cost of $70 million (in 2008 US dollars). Table 1 highlights several of the most severe roadway tunnel fires that have occurred within the United States (US) in the last 75 years. Since 1949, the average vehicle miles traveled through roadway tunnels has increased substantially, which in turn increases the potential for vehicular accidents and subsequent fire (Pearlman and Meltzer 2012). The constant presence of moving vehicles carrying combustible materials (including both vehicle fuel and cargo) through an enclosed environment make tunnels susceptible to severe fire events.

Table 1 List of Roadway Tunnel Fires in the US during 1949 - 2007

Year	Tunnel Name	Length [m (ft)]	Fire Duration [min]	Cause
1949	Holland Tunnel	2550 (8365)	240	HGV Fire, Hazardous Material
1965	Blue Mountain Tunnel	1323 (4339)	not reported	HGV Fire, Engine
1970	Wallace Tunnel	1000 (3280)	not reported	Truck RV Fire, fuel line
1974	Chesapeake Bay Bridge Tunnel	2440 (8000)	240	Collision, HGV Truck
1982	Caldecott Tunnel	1028 (3372)	160	Collision, Car
2002	Ted Williams Tunnel	2600 (8530)	not reported	Bus Fire, Electrical
2007	Caldecott Tunnel	1028 (3372)	not reported	Car Fire, Engine
2007	Santa Clarita I-5 Tunnel	165 (544)	not reported	Collision, Multiple Vehicles

The Permanent International Association of Road Congresses (PIARC) Committees define road tunnel (system) resilience as *"The ability to prepare and plan for, absorb, recover from, or more successfully adapt to actual or potential negative effects of events or developments affecting the availability of a road tunnel. In this context, an acceptable safety level is a mandatory constraint for the availability of the road tunnel."* Explained in more detail by Bruneau et al.(Bruneau et al. 2003), the characteristics of resilience include reducing the failure probabilities; reducing the consequences (e.g., loss of life, damage, and negative economic and social consequences) from hazard events; while reducing the recovery time. From a structural system perspective, this concept has been adopted to optimize the design of roadway tunnels subjected to the hazards including seismicity (Bruneau et al. 2003), flood, and climate change (PIARC Technical Committee C.4 2021). This study extends the application of resilience to tunnel fire hazards by minimizing tunnel traffic disruptions following fire events. The evaluation process, herein, allows for the determination of the most effective tunnel fire mitigation methods for a given tunnel and traffic conditions.

CHAPTER 2 – TUNNEL FIRE RESILIENCE ASSESSMENT FRAMWORK

2.1. Tunnel Resilience

Resilience consists of four properties: (1) *Robustness*: the ability of a structural (or system) to withstand a given level of demand without suffering degradation; (2) *Rapidity*: the capacity to meet priorities and achieve goals in a timely manner to contain losses and recover functionality; (3) *Redundancy*: multiple element systems that retain the functionality when one or more elements fail; and (4) *Resourcefulness*: the capability to identify problems and mobilize alternative external resources to solve the identified problems. For the tunnel fire structural resilience analysis conducted in this study, only the robustness and rapidity are considered. The quantification of redundancy largely depends on the tunnel's role in the entire road network while resourcefulness is an ad-hoc action that varies based on specifications within each transportation jurisdiction. Schematically, the robustness and rapidity for a typical structure or system are illustrated in Figure 2. The resilience of the structure subjected to a single event is quantified using Eq. (1) (Bruneau et al. 2003) and graphically expressed as the shaded area underneath the functionality curve, where t_0 is the time of hazard and t_r is the time of recovery to full functionality.

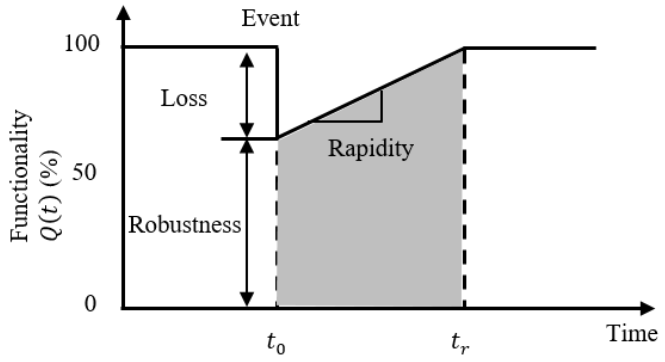

Figure 2: Typical schematic representation of resilience

$$r = \int_{t_0}^{t_r} Q(t)\, dt \tag{1}$$

The functionality curve is determined based on the post-hazard rehabilitation procedures. For the tunnel fire event, there is no consistent detailed post-fire protocol (for inspection or maintenance) across the United States (Gerasimidis and Civjan n.d.). Most Departments of Transportation (DOTs) rely on the guidelines in FHWA's *Tunnel Operation Maintenance*,

Inspection, and Evaluation Manual (TOMIE), which briefly outline methods of tunnel post-fire inspection, which includes on-site visual techniques and rebound hammer residual strength methods. The manual states that tunnels should be closed following the hazard event until inspection has been completed. Following the inspection, the reinforced concrete liner should be repaired as needed. The main steps include the (1) removal of unsound concrete, (2) replacement or supplementation of weakened reinforcement, and (3) restoration of concrete elements to their original cross-sectional dimensions (Gerasimidis and Civjan n.d.). Though not specified in the protocol, in most cases the tunnel remains closed during the repair processes, especially for single bore tunnels (Barry 2010; Tunnel (digital) 2020). The functionality for fire hazard exposed tunnels can be categorized into the two cases shown in Figure 3. For small fire hazards (i.e., car fire with Heat Release Rates (HRR) around 5MW per NFPA 502 (NFPA 2017)), which impose minor thermal impact to the tunnel structural elements, the functionality is considered to retain 100% as presented in Figure 3a. For relatively large fires (i.e., bus fire and HGV fire with HRR ranges from 25 to 200MW), the intense thermal magnitude in conjunction with prolonged exposure results in structural damage requiring inspection and repair. This case corresponds to the functionality diagram presented in Figure 3b, indicating tunnel closure for repair.

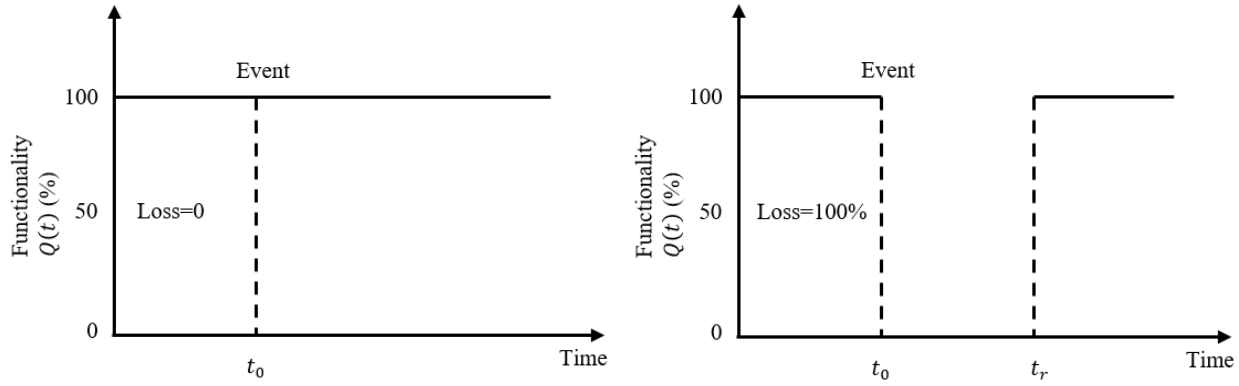

(a) Full resistance to fire impact (b) Fire impact resulting in downtime and repair

Figure 3: Functionality of tunnel subjected to fire hazard

It is clear that the quantification of tunnel resilience using Eq. (1) for these two cases is either 100% for small fires or zero for large fires, regardless of the recovery time. This simplifying assumption of full tunnel bore closure for large fire events and maintained operation for small events can be characterized with the consequence function as expressed in Eq. (2), applied as an inverse to resilience:

$$c = \int_{t_0}^{t_r} 100 - Q(t)dt = \begin{cases} 0 & small\ fire \\ (t_r - t_0) \cdot 100\% & large\ fire \end{cases} \quad (2)$$

This consequence-based resilience assessment is similarly proposed in blast engineering (Quiel et al. 2016). The higher the consequence, the lower the structural resilience. This single event consequence function can be combined into a probabilistic framework to consider the uncertainties associated with both the fire event demand and the tunnel structural capacity. Inspired by the probabilistic resilience assessment methodology proposed by Cimellaro et al. (2010) (Cimellaro et al. 2010), the consequence function for this study is derived by simplifying the performance-based loss function proposed by the Pacific Earthquake Engineering Research (PEER) Center (Muntasir Billah and Shahria Alam 2015; Shinozuka et al. 2000) as in Eq. (3),

$$C = \iint \underbrace{G(CM|DM)}_{Loss\ model} \cdot \overbrace{p(DM|IM)}^{\text{Fragility model}} \cdot \underbrace{p(IM)}_{Hazard\ model} \cdot dDM \cdot dIM = \iint c(DM|IM) \cdot p(DM|IM) \cdot p(IM) \cdot dDM \cdot dIM \quad (3)$$

where *IM* represents the hazard intensity; *DM* is the damage measurement; *CM* is the consequence measurement; p (…|…) and G (…|…) are the conditional probability density function and conditional cumulative distribution. Replacing the original loss model in the original expressing with the consequence function in Eq. (2), which is determined by the severity of thermal impact, generates the probabilistic loss function used to measure resilience in this study.

2.2. Quantification framework

This study proposes a streamlined framework to quantify the tunnel resilience subjected to fire hazards by accessing the functionality loss, shown as a flowchart in Figure 4. It contains the following steps: (1) concrete liner damage assessment tool development; (2) tunnel functionality loss for a range of fire intensities; and (3) overall tunnel loss functionality accounting for traffic composition. In the first step, the tunnel liner damage and amount of removal is determined as function of heat flux and fire duration considering the concrete thermal material properties and their uncertainties which informs the repair procedure post fire. The concrete spall behavior is accounted for and is simulated with MATLAB (MathWorks 2014) – SAFIR (Franssen 2005) interactive finite element analysis. In the second step, the thermal impact on the actual tunnel geometry resulting discrete vehicular fires of various size are calculated via the Confined Discretized Solid Flame (CDSF) model developed by the authors' research team (Guo et al. 2019). The CDSF model allows for computational efficiency and integration of the uncertainties

associated with the fire event (i.e., intensity and combustion energy) along with factors that influence the thermal impact intensity such as tunnel dimension, longitudinal ventilation, Fixed Fire Fighting Systems (FFFS). The recovery time is calculated based on the concrete liner damage state over the tunnel length and the estimated inspection and repair requirements. In the third step, the tunnel traffic is introduced to provide the distribution of fire hazard intensity which is then combined with step 1 and 2 to provide a measure of resilience to potential fire events over a period of time. This framework is applied to parametrically study the efficiency of active fire mitigation methods including ventilation and FFFS in increasing tunnel resilience for structural safety. Moreover, it could provide optimized fire mitigation strategies according to specific tunnel conditions including geometry and traffic composition. To note, each step in this framework is conducted with stochastic analysis. These three steps can be calculated separately because they are in effect independent. For instance, decisive factors for the concrete liner damage are concrete thermal properties, which are independent of the thermal impact calculation in step 2 and traffic conditions in step 3.

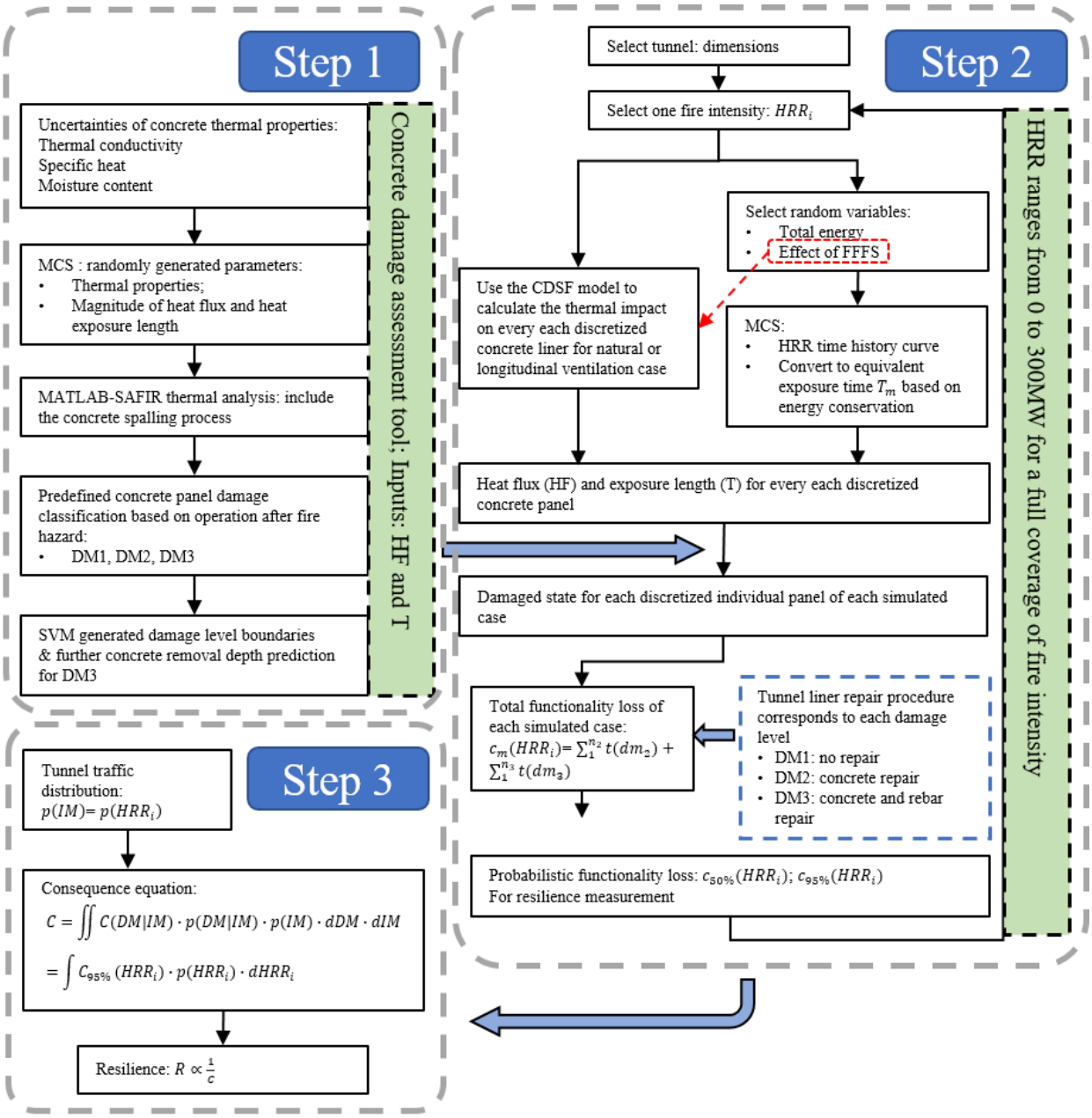

Figure 4: Tunnel fire resilience analysis flowchart.

CHAPTER 3 – CONFINED DISCRETIZED SOLID FLAME MODEL (NATURAL VENTILATION)

3.1. Confined Discretized Solid Flame (CDSF) Model

The CDSF is a hybrid analytical model that includes both radiative and convective effects for calculating the total incident heat flux on the interior surface of a tunnel liner due to an enclosed fire. Similar to the previously proposed MDSF models for large open-air fires (Quiel et al. 2015), the flames are represented as a solid 3D object whose surfaces are discretized and assigned an emissive power. As shown in Figure 5 (left), each target surface on the tunnel liner receives straight-line radiation from each discretized solid flame element in accordance with their relative emissivity, standoff, and angles of orientation. When developing the solid flame model, the flame height is initially generated without consideration of tunnel confinement using semi-empirical equations for open-air fires (Heskestad 1983). If the calculated "free flame" height extends beyond the tunnel ceiling, the flame shape is compressed and becomes "confined" by the tunnel – the result is regarded as the confined flame shape. Radiative energy conservation is considered for the flame confinement. A convective region is then defined along the tunnel ceiling to account for thermal demands from ceiling jets of smoke and hot gas (Figure 5, right). Each target surface on the liner receives convective heat flux in accordance with its location within the convective region. The summation of radiative and convective effects, illustrated below in Figure 5, represents the total fire-induced heat flux experienced by the interior face of the tunnel liner mesh.

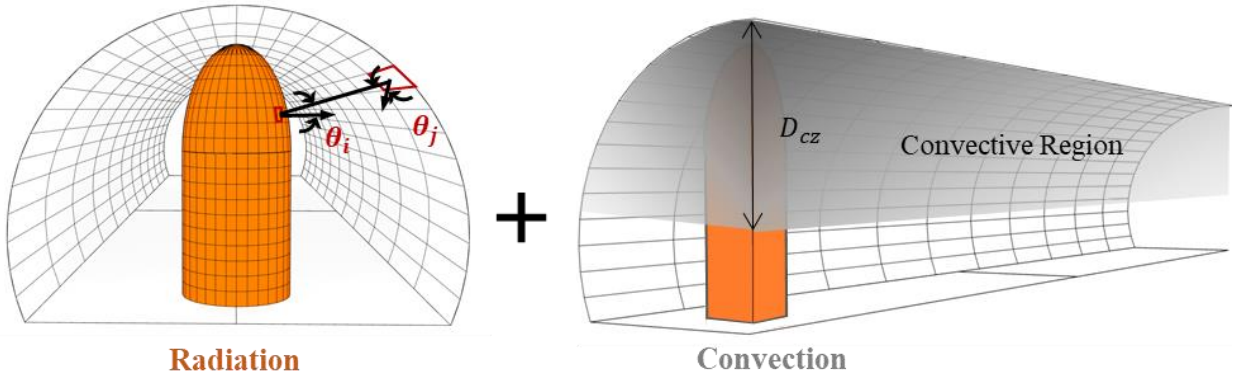

Figure 5 Illustrations of radiative (left) and convective (right) heat transfer for the CDSF model

3.1.2 Modeling Assumption

Two simplifications are made regarding the tunnel prototypes for this first phase of CDSF model development. First, the tunnels are assumed to have no longitudinal grade to obtain a symmetric distribution of fire effects in both longitudinal directions. Future work will include the effects of the tunnel grade on the longitudinal movement of the smoke and hot gases. Second, all fire scenarios in this paper are evaluated assuming natural (i.e. unforced) ventilation in the tunnel during the fire event. Though many tunnels are designed with forced ventilation systems along their ceilings, their fans, ducts, and electrical power may be disrupted, damaged, or ineffective during a severe fire. If it remains operational, the ventilation system can move the combustion byproducts and alter the resulting distribution of convective heat flux, as well as the progression of combustion due to increased air flow. The next phase of development for the CDSF model will incorporate the effects of realistic ranges of ventilation volume and velocity.

For this first phase of CDSF model development, the fire location is assumed to be at the longitudinal and transverse center of the tunnel to enforce symmetry and neglect the increased air inflow and ventilation when the opening is close to the fire. Different longitudinal and transverse fire locations relative to the tunnel liner and openings will be explored in future work. The longitudinal distance from the tunnel openings to the fire may influence airflow during the fire, potentially affecting the HRR and resulting heat transfer to the liner. If the fire is located in an off-center transverse location, the standoff to the liner will be less on one side and generate a localized increase in radiation heat flux.

3.1.2. Solid Flame Geometry

Severe fires in tunnels are typically generated from fuels that include vehicles (cars, buses, trucks, train cars, locomotives, etc.) and the cargo they carry (the most severe being hydrocarbons and flammable consumer or industrial products). This study focuses on severe fires due to buses and heavy goods vehicles (HGV's), which are identified in NFPA 502 as typical design fire scenarios for tunnels (*NFPA 502, Standard for road tunnels, bridges, and other limited access highways* 2011). Empirical estimates of HRR for a range of bus and HGV fires is available in the published literature. Fires due to these vehicles and their cargo will have an elongated, approximately rectangular footprint that resembles the actual vehicle dimensions, as illustrated in Figure 6 for an HGV. These fires would realistically involve an eclectic mix of burning materials such as hydrocarbon fuel, lubricants, plastics, foams, wood, batteries, electronics, etc. Estimating the aggregate combustion properties of these materials, which would be needed to calculate the geometry and intensity of the resulting fire, is difficult due to limited availability of key data such as mass loss rate and heat of combustion.

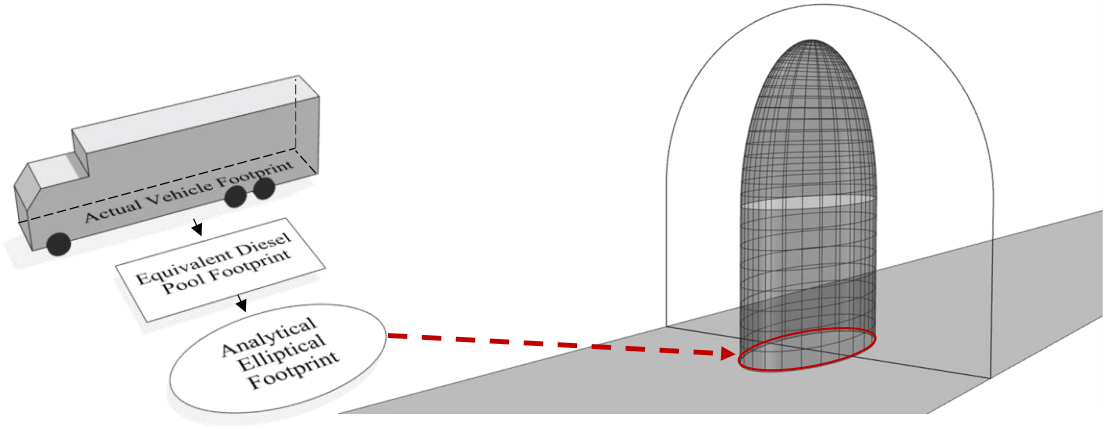

Figure 6 Development of the CDSF footprint based on an HGV fire scenario

Rather than explicitly modeling the aggregate combustion of the various materials, the vehicle fire scenarios in this study are represented more simplistically as hydrocarbon pool fires with equivalent HRR. Semi-empirical predictions of the intensity and geometry of hydrocarbon pool fires are well established from decades of previous research, and combustion properties for these fuels are readily available in the published literature. This approach is analogous to the use of equivalent weights of TNT as a measure of explosive energy when evaluating blast effects on structures (Department of Defense (DoD) 2014). In this study, the equivalent footprint of a diesel pool fire is used to provide the same energy release as an actual vehicle and/or cargo fire. Diesel

is chosen as the fuel type because the experimental data used for model validation (shown later in this paper) was generated from fire tests performed with diesel (Bechtel/Parsons Brinckerhoff. and Bechtel/Parsons Brinckerhoff. 1995). The rectangular footprint of the equivalent diesel pool fire (see Figure 6) is scaled from the vehicle footprint to obtain the same HRR as the pre-defined vehicle fire scenario. Further research is needed to demonstrate the equivalence of exposure to an idealized diesel fire versus a realistic fire involving a combination of vehicles and cargo, particularly regarding mass loss rate, soot yield, and radiative fraction.

In the existing literature, almost all semi-empirical expressions for calculating hydrocarbon pool fire characteristics (including HRR (Babrauskas 2016), radiative fraction (McGrattan et al. 2000; Muñoz et al. 2007), and flame height (Hurley 2016a)) are based on experiments performed with circular pool footprints. The characteristics of a solid flame model with a non-circular footprint can be obtained by calculating an effective circular fire diameter, $D_{f,eff}$ (m), based on the area of the non-circular footprint. For a rectangular fire footprint with length L_f (m) and width W_f (m), $D_{f,eff}$ is calculated as follows:

$$D_{f,eff} = \sqrt{\frac{4\left(L_f \cdot W_f\right)}{\pi}} \tag{4}$$

$D_{f,eff}$ can then be used as input for semi-empirical calculations of HRR and flame height that assume a circular pool fire footprint. Previous literature has indicated that $D_{f,eff}$ can be calculated directly from the full area ($A_f = L_f \cdot W_f$) of rectangular footprints that have an aspect ratio (i.e. ratio of longer edge length to shorter edge length) less than 2.5 (McGrattan et al. 2000). For this study, the equivalent diesel pool fire footprint as shown in Figure 6 is conservatively set to an aspect ratio of 2.

Peak HRR, $\dot{Q}_{f,max}$ (kW), for the rectangular pool fire is calculated using $D_{f,eff}$ (Babrauskas 2016):

$$\dot{Q}_{f,max} = \dot{m}''\Delta H_{c,eff} A_f \left(1 - e^{-k\beta \cdot D_{f,eff}}\right) \tag{5}$$

where $\dot{m}''$ is the mass loss rate per unit area (kg/(m^2-s)), $\Delta H_{c,eff}$ is the effective heat of combustion (kJ/kg), and $k\beta$ is an empirical constant (m^{-1}). These variables are fuel specific and can be obtained from available references (Siddapureddy 2013). The free flame height, H_f (m), is calculated as a function of $\dot{Q}_{f,max}$ (kW) and $D_{f,eff}$ (Hurley 2016a):

$$H_f = 0.235\dot{Q}_{f,max}^{0.4} - 1.02D_{f,eff} \tag{6}$$

If the free flame height is less than the ceiling height, then the 3D solid flame could be simply extruded as a rectangular box with height H_f (Quiel et al. 2015). An extruded rectangular shape, however, can produce "blind spots" when calculating the radiation heat flux to a nearby target from the corners of the solid flame. Specifically, steep angles between the normal vectors of the target surfaces and those of the discretized fire surfaces at the corners can artificially decrease the calculated radiation when compared to a realistic fire. To mitigate corner effects, the "analytical" footprint for the CDSF model in Figure 6 is approximated as an ellipse with the same perimeter (and thus the same overall radiation emission) as the equivalent diesel fire's rectangular footprint. The ratio of major axis to minor axis for the analytical elliptical footprint is the same as the aspect ratio of the equivalent diesel pool footprint, which equals 2.0.

Figure 7 shows that the free flame is vertically bifurcated into a main body (which is vertically extruded from the elliptical footprint over the lower $0.4H_f$) and a tapering top section (which approximates the flaring or whirling nature of the flames over the upper $0.6H_f$) per previous research by Zhou et al. (Zhou et al. 2014). To again avoid sharp transitions in the CDSF's shape, the conical shape proposed by Zhou et al. (Zhou et al. 2014) is replaced with a truncated ellipsoid dome as shown in Figure 5 and Figure 7.

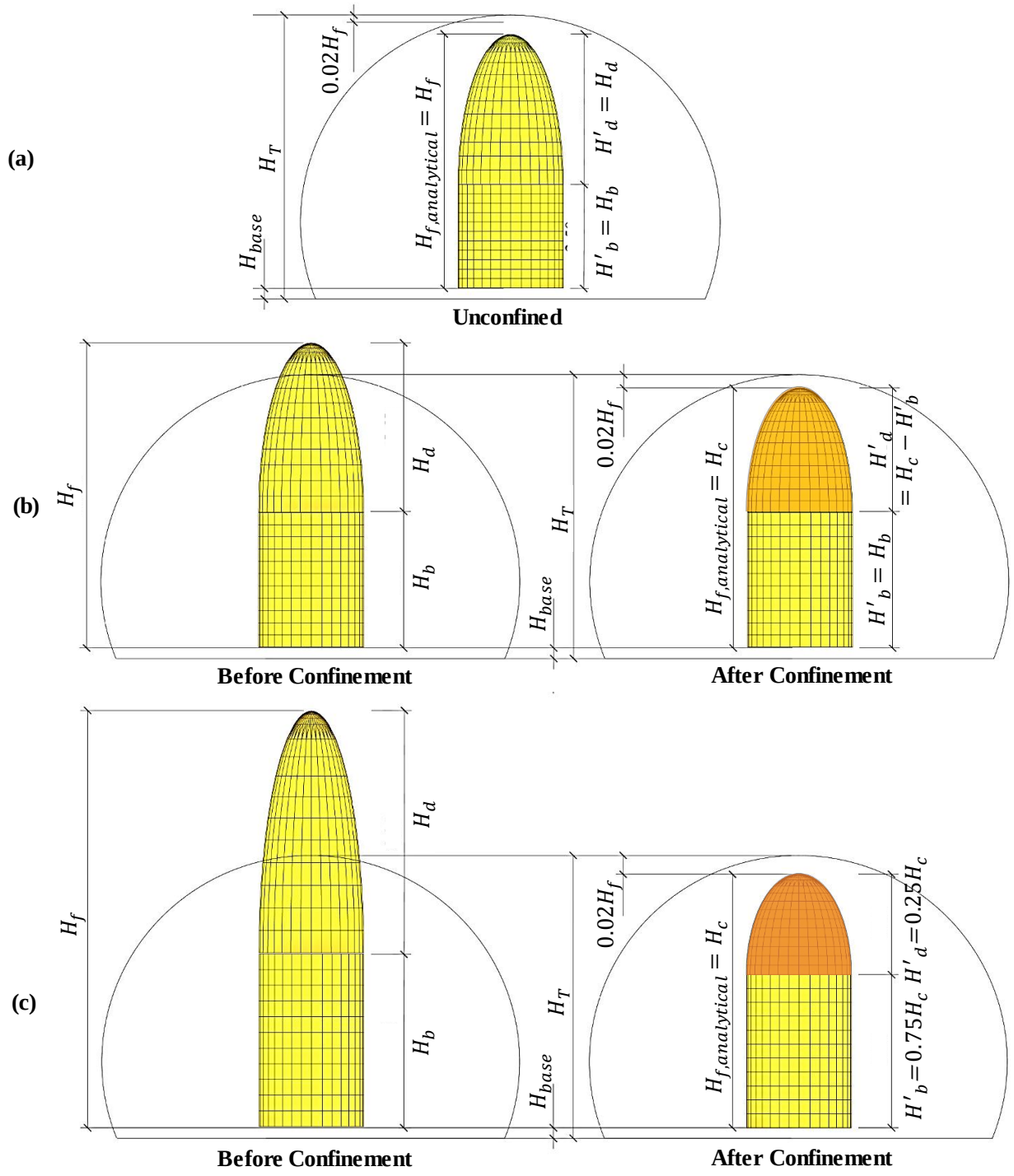

Figure 7 Schematic comparison of the free flame and confined flame models in the tunnel cross-section

3.1.3. Radiation Heat Transfer

The emissive power, E (kW/m^2), of the flames is assumed to be uniform across the surface of the 3D free flame shape and is calculated as a function of $\dot{Q}_{f,max}$ (kW); total free flame surface

area, A (m^2); and radiative fraction, χ_r (i.e. the fraction of the energy released from the fire as thermal radiation (McGrattan et al. 2000; Muñoz et al. 2007)):

$$E = \frac{\chi_r \dot{Q}_{f,max}}{A} \tag{7}$$

Values of χ_r are readily available in the current literature on hydrocarbon pool fires, either as a general expression for common fuel types (McGrattan et al. 2000) or specific to individual fuels based on experimental testing (Muñoz et al. 2007). In this study, χ_r for diesel is calculated according to Munoz et al. (Muñoz et al. 2007) as a function of the fire's effective diameter:

$$\chi_{rad} = \begin{cases} for\ D_{f,eff} \leq 5m: & 0.158 D_{f,eff}^{\ 0.15} \\ for\ D_{f,eff} > 5m: & 0.436 D_{f,eff}^{\ -0.58} \end{cases} \tag{8}$$

As shown in Figure 7, the height of the fire's base above the road surface, H_{base} (m), approximately accounts for the bumper height of the burning vehicle. If H_f plus H_{base} remains below the tunnel height (Figure 7a), then H_f is used as the "analytical" flame height, $H_{f,analytical}$ (m), for CDSF modeling. However, the free flame height from Eq. 9 will often exceed the height of the tunnel, H_T (m), for significant fires. In those cases, the free flame height is reduced to fit inside the tunnel enclosure, thus "confined", to obtain $H_{f,analytical}$. The confined flame height, H_c, (m) is therefore calculated as follows:

$$H_c = H_T - 0.02H_f - H_{base} \tag{9}$$

To provide the flame surfaces with adequate view of the tunnel liner at close range (i.e., to "engulf" those targets with appropriately high radiation heat flux), the top of the ellipsoid dome is offset from the tunnel ceiling by a small value equaling $0.02H_f$.

For free flame heights that just exceed the tunnel height (Figure 7b), the dome is compressed while the height of the extruded ellipse body remains at $0.4H_f$. For increasingly severe fires (Figure 7c), the free flame height can become so tall that the ellipsoid dome would be unrealistically compressed or even eliminated (resulting in poor analytical calculations of radiation heat flux on the ceiling) if no height adjustments were made to the $0.4H_f$ main body. To preserve the bifurcated structure of the confined solid flame, the height of the confined flame body is modeled as no greater than $0.75H_c$, and the ellipsoid dome can therefore be no less than $0.25H_c$. The confined flame shape will naturally have less surface area than the free flame shape; however, since the HRR output is unchanged, both the free flame and confined flame shapes should emit the same total radiation from their discretized surfaces. The emissive power in the ellipsoid dome,

E_d (kW/m^2), of the confined flame is therefore increased from the free flame emissivity, E, from Eq. 7 by the ratios shown below to account for engulfment of the ceiling:

$$E_d = E\left(\frac{A_d}{A_d{}'}\right)\left(\frac{A_b}{A_b{}'}\right)^2 \tag{10}$$

where A_b and A_d (m^2) are the surface areas of the free flame body and dome, and A_b' and A_d' (m^2) are the surface areas of the confined flame body and dome. The ratio of A_d to A_d' will be greater than unity for any confined flame shape. The ratio of A_b to A_b' will be greater than unity only if the free flame body height exceeds $0.75H_c$. This second ratio is squared in Eq. 10 to account for the increasing flame turbulence when the free flame height is much higher than the tunnel height. The emissive power in the ellipsoid body remains at the free flame emissivity from Eq. 7 ($E_b = E$). As will be demonstrated later in this paper, predictions of radiation heat fluxes from this approach to energy conservation compare well with validated high-fidelity FDS solutions for a wide range of fire severities.

Having defined the analytical flame shape and surface emissive power, the radiative heat flux received on the visible surfaces of the tunnel liner can be calculated as follows:

$$q''_{rad,j} = \sum_{i=1}^{n} E_i F_{i\to j} = \sum_{i=1}^{n} E_i \frac{A_i \cos\theta_i \cos\theta_j}{\pi r_{i\to j}^2} \tag{11}$$

The radiative contribution from each emitting flame surface, i, is summed at each target surface, j. Total radiation heat flux at each target surface, $q''_{rad,j}$, is calculated as a function of the flame surface emissive power, E_i (kW), and the dimensionless view factor, $F_{i\to j}$, between receiving and emitting surfaces.

3.1.4. Convective Heat Transfer

A convective region at the tunnel ceiling is included in the CDSF to simulate the heat flux contributed by the ceiling jet and smoke effects. Through FDS-informed calibration (which will be demonstrated later in this paper), convective heat flux is applied to target elements within the predefined convective zone, which has a vertical depth D_{cz} (m) along the total length of the tunnel (see Figure 5). The value of D_{cz} is based on the luminous flame fraction, χ_{lum} (i.e. the luminous height of a pool fire flame that is unobstructed by smoke (Muñoz et al. 2007)). Values of χ_{lum} for a diesel pool fire can be calculated as a function of $D_{f,eff}$ per previous experimental work by Munoz et al. (Muñoz et al. 2007):

$$\chi_{lum} = \begin{cases} for\ D_{f,eff} < 5m: & 0.3 \\ for\ 5m \le D_{f,eff} < 20m: & 1.26{D_{f,eff}}^{-0.2577} - 0.533 \\ for\ D_{f,eff} \ge 20m: & 0.05 \end{cases} \quad (12)$$

The analytical flame height $H_{f,analytical}$ (equal to H_f for unconfined flame shapes and H_c for confined shapes) is thereby multiplied by χ_{lum} to obtain the depth of the convective zone:

$$D_{cz} = H_T - H_{base} - \chi_{lum} H_{f,analytical} \quad (13)$$

Previous studies of tunnel fires have shown strong correlation between the spatial distributions of convective heat flux and ceiling jet gas temperature. For example, Li and Ingason (Li and Ingason 2015) developed an exponential scaling fit for longitudinal temperature distribution within the smoke region based on model-scale tunnel fire tests. Using an FDS-informed fit that is correlated to peak HRR and tunnel size, the authors have developed a similar model for the longitudinal decay of convective heat flux under the tunnel ceiling, beginning with the calculation of the maximum convective heat flux directly above the fire:

$$q_{c,max} = 68 \ln\left(\dot{Q}_{f,max}\right) - 702 \quad (14)$$

The longitudinal decay of q_c (kW/m^2) away from the fire location is calculated via Eq. 15, where x (m) represents the longitudinal distance from the fire's center:

$$\frac{q_c(x)}{q_{c,max}} = 0.38e^{-6.75\left(\frac{x-x_v}{H_T}\right)} + 0.5e^{-0.27\left(\frac{x-x_v}{H_T}\right)} \quad (15)$$

The "virtual origin" of the fire, x_v, (m) is a function of the flame length, L_{flame}, (m) and the height of the tunnel, H_T (Li and Ingason 2015):

$$x_v = \begin{cases} for\ L_{flame} > 5.2H_T: & L_{flame} - 5.2H_T \\ for\ L_{flame} \le 5.2H_T: & 0 \end{cases} \quad (16)$$

$$L_{flame} = 12H_T\dot{Q}_f^* \quad (17)$$

Dimensionless HRR ratio, $\dot{Q}_f^*$, is calculated via Eq. 18 as a function of peak HRR, $\dot{Q}_{f,max}$ (kW); air density, ρ_0 (kg/m^3); air heat capacity, c_p (kJ/kg-K); ambient air temperature, T_0 (K); gravitational constant, g (m/s^2); the tunnel opening area, A_o (m^2); and effective tunnel height H_{ef} (m) (equal to H_T minus H_{base}):

$$\dot{Q}_f^* = \frac{\dot{Q}_{f,max}}{\rho_0 c_p T_0 g^{\frac{1}{2}} A_o H_{ef}^{\frac{1}{2}}} \quad (18)$$

Previous research by Rafiei (Rafiei 2015) on rectangular tunnels examined the relationship between transverse and longitudinal movement of the smoke along the ceiling as a function of its buoyancy. Based on that study, the convective heat flux in the CDSF model decreases linearly along the radial length of the ceiling from $q_c(x)$ at H_T to zero at the bottom of the convective region (i.e. at a height of H_T minus D_{cz}).

By combining the radiative and convective effects, the spatial distribution of total incident heat flux can be mapped to the discretized tunnel liner. A detailed flowchart which illustrate steps for both radiation and convection computation in the proposed model is shown in Figure 8. An example distribution for a large fire in a circular tunnel is shown in Figure 9. Later sections of this paper will show good comparisons of heat flux predictions between the CDSF model and experimentally validated FDS solutions.

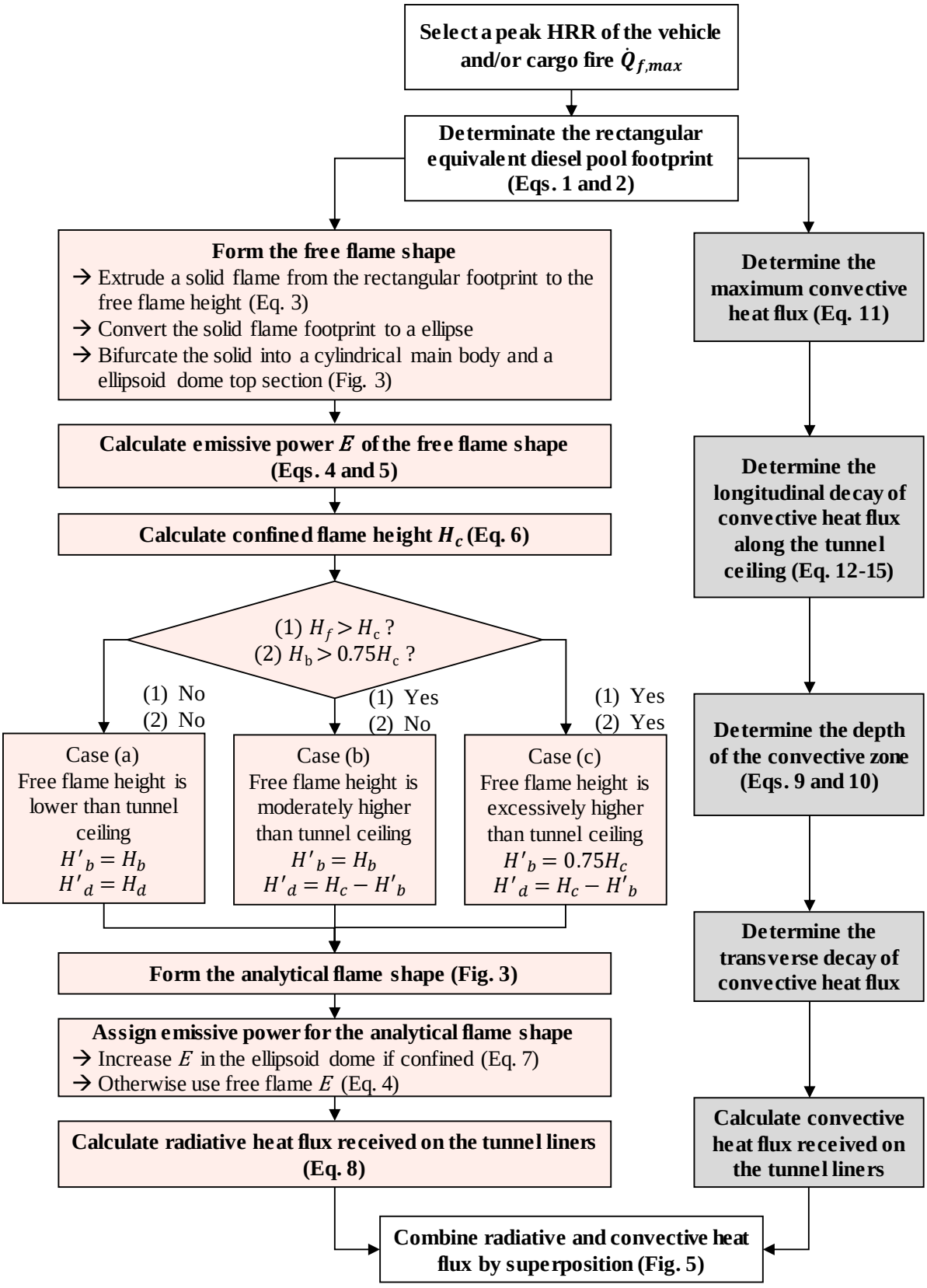

Figure 8 Flowchart of the proposed CDSF framework

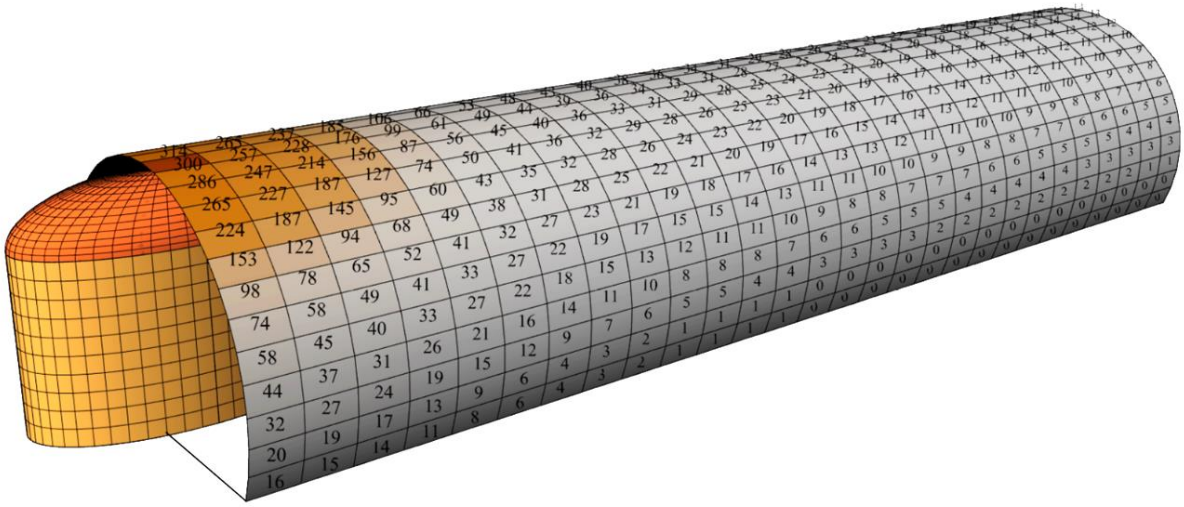

Figure 9 Section cut at the longitudinal center showing typical CDSF output (heat flux values in kW/m^2)

3.2. Computational Model Validation

Given the current literature, direct experimental validation of total heat flux is not feasible since most full-scale fire tests in tunnels to date have focused on temperature distributions, combustion dynamics, and smoke movement. Temperature data from a full-scale tunnel fire test program in the Memorial Tunnel in West Virginia, USA (Bechtel/Parsons Brinckerhoff. and Bechtel/Parsons Brinckerhoff. 1995) and heat flux data from the fire test program in the Runehamar Tunnel in Norway (Ingason et al. 2015b) are used for FDS model validation (McGrattan et al. 2013a). A mesh sensitivity study was conducted for the Memorial Tunnel fire tests, and the resulting mesh zone distribution was then used for both validation cases. The validated FDS modeling approach is subsequently used to develop several benchmark fire scenarios within a selection of tunnel cross-sections that are typical of the current US inventory. When adapting the FDS model for these tunnel fire scenarios, the meshing approach, combustion modeling parameters, and material inputs are kept consistent with the validation cases. Total heat flux results from those FDS simulations are then used to computationally calibrate the CDSF approach in the next section of this paper.

3.2.1. Modeling the Memorial Tunnel Fire Tests

The Memorial Tunnel, decommissioned in 1987, has a horseshoe-shaped cross-section with a width of 8.77 m, maximum height of 7.87 m, total length of 854 m, and a longitudinal grade of 3.2% (Bechtel/Parsons Brinckerhoff. and Bechtel/Parsons Brinckerhoff. 1995). The tunnel was subjected to controlled fire events located 617 m from the north portal. Two tests from the Memorial Tunnel program that were conducted without forced ventilation (Nos. 501 and 502) are

used in this study for FDS validation. The tests had target HRR of 20 MW and 50 MW and used diesel in rectangular pans as the fire source, which was located in the transverse center of the tunnel section. The fire source was modeled in FDS as a rectangular burner surface whose area and heat release rate per unit area (HRRPUA) were defined to achieve the same HRR as that recorded during the tests. Soot yield is taken as 0.1 for diesel (Siddapureddy 2013), and the fire's radiative fraction is calculated per Eq. 8 as a function of the effective diameter of the fire (Muñoz et al. 2007). Default FDS parameters for radiation simulation, such as the number of solid angles (100 angles) and the application of the gray gas radiation transport solver, were implemented for all analysis cases.

A layered surface with thickness of 0.3 m (the same thickness as the actual tunnel liner) was used to model the tunnel liner surfaces with concrete material properties per default settings in accordance with NIST online resources for FDS (McGrattan et al. 2013a). The slope of the tunnel was applied by specifying gravity components in FDS. The fuel pans and road surfaces were defined as inert. Tunnel openings were modeled using open vents, beyond which the ambient environment is assumed to exist. These boundary conditions allow longitudinal air movement across the opening through the length of the tunnel during the fire.

Both the gas temperature and total heat flux were measured longitudinally along the crest of the tunnel ceiling in FDS. Temperature measurements in the test were taken at several time increments using thermocouple trees at 15 cross-sections throughout the length of the tunnel with expected measurement accuracy of 0.75%. Gas temperature data was provided in the test report as contour lines in 37.8°C (100°F) increments – comparisons with FDS were made by linearly interpolating across those contours. The time history of the FDS gas temperatures just below the ceiling were measured at the same locations reported from the fire tests as well as at a denser spacing directly above the fire. Time-dependent heat flux was measured at increments ranging from 2 m to 5 m, again with more measurements taken near the fire.

The interior volume of the tunnel is discretized into approximate cubic cells – for improved computational efficiency, the mesh is finest near the location of the fire and then increasingly coarse toward the ends of the tunnel. A mesh sensitivity study was performed for the larger 50 MW fire to determine an adequate size of the finest mesh at the fire location as well as an appropriate mesh zone distribution along the tunnel length. Mesh selection is based on good agreement with the Memorial Tunnel fire test data as well as solution convergence. In a separate

study, McGrattan et al. (McGrattan and Hamins 2002) also used FDS to model the Memorial Tunnel fire tests and adopted a 0.30-m cubic mesh over a length of 130 m centered on the fire location (with coarser mesh beyond). In this study, the finest mesh size is similarly set to 0.25 m and applied over lengths of either 30 m, 60 m, or 100 m centered on the fire location, as shown in Figure 10. This figure also shows that the mesh size is doubled over a 100-m length beyond the finest mesh zone and then doubled again for the remaining tunnel length.

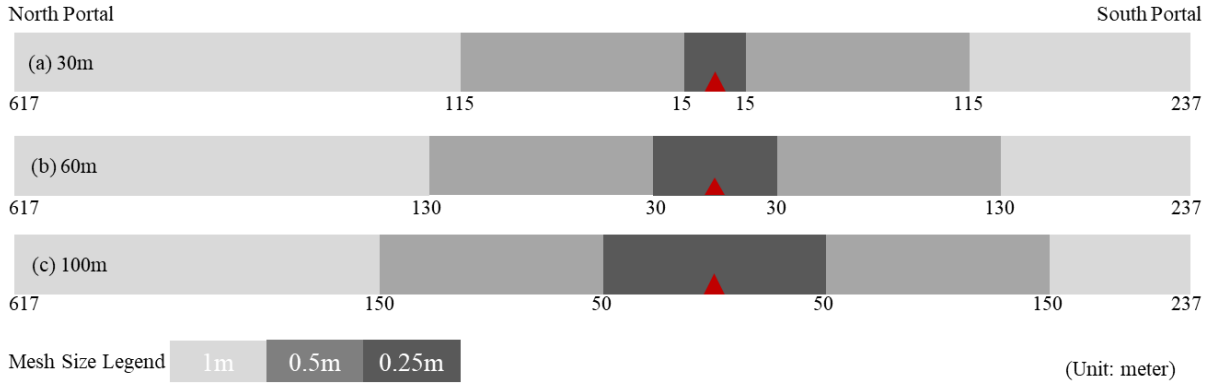

Figure 10 Mesh distributions for the FDS sensitivity study in the Memorial Tunnel

Figure 11a shows that FDS results from all three mesh variations agree well with the experimentally measured ceiling temperatures. The plot also shows that the temperature distribution is negligibly sensitive to changes in mesh size distribution. Figure 11b shows noticeable yet relatively small mesh sensitivity for total heat flux at the ceiling. In particular, each model experiences a small jump in heat flux at the transitions between mesh sizes. To reduce the influence of turbulence in the FDS time history results, note that the gas temperature from FDS at 3 min was the time-average of temperature data in the 10 second interval at 3 min ± 5 seconds. The FDS heat flux is the average heat flux during the steady state. Since the heat flux reduces to less than 50 kW/m^2 within +/- 25m for the 50 MW fire scenario, mesh option (b) (with the finest mesh at +/-30 m from the fire) experiences a less significant heat flux jump than option (a) and is more computationally efficient than option (c). Mesh option (b) is therefore selected for the remaining FDS analyses in this study. Using this meshing approach, the FDS ceiling temperatures show good agreement with the corresponding test results for both the 50 MW and 20 MW fire scenarios (see Figure 12). The same 10-second time averaging is used for temperatures in the 20 MW scenario at the 5 min mark.

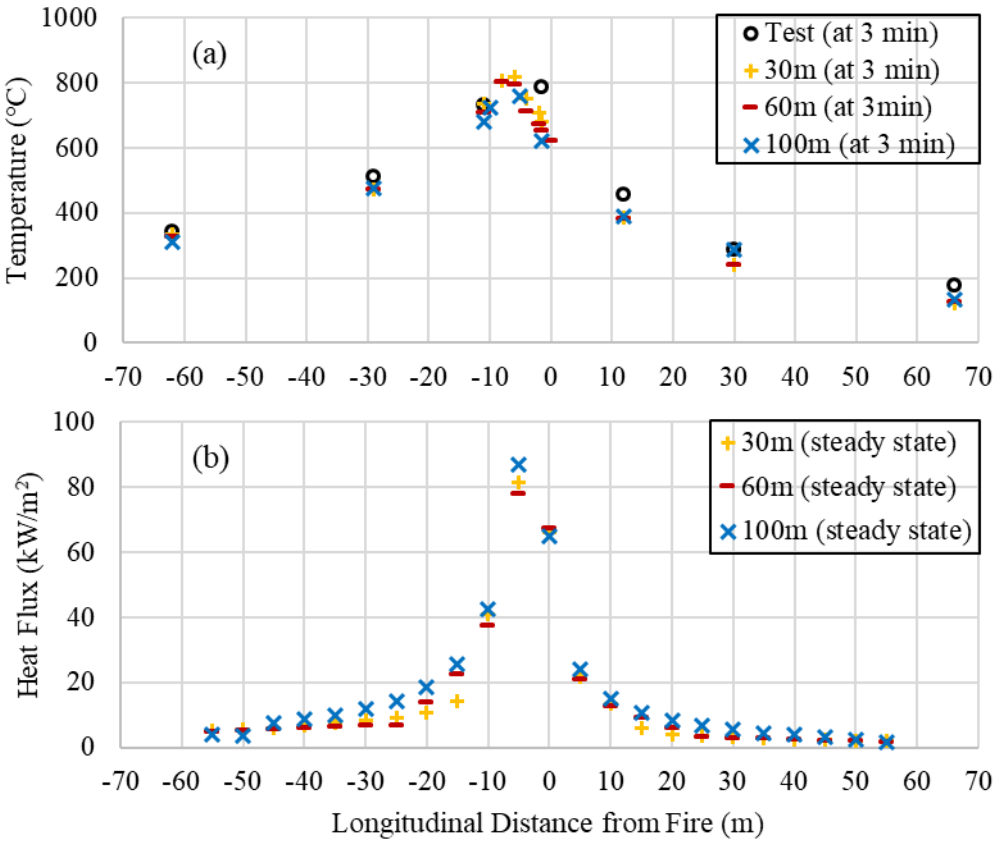

Figure 11 Comparison of ceiling measurements for the 50 MW Memorial Tunnel fire: (a) gas temperature after 3 min elapsed time (test (Bechtel/Parsons Brinckerhoff. and Bechtel/Parsons Brinckerhoff. 1995) vs. FDS), and (b) average steady state heat flux (FDS only)

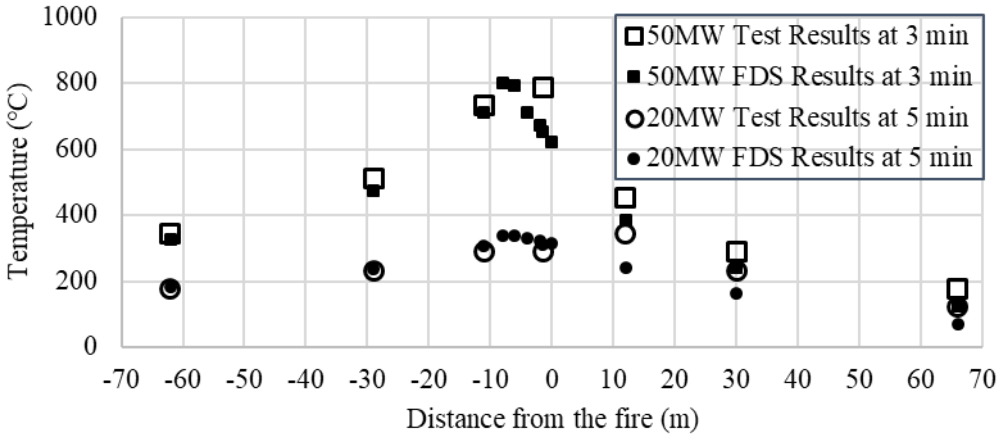

Figure 12 Comparison of FDS ceiling temperature (meshing option (b)) and test data (Bechtel/Parsons Brinckerhoff. and Bechtel/Parsons Brinckerhoff. 1995) for the 20 MW and 50 MW Memorial Tunnel fires

Due to its complexity and computational cost, FDS analysis may be impractical for conventional design or stochastic parametric analysis, which requires a less demanding tool to accurately predict thermal demands due to tunnel fires. For the same analysis of the 50 MW Memorial Tunnel fire test, the CDSF approach (resulting in heat flux data similar to that shown in Figure 9) required only 0.5% of the computational runtime for an analysis with 200-second fire duration (which adequately achieves steady state) compared to FDS 6 (run with parallel processing and full system dedication).

3.2.2. Modeling the Runehamar Tunnel Fire Test

The decommissioned Runehamar Tunnel has an approximate rectangular cross-section with a width of 9 m, height of 6 m, and total length of 1600 m with variable longitudinal grade. The fire source was located at the transverse center and about 1037 m from the east portal in a location with 1% grade (Ingason et al. 2015b). To shield personnel and the tunnel liner from the fire effects, a steel frame portal with fire protection boards on its interior face was erected around the fire location. Mobile fan units placed near the east portal generated an average longitudinal velocity ranging from 2.0 m/s to 2.5 m/s during all tests. Heat flux data was measured at longitudinally at 0 m, 10 m, 20 m and 40 m downstream from the fire center along the ceiling of the fire protection boards. Since it shared the same fuel as the proposed approach, a 6 MW diesel fire test from this test program is selected for validation of the model in FDS with respect to ceiling heat flux.

The fire source for the Runehamar Tunnel fire test was modeled as a rectangular burner surface, similar to that used for the Memorial Tunnel fire tests. The height of the burner surface was assumed to be 0.5m from the ground. Parameters for the reaction such as soot yield and radiative fraction were selected to be consistent with the validation analyses of the Memorial Tunnel fire tests. Modeling parameters such as the material properties and open boundary condition at the tunnel opening is also the same as that used to model the Memorial Tunnel fire tests. Initial wind velocity from the east portal of the tunnel was taken to be 2.1 m/s. As in the test, the model included the fire protection boards, with the geometry and material properties from the test report (Ingason et al. 2015b), that were placed around the fire source. The steel frame was not modeled in FDS due to a lack of specific information. Incident heat fluxes on the ceiling were measure in FDS at the same location as in the test.

Figure 13 shows the comparison of heat flux time history measurement between the 6 MW diesel pool fire test in Runehamar Tunnel and the FDS results. Right above the fire at 0 m, the

FDS heat flux time history is conservatively consistent with the steady state heat flux from the test. The FDS simulation does not capture the initial spike in heat flux as the fire ramps up around ~1 min; however, the duration of the spike is short and therefore not structurally significant. At 10m, 20m and 40m, the FDS heat flux shows overall good agreement with the test results, with differences less than 1 kW/m^2.

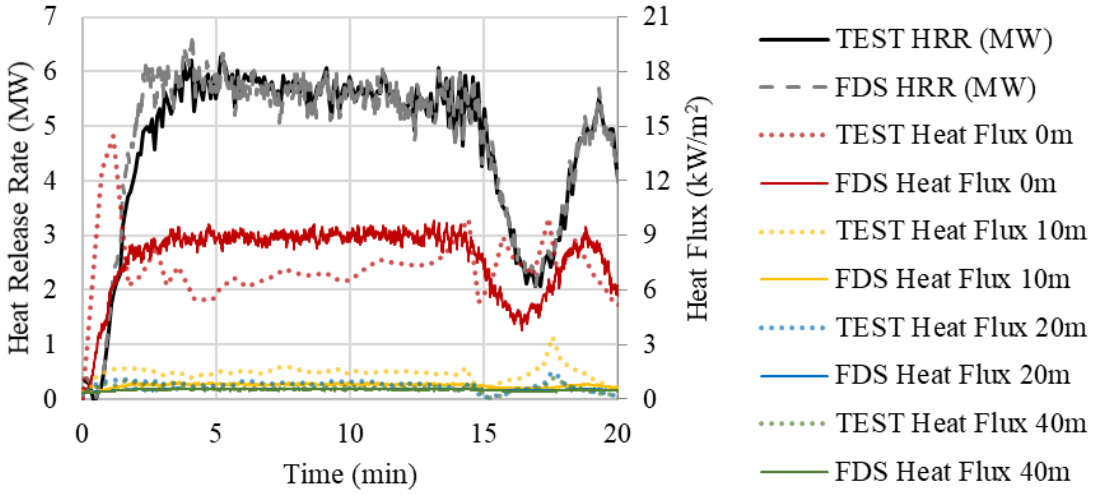

Figure 13 Heat release rate and ceiling heat flux time histories for the 6 MW Runehamar Tunnel fire

3.3. Parametric Study

The proposed CDSF model and experimentally validated FDS approach are subsequently used to evaluate the total heat flux distribution on the interior face of the tunnel liner for a wider matrix of fire scenarios and tunnel cross-section shapes and sizes. In each FDS analysis, the HRR is modeled with an initial 30-second parabolic t^2 ramp-up and then maintained at steady state. For all fire scenarios considered in this study, a total FDS time history of 5 minutes is sufficient to develop steady state heat flux exposure to the liner. Heat flux measurements in the CDSF model are taken at every liner discretization as illustrated in Figure 14. Heat flux time histories are recorded in the FDS model at discrete points in the longitudinal direction (at the ceiling and along the sidewall) as well as radially around the fire location. These points correspond to the centers of select liner discretization in the CDSF model.

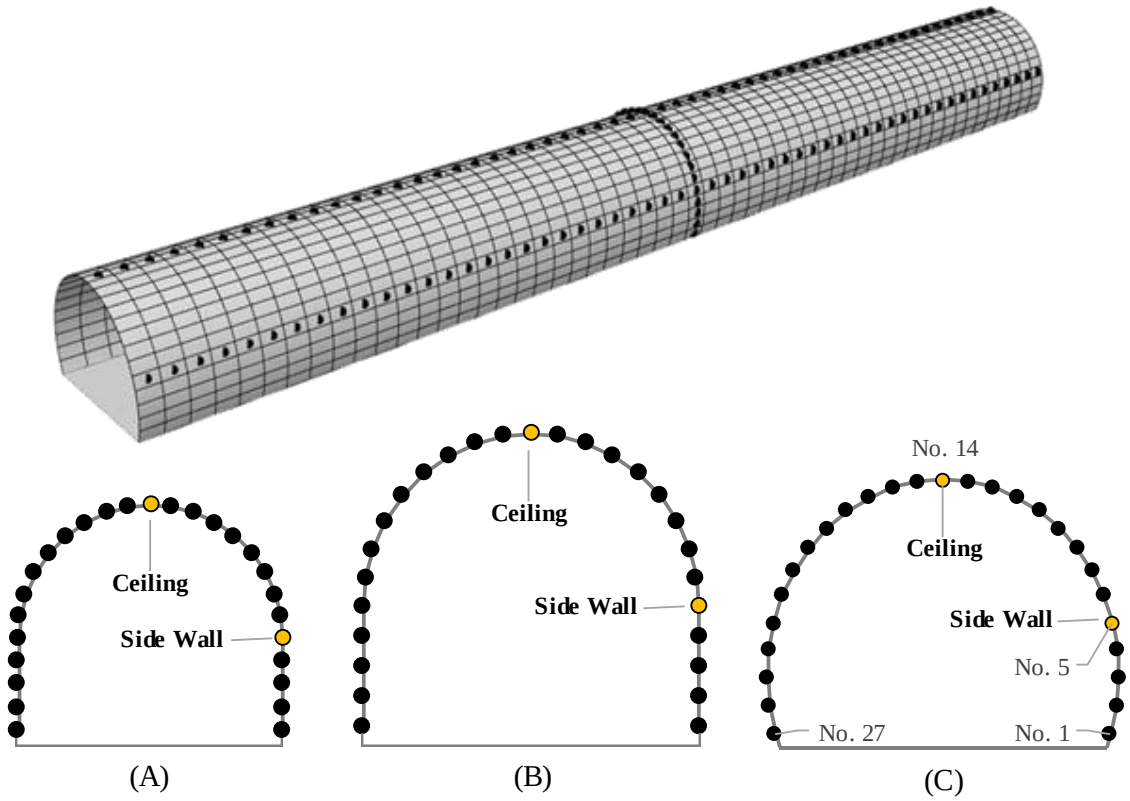

Figure 14 Locations of heat flux measurement to compare the CDSF and FDS models

3.3.1 Tunnel Prototypes

According to current data (USDOT 2015), four cross-sectional shapes are typically used for the majority of the current tunnel inventory in the US: horseshoe, rectangular, circular, and oval. The accumulated inventory from 1882 to 2015 for each tunnel shape is plotted in Figure 15. The data clearly shows that cross-sections with curved ceilings are the most common. It is interesting to note that some tunnels with curved structural ceilings are identified in the inventory database as rectangular due to the installation of flat false ceilings (such as the Fort Pitt Tunnel (Shumway 2014)) which separate the traffic passageway from the ventilation conduit. The CDSF model proposed in this paper is developed for tunnels with curved ceilings in order to address the largest segment of the current inventory. Future work will adapt the CDSF model for rectangular shapes, which pose additional modeling challenges due to lower clearance and cornering effects on the movement of smoke and gas, which lead to increasingly turbulent combustion results.

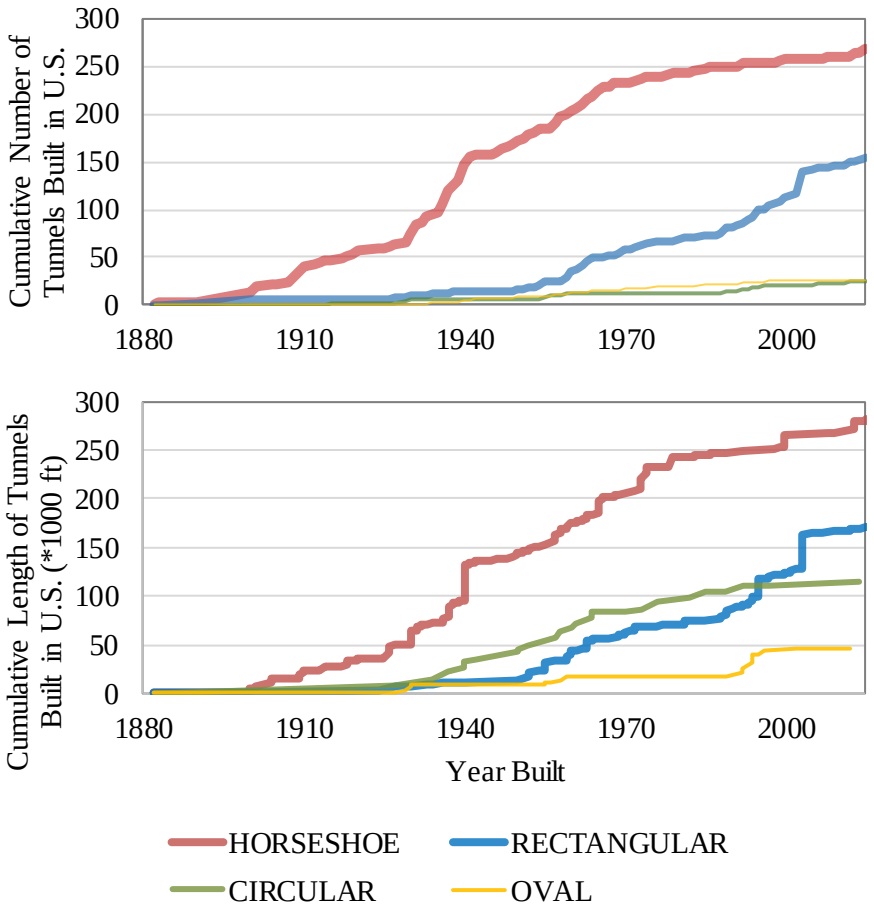

Figure 15 Accumulated number and length of tunnels from 1882 to 2015 (USDOT 2015)

Figure 16 shows the cross-sections of the three tunnel prototypes that are used to demonstrate the CDSF model in this paper. Per the current limitations of the CDSF approach, all tunnel prototypes are assumed to be naturally ventilated with no longitudinal grade. As was shown in Figure 15, the horseshoe shape is by far the most common in US practice. Due to the technological development of tunnel boring machines (TBM's) (Li 2017), the segmented circular cross-section is predicted to be an increasingly common tunnel shape and is therefore highlighted in this study. Prototype (A) has similar dimensions as the aforementioned Memorial Tunnel (Bechtel/Parsons Brinckerhoff. and Bechtel/Parsons Brinckerhoff. 1995). Prototype (B) has the same shape and proportions as (A) but has a larger section area. Prototype (C) is a circular cross-section whose base is cross-cut by the roadway surface. The section area of (B) and (C) are the same. Figure 17 shows that the widths of these prototypes are typical compared to circular and horseshoe tunnels currently in the US inventory (USDOT 2015).

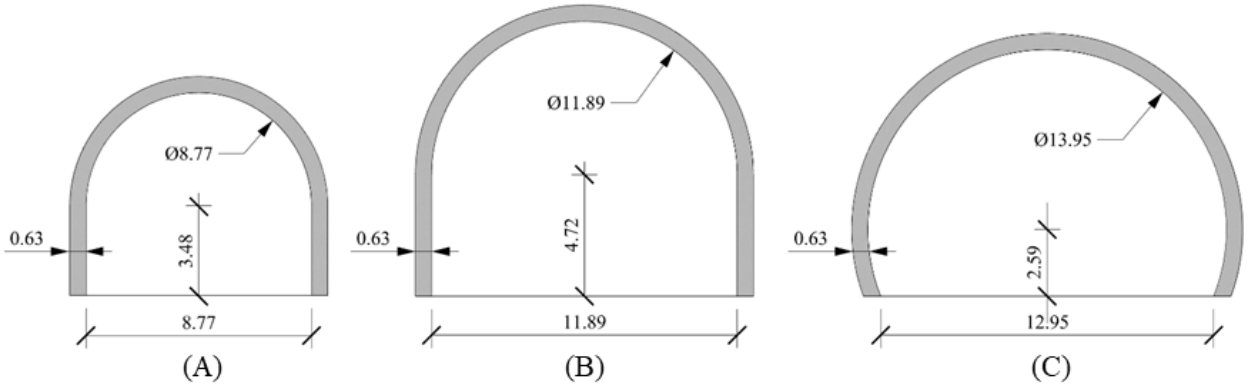

Figure 16 Cross-sectional dimensions (in meters) for the horseshoe, larger horseshoe, and circular tunnel prototypes

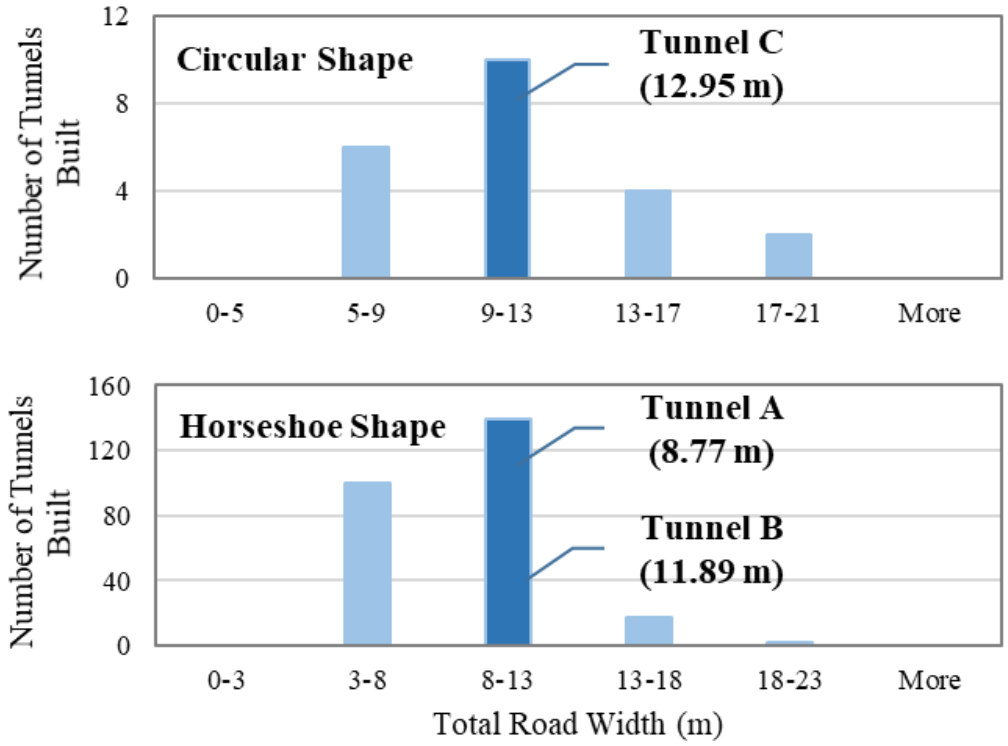

Figure 17 Tunnel roadway width frequency for circular and horseshoe tunnel shapes (USDOT 2015)

3.3.2. Fire Scenarios

Design fires for transportation infrastructure are typically defined in terms of HRR and based on the calorific value and size of the fuel source (Ingason 2009). For example, NFPA 502 (*NFPA 502, Standard for road tunnels, bridges, and other limited access highways* 2011) specifies 20MW-30MW as the peak HRR for bus fires and 70MW-200MW for HGVs. Four fire scenarios

are selected for this study with HRR values that are representative of these vehicles: 30MW, 70MW, 100MW, and 200MW (Ingason 2009; *NFPA 502, Standard for road tunnels, bridges, and other limited access highways* 2011). Figure 18 shows the actual vehicle footprint (dashed gray lines) given by AASHTO (American Association of State Highway and Transportation Officials 2001) for the bus and HGV. As discussed earlier in this paper, these footprints are converted to an equivalent diesel pool footprint that is modeled via CDSF and FDS. To maximize flame height for the specified HRR of each vehicle, an equivalent hydrocarbon pool footprint was developed with an aspect ratio of 2 and a pool fire area A_f that satisfies Eq. 5 for diesel. These equivalent rectangular footprints are shown with gray solid lines in Figure 18 for the four fire scenarios. An elliptical base with the same perimeter as the equivalent rectangular footprint is shown in red in Figure 18. As discussed previously, the elliptical footprints are used in the CDSF model to avoid the errors in target view factor that can occur near the corners of a boxy solid flame shape. In contrast, the FDS results are negligibly sensitive to the rectangular vs. elliptical shape of the pool fire footprint. The rectangular footprints are therefore directly implemented in the FDS simulations due to their easier implementation.

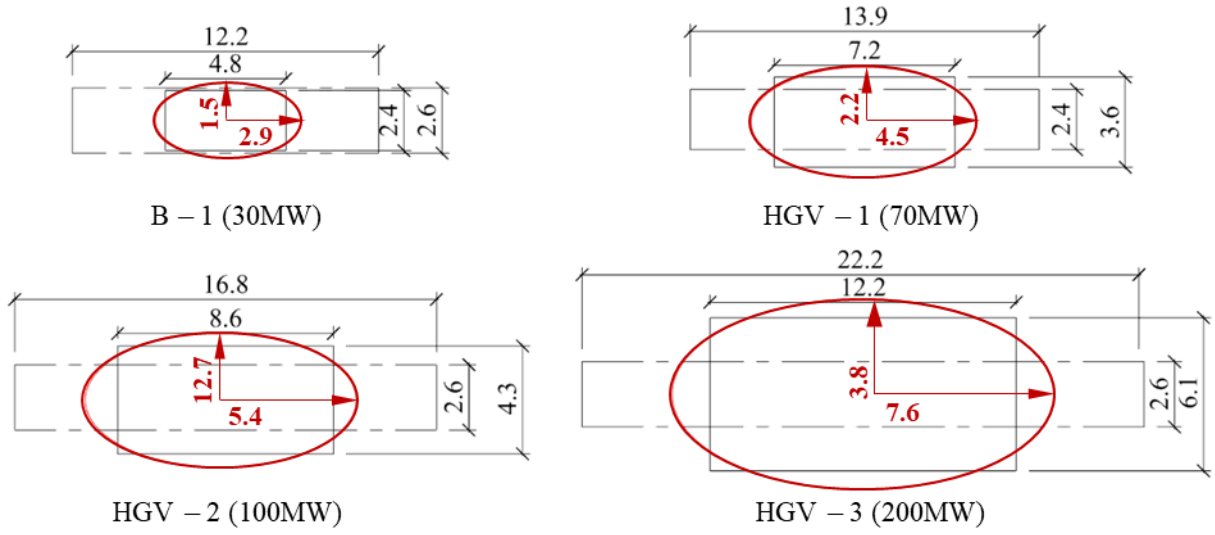

Figure 18 Dimensions (in meters) of the actual vehicle footprint (dashed gray), equivalent diesel pool footprint (solid gray) for FDS, and equivalent elliptical footprint (solid red) for CDSF

Table 2 summarizes the matrix of fire scenarios that are considered for each tunnel prototype. The 200 MW fire is not considered for the smaller horseshoe tunnel since its width is slightly smaller than that of the equivalent diesel elliptical footprint for that fire (i.e. the width of the CDSF solid flame shape won't fit in this tunnel). Future work will explore alterations in the footprint

geometry such that very large fires can be confined within smaller tunnel openings. For this paper, however, the CDSF approach is kept consistent with the elliptical footprint and solid flame approach described in Section 3.2.

Table 2 Matrix for comparative parametric analyses in FDS and CDSF

		TUNNEL PROTOTYPES		
		A. Smaller Horseshoe	B. Larger Horseshoe	C. Circular
FIRE SCENARIOS	B-1 (30MW)	Yes	Yes	Yes
	HGV-1 (70MW)	Yes	Yes	Yes
	HGV-2 (100MW)	Yes	Yes	Yes
	HGV-3 (200MW)	No	Yes	Yes

Preliminary analyses of the CDSF were performed to determine a sufficient resolution of flame surface discretization to achieve solution convergence. The 200MW scenario had the largest solid flame dimensions and comfortably achieved convergence with 54 elements around the elliptical perimeter, 10 elements over the body height, and 50 elements over the dome height. The same discretization pattern was used for the smaller fires, though a coarser mesh could be tailored to a smaller flame height and fire footprint.

3.4. Comparison and Discussion

Heat flux results from the CDSF and FDS models are compared at the locations marked with black dots in Figure 14 along the ceiling, sidewall, and cross-section. The CDSF output predicts the steady state total heat flux at each target location, while FDS provides a heat flux time history at the selected measurement points. For example, FDS time histories of total heat flux on the ceiling directly above the fire are plotted in Figure 19 for all four fire scenarios in Tunnel B. Results for all fire scenarios show oscillation about a steady state mean value, with the 200 MW fire showing the largest relative fluctuation. The statistical mean value of the steady state heat flux (after t = 30 seconds) is plotted along with upper and lower bounds representing +/- one standard deviation. All statistical values are plotted as time histories with an initial 30-second t^2 ramp-up to the steady state heat flux (Ingason 2009):

$$q''(t) = \begin{cases} for\ t < 30\ sec: & q''_{max} \cdot \left(\frac{t}{30}\right)^2 \\ for\ t \geq 30\ sec: & q''_{max} \end{cases} \quad (17)$$

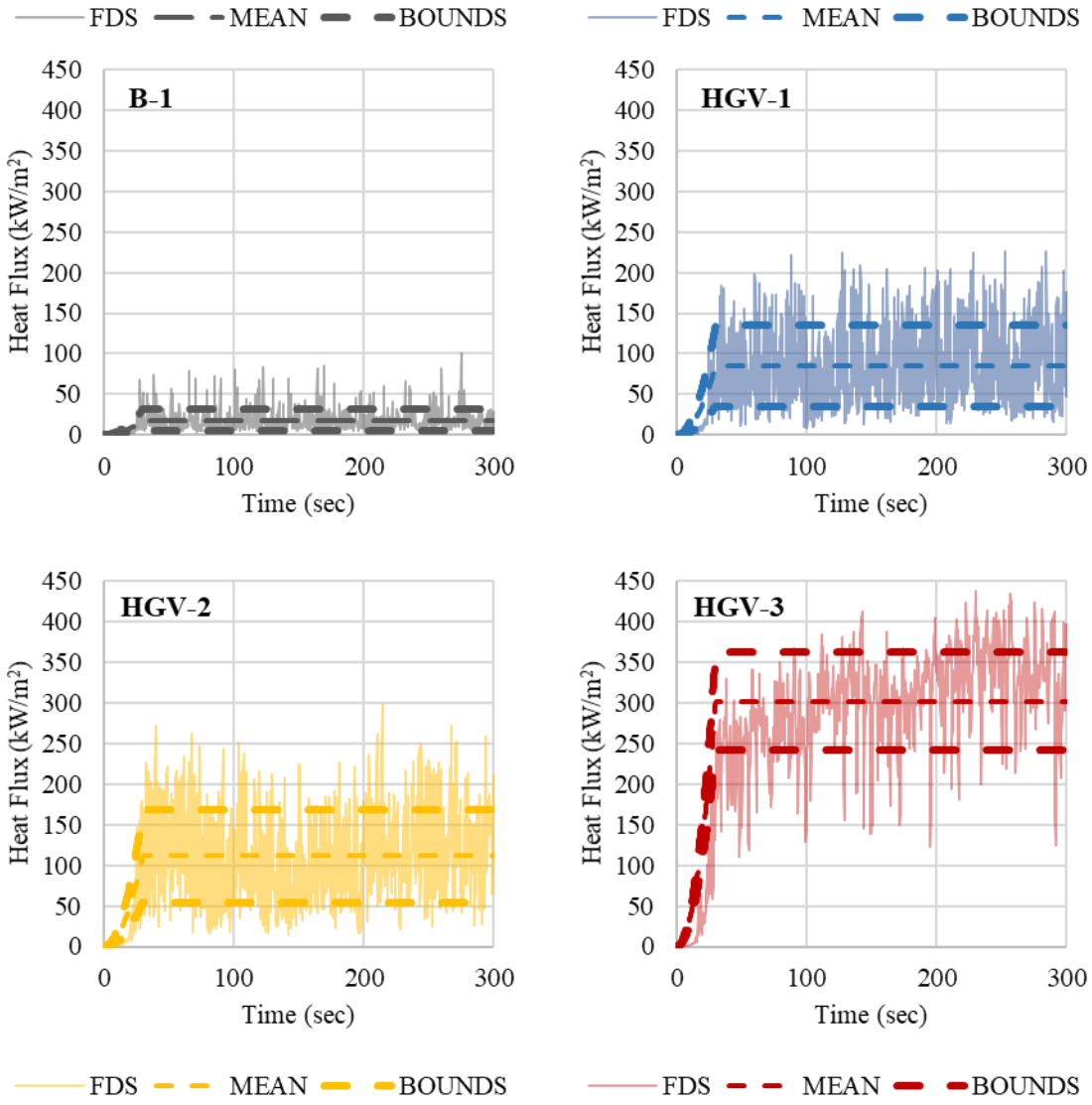

Figure 19 Total heat flux time histories at the ceiling of Tunnel B directly above each fire

When considering thermal exposure to tunnel occupants in the event of a tunnel fire, it may be appropriate to consider peak values. However, the temperature increase in the concrete liner is governed by the cumulative fire exposure. Temperature gradients that develop through the liner thickness will characterize the structural response of the concrete via spalling, weakening, and restraint of thermal expansion (Le et al. 2016). The sensitivity of the development of these gradients is examined by comparing thermal analyses of the tunnel liner thickness for four heat flux exposure time histories from FDS: the mean, the upper and lower bounds (i.e. +/- one standard deviation), and the complete time history. The 63-cm liner thickness (see Figure 16) is equally discretized into 100 layers for 1D heat flow analysis, which is performed using SAFIR (Franssen

and Gernay 2017a). The concrete is assumed to be normal weight, with a density of 2300 kg/m^3 and moisture content of 46 kg/m^3. The concrete material type in SAFIR is defined as SILCONC_EN (i.e. normal-weight siliceous concrete), and the thermal properties are assumed according to Eurocode 2 (CEN 2008 p. 2). For each analysis, the heat flux time history is applied on one "exposed" face of the concrete panel, and the time histories of temperature gradient development are calculated. All time histories are analyzed with a constant 0.2-second time step, which is sufficiently small based on preliminary calculations and smaller than the minimum time step from the full FDS results. Ambient temperature is applied as a thermal boundary condition to the unheated face, which is assigned a relative emissivity of 0.5 and a convective coefficient of 4 kW/m^2 (CEN 2008).

Figure 20 plots the temperature gradients that develop through the panel thickness after 5 minutes of exposure to the heat flux time histories from Figure 19. The gradient due to the mean heat flux curves shows very close agreement with those developed from the full FDS time history. For the HGV-3, the gradients due to the upper and lower bounds have little variation from the mean exposure. The CDSF is therefore calibrated to predict heat flux values between the upper and lower bound for this fire. For the other three fires, the difference in gradient between the lower bound and mean heat flux is larger than that between the mean and upper bound. Based on these results, the CDSF model is calibrated to target heat flux predictions for the B-1, HGV-1, and HGV-2 fires that fall between the mean and upper bound FDS values.

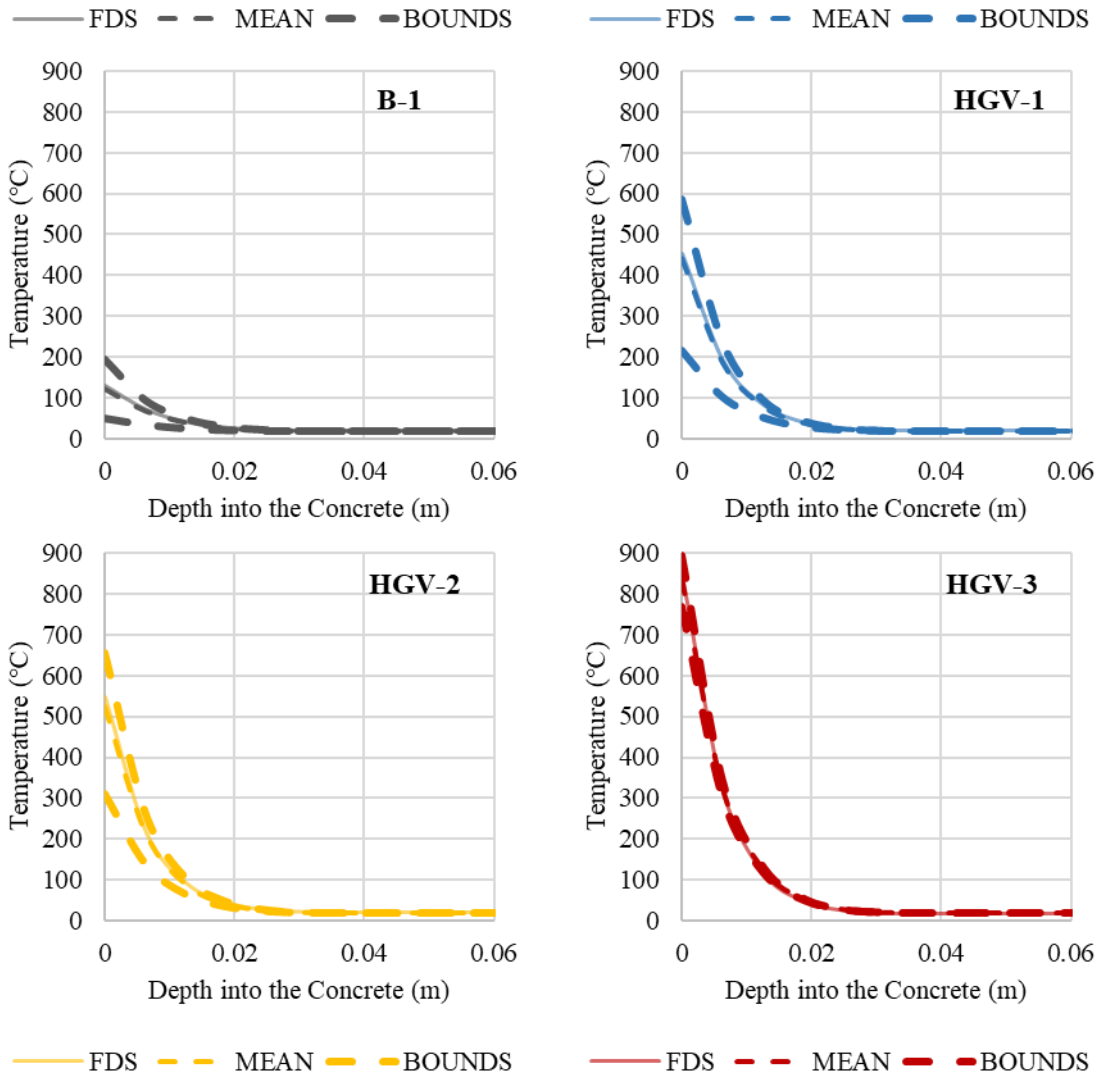

Figure 20 Comparison of thru-thickness temperature gradients at the ceiling of Tunnel B directly above each fire

Figure 21 compares the FDS and CDSF steady state heat fluxes at the locations in Figure 14 for the HGV-2 fire in all three prototype tunnels. The region between the upper and lower bound FDS solutions is shaded in red and the mean value is shown as a black solid line. The presence of a strong ceiling jet (i.e. where the heat flux distribution has a "bump") at the ceiling is exhibited by the FDS results and also captured by the CDSF model. The plots show good overall consistency between the CDSF results and the mean value of the FDS results. The CDSF model not only provides an accurate prediction of the maximum heat flux at the fire location but also shows good consistency with FDS for the decay of heat exposure longitudinally and transversely.

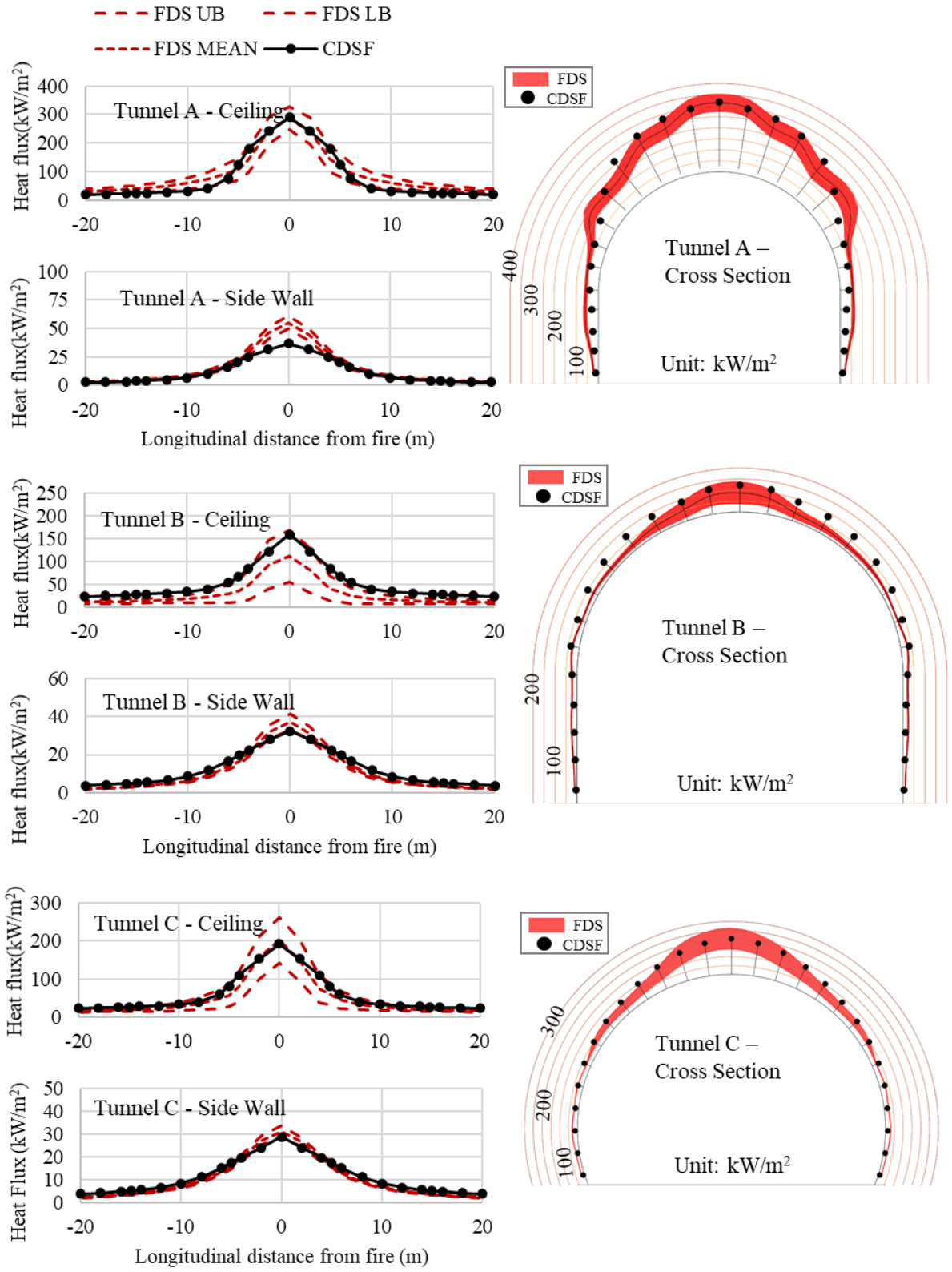

Figure 21 Comparison of steady-state heat flux predicted by FDS and CDSF for fire scenario HGV-2

Similarly good agreement for all fire scenarios and tunnel prototypes is demonstrated by comparing two values of root mean square error (*RMSE*): (1) between the CDSF results and the FDS mean ($RMSE_{CDSF}$), and (2) between the FDS upper/lower bound and the FDS mean ($RMSE_{BOUND}$). If the $RMSE_{CDSF}$ is smaller than $RMSE_{BOUND}$, then the discrepancy of the CDSF results from the FDS results is within the range defined by the standard deviation. The *RMSE*'s are calculated via Eqs. 17 and 18, in which n is the device number and N is the total number of devices for each set of measurements. For the longitudinal comparisons (ceiling and side wall), heat flux data measured around fire location is weighted more heavily due to the denser locations of devices.

$$RMSE_{CDSF} = \sqrt{\frac{\sum_{n=1}^{N}\left(q''_{n,CDSF} - q''_{n,FDS_{MEAN}}\right)^2}{N}} \tag{17}$$

$$RMSE_{BOUND} = \sqrt{\frac{\sum_{n=1}^{N}\left(q''_{n,FDS_{BOUND}} - q''_{n,FDS_{MEAN}}\right)^2}{N}} \tag{18}$$

Figure 22 compares the *RMSE* for all tunnel prototypes and fire scenarios. Figure 22b shows that the *RMSE*'s for all side wall measurements are less than 5 kW/m^2, demonstrating good relative agreement between the CDSF and FDS results. For the ceiling and radial cross-sectional measurements in Figure 22a and c, the variation between CDSF and FDS mean values are larger than for the side wall but generally remain within one standard deviation of the FDS mean value. The exceptions are for HGV-1 and HGV-2 in Tunnel B, where $RMSE_{CDSF}$ for the radial cross-sectional measurement (Figure 22c) is up to 12 kW/m^2 greater than the corresponding $RMSE_{BOUND}$. Despite this, cross-section plots of these heat fluxes in Figure 23 show that the CDSF results are almost all conservatively larger than the FDS mean, especially at the locations of higher heat flux. All other tunnel prototypes and fire scenarios show similarly conservative comparisons for radial cross-sectional heat fluxes.

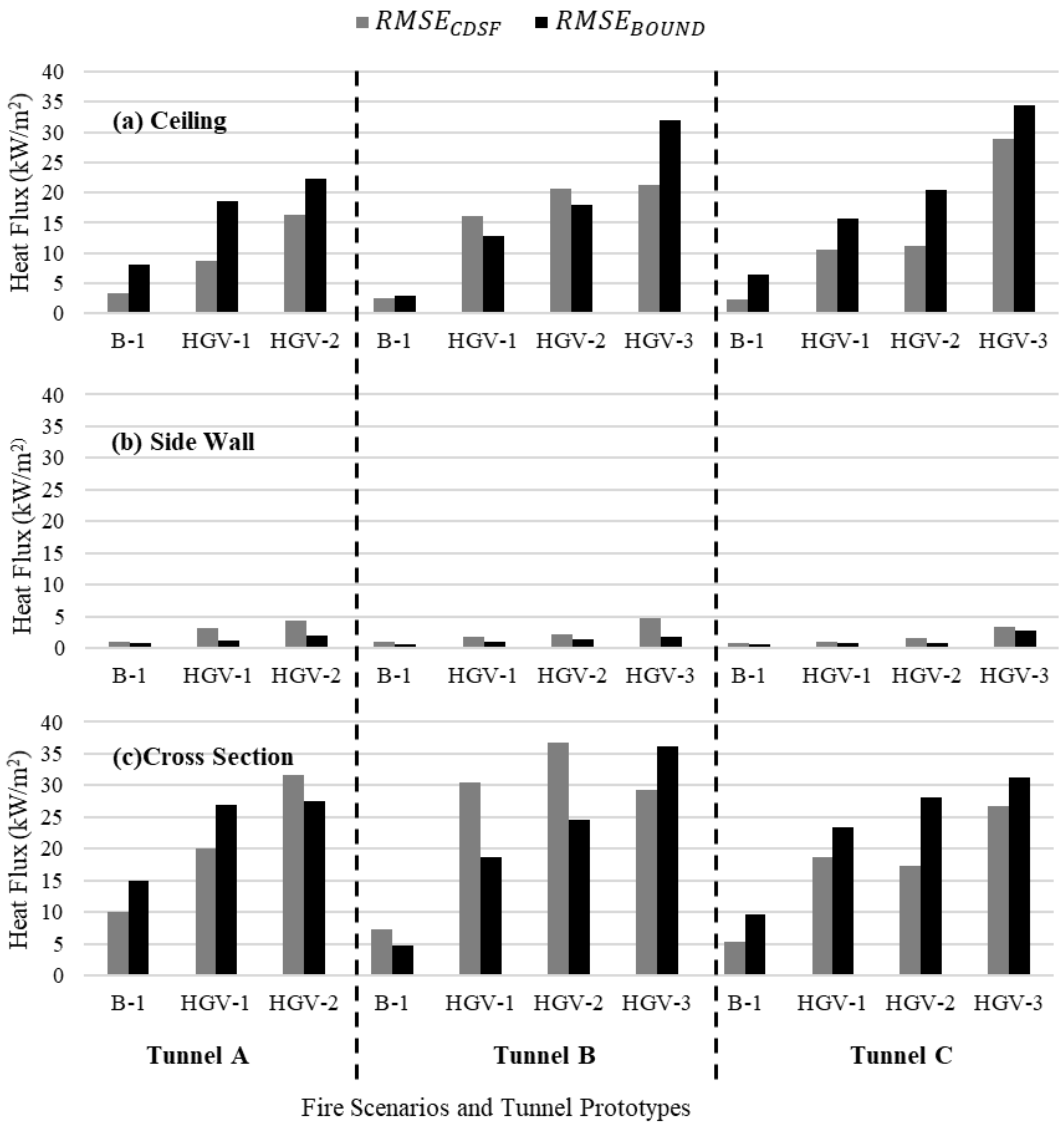

Figure 22 Comparison of $RMSE_{CDSF}$ and $RMSE_{BOUND}$ for all fire scenarios and tunnel prototypes

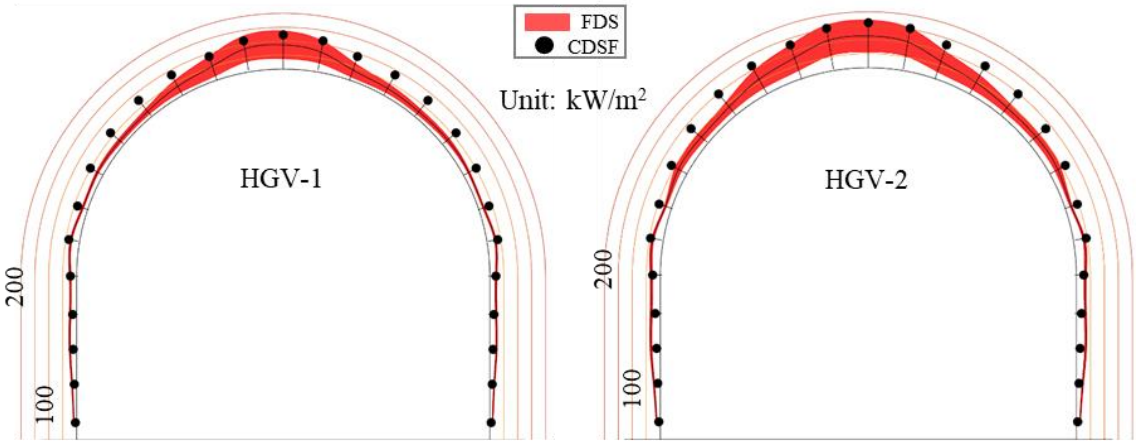

Figure 23 Comparison of radial cross-section heat fluxes for HGV-1 and HGV-2 in Tunnel B

Figure 22a shows that the longitudinal heat fluxes along the ceiling have even lower *RSME* than the radial cross-sectional measurements. Figure 24 plots the raw error between the CDSF longitudinal ceiling heat flux and the FDS mean to demonstrate that these values meet the aforementioned calibration objectives. The circles represent the raw error (CDSF minus FDS mean) at every *x* location from the fire location up to 60-m away (again, assuming symmetric fire effects due to natural ventilation and zero grade). The dashed lines represent the upper and lower bounds (+/- one standard deviation) from the mean FDS heat fluxes – these values converge to near-zero as the FDS results become significantly less turbulent at locations further from the fire. Per the calibration objective, the CDSF predictions for HGV-3 in Tunnels B and C are bracketed between the FDS lower and upper bounds. CDSF predictions for the other three fire scenarios are also bounded by their target range between the FDS mean and upper bound with one exception. The HGV-2 fire in Tunnel A follows the lower bound beyond a distance of ~8m from the fire's center; however, predictions near the fire (where the liner response will be most severe) are closer to the FDS mean and meet the calibration objective.

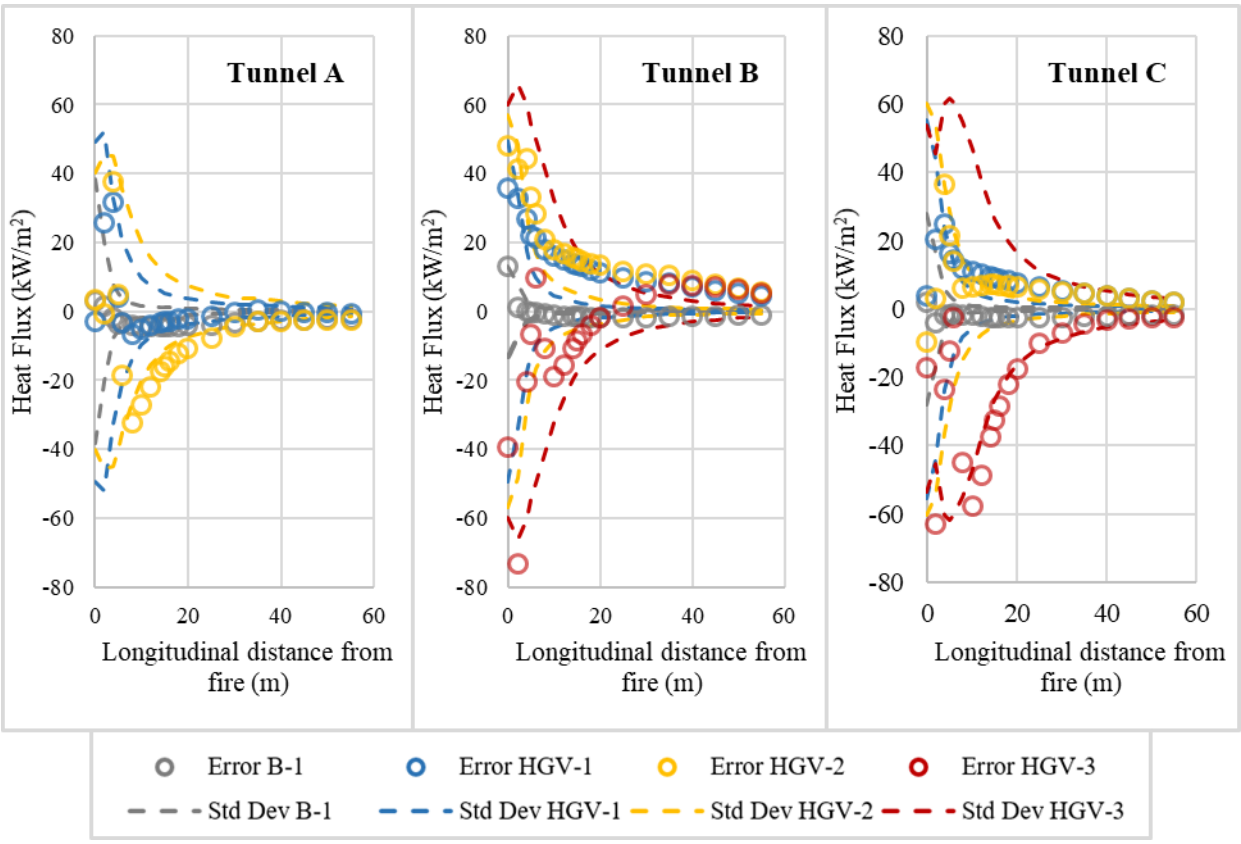

Figure 24 Comparison of raw error from the FDS mean for the longitudinal ceiling heat flux

3.5. Summary

This paper proposes a confined discretized solid flame (CDSF) approach for rapid calculation of the total heat flux on concrete tunnel liners due to vehicular fire events. The CDSF model utilizes semi-empirical models and first principles to calculate (1) radiation heat flux via a discretized solid flame model and (2) convective heat flux from smoke and hot gases. Three tunnel prototypes that are typical of the US tunnel inventory were used to develop the CDSF approach versus validated computational models. Natural ventilation and zero slope were assumed for the tunnel prototypes. An equivalent diesel pool fire was used as a simplified representation of complex vehicular fires with the same heat release rate (HRR). The equivalence was developed from the relationship between the target HRR and the effective diameter of the pool fire.

High-fidelity computational fluid dynamics (CFD) solutions were experimentally validated using available data from previous full-scale tunnel fire tests. The validated CFD approach was implemented to model the prototype tunnels and fire scenarios as a baseline for calibrating the CDSF framework. Heat flux time histories from the CFD solutions were statistically analysed and

used for 1D heat flow analysis of the concrete liner. To conservatively calculate the temperature increase of the liner, a bounding envelope of steady state heat flux was established for each fire scenario to realistically account for the turbulence in the CFD solutions. These envelopes were used as calibration targets to verify the accuracy of the proposed CDSF framework.

The proposed CDSF framework demonstrated good agreement with the FDS results across the matrix of tunnel prototypes and fire sizes. The CDSF model predicts total incident heat fluxes on concrete tunnel liners with curved ceilings at a fraction of the computational effort needed for high-fidelity CFD solutions. The heat flux distributions produced by the CDSF model can be used as input for evaluating fire-induced spalling, the effects of restrained thermal expansion, permanent concrete deterioration, and other damage to non-structural components inside the tunnel. The proposed framework has significant potential for rapid post-fire evaluation of tunnels and for stochastic assessment of the risk of fire-induced damage and loss of functionality.

In its first iteration, the CDSF model cannot yet accommodate the effects of forced ventilation or longitudinal slope. The current CDSF model is simplified to predict a symmetric longitudinal and transverse distribution of fire effects for a zero-slope tunnel with natural ventilation. The current model assumes that the fire location is at the transverse center of the tunnel and has adequate longitudinal distance from the opening. Open boundary conditions were implemented at the openings of the high-fidelity FDS models that were used to calibrate the CDSF model; however, the influence of the openings at close proximity to the fire has not yet been validated in the CDSF model. Future phases of this project will add capabilities to CDSF to account for an increased range of realistic tunnel characteristics, particularly forced ventilation, slope, and proximity to openings.

CHAPTER 4 - CONFINED DISCRETIZED SOLID FLAME MODEL (LONGITUDINAL VENTILATION)

4.1. CDSF model with longitudinal ventilation

Longitudinal ventilation systems are designed to force the gaseous byproducts from an enclosed fire toward one end of the tunnel and are commonly sized to operate at critical air velocity per the tunnel geometry and design fire intensity (i.e., heat release rate) to mitigate smoke back-layering. The proposed wind-tilted CDSF model is therefore developed based on the assumption of steady-state conditions when the fire is fully developed and the longitudinal ventilation system is operating at critical velocity. If the jet fans, electrical conduits, or power source were disrupted or made ineffective by heat exposure, then the naturally ventilated CDSF model discussed in Chapter 3 would instead apply. Fire effects for airflow at subcritical velocity or non-steady-state conditions are beyond the scope of application for the current CDSF model and should be addressed using an alternate approach such as CFD analysis.

Longitudinal ventilation systems can typically be activated via automatic or manual controls within minutes of the fire ignition (Sturm et al. 2017) – once the critical air velocity is achieved, the smoke and hot gases are pushed downstream toward the nearest opening or ventilation shaft, creating an elongated field of convective heat transfer to the tunnel liner. As a result, back-layering (i.e., reversed smoke flow upstream of the fire) is mitigated, thus allowing unobstructed radiative heat transfer from the visible flames. The thermal demand on the liner in longitudinally ventilated tunnels can therefore be divided into two zones that are identified in Figure 25 by their dominant mode of heat transfer: the radiative (upstream) and convective (downstream) zones. In this study, the longitudinal boundary between the two zones is placed at the tip of the wind-tilted 3D solid flame object. The radiative heat transfer in the upstream zone is calculated with the wind-tilted solid flame object as shown in Figure 25, and the convective heat flux in this zone is assumed to be negligible. Conversely, the convective thermal demands in the downstream zone are represented with a semi-empirical decaying field model, and the radiative contributions from the wind-tilted solid flame are assumed to be negligible due to smoke obstruction. Note that the division of these two zones relies on the assumption of critical velocity for longitudinal ventilation, which theoretically prevents smoke back-layering. For the case of subcritical velocity, the radiation zone in Figure 25 should be considered as a conjugate heat transfer region with both

radiation and convection; however, the consideration of subcritical velocity is beyond the current scope of the research presented here. The calculation approaches for the critical velocity and the radiative and convective heat fluxes are described in detail in the following sections.

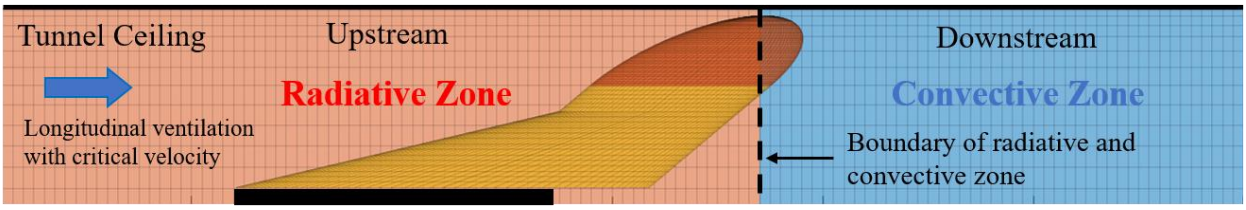

Figure 25: Illustration of the proposed wind-tilted CDSF model

The overall process of calculating the thermal demands on tunnel liners can be computed using the flowchart in Figure 26. If the longitudinal airflow velocity is low, then the naturally ventilated CDSF model presented in Chapter 3 would be used to predict total incident heat flux on the interior surface of the tunnel liner. If the airflow is at critical velocity per Section 4.1.1, then the proposed wind-tilted CDSF model would be utilized in two parts to obtain heat flux predictions in the radiative zone (the orange blocks in Figure 26, corresponding to Sections 4.1.2 to 4.1.4) and convective zone (the blue blocks in Figure 26, corresponding to Section 4.1.5).

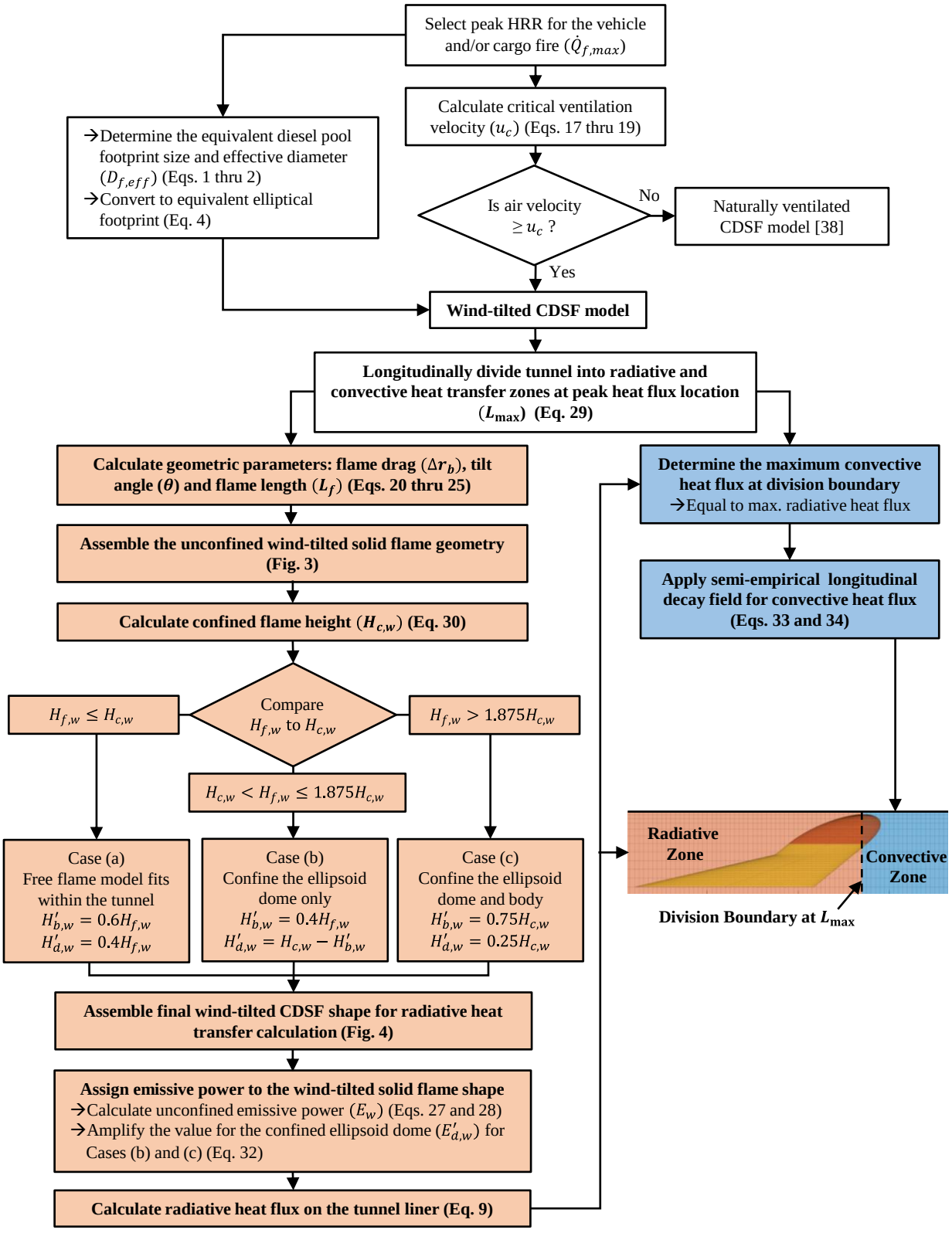

Figure 26: Flowchart for applying the proposed wind-tilted CDSF model

4.1.1. Calculate critical velocity

To prevent smoke from back-layering during an enclosed fire, Thomas (Thomas 1958, 1968) proposed that the velocity of the head of fresh air should be comparable or greater than the buoyancy head of smoke flow. Based on this theory, Danziger and Kennedy (Kennedy and Lowndes 1996) developed the following expression for critical velocity u_c (m/s):

$$u_c = K_g \left(\frac{g \dot{Q}_c H_{T,eff}}{\rho_0 c_p T_f A_T Fr_c} \right)^{1/3} \tag{19}$$

where critical Froude number Fr_c ranges from 4.5 to 6.7 based on experiments by Lee et al. (LEE et al. 1979). In this study, a conservative value of 4.5 is applied for a large tunnel fire. The average downstream temperature T_f (K) is expressed as:

$$T_f = \frac{\dot{Q}_c}{\rho_0 c_p A_T u_c} + T_0 \tag{20}$$

where $\dot{Q}_c$ (kW) is the convective HRR, assumed to be 60-80% (Ingason et al. 2015a) of the total heat release rate $\dot{Q}_{f,max}$ (a median value of 70% is applied in this study); $H_{T,eff}$ (m) represents the effective tunnel height, which measures the distance from the base of the fire source to the highest point of the tunnel ceiling ($H_{T,eff} = H_T - H_{base}$); ρ_0 (kg/m^3), c_p (kJ/kg-K), and T_0 (K) are the density, specific heat, and temperature of ambient air, respectively; A_T (m^2) is the cross-sectional area of the tunnel; g(m/s^2) is the acceleration of gravity; and K_g is a coefficient that accounts for the effect of the tunnel's *grade* (expressed as a percentage):

$$K_g = 1 + 0.0374(grade)^{0.8} \tag{21}$$

This method is currently the most widely-used approach for critical velocity calculation (Carvel and Ingason 2016) and was utilized in the Memorial Tunnel fire ventilation test program (Bechtel/Parsons Brinckerhoff. and Bechtel/Parsons Brinckerhoff. 1995), the data from which will be used to validate the proposed wind-tilted CDSF model in Section 4 of this paper. Other methods can also be used to calculate the critical velocity, such as the non-dimensional model developed by Oka and Atkinson (Oka and Atkinson 1995) based on model-scale tunnel fire experiments.

4.1.2. Apply wind tilt to the initially unconfined solid flame model

To account for the influence of longitudinal ventilation on the solid flame model from Section 2.1, new geometric modifications such as flame drag, flame tilt angle, and flame length are introduced. Similar to the naturally ventilated model, an unconfined wind-tilted solid flame model

is developed first and then modified to account for the confinement of the tunnel. The procedure for developing the unconfined wind-tilt solid flame model is illustrated in Figure 27, starting with the free flame model for natural ventilation (see Chapter 3) as Figure 27a. The same equivalent diameter and ellipse dimensions of the footprint are applied here as the initial condition, just before the application of longitudinal ventilation. Once critical velocity is reached, the solid flame will lean downstream to form the wind-tilted model shown in Figure 27d. The transition of the solid flame model from naturally ventilated (Figure 27a) to longitudinally ventilated (Figure 27d) conditions is illustrated using two intermediate steps: the application of wind tilt (Figure 27b), and the application of flame drag (Figure 27c).

(a) Wind tilt

For Intermediate Step 1 in Figure 27b, the solid flame is tilted downstream by the longitudinal airflow at critical velocity. The inclination angle of the tilted flame is calculated by correlating the momentum flux of the entrained air (again, moving longitudinally at critical velocity) with the momentum flux of the flame gases. The tilt angle θ between the vertical and the inclined line in Figure 27b from the flame tip to the fuel pool center can be determined using the approach of the *American Gas Association* (Atllah and Raj 1974) as shown in Eq. (22). It is formulated based on time-averaged images from fire experiments conducted on LNG fires with diameters ranging from 1.8 m to 24.4 m and wind speeds ranging from 1.3 to 7.9 m/s (Atllah and Raj 1974).

$$\theta = cos^{-1}\left[\left(\frac{u_c}{U_{c,mod}}\right)^{-0.5}\right]; where\ \frac{u_c}{U_{c,mod}} > 1 \tag{22}$$

where $U_{c,mod}$ (m/s) is the characteristic wind speed, indicating the minimum value needed for flame tilt to occur:

$$U_{c,mod} = \left(\frac{g\dot{m}^{"}D_{f,eff}}{\rho_g}\right)^{1/3} \tag{23}$$

where $\dot{m}^{"}$(kg/m^{2}s) is the mass burning rate per unit area of fuel; and ρ_g(kg/m^3) is the vapor density of the fuel at boiling point. Since the vapor density of diesel is approximately 3 to 5 times the density of ambient air (Crude Logistics 2012; VALERO 2014), $\rho_g = \rho_{g,diesel}$ is taken as 5 kg/m^3 in this study.

The flame length L_f (m) in Figure 27b represents the distance from the center of the fire footprint to the flame tip. For this study, L_f is calculated using expressions developed for a conical flame

from experiments on large LNG fires with wind speed ranges from 1.8m/s to 14.4m/s (Moorhouse 1982):

$$\frac{L_f}{D_{f,eff}} = 4.7\left(\frac{\dot{m}''}{\rho_a\sqrt{gD_{f,eff}}}\right)^{0.121}\left(\frac{u_c}{U_c}\right)^{-0.114} \quad (24)$$

where U_c (m/s) is similar to $U_{c,mod}$ in Eq. (22) but instead utilizes the ambient air density ρ_a(kg/m^3) instead of the fuel vapor density ρ_g:

$$U_c = \left(\frac{g\dot{m}''D_{f,eff}}{\rho_a}\right)^{1/3} \quad (25)$$

In Eq. (22), the velocity ratio u_c/U_c characterizes the wind speed required to counteract the buoyancy-induced acceleration from the fire.

In Figure 27b, L_f and θ are used in intermediate step 1 to determine the location of the flame tip, marked with a red star. This location remains unchanged throughout the remaining steps for developing the wind-tilted solid model. The overall unconfined flame height $H_{f,w}$ (m) is calculated as follows:

$$H_{f,w} = L_f \cdot \cos\theta \quad (26)$$

$H_{f,w}$ includes both the upper "dome" portion ($0.6H_{f,w}$) and lower "body" portion ($0.4H_{f,w}$) as was done for the unconfined H_f of the naturally ventilated CDSF solid flame in Chapter 3. Note that the wind-tilted solid flame shown in Figure 27b for intermediate step 1 is a lighter color, which indicates that this shape will be modified again in subsequent intermediate steps before reaching the final configuration.

(b) Flame drag

Flame drag (i.e., the trailing of the flame along the ground beyond the downwind edge of the pool fire footprint) occurs when the combustion of a mixture of air and fuel vapor is carried just beyond the fire footprint by the longitudinal airflow (Lam and Weckman 2015). Several experimental studies have previously indicated that flame drag for open-air hydrocarbon pool fires is generally considered to be proportional to the diameter of a circular pool fire and can be expressed as a function of the wind velocity, fire size, fuel vapor density, and heat of combustion (Lautkaski 1992; Raj 2010; Welker and Sliepcevich 1966). In Intermediate Step 2, flame drag is applied to the wind-tilted solid flame in Figure 27b in two increments in order to develop the solid flame shape shown in Figure 27c. First, the tilted flame shape is "dragged" downstream such that the trailing edge of its footprint is

now located at Δr_b (relative to its major axis length r_b) from the back edge of the original footprint. Increment Δr_b (m) is calculated via a generalized equation proposed by Raj (Raj 2010) for liquid fuel pool fires, which is adopted here since similar expressions specific to tunnel-enclosed fires are not available in the current literature:

$$\frac{\Delta r_b}{2r_b} = \Gamma Re^{-0.25} Fr^{0.5} \tag{27}$$

where the dimensionless fuel property constant Γ is taken as 28.68 (Raj 2010); $Re = u_c D_{f,eff} / (1.57 \times 10^{-5} [\mathrm{m}^2/\mathrm{s}])$ is the Reynolds number; and $Fr = u_c^2 / g D_{f,eff}$ is the Froude number.

Next, the extruded flame from Intermediate Step 1 is compressed by the airflow in the longitudinal direction (i.e., along the major axis of the ellipse). The compressed major axis length is calculated by multiplying the initial major axis length r_b from Figure 27b by a dimensionless reduction factor, S_c, which is calculated as follows for this study:

$$S_c = \frac{A_{T,Mem}}{A_T} \leq 1 \tag{28}$$

where $A_{T,Mem}$ (m^2) is the free cross-sectional area of the Memorial Tunnel (60.8 m^2); and A_T (m^2) is the free cross-sectional area of the tunnel being examined. Recall that FDS model validation will be performed for this study using fire test data from the Memorial Tunnel fire test program in West Virginia, USA (Bechtel/Parsons Brinckerhoff. and Bechtel/Parsons Brinckerhoff. 1995) – a value of $S_c = 1$ is therefore assigned to that case as a baseline due to good fit between the wind-tilted CDSF and FDS results (as will be shown in Section 4.2). The Memorial Tunnel has a smaller opening relative to most tunnels in the current operational inventory – S_c values less than 1 for larger tunnel openings are therefore calculated relative to that of the Memorial Tunnel using Eq. 28. As shown later in Section 4.3, good agreement between CDSF results and FDS analyses for a suite of parametric fire scenarios and tunnel geometries will demonstrate that Eq. 28 is an effective normalization for the size of the tilted and dragged solid flame shape in Figure 27c as a function of the tunnel's free cross-sectional area. Note that using $S_c = 1$ for any tunnel with $A_T > A_{T,Mem}$ would be conservative since the resulting tilted solid flame would be not be compressed relative its shape in Figure 27b, thus increasing its surface area and total radiant emission.

(c) Unconfined flame shape

The darker shaded upper dome portion in Figure 27c is retained as part of the final configuration in Figure 27d. The leading edge of the lighter colored "virtual body" in Figure 27c, on the other

hand, was overly compressed by the airflow-driven compression via parameter S_c (which is applied to the entire height of the wind-tilted solid flame in intermediate step 2 for simplicity). The leading edge at the bottom of the lower body portion would realistically still be connected to the windward edge of the pool fire footprint and is therefore stretched back to its original position in Figure 27d. The elliptical footprint of the unconfined, wind-tilted solid flame's final configuration now has a semi-major axis length of $r_b + \frac{\Delta r_b}{2}$ and retains the semi-minor axis length remain r_a, as shown with the solid red outline above Figure 27d.

(d) Unconfined emissive power

The tapering elliptical cylinder of the lower body portion links up with the base of the upper dome portion, and the resulting surfaces of this irregular piecewise shape can be discretized for calculating radiation emission. The emissive power E_w (kW/m^2) corresponding to this unconfined wind-tilted solid flame model and is modified to account for airflow effects:

$$E_w = \frac{\chi_r \cdot \dot{Q}_{f,max}}{A_{flame,w}} \tag{29}$$

where $A_{flame,w}$ (m^2) is the total surface area of the unconfined wind-tilted solid flame model; and χ_r is the radiative fraction, calculated per McGrattan (McGrattan et al. 2000):

$$\chi_r = 0.35e^{-0.05 \cdot D_{f,eff}} \tag{30}$$

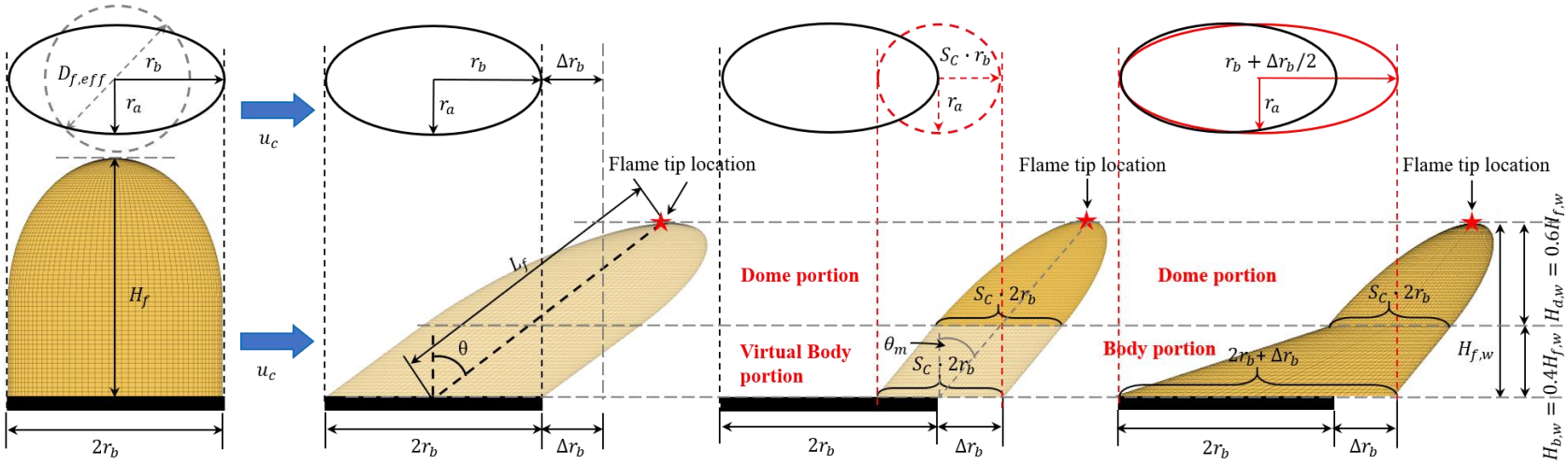

(a) Free solid flame model for natural ventilation (b) Intermediate Step 1: Apply wind tilt (c) Intermediate Step 2: Apply flame drag (d) Unconfined wind-tilted solid flame model

Figure 27: Step-by-step procedure for developing the geometry of the unconfined wind-tilted solid flame model

4.1.3. Apply confinement to the wind-tilted solid flame model

It is essential to again stipulate that the flame model developed above in Section 4.1.2 does not account for confinement provided by the geometry of the tunnel enclosure – modifications to account for such confinement are described here. Three possible states of confinement can occur, as illustrated in Figure 28. The horizontal location of the flame tip remains unchanged for all three cases and is calculated via Eq. (31):

$$L_{max} = L_f \sin\theta \tag{31}$$

where L_f(m) and θ (°) are the flame length and tilt angle from Eqs. (24) and (22), respectively, which were used to construct the unconfined wind-tilt flame model in Section 4.1.2. The determination of each unconfined case is based on a comparison of the unconfined flame height, $H_{f,w}$, with the confined flame height, $H_{c,w}$, which is calculated similarly to Eq. (32):

$$H_{c,w} = H_T - 0.02L_f - H_{base} \tag{32}$$

Similar to H_c, the confined height $H_{c,w}$ also incorporates a small standoff between the top of the ellipsoid dome and the tunnel ceiling (equal to $0.02L_f$) so that the flame surfaces have an adequate view of the tunnel liner at close range (Guo et al. 2019). Values that represent transition points in this model are determined based on a good fit with validated FDS results, as will be shown later in Section 4.3.

(a) Unconfined: $H_{f,w} \leq H_{c,w}$

For fire scenarios with $H_{f,w} \leq H_{c,w}$, no confinement modification is needed as shown in Figure 28a. The unconfined wind-tilted configuration per Section 4.1.2 would apply, with $H'_{b,w} = 0.6H_{f,w}$ and $H'_{d,w} = 0.4H_{f,w}$ (where $H'_{b,w}$ and $H'_{d,w}$ are the height of the lower body and upper dome of the wind-tilted CDSF model, respectively).

(b) Partially Confined: $H_{c,w} < H_{f,w} \leq 1.875H_{c,w}$

Similar to the naturally ventilated CDSF model, only the dome portion of the solid flame model is confined if the unconfined flame height exceeds the confined height but is less than $1.875H_{c,w}$. The height of the lower body portion remains at $0.4H_{f,w}$ while the ellipsoid dome occupies the remaining height up to $H_{c,w}$ ($H'_{b,w} = 0.4H_{f,w}$, $H'_{d,w} = H_{c,w} - H'_{b,w}$). In a departure from the unconfined case, the transition from the lower tapering ellipsoid (with the longitudinal based dimension of $2r_b + \Delta r_b$) to the upper portions of the flame body is compressed to a height lower than $0.4H_{f,w}$. The height of the transition, H_{trans}, can be calculated as follows:

$$H_{trans} = \min\left(H'_{b,w}, \frac{S_C \cdot r_b}{tan\theta_m}\right) \quad (33)$$

where θ_m measures the angle from the vertical direction to the central line of the ellipsoid dome. This angle was plotted previously in Figure 27c for intermediate step 2 of the unconfined wind-tilted solid flame development.

In Figure 28b, the gap between H_{trans} and $0.4H_{f,w}$ (i.e., the gap between the tapering ellipsoid base and the dome) is filled with a tilted elliptical cylinder which corresponds to a slice of the body portion from the unconfined intermediate step 2 in Figure 27c. Note that the parallel red-dashed lines in Figure 28b represent the outline of the tilted elliptical body cylinder from intermediate step 2 in Figure 27c. The cross-section of this gap section therefore corresponds to the red-dashed footprint outline above Figure 27c for intermediate step 2.

(c) Fully Confined: $H_{f,w} > 1.875H_{c,w}$

For increasingly large fires for which $H_{f,w} > 1.875H_{c,w}$, both the dome and body portions of the wind-tilted solid flame model are now vertically compressed to account for additional confinement. As shown in Figure 28c, the dome height is set to $0.25\,H_{c,w}$ to prevent over-compression of the dome, which makes the body height (which includes both the tapering ellipsoid base and the elliptical cylinder gap section) equal to $0.75H_{c,w}$. Otherwise, the development of the fully confined wind-tilted solid flame in Figure 28c is the same as for the partially confined case in Figure 28b. The transition height at the top of the tapering ellipsoid base is again calculated via Eq. 33, and the gap section between the tapering ellipsoid base and the dome is also taken from the elliptical cylinder of intermediate step 2 in Figure 27c.

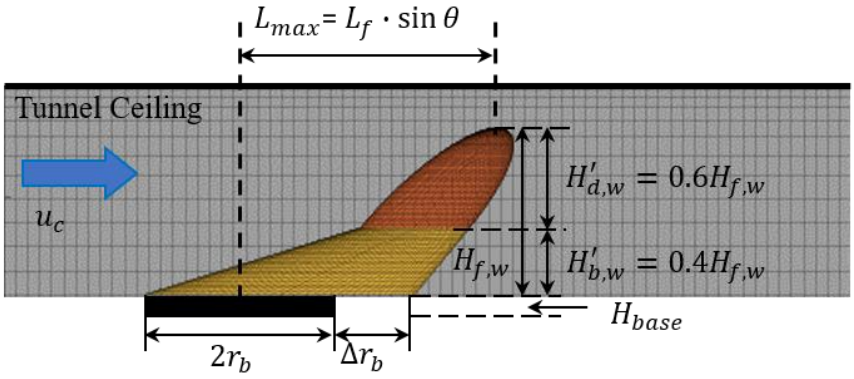

(a) $H_{f,w} \leq H_{c,w}$: unconfined

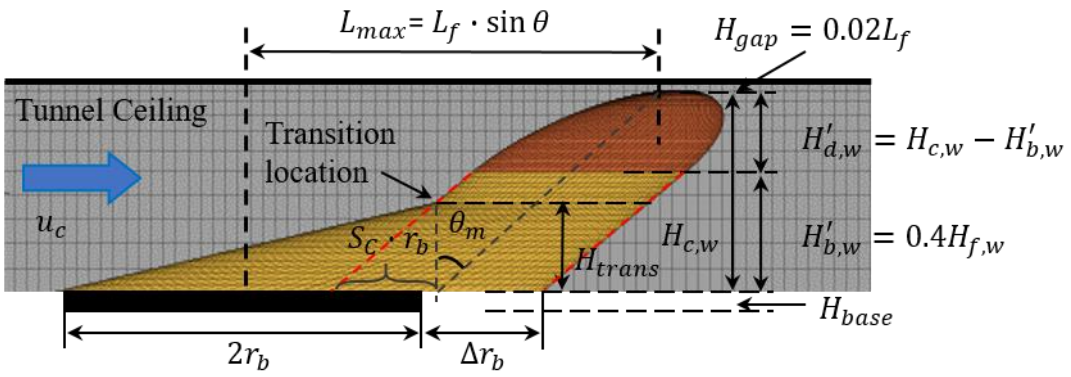

(b) $H_{c,w} < H_{f,w} \leq 1.875H_{c,w}$: partially confined (dome only)

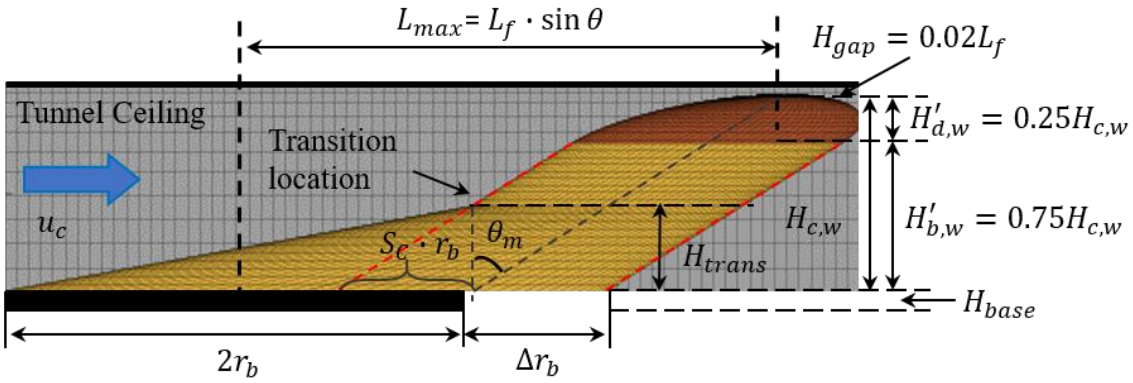

(c) $H_{f,w} > 1.875H_{c,w}$: fully confined (dome and body)

Figure 28: Schematic comparison of wind-tilted CDSF models with escalating levels of confinement within a tunnel

(d) Confined emissive power

Recall that the emissive power assigned to all surfaces of the unconfined solid flame shape in Figure 28a is constant per Eq. (29). If the flame shape is modified due to confinement, the total radiative energy of the flame is assumed to remain unchanged from its unconfined state. Different emissive powers are therefore assigned to the body (yellow) and dome (orange) portions of the confined wind-tilted CDSF models in Figure 28b-c:

$$E'_{b,w} = E_w \tag{34a}$$

$$E'_{d,w} = (\chi_r \cdot \dot{Q}_{f,max} - E'_{b,w} \cdot A'_{b,w})/A'_{d,w} \tag{34b}$$

where $E'_{b,w}$ and $E'_{d,w}$ (kW/m^2) are the emissive power of the body (yellow shaded) and dome (orange shaded) portions of the solid flame shape, respectively; $A'_{b,w}$ and $A'_{d,w}$ (m^2) are the surface area of the body and dome portions, respectively; and E_w(kW/m^2) is the emissive power of the

unconfined wind-tilted solid flame model via Eq. (29). Specifically, the emissive power of the body remains the same as for the unconfined case, and that for the ellipsoid dome increases inversely to its reduction in surface area due to confinement in Figure 28b-c.

4.1.4. Calculate radiative heat transfer

Having defined the wind-tilted geometry and surface emissive power, the surface of the solid flame object is then discretized into small rectangular elements. Horizontally, the perimeter of the ellipsoid body (including both the tapering base and the cylindrical gap section) and dome are both discretized into 50 elements; vertically, the ellipsoid body and dome are discretized into 20 and 50 elements, respectively. Preliminary convergence analyses with the wind-tilted CDSF model have indicated that this level of discretization is comfortably adequate for calculating heat flux for the largest fire scenarios considered for this study (300MW) and can be appropriately applied to smaller fire cases. The inner surface of the tunnel is also discretized into small rectangular tiles, with each acting as a target that receives heat flux. In this study, the fire-exposed perimeter of the tunnel cross-section is transversely meshed into 27 elements. Longitudinally, the discretization is implemented such that each element is approximately square. This tunnel liner discretization can be readily adjusted based on user requirements for data resolution. The total radiative heat flux imparted to the discretized tunnel liner surface is computed via Eq.11) (also visually illustrated in Figure 29). Recall that per Figure 25, the radiative heat flux is computed only for discretized tunnel liner elements that lie in the "radiative zone" on the windward or upstream side of the CDSF model to the longitudinal location of the flame tip.

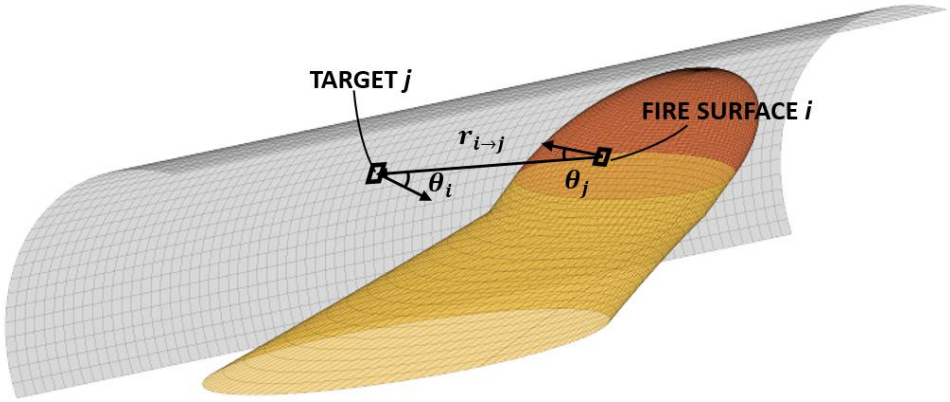

Figure 29: Illustration of radiative heat transfer from the wind-tilted CDSF model

4.1.5. Calculate convective heat transfer

The "convective zone" in Figure 25 starts at the flame tip and then extends longitudinally to the leeward or downstream direction of the CDSF model. Longitudinally, the thermal demands on the

tunnel liner will reach a maximum value at the boundary between the radiative and convective zones (Bechtel/Parsons Brinckerhoff. and Bechtel/Parsons Brinckerhoff. 1995; Li and Ingason 2014, 2015; Vega et al. 2008). To provide a smooth transition from zone to zone, the maximum heat flux in the convective zone is set equal to the radiative heat flux value at the flame tip location. The decay of convective heat flux in the downstream direction from the zone-to-zone boundary follows an exponential decay based on the work by Li and Ingason (Li and Ingason 2014), who examined the temperature distribution within the smoke region of a longitudinally ventilated tunnel fire. The incident heat flux on the tunnel liner in the convective zone can be calculated as follows based on a good fit with validated results (again, presented later in Section 4.4):

$$q_{conv}(x) = q_{radi}^{max}\left(0.55e^{a(x-L_{max})} + 0.45e^{b(x-L_{max})}\right) \tag{35}$$

where x (m) is the longitudinal distance from the center of the fire footprint; L_{max}(m) is the longitudinal distance from the zone-to-zone boundary to the fire footprint center (calculated via Eq. (31)); q_{radi}^{max}(kW/m^2) is the radiative heat flux at the boundary of the two zones at L_{max} (obtained via Section 4.2); and a (m^{-1}) and b (m^{-1}) are parameters implemented to calibrate the decay rate. These parameters are associated with $D_{f,eff}$ (m) of the fire footprint as well as the tunnel height H_T (m) as follows:

$$a = -0.95e^{-2.55\times\left(\frac{D_{f,eff}}{H_T}\right)}$$

$$b = \begin{cases} -0.04 & \frac{D_{f,eff}}{H_T} \leq 1.2 \\ -0.05 & \frac{D_{f,eff}}{H_T} > 1.2 \end{cases} \tag{36}$$

4.2. FDS model validation

In chapter 3, the authors validated FDS models of naturally ventilated tunnel fires against experimental data from the aforementioned fire test programs in the Memorial Tunnel (Bechtel/Parsons Brinckerhoff. and Bechtel/Parsons Brinckerhoff. 1995) (using temperature data) as well as the Runehamar Tunnel (Ingason et al. 2011) (using both temperature and heat flux data). A parametric suite of FDS models based on the validated approach was then used to calibrate the naturally ventilated CDSF model for a wider range of fire sizes and tunnel opening geometries. A similar approach is used in this study to calibrate the proposed wind-tilted CDSF model.

4.2.1. MTFVTP Test 615B

The Memorial Tunnel Fire Ventilation Test Program (MTFVTP) was conducted in the early 1990s and focused on the smoke extraction and temperature management capabilities of various types of ventilation systems (including full and partial transverse ventilation, natural ventilation, and longitudinal ventilation) (Bechtel/Parsons Brinckerhoff. and Bechtel/Parsons Brinckerhoff. 1995). In the test series, Fuel Oil No. 2 (i.e., diesel) was used to generate pool fires with HRR ranging from 10 to 100 MW. Among the 98 total MTFVTP tests, Test 615B was designed to observe the back-layering control for a 100 MW fire (which represents a low-end heavy goods vehicle or HGV) when a longitudinal ventilation system with jet fans is operating at critical velocity. The results of that test are used here for FDS validation.

The Memorial Tunnel has a horseshoe-shaped cross-section (see Figure 30a) with dimensions of 7.9 m height from the roadway and 8.8 m width, for a cross-sectional area of 60.8 m^2. The tunnel has an 853.7-m length with a longitudinal grade of 3.2% from the south to the north portal - for the longitudinal ventilation tests, the tunnel was subjected to controlled fire events at 617 m from the north portal at the transverse center of the tunnel cross-section, as shown in Figure 31. To generate a 100 MW fire, the fuel pan size was set to approximately 45 m^2, with a heat release rate per unit area (HRRPUA) of 2222 kW/m^2. The pan was set 760 mm above the tunnel floor and filled with 150 mm of water on which the measured supply of fuel floated.

The forced longitudinal ventilation is supplied by eight banks of jet fans, with each bank consisting of three fans placed on the curved ceiling transverse to the tunnel longitudinal axis. The air supply capacity of each jet fan was 43 m^3/s, with a discharge velocity of 34.2 m/s. Jet fans JF1 through JF18 are located to the north of the fire, while JF19 to JF24 are located to the south (see Figure 31). For test 615B, six jet fans upstream of the fire (marked as "on" in Figure 31) were activated 2 minutes after full ignition of the fuel pan fire, and the steady-state with regard to combustion effects and smoke back-layering was achieved 3 mins after the jet fans were activated. During the test, a critical air velocity of 3.15 m/s, computed by the MTFVTP team via Eqs. (19) and (20) (Bechtel/Parsons Brinckerhoff. and Bechtel/Parsons Brinckerhoff. 1995), was sufficient to prevent back-layering for the 100 MW fire. All sensors were arranged in instrumentations trees (referred to as a "loop" in the project report (Bechtel/Parsons Brinckerhoff. and Bechtel/Parsons Brinckerhoff. 1995)) to collect experimental data such as temperature, air velocity, gas concentrations, etc. At each loop location, sensors to measure temperature and air velocity were

placed at 1.5-m vertical increments from the ground to the ceiling at the transverse centerline of the tunnel cross-section. The longitudinal locations of these loops are marked in Figure 31. The raw test data used in this study was obtained from the real-time measurements that are publicly available online (KBwiki 2017). The time averaged value from 5 min to 10 min after fire ignition (i.e., 3 min to 8 min after longitudinal ventilation activation) during steady-state is used for FDS model validation in the following section.

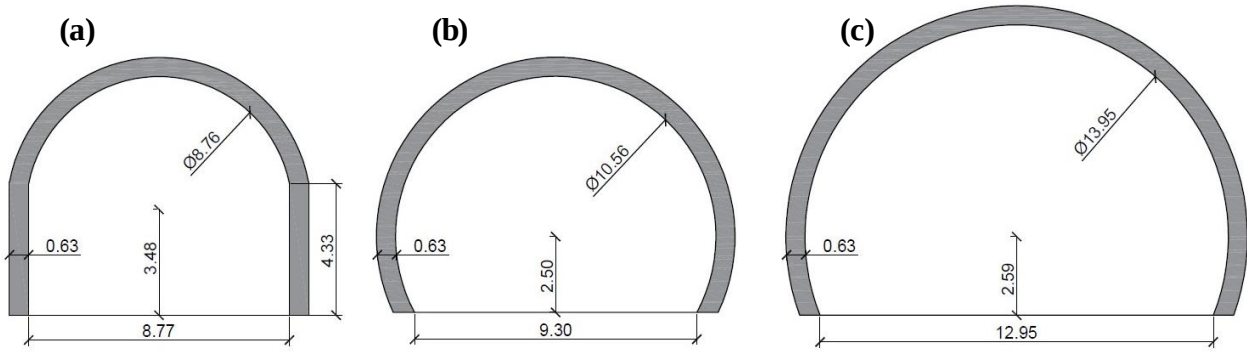

Figure 30: Tunnel cross-section dimensions (in meters) for (a) the horseshoe-shaped Memorial tunnel (Bechtel/Parsons Brinckerhoff. and Bechtel/Parsons Brinckerhoff. 1995), (b) a prototype 2-lane circular tunnel, and (c) a prototype 3-lane circular tunnel

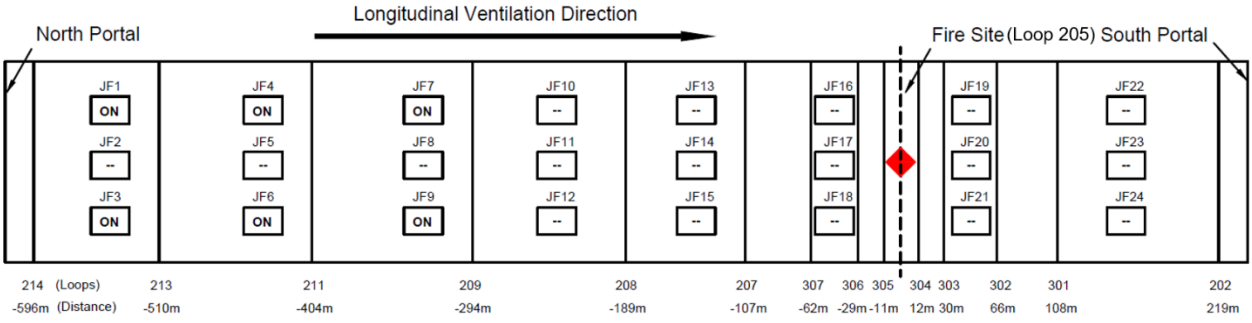

Figure 31: Plan view of fire location and jet fan arrangement for Test 615B in the Memorial Tunnel (Bechtel/Parsons Brinckerhoff. and Bechtel/Parsons Brinckerhoff. 1995)

4.2.2. CFD modeling approach

The FDS model for Test 615B is illustrated in Figure 32. The cross-sectional geometry and full length of the Memorial Tunnel in Figure 31 are modeled in FDS version 6.7.4. The liner thickness per Figure 30a is modeled as layered surface elements with concrete material properties per default settings in the NIST online resources for FDS (McGrattan et al. 2013a). The tunnel floor is also defined as concrete material. These surfaces will realistically absorb heat and provide thermal feedback during fire exposure. The slope of the tunnel was applied by specifying gravity

components in FDS. To simulate Test 615B, a rectangular 4.74 m by 9.48-m burner vent (with the long side in the longitudinal direction) is centered at the fire location in Figure 31 with a defined HRRPUA of 2222 kW/m^2 per the MTFVTP test report (for a total HRR of 100 MW). The reaction associated with the burner corresponds to diesel ($C_{14}H_{24}$) fuel. The burner vent is also elevated 1 m from the tunnel floor to account for the pan height and water depth upon which the diesel fuel was supported during the test. The burner vent (i.e., fuel pan) surfaces were defined as inert. Tunnel openings were modeled using open vents, beyond which the ambient environment is assumed to exist. These boundary conditions allow longitudinal air movement across the opening through the length of the tunnel during the fire.

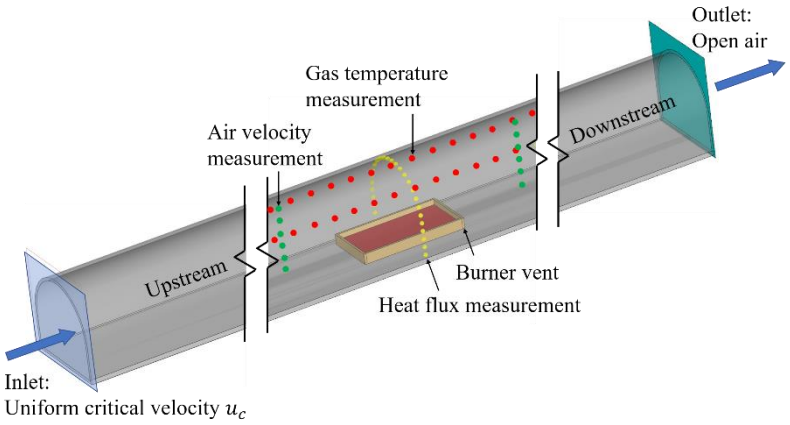

Figure 32: FDS model for Test 615B

The inputs for the FDS simulation of Test 615B are summarized in Table 3. FDS numerically solves a form of the Navier-Stokes equations appropriate for low-speed, thermally-driven flow with an emphasis on smoke and heat transport from fire (McGrattan et al. 2013b). Radiative heat transfer is calculated via the Finite Volume Method (FVM), which is a similar technique to that used for convective transport simulation, with either a "wide band" model (Hostikka et al. 2003) or a "gray gas" assumption (McGrattan et al. 2003). The latter is more applicable for larger fires that have significant soot production and is therefore used for this study. Due to the gray gas assumption, the value of soot yield plays a significant role in radiation energy transport in FDS for a diesel pool fire with a large footprint. A soot yield of 0.10 for diesel is taken from similar FDS simulations by Sudheer (Sudheer 2013), and a CO yield value of 0.012 is taken from Appendix 3 of the SFPE Handbook (Hurley 2016b p. 3) (also used by Sudheer (Sudheer 2013)). A radiative source temperature of 900°C is generally consistent with experimental measurements from diesel pool fire tests (Muñoz et al. 2004; Sudheer and Prabhu 2012). The radiative fraction χ_r input

parameter is calculated per McGrattan's expression in Eq. 30 (McGrattan et al. 2000) using the effective diameter $D_{f,eff}$ for the rectangular footprint area.

Table 3:FDS input parameters for MTFVTP Test 615B

Fuel Characteristics	Fuel type	Diesel
	Chemical Formula	$C_{14}H_{24}$
	CO yield (g/g)	0.012
	Soot yield (g/g)	0.1
	Footprint dimension L x W (m)	4.74 x 9.48
	HRR (MW)	100
Ventilation and Volumetric Meshing	Ventilation air velocity (m/s)	3.15
	Time of ventilation activation (s)	120
	Finest mesh grid dimension (m)	0.25
	Finest mesh boundary (m)	-30 to +80
Radiation Parameters	Radiation model	Gray gas
	Solid Angle	500
	Polar Angles	30
	Radiative source temperature (°C)	900
	Angle increment, f_n	5
Turbulence Parameters	Smagorinsky constant	0.2
	Prandtl number	0.5
	Schmidt number	0.5
Simulation Parameters	Total time period (s)	600
	Time step increment, f_t	3
	FDS version	6.7.1

The enclosed air volume is discretized into semi-cubic cells with a similar discretization pattern as used previously by Guo et al. (Guo et al. 2019). To enable accurate heat flux and temperature measurement, a finer mesh (with a maximum 0.25-m cell dimension) is applied from -30m ("-" indicates upstream of the fire as indicated in Figure 32) and ends at +80m ("+" represents downstream). Beyond this zone, the maximum cell dimension is increased to 1-m to improve computational efficiency. The finer mesh zone is longer in the downstream direction due to the ventilation-induced movement of hot gasses, and preliminary analyses indicated that heat fluxed measured beyond the -30m and +80m extents of this zone would be less than 10kW/m^2 for all fire intensities considered in this study. At such a low heat flux, the numerical impact of transitioning from the finer mesh zone to the coarser mesh zone would be mitigated. In the simulation, the air

velocity, gas temperature, and heat flux are recorded with corresponding devices at the location of interest (i.e., air velocity on each loop) as illustrated in Figure 32.

Previous studies have used various approaches to implement longitudinal ventilation in a CFD model of an enclosed tunnel fire, including the following: physically modeling the discrete contributions of each jet fan as an airflow-inducing object (Vega et al. 2008); assigning a constant volumetric flow rate at the tunnel exit portal to induce a stable inlet air draw (Hua et al. 2021; Hwang and Edwards 2005); or directly applying an air velocity profile that was measured during a fire test (Jia et al. 2010; Kim et al. 2008a). In this study, the longitudinal ventilation in FDS is simulated by simply implementing a uniform longitudinal air velocity at 3.15 m/s (i.e., the calculated value for critical velocity per Section 4.4.1) along the full height of the tunnel at the North portal, as shown in Figure 32 and Figure 35b. The assumption of constant air velocity at the North portal is consistent with the measured steady-state airflow profile for Test 615B in the leftmost markings in Figure 35a. Similar to the test, the longitudinal ventilation airflow starts 120 sec after the burner is initiated in FDS and stays active throughout the remaining 480-sec simulation duration, during which the steady-state has been achieved.

FDS utilizes a Large Eddy Simulation (LES) with a Smagorinsky turbulence sub-model (Kim et al. 2008b; McGrattan et al. 2013b). The Smagorinsky constant is used in the Smagorinsky sub-grid model in LES to influence the dynamic viscosity of the fluid flow. A large Smargoinsky constant adds an artificial viscosity to the flow, which mitigates the upstream flow of hot gases (i.e., reduced back-layering). Within the turbulence model, the Prandtl and Schmidt numbers determine the thermal conductivity of the turbulent flow and the diffusivity of the airborne materials within that flow, respectively. Sensitivity analysis by Kim et al. (Kim et al. 2008a) showed that varying the Prandtl number can affect the velocity prediction in the back-layering and near-field regions of the fire simulation while varying the Schmidt number can impact the flame length. However, Kim et al. also noted that the overall simulation results are not overly sensitive to these parameters, but their improper selection can lead to significant increases in computation time (Kim et al. 2008a). There are currently no consensus recommendations for these three parameters when simulating turbulent flow from tunnel-enclosed fire hazards. As a result of preliminary sensitivity analyses by the authors, FDS default values of 0.2, 0.5, and 0.5 were used in this study for the Smagorinsky constant, turbulent Prandtl number, and turbulent Schmidt number, respectively.

4.2.3. Validation results

Screenshots of the FDS fire simulation before and after the longitudinal ventilation activation are shown provided in Figure 33. Initially, the fire remains within the fuel pan footprint in Figure 33a under naturally ventilated conditions. In Figure 33b, the fire plume is pushed downstream by the longitudinal ventilation, thus shifting the maximum temperature location from loop 205 to loop 304. The gas temperature-time histories close to the tunnel ceiling at loops 205 and 304 (marked with blue stars in Figure 33) are plotted in Figure 34a. The air velocity measured at loop 304 is similarly plotted in Figure 34b.

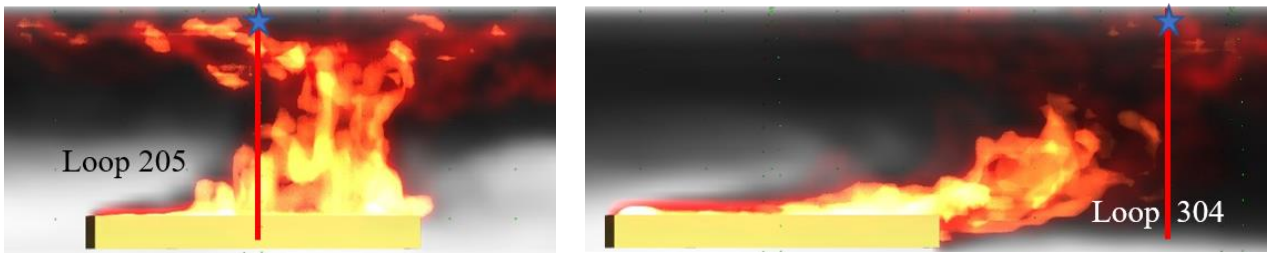

(a) Before longitudinal ventilation activation (b) 3 min after longitudinal ventilation activation

Figure 33: Screenshots of the Test 615B tunnel fire simulated in FDS

As shown in Figure 34, steady state of Test 615B with regard to temperature and air velocity was achieved 5 mins after the activation of the longitudinal ventilation. For the FDS simulation, the steady-state is achieved 3 mins after the ventilation activation, though with more fluctuation in the recorded data. For the following validations, the average values over the steady-state period are compared. Specifically, the values of the test are averaged over the period between 7-14 mins while the FDS results are averaged over the 3-min period between 5-8 mins. The FDS mean value in each plot in Figure 34 is accompanied by a pair of lines at plus/minus one standard deviation, which is calculated from the raw FDS data over the steady-state period.

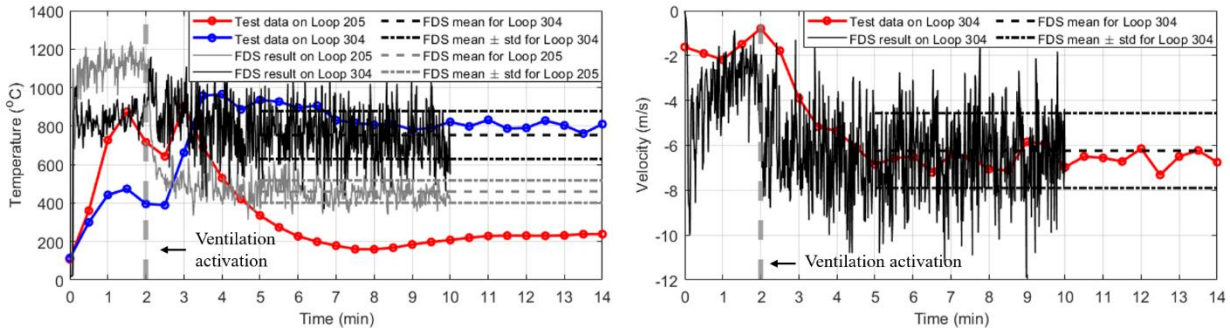

(a) Temperature (b) Air velocity

Figure 34: Time histories of data measured close to the tunnel ceiling from Test 615B and FDS simulation

(a) Longitudinal airflow velocity

Figure 35 compares the steady-state longitudinal air velocity at each instrumentation loop during Test 615B with the corresponding FDS results. The solid black vertical lines represent the loop locations, which are plotted to scale in the longitudinal direction. The longitudinal airflow velocity measured at each gauge over the loop height is plotted as a blue block diagram from left to right. The velocity values are horizontally scaled to avoid overlap between the closely spaced loops near the fire location. The left-to-right scale of plotted airflow velocity is consistent among all loop locations in both parts of Figure 35, which show the (a) experimental and (b) simulated values for Test 615B. The average velocity among all gauges at each loop is plotted as a vertical dashed black line with the same left-to-right scale as the velocity profile.

As mentioned previously, the airflow at loop 209 in Figure 35b was uniformly defined at the critical velocity as a simplified FDS input. Both the simulated and experimentally measured air velocities at upstream loops 208 and 207 (which get progressively closer to the fire location) remain relatively uniform along the tunnel height, with the FDS values about 20% larger than the experimental data on average. Closer to the fire between loops 307 and 301, FDS overpredicts the airflow velocity in the upstream region and underestimates the velocity at the downstream region. Despite these differences, it is important to note that both the FDS predictions and experimental data show a rapid rise (by a factor of about 2-2.5) in longitudinal airflow velocity at the fire location due to the temperature increase and subsequent air density decrease during the combustion process. Also, that burst of increased velocity then decays in the downstream direction until reaching a value at loop 301 (i.e., the Southmost position at which measurements were taken) that is 1.5-2 times greater than the inlet critical velocity.

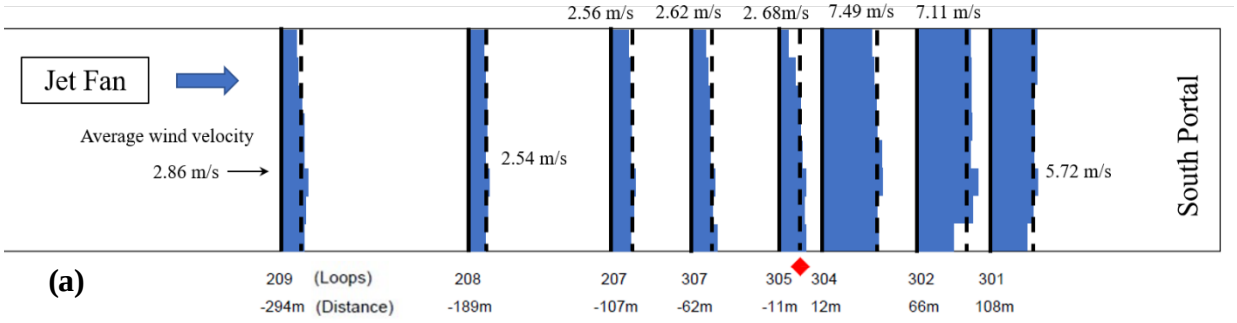

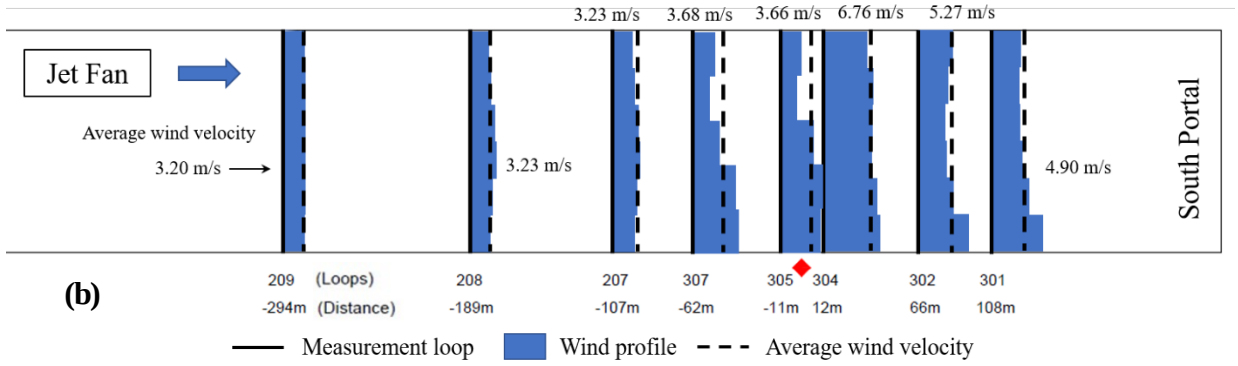

Figure 35: Longitudinal air velocity profiles for MTFVTP Test 615B at steady state: (a) test results (KBwiki 2017) and (b) numerical FDS results

(b) Temperature distribution

Figure 36 compares the FDS and experimental temperatures that are measured longitudinally along the top of the Memorial Tunnel's curved ceiling. The mean FDS curve is bracketed by additional gray curves that represent the mean plus (upper bound) or minus (lower bound) one standard deviation. Figure 36 shows that the FDS simulation can accurately capture both the location and magnitude of maximum ceiling temperature. Upstream of the maximum temperature, FDS temperatures are conservative, with the lower bound curve just slightly higher than the experimental measurements. The reverse trend is shown downstream of the maximum temperature, with the FDS upper bound slightly lower than the experimental values.

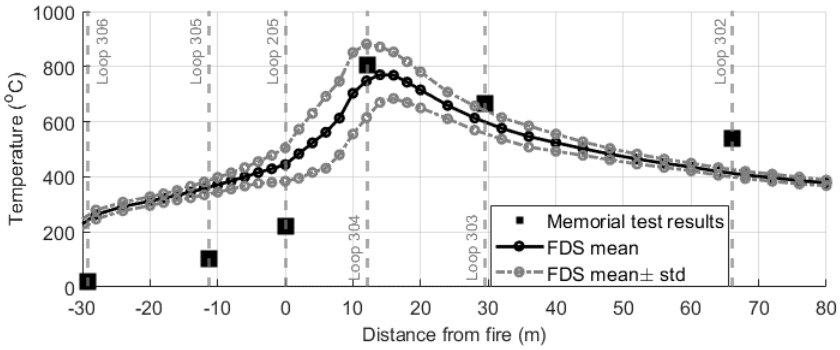

Figure 36: Comparison of ceiling temperatures for MTFVTP Test 615B at steady state: test results (KBwiki 2017) versus FDS results

Contours of temperature distribution from the test and FDS are plotted in Figure 37 as a vertical slice along the transverse centerline. The maximum temperature regions, which are denoted with an increase in yellow shading, are comparable between the test and simulation. However, the FDS contours are more concentrated along the fire's wind-tilted flame column. The physical

combustion of the diesel fuel in the test produced a slightly more dispersed temperature field at the location of the tilted flame. In the upstream direction, the FDS predictions show a more elongated extension of the 100-450°C contours along the crown of the ceiling, though the contours below mid-height are much closer to the test measurements. Also, the downstream contours show closer agreement between the test and the simulation, as was indicated in Figure 36. Recall that at loops 304 and 302 in Figure 35a, the experimentally measured longitudinal airflow velocity experienced a larger downwind increase just past the fire location than those from the FDS simulation in Figure 35b. This difference in downwind is manifested in Figure 37, in which the test results show slightly higher temperature values in the downstream contours.

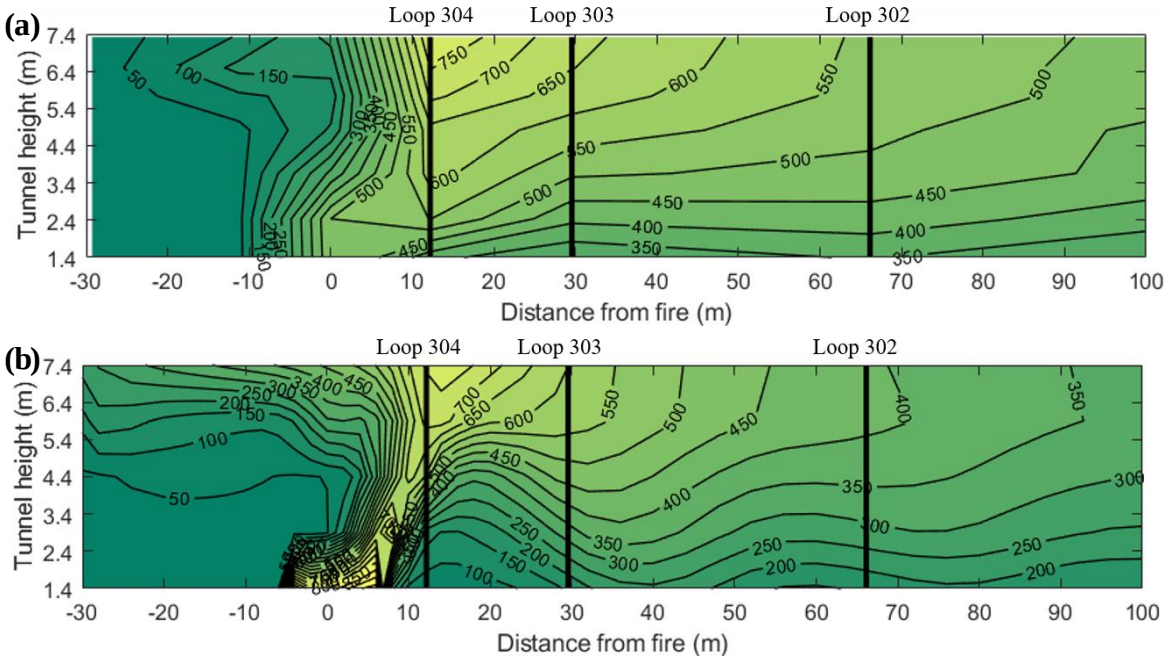

Figure 37: Longitudinal temperature contours along the transverse centerline for MTFVTP Test 615B at steady state: (a) test results (KBwiki 2017) and (b) FDS mean

In summary, the variations between the FDS predictions and experimental data for Test 615B appear to be caused by the following modeling simplifications: (1) the implementation of uniform longitudinal airflow velocity at the upstream inlet to approximate the jet fan contributions, and (2) the use of a burner vent with a prescribed HRRPUA and footprint size to approximate the physical fire. The alternative to these simplifications would require significantly more computational calibration and effort – specifically, modeling each jet fan discretely or modeling the combustion reaction directly would introduce a higher level of input complexity and case-by-case variability that would not be conducive to parametric analysis. With these simplifications, the FDS

predictions demonstrate a level of agreement with the experimental data in Figure 36 and Figure 37 that is acceptable for parametric study and calibration of the wind-tilted CDSF model. That being said, future iterations of the wind-tilted CDSF model could be easily adapted to account for additional test data or refinements in the FDS modeling approach.

Note also that the experimental data and FDS results both show that back-layering in the upstream direction was not completely prevented by the application of the theoretical critical velocity, calculated per Section 4.1.1. As will be shown in Section 4.3, this reality is reflected in all subsequent FDS analyses (and subsequent CDSF model development) due to the usage of the theoretical critical velocity equations per the 2017 edition of NFPA 502. The results of this study could be readily adapted to accommodate other critical velocity calculation approaches in future work.

4.3. Parametric study

Three tunnel geometries (presented in Section 4.3.1) and a wide range of fire scenarios (presented in Section 4.3.2) are used to compare predictions of heat flux distribution on the interior surface of the liner from the proposed wind-tilted CDSF model (per Section 4.1) and from FDS (per Section 4.2). The results are presented in detail in Section 4.3.3 to illustrate the ability of the CDSF model to capture both the peak value as well as the longitudinal and transverse distribution of incident heat flux at steady state.

4.3.1. Tunnel prototypes

Per recent reviews by the authors (Guo et al. 2019; Ouyang et al. 2020), a large portion of roadway tunnels in the current US inventory have circular or horseshoe cross-sections and accommodate 2-3 lanes of traffic, with road widths ranging from 8 m to 13 m. The cross-section of the Memorial Tunnel in Figure 30a is therefore typical of the current inventory (horseshoe-shaped with 2 lanes) and is used as Prototype A for parametric study. Circular tunnel shapes are increasingly used due to the deployment of tunnel boring machines (TBM) (Li 2017) – Prototypes B and C in Figure 30b-c are therefore used to represent typical 2-lane and 3-lane circular tunnels. The total length of all prototypes is taken as 800 m, which is comparable to the Memorial Tunnel's length. Longitudinal grade is not considered for any prototype in the parametric study for simplicity. The grade also has minimal influence on the airflow compared to the effects of the forced ventilation, as confirmed via preliminary analyses (not shown here for brevity) that

compared temperature and heat flux distributions from the FDS validation for Test 615B in the actual Memorial Tunnel (with 3.2% grade from the South to the North portal) against the same 100MW fire in the Prototype A tunnel with no grade.

4.3.2. Fire scenarios

To demonstrate the broad applicability of the proposed wind-tilted CDSF model, fire scenarios are selected with peak HRR ranging from 30-300MW (i.e., from a bus fire to an upper-bound tanker truck fire per NFPA 502 (NFPA 2017)). A detailed parametric analysis matrix is provided in Table 4. The equivalent diesel pool fire approach is again used to calculate the equivalent rectangular (FDS) and elliptical (CDSF) footprints according to the maximum HRR, per the approach presented in Section 4.1. The footprint aspect ratio, *ASP*, for fires with HRR of 30-100MW is set equal to 2.0. For HRRs greater than 100MW, the aspect ratio is increased to ASP_{max} = 2.5 to prevent the footprint from contacting the tunnel sidewall (i.e., to keep the footprint for such a large fire contained within the tunnel's transverse dimension). For Prototype A, the fire is located 617 m from the North portal, the same as the experimental setup for MTFVTP Test 615B. For Prototypes B and C, the fire is placed at the longitudinal center of the tunnel for simplicity. The critical inlet airflow velocity is calculated via Eqs. (19) and (20) for each scenario and used as input for both models.

Table 4: Matrix of comparative parametric analyses via FDS and the wind-tilted CDSF model

Fire HRR (MW)	Footprint Dimensions (m×m)		Critical Velocity (m/s)		
	Elliptical for CDSF model (semi-minor axis × semi-major axis)	Rectangular for FDS simulation (width × length)	Tunnel Prototype A	Tunnel Prototype B	Tunnel Prototype C
30	1.60 × 3.20	2.60 × 5.20	2.17	2.06	1.96
50	2.08 × 4.15	3.35 × 6.70	2.46	2.35	2.26
70	2.46 × 4.92	3.97 × 7.94	2.65	2.53	2.47
100	2.94 × 5.88	4.74 × 9.49	2.85*	2.73	2.70
150	3.16 × 7.90	5.20 × 13.00	3.00	2.95	2.95
200	3.65 × 9.12	6.00 × 15.00	3.20	3.08	3.12
250	4.08 × 10.20	6.71 × 16.77	3.30	3.19	3.26
300	4.47 × 11.18	7.35 × 18.37	3.38	3.26	3.36

*Note: Critical velocity is different from the validation cases in Section 4.2 because zero tunnel grade is considered here

4.3.3. Parametric results

(a) Prototype A: 2-lane horseshoe tunnel

Figure 38 plots the steady-state heat fluxes from the wind-tilted CDSF model and FDS simulations along the longitudinal axis at the top of the ceiling for Prototype A. Note that the FDS data corresponds to the gauge heat flux output. All fire scenarios in Table 4 are included in Figure 38 except for the 100MW and 200MW cases, which are instead plotted in Figure 39a and Figure 40a and accompanied by cross-sectional plots of heat flux at three longitudinal locations: (b plot) the center of the fire footprint; (c plot) the location of the max ceiling heat flux from the CDSF model, which coincides with the location of L_{max}; and (d plot) at $(L_{max} + D_{eff})$ downstream from the fire center. These locations are selected to showcase the performance of wind-tilted CDSF within the radiative zone, at the boundary of the radiative and convective zones, and in the convective zone, respectively, per Figure 25.

Recall that the proposed wind-tilted CDSF model is applicable only when the critical longitudinal ventilation velocity has been achieved (see Figure 26). In FDS, the ventilation activation time for each case is assumed to be the same as for MTFVTP test 615B (i.e., 2 minutes after fire ignition). To ensure that heat flux is measured at a steady-state and to reduce the influence of turbulence in the FDS time history, time-averaged values over a 60 s interval at 6 min ± 30 s (i.e., 3 min after ventilation starts) are calculated as an appropriate comparison with heat flux values from the wind-tilted CDSF model. The plots in Figure 38 through Figure 40 also include an upper and lower bound ("UB" and "LB") for the FDS results which correspond to one standard deviation (calculated over the same time-averaged 60-s period) above and below the mean value.

These plots for Prototype A show good overall agreement between the CDSF results and the steady-state FDS predictions of total heat flux for all fire sizes from 30-300MW. In Figure 38, this agreement is particularly close for fire scenarios with HRR ≤ 150MW, with the CDSF peak heat flux falling between the mean and upper bound FDS curves. As the fire size increases, the ellipsoid dome in the wind-tilted CDSF model is increasingly confined and leans downstream at a larger tilt angle. The windward surface of the ellipsoid dome therefore becomes flatter as illustrated in Figure 28c. For the 250MW and 300MW cases in Figure 38, the increased flattening of the confined dome creates somewhat of a heat flux plateau from +10m downstream toward the maximum value at $L_{\max}$ from the fire center.

All fire scenarios show that the CDSF predictions trend slightly conservative in the downstream convective zone by following the upper bound of the FDS decay. The CDSF predictions for the larger fire sizes of HRR ≥ 150MW are also conservative in the upstream direction in the radiative

zone. For the lower fire sizes of HRR ≤ 100MW, the CDSF's radiative zone predictions follow the FDS mean from the fire location going upstream to -5m. Further upstream beyond -5m, the CDSF values for HRR ≤ 100MW trends low versus the FDS results; however, the raw values are below 10 kW/m^2, and these deviations for smaller fires will therefore have little structural significance for the tunnel liner.

The b, c, and d cross-sectional plots in Figure 39 and Figure 40 show good agreement between the CDSF and FDS predictions of transverse heat flux distribution for the 100MW and 200MW fire cases. These results demonstrate that the wind-tilted CDSF model can provide conservatively accurate predictions of heat flux distribution in both the longitudinal and transverse directions for structurally significant fires at a fraction of the computational effort required for the FDS solutions.

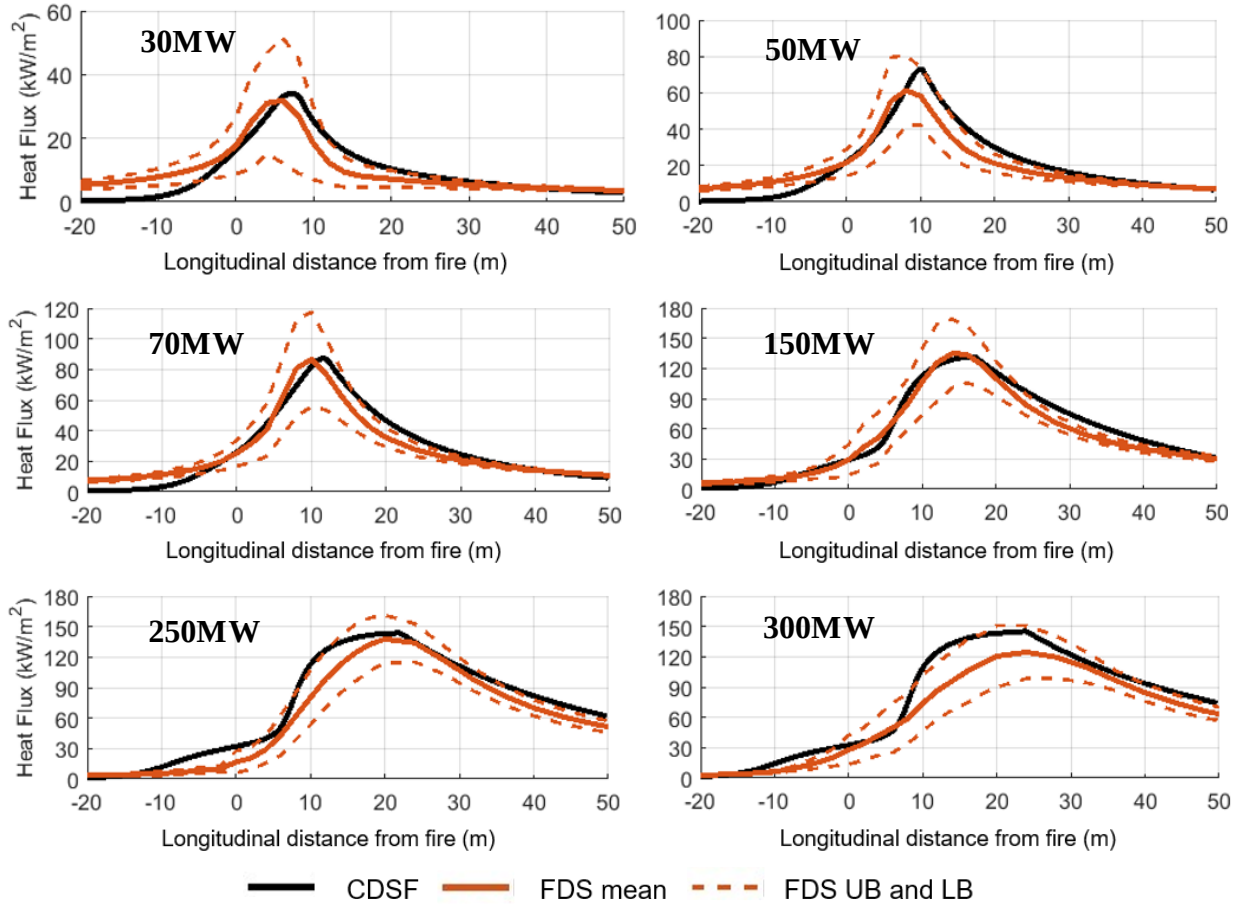

Figure 38: Comparisons of steady-state heat flux along the top-of-ceiling for Prototype A with fire HRR from 30-300 MW

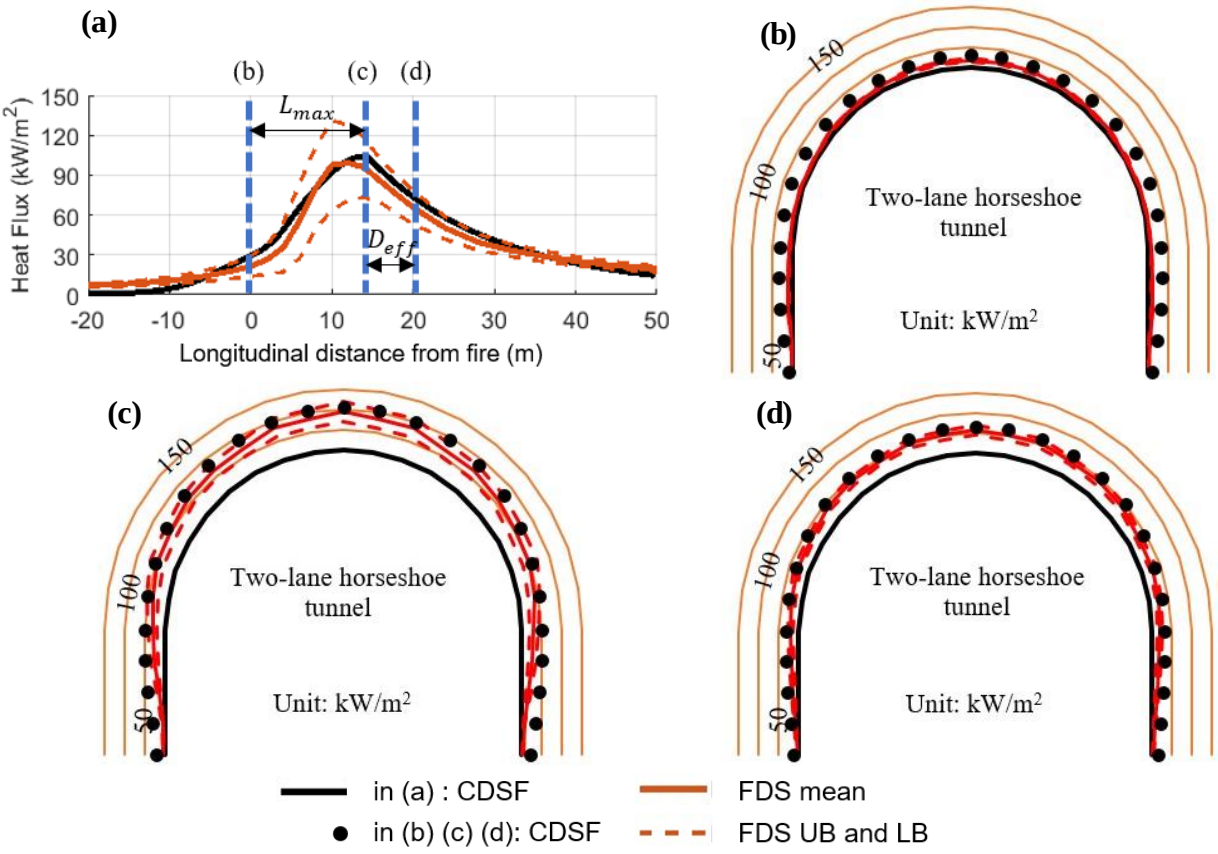

Figure 39: Comparisons of steady-state heat flux for the 100MW fire scenario in Prototype A: (a) the top-of-ceiling, and on transverse cross-sections (b) at the fire center, (c) at L_{max} downstream from the fire center, and (d) at $(L_{max} + D_{eff})$ downstream from the fire center.

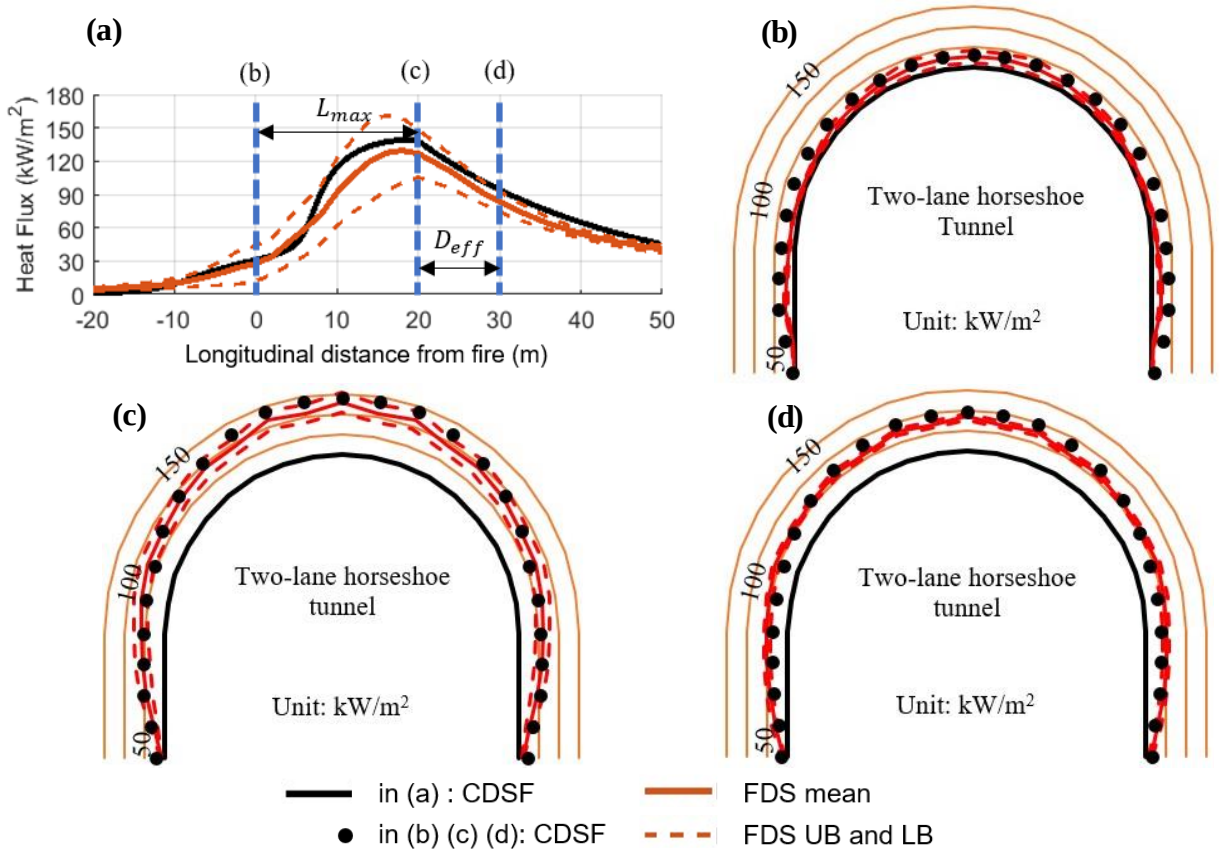

Figure 40: Comparisons of steady-state heat flux for the 200MW fire scenario in Prototype A: (a) along the top-of-ceiling, and on transverse cross-sections (b) at the fire center, (c) at L_{max} downstream from the fire center, and (d) at $(L_{max} + D_{eff})$ downstream from the fire center.

(b) Prototype B: 2-lane circular tunnel

A similar set of plots are provided in Figure 41 through Figure 43 for the circular Prototype B tunnel, which has similar ceiling height and roadway width as the horseshoe-shaped Prototype A but with 14% larger cross-sectional area (resulting in $S_c = 0.878$ per Eq. 28). As noted in Table 4, the increased cross-sectional area produces a slight (~5%) decrease in critical airflow velocity compared to Prototype A. Figure 41 plots the heat flux along the longitudinal axis at the top of the ceiling for the 50, 150, 250, and 300MW fire cases, while similar plots for the 100MW and 200MW cases are again shown separately in Figure 42a and Figure 43a with cross-sectional cut locations marked. Note that the 30MW and 70MW fire cases are not plotted in Figure 41 for brevity since they show similar trends to the 50MW fire scenario for this prototype.

All fire scenarios show similar trends of agreement between the CDSF and FDS predictions as was described in Section 4.3.3 for Prototype A. The b-d cross-sectional plots in Figure 42a and

Figure 43a again show good agreement between the CDSF and FDS predictions of transverse heat flux distribution for the 100MW and 200MW fire cases. In Figure 41, the smaller 50MW and larger 250-300MW cases show increasingly conservative CDSF predictions of peak heat flux versus the FDS results compared to those for Prototype A. The CDSF heat flux predictions along the ceiling are very similar between Prototypes A and B due to their similarities in height and critical velocity. The FDS simulations for the 50MW and 250-300MW cases become increasingly affected by the change in cross-sectional shape from horseshoe to circular, including the associated increase in cross-sectional area. Despite this, the CDSF predictions continue to provide a reasonably conservative prediction of heat flux distribution for a wide range of realistic fire sizes.

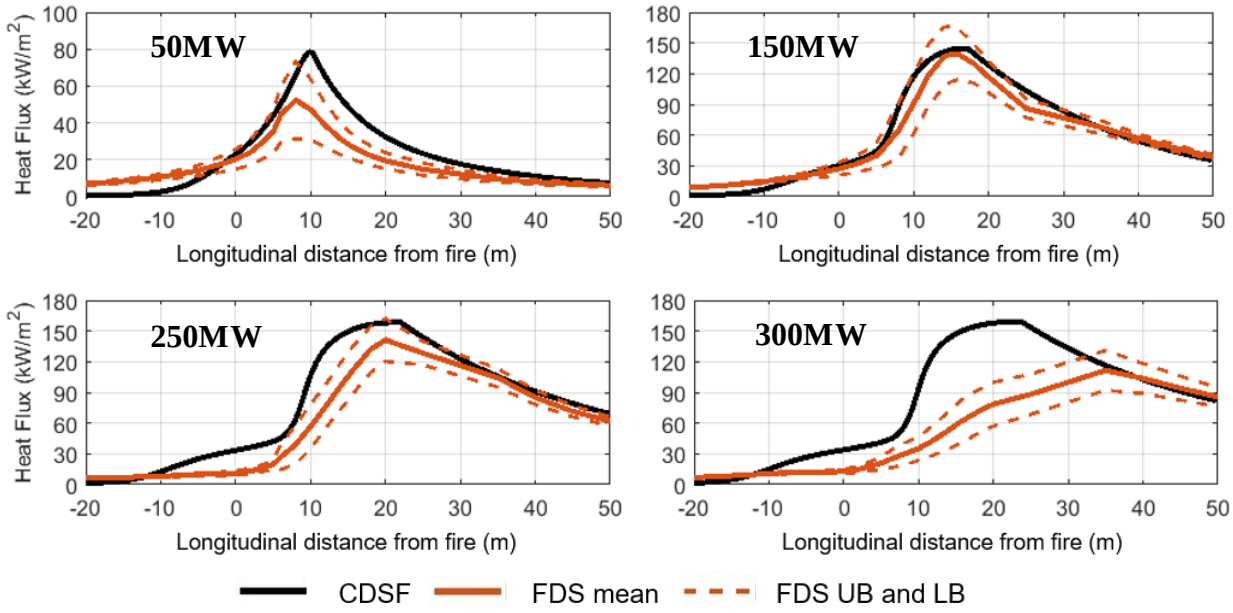

Figure 41: Comparisons of steady-state heat flux along the top-of-ceiling for Prototype B with fire HRR from 50-300 MW

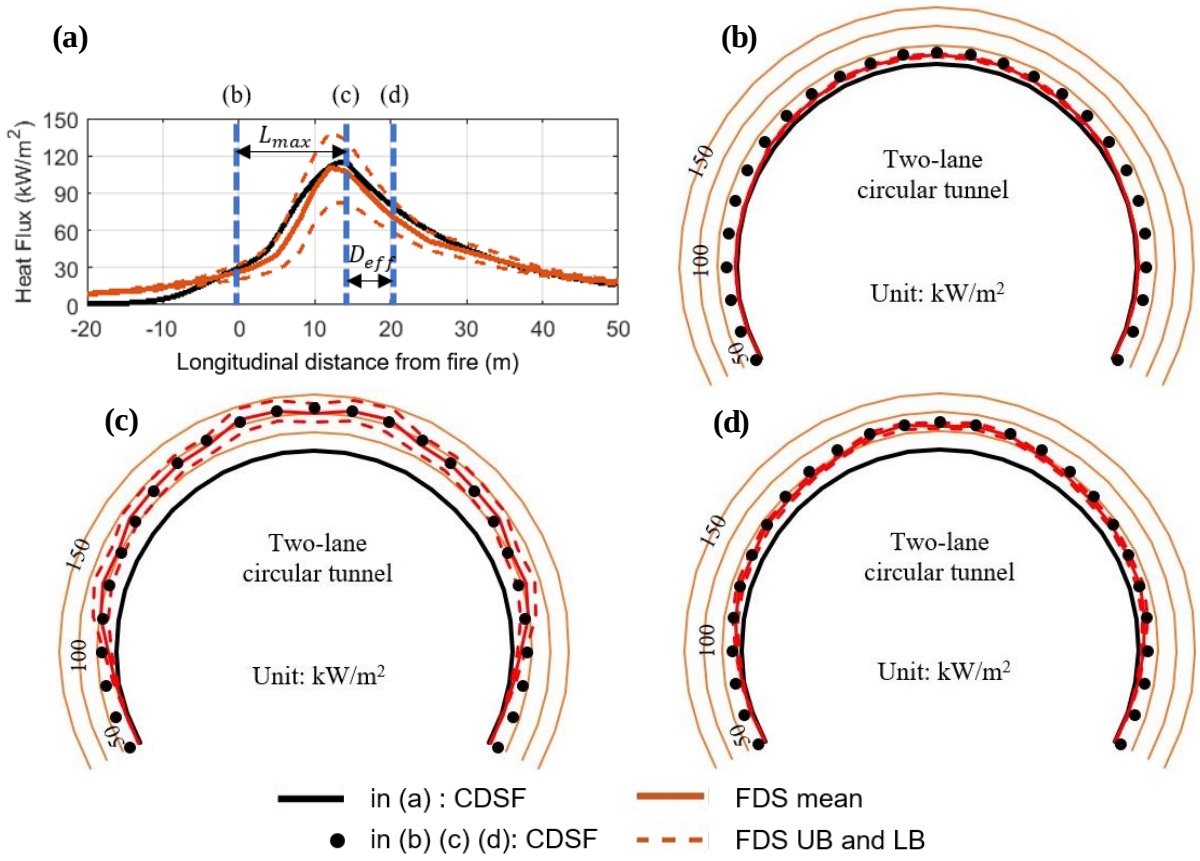

Figure 42: Comparisons of steady-state heat flux for the 100MW fire scenario in Prototype B: (a) along the top-of-ceiling, and on transverse cross-sections (b) at the fire center, (c) at L_{max} downstream from the fire center, and (d) at $(L_{max} + D_{eff})$ downstream from the fire center.

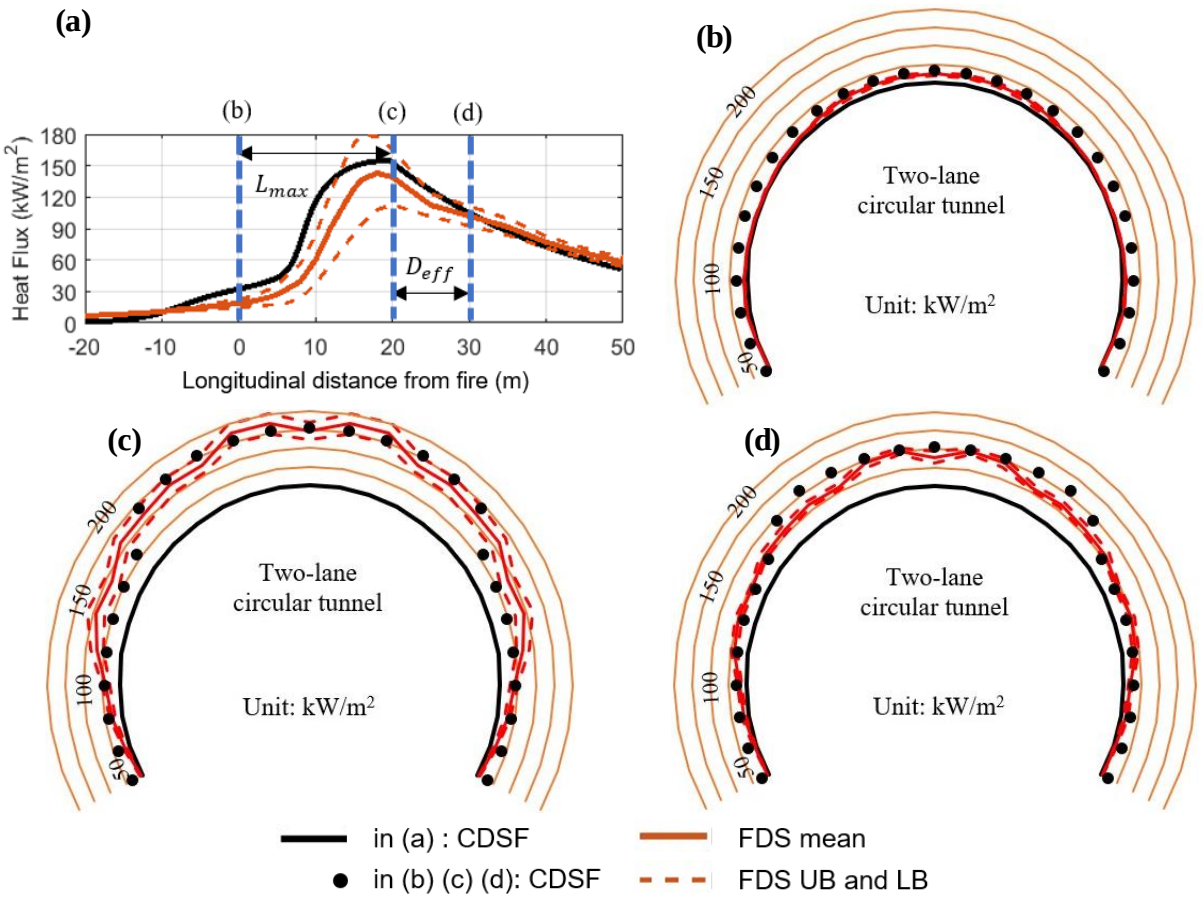

Figure 43: Comparisons of steady-state heat flux for the 200MW fire scenario in Prototype B: (a) along the top-of-ceiling, and on transverse cross-sections (b) at the fire center, (c) at L_{max} downstream from the fire center, and (d) at $(L_{max} + D_{eff})$ downstream from the fire center.

(c) Prototype C: 3-lane circular tunnel

The 3-lane circular Prototype C has 35% more ceiling height and 83.7% more cross-sectional area than the Prototype A 2-lane horseshoe shape (resulting in $S_c = 0.544$ per Eq. 28). Prototypes A and C have relatively similar critical velocities as reported in Table 4, but Prototype C will have more overall volume of airflow than Prototype A. With these changes, the results in Figure 44, Figure 45, and Figure 46 for fire scenarios with HRR from 100-200MW continue to demonstrate similar trends of close conservative agreement between the CDSF and FDS predictions as those for Prototype A. The 50MW CDSF results (again representative of the 30MW and 70MW fire cases, which are not plotted in Figure 44 for brevity) show a roughly 2 times overprediction of peak heat flux compared to the FDS mean curve, which has been reduced due to the increased cross-section area and tunnel height compared to both 2-lane prototypes. For fire sizes with HRR < 200MW, the wind-tilted CDSF model still provides reasonable predictions of maximum heat

flux along the ceiling that are not overly conservative compared to the FDS upper bound curve. For the larger 250-300MW fires, the CDSF maximum heat flux predictions now fall between the FDS mean and the lower bound curves.

The degree of wind tilt and flame drag for fires with HRR below 100MW and above 200MW appear to be more sensitive for the larger cross-sectional area of Prototype C and its associated theoretical value of critical airflow velocity. Future research should further explore the increased influence of fire size and airflow velocity on the development of heat flux intensity and distribution in tunnels with larger openings. However, the proposed wind-tilted CDSF model continues to deliver reasonable predictions of the distribution of heat flux on the Prototype C tunnel liner for a relatively wide range of fire intensities that are relevant to current design standards.

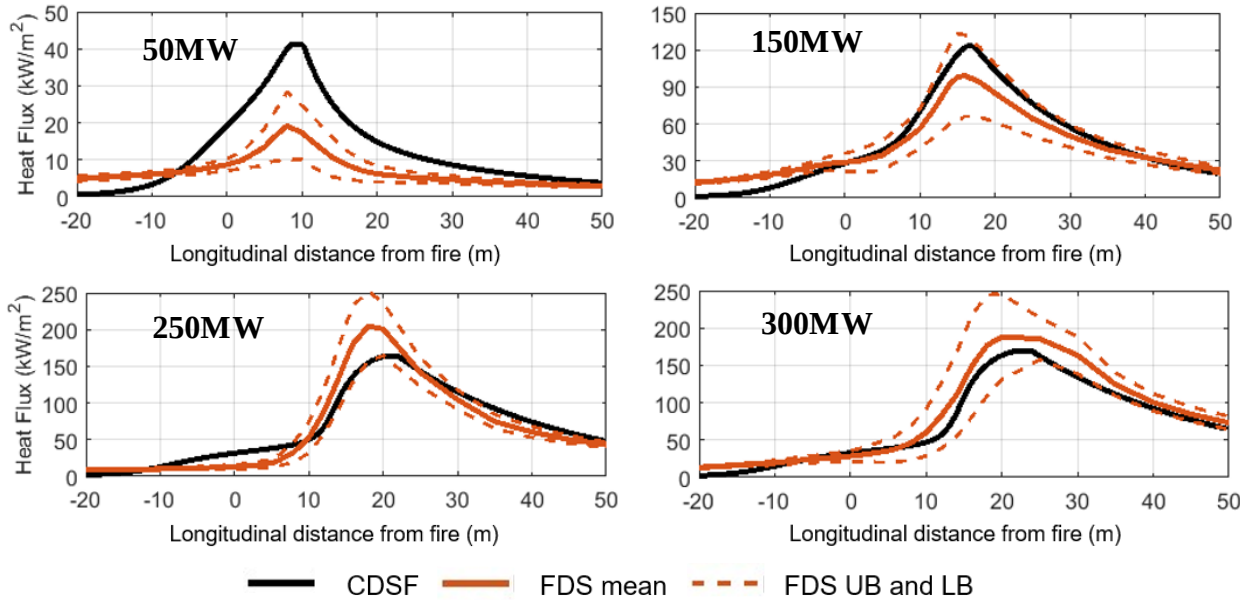

Figure 44: Comparisons of steady-state heat flux along the top-of-ceiling for Prototype C with fire HRR from 50-300 MW

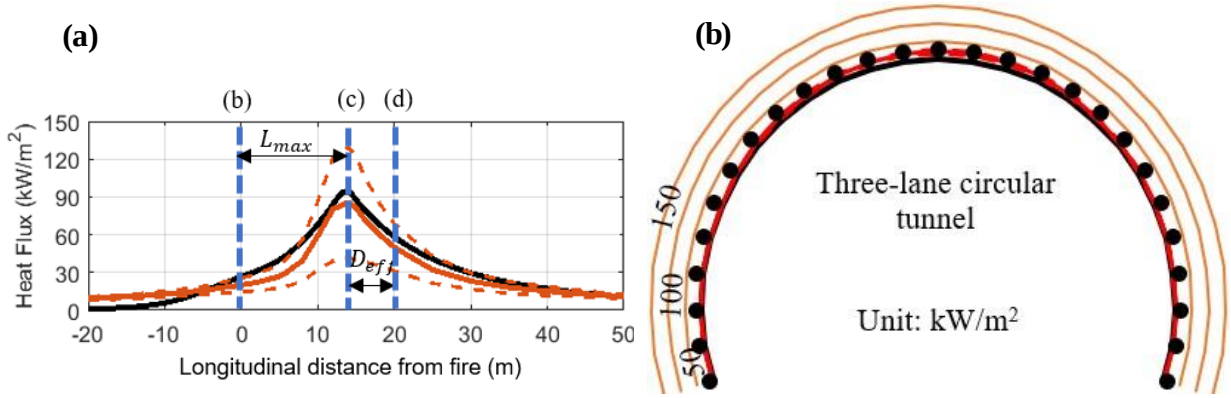

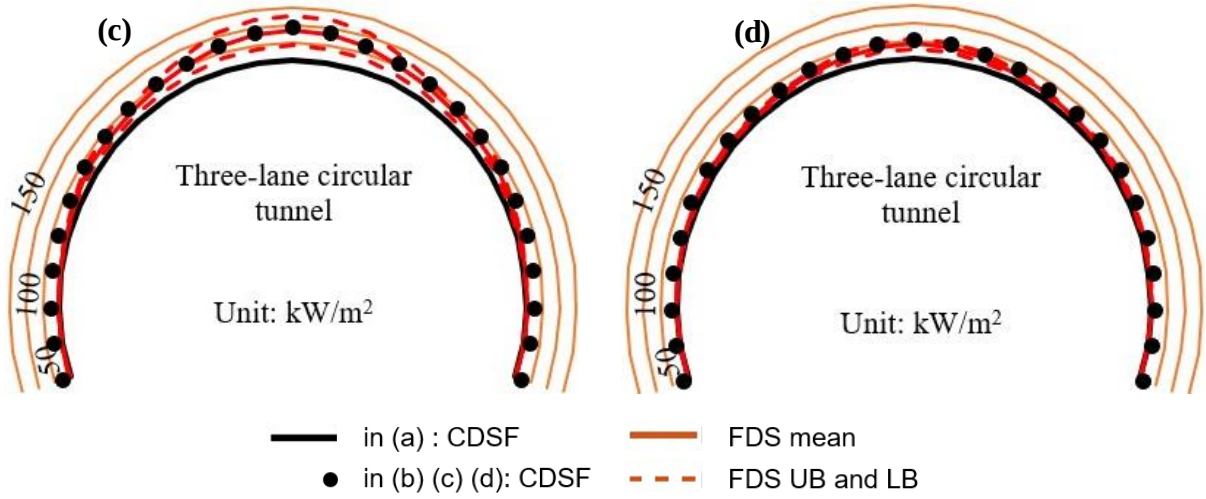

Figure 45: Comparisons of steady-state heat flux for the 100MW fire scenario in Prototype C: (a) the top-of-ceiling, and on transverse cross-sections (b) at the fire center, (c) at L_{max} downstream from the fire center, and (d) at $(L_{max} + D_{eff})$ downstream from the fire center.

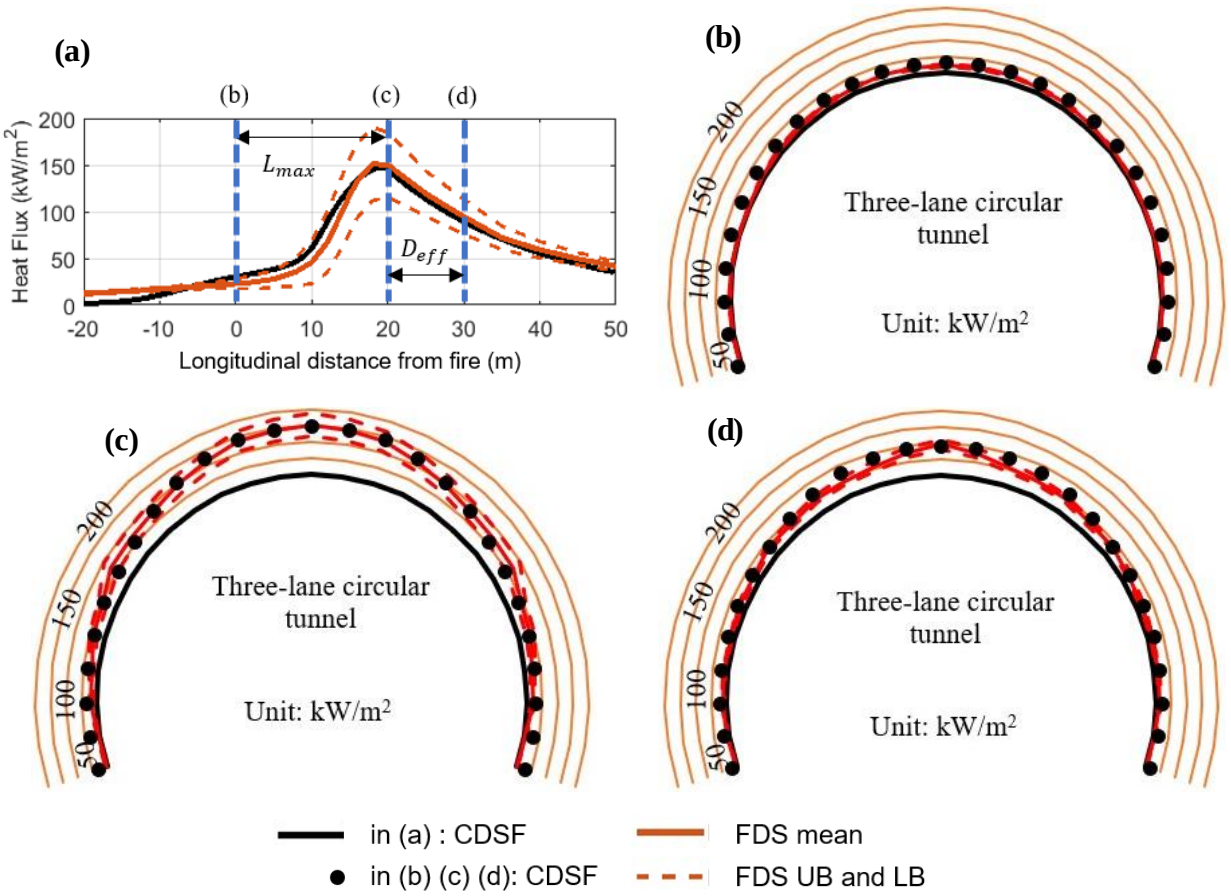

Figure 46: Comparisons of steady-state heat flux for the 200MW fire scenario in Prototype C: (a) along the top-of-ceiling, and on transverse cross-sections (b) at the fire center, (c) at L_{max} downstream from the fire center, and (d) at $(L_{max} + D_{eff})$ downstream from the fire center.

4.4. Conclusions

The confined discretized solid flame (CDSF) model, previously developed by the authors for calculating heat flux on tunnel liners with curved ceilings due to enclosed naturally ventilated fires (Guo et al. 2019), has been modified in this paper to account for the effects of longitudinal ventilation at critical velocity. The newly proposed "wind-tilted" CDSF model considers both the radiative and convective effects of the fire as its flames, smoke, and hot gases are pushed downstream by the forced airflow. Longitudinal and transverse distributions of incident heat flux on the tunnel liner from the CDSF model were compared against results compiled using NIST's Fire Dynamics Simulator (FDS) (McGrattan et al. 2013b), the modeling approach for which was validated against the results of Test 615B from the Memorial Tunnel Fire Ventilation Test Program (MTFVTP) (Bechtel/Parsons Brinckerhoff. and Bechtel/Parsons Brinckerhoff. 1995). The wind-

tilted CDSF results were generally conservative and showed reasonable agreement with FDS predictions for a range of fire sizes (for heat release rates from 30-300MW) in three prototype tunnels with either horseshoe and circular cross-sections.

Implementation of the CDSF model requires a programmed approach to calculate heat transfer between the discretized geometries of both the solid flame and the tunnel liner; however, all of its calculations are closed-form and require no iteration. The CDSF model can therefore predict total incident heat fluxes on concrete tunnel liners with curved ceilings at a fraction of the computational effort needed for high-fidelity CFD solutions. For the same analysis of the 100MW MTFVTP Test 615B, the CDSF solution (resulting in the heat flux data shown in Figure 39a) required less than 1% of the computational runtime compared to an FDS analysis (run with parallel processing on a research-grade desktop computer with full system dedication) of the same fire scenario for a 600-second burn duration.

The current CDSF model formulation assumes that the fire has adequate longitudinal distance from the tunnel openings. Open boundary conditions were implemented at the openings of the high-fidelity FDS models that were used to calibrate the CDSF model – the influence of the openings at close proximity to the fire should be considered in future updates to the CDSF methodology. It should also be noted that the FDS analyses in this study utilized several simplifications, the most prominent being the application of critical longitudinal airflow velocity (calculated per the 2017 edition of NFPA 502 (NFPA 2017)) as a uniform inlet profile at one end (i.e. at a longitudinal boundary or "portal") of the tunnel model. The resulting longitudinal airflow profiles along the length and height of the tunnel showed reasonable agreement with measured data for Test 615B; however, the influence of discrete jet fan operation and placement could be incorporated in future iterations of this work. Recent updates have also been made to the calculation of critical velocity for longitudinal tunnel ventilation in the 2020 edition of NFPA 502 (NFPA 2020), and the proposed CDSF model could be correspondingly updated in future work as needed.

Now with the ability to consider both natural and forced ventilation effects, the proposed CDSF framework has significant potential for stochastic assessment of the risk of fire-induced as well as losses of tunnel functionality (due to downtime for repair). The heat flux distributions obtained from the CDSF model can be used to conduct thermos-structural analysis of the tunnel liner. As such, the influence of passive fire protection (such as fire resistive boards or spray-applied

materials) on the post-fire resilience of the concrete liner can be evaluated. Also, the influence of active fire protection (such as fixed firefighting systems that deploy water mist, droplets, or deluge) can also be incorporated into the CDSF approach by adjusting the HRR of the enclosed fire or by mitigating the heat transfer within the CDSF calculations. Such capabilities will be the subject of future phases of this project.

CHAPTER 5 – CONCRETE LINER DAMAGE ANALYSIS AND CLASSIFICATION

Vehicular fires induce high temperatures, intense heat flux, and steep thermal gradients within tunnel liners. At elevated temperatures concrete structural strength is reduced, which, if severe, can require material replacement post-fire exposure. Moreover, heat-induced spalling, which is commonly observed at the concrete surface during intense fire exposures, generally increases the cumulative concrete liner damage state by reducing the structural cross-section and exposing the deeper concrete material and steel reinforcement to direct heat exposure. The violent ejection of concrete material during spalling increases the life safety risk of tunnel fires and results in a prolonged tunnel closure. Therefore, the inclusion of thermally-induced concrete spalling is vitally important to the characterization of concrete damage classification in this study. Neglecting concrete spalling behavior in fire can lead to unconservative damage estimations.

Concrete performance in fire is a function of the thermal exposure intensity, duration, and the concrete thermal properties. Though standards such as Eurocode 2 (European Committee for Standardization 2004) provide recommended temperature-dependent thermal properties, the uncertainties inherent in concrete (e.g., coarse aggregate: type (siliceous or calcareous), size, distribution, and volumetric fraction and water distribution), as well as physical tunnel conditions (e.g., air humidity and ambient temperatures), inspire the use of stochastic analysis.

5.1. Concrete spall modeling via FE method

Fire induced concrete spalling has been broadly studied in past decades (Bazant et al. 1981; Harmathy 1965; Shorter and Harmathy 1961; Zhukov 1976), with various experimental testing programs evaluating thermal spalling of concrete using cylinders (Choe et al. 2019; Hertz and Sørensen 2005; Phan et al. 2001), small panels (Choe et al. 2019; Kalifa et al. 2001; Tatnall 2002), and larger structural elements (Jansson and Boström 2010; Wang et al. 2017; Yan et al. 2016). The results of these studies have led to the development of a range of prediction methods, from the simple, using concrete property thresholds (European Committee for Standardization 2004; Hertz 2003) to complex, using a myriad of numerical solutions (Bažant and Thonguthai 1979; Davie et al. 2012; Dwaikat and Kodur 2009; Gawin et al. 2006; Ichikawa and England 2004; Kodur and Banerji 2021; Li et al. 2010; Lu 2015; Majorana et al. 1998; Tenchev and Purnell 2005). Hua et al. (2021) tabulated a comprehensive review of spalling behavior test results (Hua et al. 2021). The

literature suggests the contributing factors of thermally-induced explosive concrete spalling behaviors include thermal stresses from elongation and restraint conditions, mechanical stresses from the applied loads, the pore pressures generated from water vapor present at ambient condition and liquid water phase changed during heating, and reductions in the concrete strength at elevated temperatures. However, none of the proposed prediction methodologies accurately describe the spalling phenomenon well, i.e., accurately predicting time, depth, and occurrence of spall for both high performance and normal weight concretes. To avoid overly complex hygro-thermal finite element modeling that would make the computational expense untenable, this paper will focus on providing a straightforward, while also conservative, methodology of spall prediction based upon the following parameters. (1) From the literature review by Hua et al. (2020), spalling behavior was triggered when the hottest concrete material layer reached a uniform temperature of 740°C (Hua et al. 2021). (2) Based upon the experimentally validated work of Lu (2015), the range of material temperatures at the spalling failure depth was found to be between 250°C and 400°C (Lu 2015). Therefore, in this study concrete spalling is assumed to occur from the triggering surface temperature of 740°C to the internal layer which is at 250°C. After this event is reached in time, the spalled materials is removed from the model and the remaining concrete is exposed to the remaining heat flux demand. The temperature distribution in the un-spalled concrete is maintained from the thermal state prior to spalling and temperature penetration is monitored for additional spalling. The determination of additional spalling is continued until the exhaustion of the fire duration or when the spalling front has reached a reinforcement layer. The reinforcement layer was defined as a stopping depth, based upon the assumption that rebar provides additional concrete confinement that will impede spall advancement. The general concept of this step-by-step spall advancement was first proposed by Hua et al. (2020) and is herein adjusted based upon the authors' experimental spalling observations (Carlton et al. 2022), the temperature parameters defined in Lu (2015) based upon the spalling condition identified by Zhukov (1976) (Lu 2015; Zhukov 1976), and engineering judgment to arrive at a reasonably conservative estimation of the spalling condition.

The concrete thermal response is established using SAFIR (version 2019), a finite element software specially developed for thermal-structural analysis. The analysis procedure to simulate the concrete spalling behavior is presented in Figure 47. A MATLAB script is introduced to evaluate the spalling temperature criteria at each step with respect to the SAFIR determined

temperature gradient in the concrete section. After the spalling criteria is reached, the MATLAB script automatically creates an updated input file, which removes the spalled concrete layers and applies the next time step of the heat flux time history to the new exposed concrete layer for the next SAFIR time step. The new SAFIR thermal analysis restarts directly after the spalling time step while retaining the temperature field from the previous time step. This MATLAB-SAFIR interactive process is repeated until either the heating duration ends or the reinforcement layer is reached. To accurately detect the spall depth of each step, a fine discretization is used for the concrete cover mesh. This particular study utilizes 20 layers for the 51 mm (2.0 in.) concrete cover. Each concrete spalling analysis iteration takes approximately 1 to 3 minutes from initiation to spall occurrence, and is related to the heating rate intensity (i.e., the greater the heat intensity the earlier the spalling condition is satisfied).

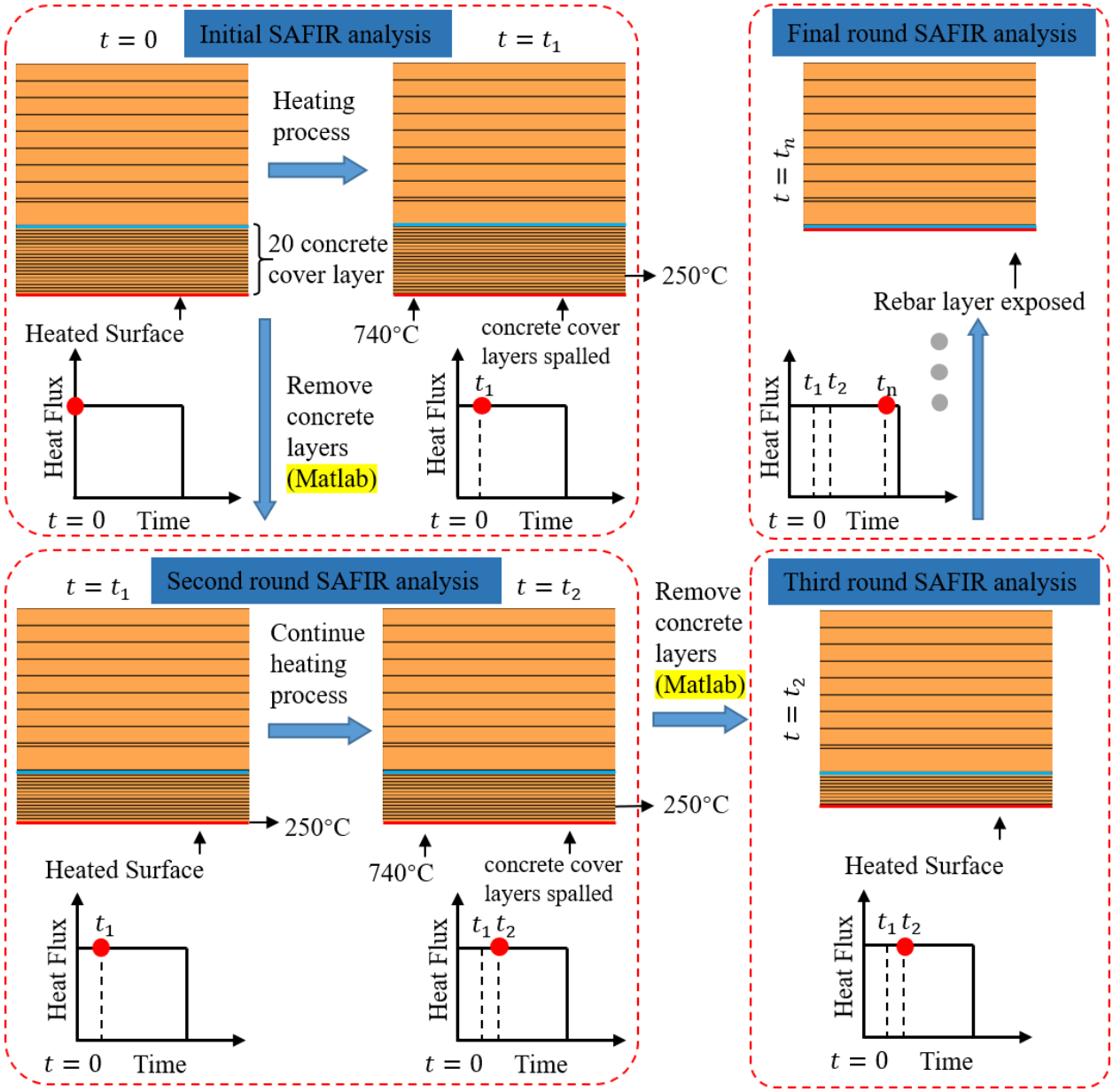

Figure 47: FE method of simulating the concrete spalling with MATLAB/SAFIR interactive process

5.2. Uncertainties of concrete thermal properties

The concrete thermal properties, specifically thermal conductivity and specific heat, control the temperature propagation. Experimentation has shown large uncertainty in the thermal behavior of concrete of different constitutive components and in-situ conditions (Jovanović et al. 2020). As suggested in Eurocode 2 (European Committee for Standardization 2004), temperature-dependent thermal conductivity can be bounded between lower and upper limit values while the specific heat

is highly influenced by the moisture content. As such, stochastic estimations of the thermal properties and moisture condition are used herein to account for the variety in concrete mix design and in-situ condition.

This study adopts the stochastic model proposed by Jovanović, B., et al. (2020)(Jovanović et al. 2020), with thermal conductivity, λ_c (W/m·K), defined by data collected from 12 sources and specific heat c_p (kJ/kg· K), defined via 9 sources. The mean and standard deviation for each variable is a function of temperature T (°C) and is calculated via Equations (4) and (5):

$$\lambda_{c\_mean} = 6.627 \times 10^{-7} \times T^2 - 1.458 \times 10^{-3} \times T + 1.772 \quad (37a)$$

$$\lambda_{c\_std} = 3.139 \times 10^{-7} \times T^2 - 0.691 \times 10^{-3} \times T + 0.434 \quad (37b)$$

$$c_{p\_mean} = -2.953 \times 10^{-7} \times T^2 - 6.498 \times 10^{-4} \times T + 0.872 \quad (38a)$$

$$c_{p\_std} = -3.500 \times 10^{-7} \times T^2 - 7.700 \times 10^{-4} \times T + 0.042 \quad (38b)$$

Both thermal conductivity and specific heat for a given temperature are assumed to be Gamma distributions. Therefore, the process of generating the range of temperature-dependent thermal property curves includes two steps: (a) calculate mean and standard deviation value for each specific temperature via Equations (4) and (5); and (b) generate range of thermal properties based on a defined quantile value following a Gamma distribution. As presented in Figure 48, the mean value of thermal conductivity and the specific heat of dry concrete (moisture content u = 0%) are represented as black solid lines while the gray dashed lines represent the 5% and 95% quantiles. Figure 48 (a) illustrates a sample of twenty randomly generated concrete thermal conductivity curves used for stochastic analysis in the following sections.

The stochastically generated specific heat-temperature curves computed using the mean and gaussian distribution, which are illustrated with black solid and gray dash lines in Figure 48 (b), are modified to account for a spike which occurs near the vaporization point of water. Noted in Eurocode 2, a constant peak, which is directly related to the moisture content, is located between 100°C and 115°C, and linearly decreases between 115°C and 200°C. Based upon moisture content percent interpolated between Eurocode 2 and 4 defined peak values of: 0% at 900 J/kg· K, 1.5% at 1470 J/kg· K, 3.0% at 2020 J/kg· K, and 10% at 5600 J/kg· K. Therefore, the moisture content can be defined by random variation to determine the concrete thermal behavior. Since the specific heat is highly sensitive to the moisture content percentage, the constant peak within the specific heat definition requires the moisture content to be defined before interpolation within Eurocode 2 and 4's values could be completed.

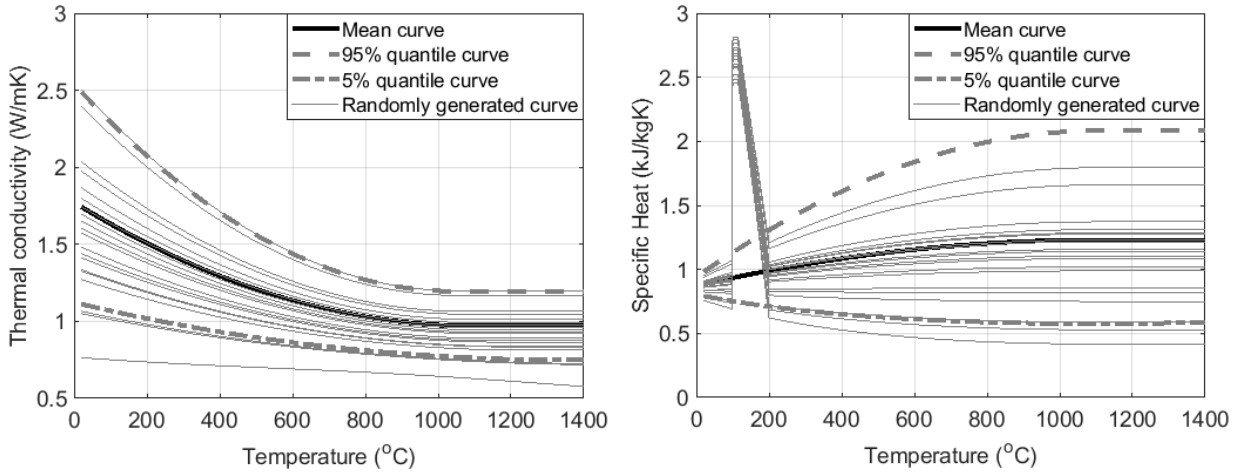

(a) Thermal conductivity (b) Specific heat

Figure 48: Probabilistic model for concrete at elevated temperature: mean value, 5%, and 95% quantiles and 20 randomly generated curves used as thermal analysis inputs

The moisture content is calculated as the weight of the water, W_w (kg), over the weight of the dried concrete, W_s (kg). The weight of water is determined from the water-permeable void space percentage, V_w (%), and saturation, S_w (%), as presented in Eq. (39):

$$u = \frac{W_w}{W_s} = \frac{V_w \cdot S_w \cdot \rho_w}{\rho_s} \tag{39}$$

where water density, ρ_w = 1000 kg/m^3, and ρ_s (kg/m^3) is the bulk dry density of concrete.

As tunnels are artificial underground passages, many tunnel systems have relatively high air humidity and groundwater contact which keep tunnel liner concrete saturation high, in range from 85% to 95% (Holter and Geving 2016). The mean value of concrete saturation rate S_w (%) was set to 90% with a standard deviation of 1.67%, which is calculated as one-third of the gap from upper/lower bound to the mean value. According to Eurocode 1(Eurocode 1 1991-1-1 n.d.), the density of normal-weight concrete is 2400 kg/m^3. Considering the water evaporation in the oven-drying process, the weight of dry concrete ρ_s (kg/m^3) used in Eq. (39) is assigned with the mean value of 2350 kg/m^3 and standard deviation of 16.7 kg/m^3.

The water-permeable void volume percentage was defined though stochastic estimation using the Federal Highway Administration (FHWA) national United States (US) roadway tunnel inventory, the American Society of Civil Engineers-Structural Engineering Institute's (ASCE/SEI) Evaluation and Retrofit of Existing Buildings, and an ASTM C642 standard study (Abdul Kreem 2012; American Society of Civil Engineers 2007; ASTM International 2013 p. 642; USDOT

2015). To arrive at a reasonable random variation for the void percentage, a resultant distribution was created assuming Gaussian behavior of US roadway tunnel concrete properties based upon the tunnels' construction date, typical concrete strength within the era of construction, and the relative relationship between concrete compressive strength and ASTM C642 defined water-permeable void volume percent.

Figure 49 shows the total US roadway tunnel inventory total tunnel values by date of construction, blocked with the construction eras defined by ASCE/SEI 41 Table 10-2. Here the total number of tunnels constructed within each era are given at the top of each block, for example the 1920-1949 construction era represents 137 tunnels in today's current US roadway inventory and are shown in the second block at the center-left of Figure 49. Tunnels constructed before 1900 still in operation were assumed to have the same strength approximations of those in the 1900-1919 era.

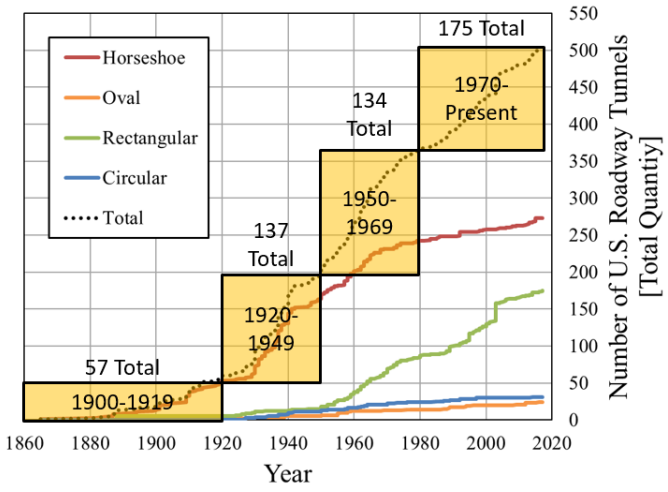

Figure 49: FHWA 2015 US Roadway Tunnel Inventory

Figure 50 shows the distributions extrapolated from the values defined in ASCE/SEI 41 Table 10-2, which define the default compressive strengths for structural concrete for each construction era. This paper assumes that the values from ASCE/SEI 41 Table 10-2 represent a good faith estimate of the typical concrete strength available for US roadway tunnel liner construction within the same time periods. As such, the maximum value and minimum values under each construction era from ASCE/SEI 41 were assumed to represent two standard deviations from the mean value of the era range. Figure 50 shows the Gaussian distribution estimates from ASCE/SEI 41 as box and whisker plots with the central bar as the mean and the upper and lower quartile boundaries at two standard deviations from the mean. Therefore, the assumed Gauss distributions in Figure 50

were then assigned in weighted average of the tunnels constructed within each era to the total number of US roadway tunnels currently in the FHWA inventory report shown in Figure 49.

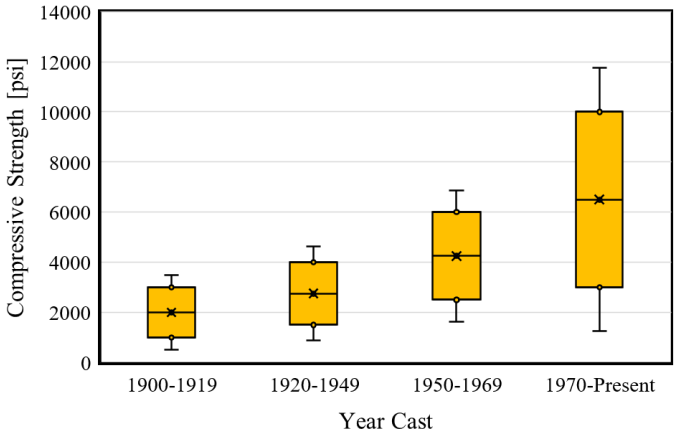

Figure 50: ASCE/SEI 41 concrete strength by construction era assumptions

Table 5 summarizes the total constructed roadway tunnel numbers in the US within different years and their corresponding concrete compressive strength distribution extrapolated from the values defined in ASCE/SEI 41. Based on the bounds of compressive strength, the approximate water permeable void volume percentage is estimated according to work by Abdul Kreem (Abdul Kreem 2012), in which the porosity was tested and calculated according to ASTM C642. Generally, the void percentage decreases as the concrete strength increases. For calculation purposes, the maximum and minimum values of concrete strength and permeable water void under each construction era were assumed to represent two standard deviations from the mean value. The representative probabilistic distribution of the void percentage of US roadway tunnel liners was determined by sampling the porosity for each year with a sample size of 10,000, and applying a weight based on the number roadway tunnels of the corresponding tunnel construction in that year. The water-permeable void percentage V_w (%) follows a general Gaussian distribution shape with the mean value of 11.41% and standard deviation of 0.46%.

Table 5: ASCE/SEI 41 to ASTM C642 via Abdul Kareem Void Percent by Strength Assignment

ASCE/SEI 41					ASTM C642 Estimated via Abdul Kreem (Abdul Kreem 2012) [Void %]		
Construction Era	No. of Tunnels	Compressive Strength [MPa]					
		Lower Bound	Mean	Upper Bound	Lower Bound	Mean	Upper Bound
1900-1919	57	6.89 (1000 psi)	13.79 (2000psi)	20.68 (3000 psi)	11.2	13.35	15.5
1920-1949	137	10.34 (1500 psi)	18.96 (2750 psi)	27.58 (4000 psi)	10.5	13	15.5
1950-1969	134	17.24 (2500 psi)	29.30 (4250 psi)	41.37 (6000 psi)	9.6	11.4	13.2
1969-Present	175	20.68 (3000 psi)	44.82 (6500 psi)	68.95 (10000 psi)	8.6	9.55	10.5

The uncertainty parameters used to calculate the tunnel concrete liner moisture content via Eq. (39) were developed by Monte Carlo Simulation with a sampling size of 100,000. All the parameters were assumed to follow Gauss distribution in the absence of available experimental data. Overall, the moisture content, u (%), of US roadway tunnel liners from this analysis method reveals a Gaussian-shaped distribution with a mean value of 4.46% and a standard deviation of 0.20%. Figure 48 (b) illustrates 20 specific heat curves for the stochastic concrete thermal analysis in the following sections.

5.3. Concrete liner damage classification

Assessment of the damage to the remaining concrete surface after the fire exposure event is important to determine repair required. Concrete loses strength and stiffness at elevated temperatures, and under fast heating rates the probability of explosive spalling increases. Concrete tunnel liners subject to fire, therefore, experience structural integrity, residual strength, and durability reductions. Damage state definition for concrete tunnel liners post fire event is important due to the influence on subsequent inspection and repair tasks, and must also account for functionality and recovery to provide a helpful measure of resilience. The following discussion provides the rationale and definitions of the damage states selected in this study.

A number of standards (Bergeson and Ernst 2015; Ingham 2009; Joint ACI/TMS Committee 216 and Masonry Society (U.S.) 2007) suggest 300°C as the recommended temperature threshold for significant concrete material damage. Concrete reaching this temperature changes color from light gray to red/pink, and is easily discernable via visual inspection. Therefore, the presence of

red/pink concrete in a fire-damaged structure should be treated as potentially damaged and would warrant further investigation. As demonstrated in multiple experiments and observations, concrete experiencing temperature higher than 300°C undergoes permanent strength reductions, which typically requires removal and replacement. According to the concrete repair procedure provided by PennDOT, once the damaged area is delineated, the deteriorated concrete is removed either to 19 mm (0.75 in.) behind the first mat of reinforcing bars or to the depth of sound concrete. Moreover, the reinforcement embedded in the liner may experience high temperatures as the concrete cover spalls. Cold-worked steel including welded wire reinforcement exhibits permanent yield strength loss if 450°C is reached, while the benchmark for hot-rolled steel (e.g. conventional rebar) is 600°C (Ingham 2009). Structurally, the reinforcement directly exposed to fire may eventually experience buckling and residual deflection due to removal of the protective concrete cover and subsequent heating. Therefore, spall exposed steel reinforcement should be replaced to retain structural capacity. The following damage classes were defined relative to the repair procedure and correspond to the concrete tunnel functionality loss and recovery process:

- **Superficial**: The temperature of the heated surface was below 300°C. The concrete surface color remains unchanged. The residual strength is consistent with the value prior to the fire. No repair is required and structurally, the tunnel can be reopened to its full functionality following the event.
- **Moderate**: The concrete experienced a temperature higher than 300°C and the estimated spall depth is shallower than the concrete cover. For this damage level, the strength of concrete was permanently reduced as aforementioned. Moreover, the liner surface may spall in the heating process. However, the unexposed reinforcement is considered intact as the remaining concrete cover provides adequate thermal insulation and constraint. Repair consists of removal of the deteriorated concrete to a depth of 19 mm behind the reinforcement, which is presented in Figure 51, and replacement with shotcrete. The repair process requires full tunnel closure.
- **Heavy**: The concrete has spalled to the depth of the reinforcement. During the event, the exposed reinforcement has experienced temperatures exceeding 600°C resulting in permanent yield strength reduction (Ingham 2009). The compromised reinforcement should be removed and replaced. Concrete should be removed to a depth of 19 mm behind the reinforcement. Unsound concrete will likely be present beyond this point and further removal should be performed with the

permission of the responsible structural engineer to ensure that the global structural integrity is not compromised (indicated in Figure 51). The repair process requires full tunnel closure.

5.4. Stochastic analysis

The performance of tunnel liners subjected to fire hazards largely depends on the concrete thermal properties, which has large uncertainties as aforementioned. They vary according to the material composition (i.e., siliceous or calcareous aggregates), the tunnel environmental conditions, and the year of construction. Moreover, differences in concrete properties from one location to another even for the same tunnel (i.e., close to the portal vs in the middle section of the tunnel) can reasonably be expected. However, compared to the uncertainties associated with fire characterization (such as the exposure magnitude and duration; which are largely influenced by the vehicle fire type), tunnel system performance (e.g., ventilation systems, fire warning systems, and/or fire suppression systems), and human to fire reactions, the uncertainty of concrete thermal properties plays a relatively minor role in determination of the damage state. Therefore, to avoid unnecessarily large computational expense, which would include the uncertainties of fire and concrete thermal properties simultaneously, the concrete liner performance is investigated of the fire event through stochastic analysis.

The stochastic analysis provides a concrete damage assessment relative to deterministic thermal impacts, while including the uncertainty in the concrete thermal properties. The Monte Carlo simulation utilized Latin Hypercube sampling to increase computational efficiency. The 2D thermal analysis finite element model as illustrated in Figure 51 is considered to be deterministic. In this example, the thickness of the concrete cover was defined at 50 mm (2 in.) (Commonwealth of Pennsylvania 2016), while the cross-sectional thickness of the liner was assumed to be 0.3 m (11.8 in.) (Guo et al. 2019). The reinforcement was represented as a thin smeared layer, as opposed to individual circular cross-sections, and was located behind the concrete cover. The cover was discretized into 20 fiber elements (in 2.5 mm thick layers) to accurately simulate spall behavior depths. A thin concrete layer is placed 19 mm (0.75 in.) behind the steel reinforcement layer to assess if the temperature at the removal thickness is thermally compromised for the “Heavy” damaged concrete liner as stated in the damage classification discerption in section 5.3. The remaining concrete liner is meshed at 12.7 mm (0.5 in.) per layer to capture the thermal penetration and help quantify the thickness of unsounded concrete that requires further removal.

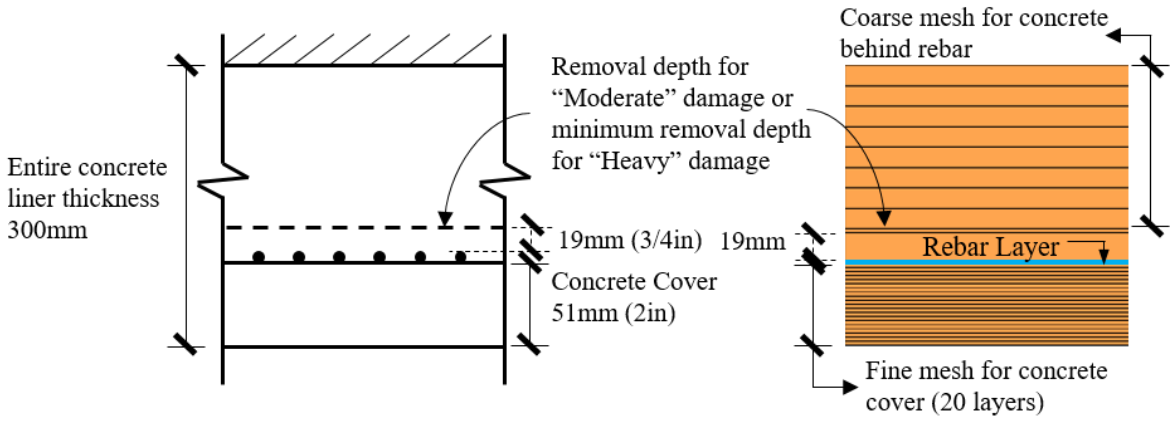

Figure 51: Tunnel concrete liner model in SAFIR

The input parameters for a single thermal analysis are summarized in Table 6. As mentioned in the previous section, the temperature-dependent concrete conductivity and specific heat (at a moisture content, u = 0.0%) are sampled via Gamma distribution, while the moisture content, which determines the peak specific heat, was determined from intermediate variables following the assumed Gaussian distribution. The magnitude of the heat flux is randomly chosen from 0 to 300 kW/m^2, while the exposure duration ranges from 0 to 80 min. The convective coefficients for the fire-exposed and unexposed surfaces were 25 W/m^2-K and 9 W/m^2-K, respectively, per Eurocode 1, Part 1-5 (CEN 2002). The emissivity of concrete was defined at 0.7 per Eurocode 2 (European Committee for Standardization 2004). For each thermal analysis, concrete spalling estimation was model via the MATLAB-SAFIR interactive process, which was introduced in section 5.1. This study used 2,000 simulations to reach convergence of the damage classification.

Table 6: Input parameter for concrete liner damage classification development

Concrete thermal properties				
Description	Unit	Distribution	Mean Value	Standard deviation
Conductivity λ_c	(W/m^2·K)	Gamma	λ_{c_mean} via Eq. (37)	λ_{c_std} via Eq. (37)
Specific heat c_p (u=0.0 %)	(kJ/kg· K)	Gamma	c_{p_mean} via Eq. (38)	c_{p_std} via Eq. (38)
Moisture content u	-	Gaussian	4.46%	0.2%
Fire exposure parameters				
			Lower bound	Upper bound
Heat Flux $\dot{q}$	kW/m^2	Uniform	20	300
Exposure duration t	min	Uniform	0	80

For each simulated case, the concrete damage is classified as superficial, moderate, or heavy as will be defined in section 5.3. The full result set for the 2,000 randomized simulations are presented in Figure 52a as a function of the heat flux and exposure duration. Each point is colored according to damage level. As expected, damage level increases as the thermal impact magnitude and duration increases. The analysis results in delineated boundaries for each damage level region. Transferring to the *ln-ln* space as shown the Figure 52b, the boundaries between the data clusters corresponding to each damage level can be detected using the Support Vector Machine (SVM) algorithm, which is a supervised machine learning approach (Cortes and Vapnik 1995). This algorithm draws the hyperplanes to maximize the surrounding margins of each region. The built-in SVM function in MATLAB is applied herein to develop the binary classification for the superficial to moderate and the moderate to hazardous damage regions using the linear SVM score function, expressed in Eq. (40):

$$w_1 \cdot \ln(\dot{q}) + w_2 \cdot \ln(t) + b = 0 \tag{40}$$

where w_1 and w_2 are weighting factors and b is the bias term. The linear boundaries between each damage level are plotted with black dash lines in Figure 52b and the value of the coefficients associated with each boundary are summarized in Table 7. The damage regions corresponding to each damage level ensure over 98% of training samples fall into the correct category. Transferring back to the heat flux- exposure time-space as in Figure 52a, the damage boundaries are nonlinear and resemble the shape of Pressure-Impulse (*P-I*) curves, commonly used blast resistant building design (U.S. Army Corps of Engineers 2008). The damage state of the concrete liner was determined by mapping the thermal impact expressed by heat flux and exposure overlaid onto the concrete damage map.

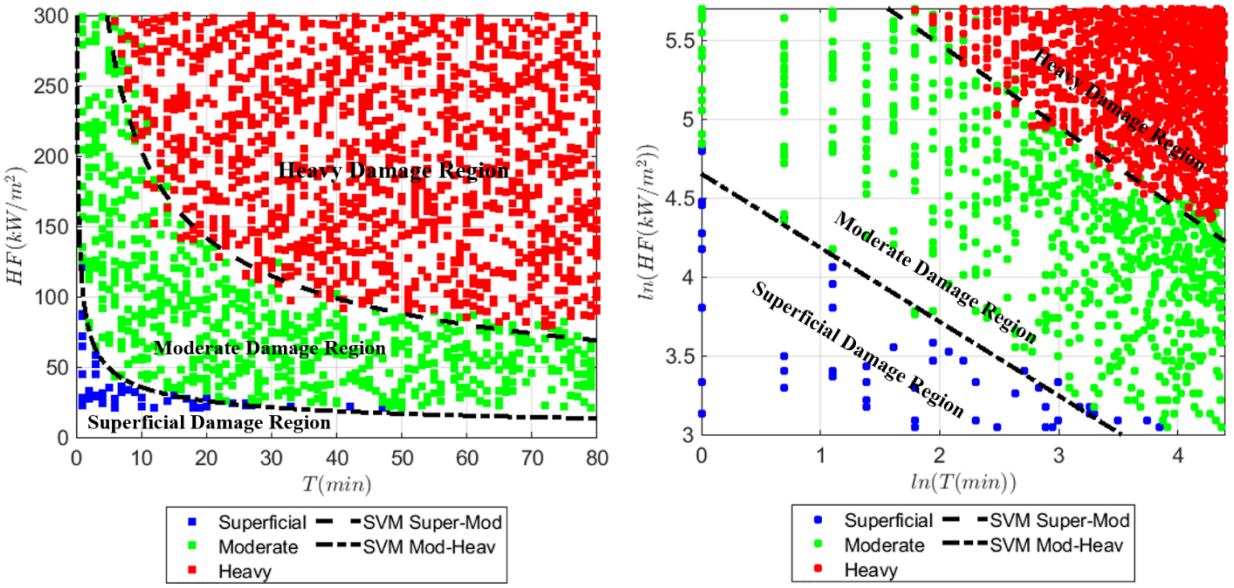

(a) Thermal impact expressed with heat flux and exposure duration

(b) Thermal impact expressed with ln (heat flux) and ln (exposure duration)

Figure 52: Damage of concrete panel as a function of heat flux and exposure duration

Table 7: Linear SVM coefficients for damage limit boundaries concrete liner

Boundary	w_1	w_2	b	Slope $(-w_1/w_2)$
Superficial-Moderate	1.852	3.953	-18.39	-0.47
Moderate-Heavy	3.609	6.924	-45.11	-0.52

Further investigation of the heavy damage cases indicates that concrete temperatures exceed the 300°C threshold deeper than 19 mm behind the reinforcement requiring additional removal. The additional removal depth (beyond cover plus 19 mm) can be determined as a function of the heat flux and exposure duration. Generally, as presented in Figure 53, the depth of unsound concrete that require further removal for the heavy damage cases increases as the thermal impact magnitude and duration increase. The heavy damage data clusters vertically in accordance with the fiber layer discretization previously defined (i.e., 12.7 mm further removal depth represents the first concrete layer, which is 19 mm behind the rebar, is unsound). In the *ln-ln* space, as shown in Figure 53a, the further concrete removal depths are fitted with a regression plane (explicit in blue), which was moved in parallel to the initial regression surface to provide conservative predictions with given thermal impact parameters. The green plane, labeled 95% confidence

prediction and expressed with Eq. (41), encompasses 95% of the data points and is parallel to the initial regression surface.

$$d_{removal}(95\%) = p_1 \cdot \ln(\dot{q}) + p_2 \cdot \ln(t) + p_0 \quad (41)$$

where p_1=0.025 and p_2=0.024 are the non-dimensional coefficients and p_0=-0.1864 is the bias term. A different confidence interval (i.e., 99%) can be implemented per user objective and risk tolerance. These planes, in Figure 53a, are transferred to curved surfaces in the normal space as presented in Figure 53b.

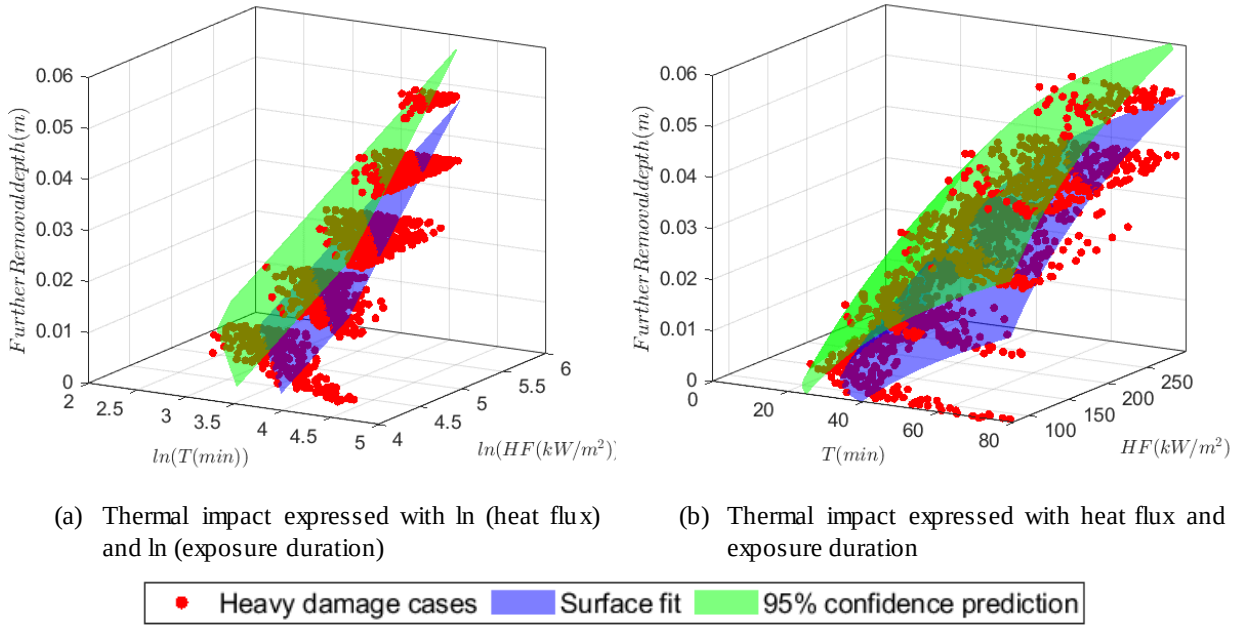

(a) Thermal impact expressed with ln (heat flux) and ln (exposure duration)

(b) Thermal impact expressed with heat flux and exposure duration

Figure 53: Further concrete removal depth of heavy damaged class and surface regression for prediction

Combining the concrete damage classification shown in Figure 52 with the greater than minimum concrete removal depth prediction presented in Figure 53, the tunnel resilience metric can be evaluated from the damage state and the estimated repair workload (i.e., replacing damaged concrete and steel reinforcement). The evaluation is packaged as a damage assessment "tool," and implemented in the following tunnel resilience process illustrated in Figure 4. To note, as concrete property uncertainty is fully considered in the "tool" development, the evaluation output is deterministic given the thermal input.

5.5. Repair procedure for concrete liners post fire

As stated in the introduction, the tunnel functionality loss directly relates to the post fire repair time. Structurally, the concrete liner should be repaired to its pre-fire condition or be enhanced thought the repair process. Though there are no detailed specifications for tunnel fire repair according to a MassDOT (2021) investigation (Gerasimidis and Civjan n.d.), a generalized procedure can be based on representative case studies. Along with the authors' engineering judgement, the following repair processes and rates are defined relative to each damage level.

- **Superficial damage repair:** The concrete is sound and as determined by visual inspection of surface color (i.e., no pink/reddish coloration indicative of temperatures below 300°C). No repair required.
- **Moderate damage repair:** The damage can be visually detected (either color indication or concrete spall), hence the following rehabilitation process is required.
  1. ***Concrete inspection***: According to Pennsylvania Department of Transportation contractors, concrete tunnel inspections are performed by two people working from a mobile elevating working platform with one person sounding and the other recording the results. The estimated inspection rate was reported to be approximately 18.6 m^2/hr (200 ft^2/hr).
  2. ***Concrete removal***: Damaged concrete is removed via hydro-demolition, which uses high-pressure water jetting. The technique is widely accepted in concrete structural repair in tunnels, and was used for the subsequent repair from the 2008 Channel Tunnel fire (Freyssinet Corporation 2021). The hydro-demolition rate varies widely because of the variations in jet pressure, available water flow rate, and concrete material properties (StoneAge n.d.). In this study, an average removal rate of 1.22 m^3/hr (1.60 yd^3/hr) for removal depth of 51 to 76 mm (2 to 3 in.) was used according to contractor experience (NLB Corp. 2021).
  3. ***Concrete replacement***: Spray applied concrete, shotcrete, is commonly installed post tunnel fires after the deteriorated concrete is removed. With the characteristics of high strength and high construction efficiency, shotcrete has been considered the most common first choice for concrete infrastructure repair. It was applied in the 1999 Tauern Tunnel fire repair in Austria (Gerasimidis and Civjan n.d.). According to the Standard Practice for Shotcrete by the US Army Corps of Engineers (1993) (US Army Corps of Engineers 1993), the application rate of dry-mix shotcrete is 0.76 to 1.53 m^3/hr (1 to 2 yd^3/hr) compared to wet-mix at 5.35 to 6.12 m^3/hr (7 to 8 yd^3/hr). An average value of 3.06 m^3/hr (4 yd^3/hr) was used

herein, consistent with the Channel Tunnel repair (Freyssinet Corporation 2021), where 4000 tons were installed in 32 days; equating to 2.98 m^3/hr (3.9 yd^3/hr) assuming a twelve-hour workday.

- **Heavy damage repair:** Concrete has spalled to the reinforcement layer, exposed rebar should be inspected and replaced. Further concrete removal may be needed. The repair process follows:
  1. ***Concrete inspection***: see moderate damage repair.
  2. ***Concrete removal (stage 1)***: see moderate damage repair.
  3. ***Concrete removal (stage 2)***: with the approval of the structural engineer of record, unsound concrete 19 mm behind the reinforcement should be removed via hydro-demolition at a lower pressure than stage 1 removal. The production rate is slower than stage 1 at 1.06 m^3/hr (1.39 yd^3/hr) with an average material removal depth of 25 to 51 mm (1 to 2 in.).
  4. ***Reinforcement inspection***: Initiate by visual inspection, identify defects such as buckling, bowing, twisting, and/or distortion, follow by closer examination to assess evidence of overheating such as metallographic grain structure changes (Ingham 2009). A referenced inspection rate could not be found in the literature review, therefore a rate equal to concrete inspection is assumed, 18.6 m^2/hr (200 ft^2/hr).
  5. ***Reinforcement replacement***: the weakened and/or distorted bars are cut and removed. New reinforcement of the same diameter are installed with sufficient lap length or through welding a minimum of 100 mm (3.93 in.) to the existing bar (Weber 2017). Reinforcement replacement rate is assumed to be 0.5 m^2/hr (5.38 ft^2/hr). This value could be adjusted based on the density and size of reinforcement used.
  6. ***Concrete replacement***: see moderate damage.

The repair procedure is summarized in Table 8. Note, the concrete liner repair rates post fire in this study are estimated for illustration purpose and can be changed to match newly available data or to client specifications.

Table 8: Tunnel concrete liner repair process post fire

Procedure	Rate	Damage State		
		Superficial	Moderate	Heavy
Concrete inspection	18.6 m^2/hr (200 ft^2/hr)	None	✓	✓
Concrete removal (stage 1)	1.22 m^3/hr (1.60 yd^3/hr)		✓	✓

Concrete removal (stage 2)	1.06 m^3/hr (1.39 yd^3/hr)	×	✓
Rebar inspection	18.6 m^2/hr (200 ft^2/hr)	×	✓
Rebar replacement	0.50 m^2/hr (5.38 ft^2/hr)	×	✓
Concrete replacement	3.06 m^3/hr (4.00 yd^3/hr)	✓	✓

5.6. Influence of convective coefficient

The non-ventilated concrete thermal analysis is conducted using a convective coefficient of 25 W/m^2-K based on Eurocode 1 (CEN 2002). This recommended value, which is applied to the standard temperature-time curve and external fire curve used for furnace tests, does not fit longitudinal ventilated tunnel conditions. Based on the experimental results from Lee et al. (2009) (Lee et al. 2009) and Chávez-Galán et al. (2014) (Chávez-Galán et al. 2014), the convective coefficient increases with higher surface airflow velocity. For properly designed longitudinally ventilated tunnels, the airflow velocity reaches the critical value. This ranges from 2 m/s to 4 m/s (6.56 ft/s to 13.12 ft/s) and is dependent on the fire intensity defined by peak heat release rate. According to Chávez-Galán et al. (Chávez-Galán et al. 2014), the convective coefficient increases to approximately 35 W/m^2-K at the critical airflow velocity typical in longitudinally ventilated tunnels. The relevance of the Eurocode specified value was evaluated by comparing the concrete surface temperature subjected to the equivalent heat method specified with heat flux or temperature. As indicated in Figure 54, temperature-based (1095°C) and heat flux-based (158kW/m^2) fire testing methods outlined in ASTM E1529 (ASTM International 2016a) generate similar stable concrete surface temperatures (1020°C for heat flux-based heating and 1038°C for temperature-based heating), indicating 25 W/m^2-K suitability for the environment of furnace testing (i.e., where airflow velocity = 0 m/s). Increasing the convective coefficient to 35W/m^2-K, the result of temperature-base heating is not influenced while heat flux-based heating is (990°C stable concrete surface temperature indicates an error of 4.8%), because more heat is transferred to the ambient air instead of the liner. This result indicates an advantage of longitudinal ventilation in design for fire hazards in tunnels.

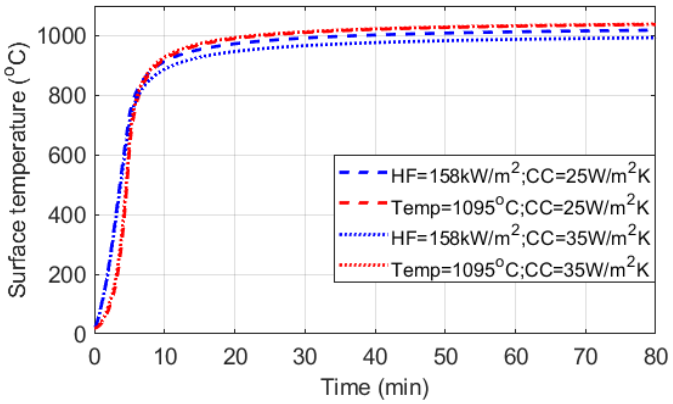

Figure 54: Surface temperatures subjected to ASTM E1529 thermal demands

The same stochastic analysis procedure was duplicated from section 5.4, but with the longitudinally ventilated tunnel convective coefficient of 35W/m^2-K. The damage map in *ln-ln* space is shown in Figure 55. Comparing the damage boundaries between the convective coefficients indicates higher heat flux magnitude and longer exposure durations are required to reach the moderate and heavy damage level classifications for longitudinally ventilated tunnel conditions. The coefficients of the damage boundaries expressed with Eq. (40) and further removal depth expressed with Eq. (41) are listed in

Table 9 for the ventilated tunnel example.

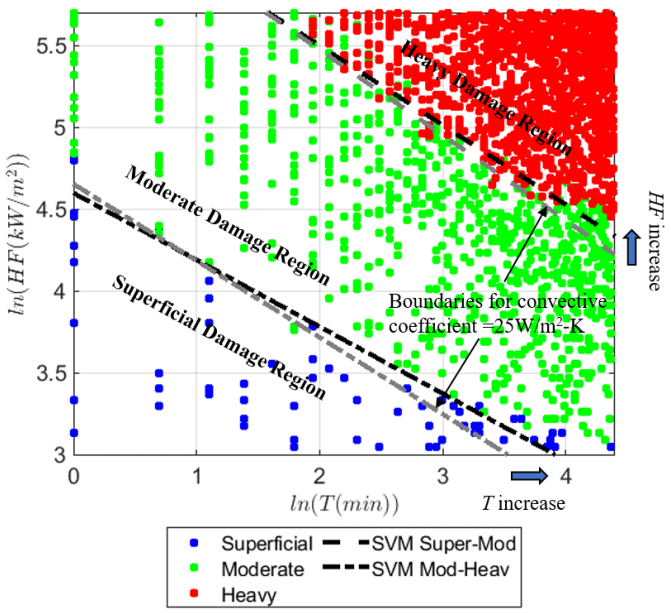

Figure 55: Data points and damage levels of the concrete panel with convective coefficient =35 W/m^{2}K

Table 9: Parameters of damage map and removal depth for convective coefficient = 35 W/m^2-K

Boundary	w_1	w_2	b	Slope $(-w_1/w_2)$
Superficial-Moderate	1.71	4.18	-19.23	-0.41
Moderate-Heavy	3.41	7.02	-45.40	-0.48
Removal depth: $d_{removal}(95\%)$	p_1	p_2	p_0	N/A
	0.243	0.253	-0.188	

CHAPTER 6 – TUNNEL FUNCTIONALITY LOSS ASSESSMENT

Using the concrete damage assessment tool developed in the previous sections, the structural safety and repair workload for the entire tunnel post fire can be evaluated with the process presented in step 2 of Figure 4. The uncertainties of fire such as the combustion energy and those associated with tunnel environmental condition like the effect from FFFS and ventilation system, which influence the integral damage state, are considered via stochastic analysis. The functionality loss is therefore conservatively accessed with defined probabilistic confidence.

6.1. Tunnel fire thermal impact calculation

The Confined Discretized Solid Flame (CDSF) model is applied to calculate the fire thermal impact on a tunnel liner for the natural and longitudinal ventilated scenarios, which has been introduced in detail in Chapter 3 and Chapter 4.

6.2. Uncertainties associated with tunnel fire thermal impact

The factors affecting the tunnel damage state considered in this study include the fire combustion energy and thermal attenuation factor of FFFS, both of which contain uncertainty. The probabilistic distribution assumptions for these two parameters were made based on collected data and available literature as discussed and referenced in this section:

(a) Combustion energy

The tunnel fire combustion energy can be estimated from tunnel fire tests categorized by vehicle type: car, bus, HGV, semi-truck tanker, and with different combustible payloads (Guo et al. 2021). The data used by Ingason (Ingason 2009) for tunnel fire design consists of large combustion energy experiments. In this study Ingason's design fires were used to generate the "upper bound" (denoted by red diamonds), while other experimental data in the literature was used to form the "lower bound" (denoted by blue circles) as presented in Figure 56.

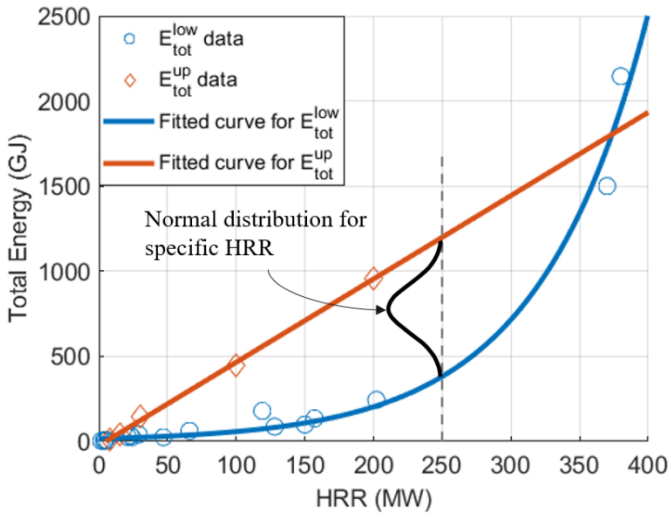

Figure 56: The combustion energy bound of vehicle fires with respect to HRR

The upper E_{tot}^{up} (GJ) and lower E_{tot}^{low} (GJ) bound of combustion energy can be approximated with regression expressions in Eq. (42), where $\dot{Q}_{max}$ (MW) is the peak heat release rate, representative of the fire intensity. For specific fire hazards, the combustion energy is sampled from a Gauss distribution, with the mean value determined as the average of E_{tot}^{up} and E_{tot}^{low} and standard deviation defined at one-third of the difference between the upper and lower bound at the HRR mean value as illustrated in Figure 56.

$$\begin{aligned} E_{tot}^{up} &= 4.9\dot{Q}_{max} - 24.13 \\ E_{tot}^{low} &= 16.47e^{0.01257\,\dot{Q}_{max}} \end{aligned} \tag{42}$$

(b) Effect of Fix Fire Fighting System (FFFS)

In the NFPA 502 (2017) (NFPA 2017 p. 502), FFFS is recommended for highway tunnel fire protection and life safety improvement. In recent years, FFFS are routinely installed in highway tunnels. The effectiveness of the sprinkler system was first recognized in Japan and Australia in the early 1990s but questioned by the World Road Association and the US National Fire Protection Association (NFPA) until 2007. In Japan, guidance from the Ministry of Land Infrastructure and Transportation requires FFFS in tunnels longer than 1000 m (3280 ft) (Beard and Carvel 2005). FFFS lessens the fire impact, by suppressing the intensity (i.e., reducing the HRR) while also attenuating the radiative and convective heat transfer. FFFS efficiency largely varies by type (i.e., water spray or water mist), water application rate, spray pressure and angle, size of the droplets, and installed location of the sprinklers or nozzles. To note, the effectiveness of FFFS could be

compromised by a delay of activation (7-10 min) according to multiple full-scale tunnel tests including the one performed in the second Benelux tunnel near Rotterdam (2002) and the Runehamar Tunnel tests (2007-2008). However as shown during the 2007 Burnley Tunnel fire, the activation time of FFFS is typically less than 90 sec for a functional fire detection system. This short activation time is rapid enough to eliminate any impact on the structural fire analysis and is therefore omitted in this study.

The Federal Highway Administration highway tunnel FFFS report (2020) (FHWA 2020) defines the reduction in HRR due to FFFS based on NFPA 502 (NFPA 2017) vehicle types. The HRR before and after the FFFS activation for different vehicle types varies greatly. Table 10 summarizes the upper and lower bound of the reduction factors, as well as the mean values. Reduction factors, including the mean and boundaries, were interpolated for HRRs between the values listed in Table 10.

Table 10: HRR reduction factor by FFFS

Vehicle Types	HRR (MW)	Reduction Factor		
		Lower Bound	Mean Value	Upper Bound
Multiple passenger cars	15	0%	13%	25%
Bus	30	20%	31%	41%
HGV	150	25%	40%	55%
Flammable / combustible liquid tanker	300	33%	64%	95%

The uncertainty associated with the HRR reduction factor is considered via stochastic sampling. Gaussian distribution was assumed with standard deviation calculated as one-third of the difference between the upper and lower bounds.

The transmission of thermal radiation to potential targets is reduced by the absorption and scattering of radiation by the droplets in the water spray. The radiative attenuation factor is influenced by droplet diameter and density. Experiments have shown a 50-70% attenuation can be achieved with typical water spray systems (Buchlin 2005). Water mist curtains can obtain an 83% thermal radiation attenuation (Zhu et al. 2015). A full-scale experiment (Meng et al. 2012) in a railway tunnel has demonstrated the efficiency of water mist at reducing radiant heat flux and the

has shown that the efficiency is not sensitive to the longitudinal ventilation speed. To avoid the complexity of accounting for the effect of FFFS on radiative attenuation in this tunnel resilience framework, a conservative value of 40% was applied. The convective thermal impact, dependent upon the temperature, was also assumed to be reduced by 40%.

6.3. Quantification of functionality loss for specific tunnel fire

The functionality loss expression from Eq. (3) can be refined into Eq. (43) by defining the hazard intensity with the peak HRR and the damage measure with the categories defined in section 5.3.

$$C = \iint c(DM_l|HRR_i) \cdot p(DM_l|HRR_i) \cdot dDM_l \cdot p(HRR_i) \cdot dHRR_i = \int \overbrace{(\int c(DM_l) \cdot p(DM_l) \cdot dDM_l|HRR_i)}^{Conditional\ probabilistic\ loss} \cdot p(HRR_i) \cdot dHRR_i \quad (43)$$

where HRR_i is the heat release rate and DM_l indicates the damage state (i.e., l=1 for superficial, l=2 for moderate and l=3 for heavy). The conditional probabilistic loss function in Eq. (43) for specific tunnel fires can be determined. The damage state of the entire tunnel subjected to fire cannot be easily classified as a benchmark has yet to be identified, contrary to seismic hazards on bridges and buildings where damage is classified based upon measured deflection or drift. Therefore, in this study, the overall tunnel damage classification is omitted in favor of directly determining the functionality loss for each specific fire hazard. By investigating the damage state of each discretized tunnel concrete liner element and its corresponding post-hazard repair time, the functionality of the entire tunnel can be calculated via Eq. (44):

$$C = \int c(HRR_i) \cdot p(HRR_i) \cdot dHRR_i$$
$$c(HRR_i) = \sum_{1}^{n_2} t(dm_2) + \sum_{1}^{n_3} t(dm_3) \quad (44)$$

where n_1, n_2, and n_3 are the number of panels of superficial, moderate, and heavy damage; $t(dm_j)$, j=1, 2, 3 represents the time to repair the discretized concrete liner of each damage state. As aforementioned in 2.1.5, the superficial damage does not require post-fire rehabilitation and is therefore omitted from consideration in Eq. (44).

The concrete liner damage state is determined following the process graphically presented in Figure 57. In ***Step (2a)*** the CDSF model is used to determine the thermal impact magnitude in

terms of heat flux for each discretized panel. The CDSF model includes the following deterministic factors: tunnel geometry, fire intensity, tunnel ventilation, and the effect of FFFS. In ***Step (2b)*** the CDSF output heat flux time history for each panel is generated by scaling the HRR time history curve, via Ingason's tunnel fire design curve (Ingason 2009), to the heat flux magnitude. In ***Step (2c)***, the heat flux time history for each panel is converted to an equivalent energy history with constant peak heat flux magnitude. The resulting exposure duration for the equivalent energy curve is determined for each panel, t_j. The energy equivalency simplification is conservative because the condensed thermal impact results in higher concrete temperatures. ***Step (2d)*** utilizes the previously developed stochastic damage assessment tool in Step 1 along with the peak heat flux and exposure time for each panel to establish the damage classification and calculate the possible concrete further removal depth if Heavy Damage (Class 3) is reached. The distribution of concrete liner damage can be visualized on the original tunnel geometry as shown in ***Step (2e)***. Following the repair procedure in Section 5.5, the total repair time can then be calculated by summation of the repair time for each discretized panel, yielding a total repair duration for the given fire.

The uncertainties in thermal impact were considered with Monte Carlo Simulation via Latin Hypercube sampling. For each fire intensity, a sample size of 10,000 was generated. Table 11 summarizes the uncertainties contained in each simulated case.

Table 11: Simulated tunnel condition and associated uncertainties

		Ventilation condition	
		Natural ventilation	Longitudinal ventilation
FFFS inclusive	No FFFS	Combustion energy	Combustion energy
	FFFS	Combustion energy; Effect of FFFS	Combustion energy; Effect of FFFS

The functionality loss (e.g., the tunnel down time) for each sampled case varies (i.e., lower combustion energy generally results in less functionality loss). The representative value can be evaluated by analyzing this data cluster. For example, the mean value is the most straightforward option. In this study, the 95% confidence interval was selected to provide a reasonably conservative estimate, while neglecting outliers that would skew the results in favor of highly unlikely extreme fire events.

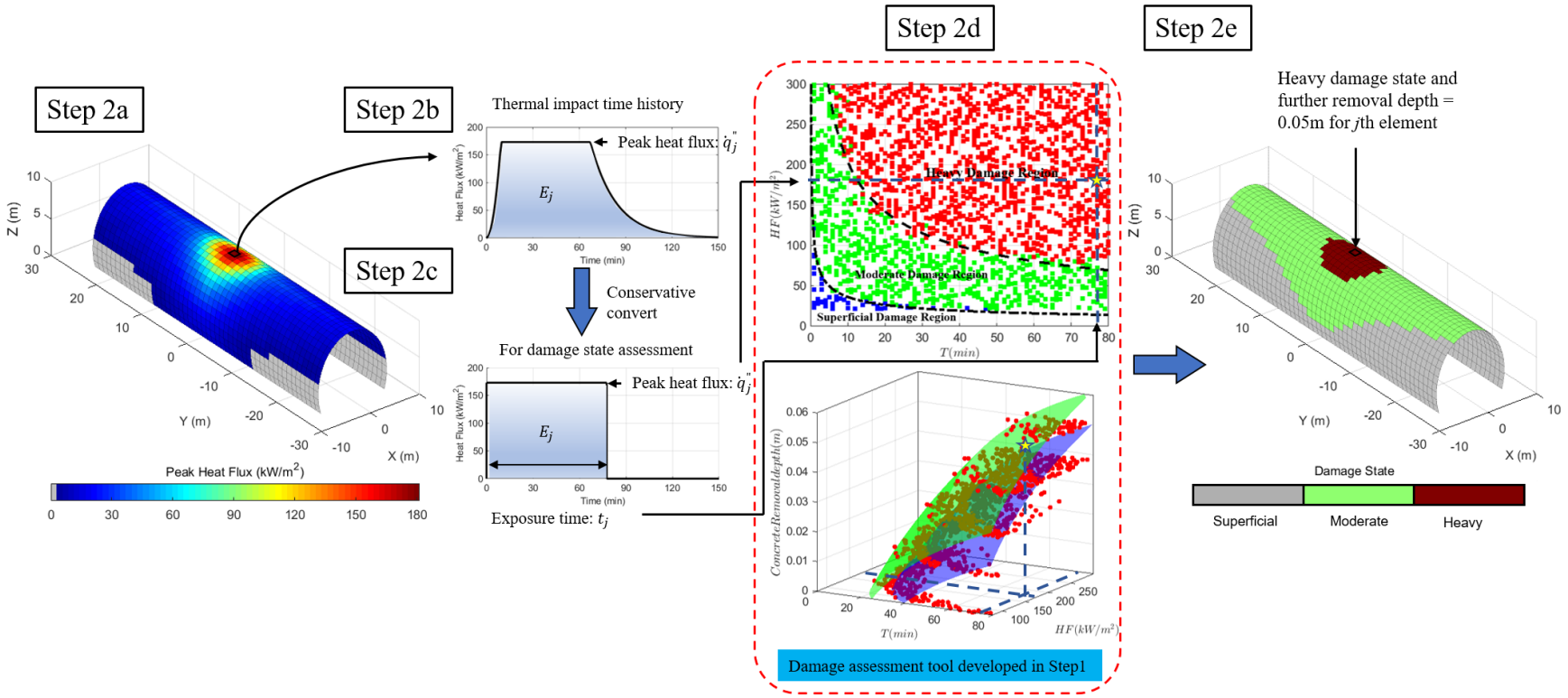

Figure 57: Process of tunnel concrete liner damage assessment using the damage assessment curve

6.4. Resilience quantification metric-functionality loss

Tunnel resilience correlates with fire intensity, as indicated in Eq. (44). Fire intensity is determined by traffic composition, and can typically be provided by state (DOTs). Proposed by the authors' research group and based upon multiple experimental datasets (Guo et al. 2021), the representative combustion weight of different vehicle types can also be used as the baseline for peak heat release rate calculation. An example will be presented in the case study in the next section.

The resilience of the tunnel subjected to fire hazard is inversely proportional to the functionality loss as described in Eq. (45), which has been used to quantify blast resistant engineering design resilience (Quiel et al. 2016).

$$R \propto \frac{1}{C} \tag{45}$$

For comparison and optimization purposes, the functionality loss is more straightforward for engineers to understand the resilience metric and provides a basis for optimization for post-fire recovery.

CHAPTER 7 – TUNNEL RESILIENCE ASSESSMENT APPLICATION

The efficiency of the tunnel fire structural resilience quantification method introduced in section 2 is demonstrated in this section. The factors affecting the tunnel resilience, such as tunnel active fire protection systems, tunnel dimensions, and traffic composition are investigated via parametric study. The case study shows that an optimized fire mitigation approach can be quantified for any specific tunnel with subject to defined traffic conditions.

7.1. Prototype tunnel

A previous investigation of the shape and dimension of tunnels in the United States (Guo et al. 2019) showed that a typical roadway tunnel has a road width ranging 8-13 m (26.2-42.7 ft), accommodates 2 to 3 travel lanes, and has a curved ceiling. The recent development and deployment of tunnel boring machines has made circular tunnel cross-section more common, and likely will become the dominate tunnel cross-section in the future. Consequently, this study focuses on circular tunnels ranging from 2-3 lanes, as shown in Figure 58. The height for the 2-lane and 3-lane circular tunnels are 7.78m and 9.57m respectively; the corresponding tunnel radius are 5.28m and 6.98m.

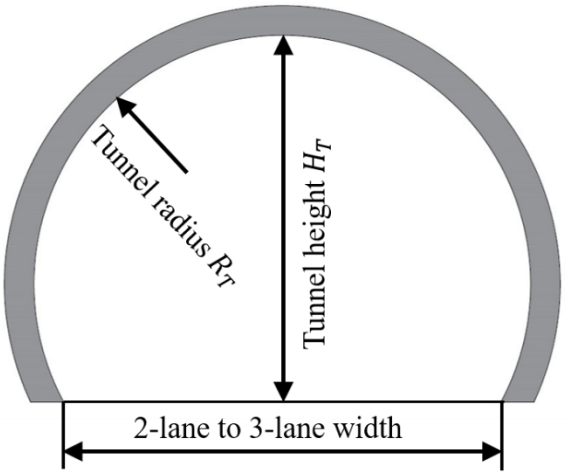

Figure 58: Circular tunnel cross-section

Example tunnel traffic data was provided by PennDOT, and is summarized in Table 12 labeled Traffic 2. The probability density function and cumulative density function of the HRR were then obtained via Monte Carlo Simulation using the aforementioned vehicle weight to HRR correlation (Guo et al. 2021). The Probability Density Function (PDF) and Cumulative Density Function (CDF) of the HRR are indicated with black and gray lines, respectively in Figure 59. Three

different levels of HGV percentage are examined: 0, 5.6%, and 20%; with 5.6% being the composition provided by PennDOT. Fire intensities ranging from 5 to 70 MW represent the highest probability as illustrated by the sharp increase in the CDF curves in Figure 59. The probability of experiencing a 100 MW fire hazard is below 10%, while exceeding a 300 MW fire is negligible.

Table 12: Parameters for prototype tunnels

	Traffic composition		
	Traffic 1	Traffic 2	Traffic 3
Motorcycle:	1.80%	0.35%	0.00%
Car:	80.50%	79.05%	68.00%
Pick-up Truck:	15.40%	13.99%	12.00%
Bus:	2.40%	0.99%	0.00%
HGV:	0.00%	5.60%	20.00%

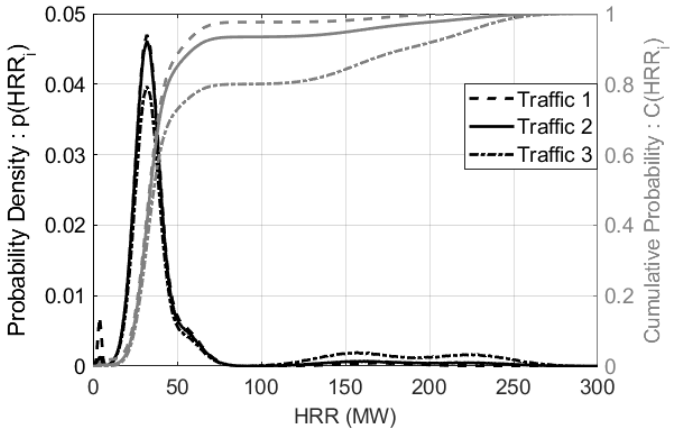

Figure 59: HRR probability distribution based on tunnel traffic

7.2. Analysis Matrix

The analysis matrix is a combination of the cases shown in Table 11 and Table 12. For example, each tunnel type is examined for each traffic condition. For each case the system is evaluated under four different conditions: 1) with natural ventilation without FFFS, 2) with longitudinal ventilation without FFFS, 3) with naturally ventilation with FFFS, and 4) with longitudinal ventilation and FFFS.

7.3. Results and Discussion

Figure 60 presents the functionality loss of the 3 lane and 2 lane tunnel configurations subjected to fire intensities ranging from low to high. In general, the smaller tunnel experienced a higher loss for each fire intensity. For the case of the larger tunnel, longitudinal ventilation reduces the

functionality loss for HRRs ranging 55W to 245 MW without FFFS. Further improvements are observed for the FFFS activated cases. For the extremely large fires (i.e., beyond 250MW), the hot gas and smoke are pushed downstream and engulf a large area of the liner resulting in equivalent or even greater loss than the naturally ventilated condition without FFFS. The effectiveness of FFFS in reducing the post-fire operational interruption is significant, especially for the longitudinally ventilated case under relatively large fires (i.e., 55% and 85% reduction for the natural and longitudinal ventilation case for 250MW fire). In Figure 60 the initiation of functionality loss for each ventilation and FFFS condition is illustrated with gray dash lines. Both longitudinal ventilation and FFFS extend the magnitude of HRR required to initiate functionality loss. For the smaller tunnel case presented in Figure 60(b), the effect of longitudinal ventilation was not particularly significant for the fire with intensities lower than 200MW when FFFS is not used. However, functionality loss dramatically increases for the natural ventilation cases under fires exceeding 200MW. This slope change can be attributed to the fire engulfing the tunnel cross-section, which induces intense thermal impact to a large area of the liner. With the activation of FFFS, the functionality loss for both natural and longitudinal ventilation cases was drastically decreased. In comparison to the larger 3-lane tunnel, the threshold of functionality loss is lower in the 2-lane tunnel. In all cases, the longitudinal ventilation accompanied by FFFS provided the most efficient damage mitigation, however, the benefits are reduced for the smaller tunnel.

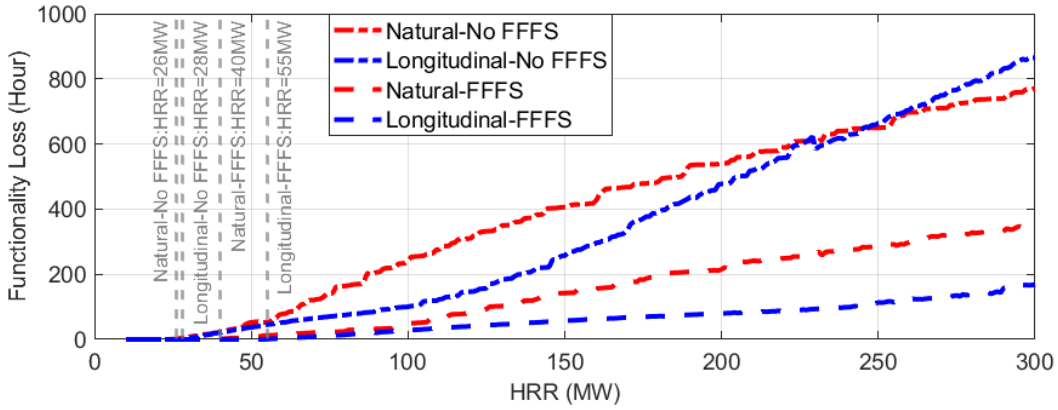

(a) 3-lane circular tunnel

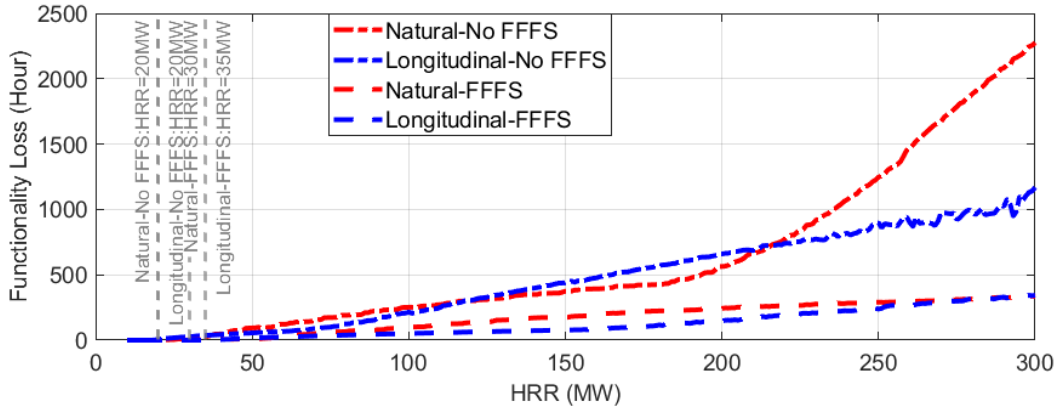

(b) 2-lane circular tunnel

Figure 60: Functionality loss of tunnel subjected to fire hazard

The overall tunnel functionality loss accounting for traffic composition (listed in Table 12), was calculated and compared in Figure 61. This figure presents th*9+-e expected downtime for each tunnel size in hours based on the occurrence of a single vehicle fire considering an equal likelihood of an event happening on any vehicle in the composition distribution. Increased HGV percentage increased the loss; indicative of lower tunnel structural resilience. The larger tunnel geometry generally experienced lower functionality loss and possessed higher resilience than the smaller. The longitudinal ventilation, though efficient for smoke extraction and increases life safety, was not effective in increasing tunnel structural resilience, especially for the smaller tunnel. The FFFS drastically decreased the operational interruption post fire, between 60% and 80%, and should be recommended for resilient tunnel design consideration.

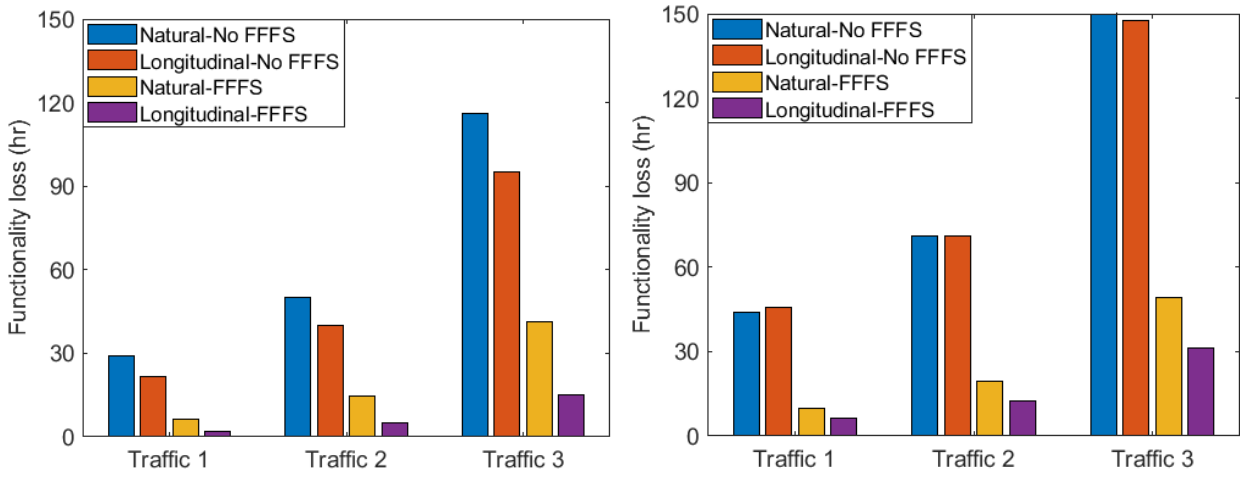

(a) 3-lane tunnel

(b) 2-lane tunnel

Figure 61: Integral functionality loss of considering tunnel traffic

CHAPTER 8 – FIRE RISK ASSESSMENT FOR TUNNEL LINEINGS

8.1 Stochastic Analysis of Vehicle Fire Hazards in Tunnels

The probability of structural consequences caused by vehicle fires inside a tunnel is governed by the frequency and intensity of the fire event. While fire frequency can be estimated in some cases using available tunnel-specific data, the likelihood of vehicular fire can be evaluated more generally through stochastic analysis. As shown in Eqn. 1, the overall fire frequency per year F_f for a given tunnel can be calculated as the product of the overall average fire rate R_f (per million vehicle-km), tunnel traffic density D (in million vehicles per year), and tunnel length L (km). While traffic data and geometry are usually accessible for most tunnels, there are limited public records for tunnel fire events or fire rates in the US. For the purpose of illustrating this framework, the statistical data for tunnel fires from the DARTS project in Denmark will be applied (Vrouwenvelder et al. 2004). The DARTS report estimates the average fire rate at 0.041 fires per million vehicle-km based on fire incident data collected from 45 tunnels in 13 European countries. The report also provides relative factors w_{veh} to weight fire rates by vehicle type, as higher fire rates were observed for heavy goods vehicles (HGVs) than for regular passenger cars (despite the fact that HGV traffic represents a much lower proportion of total traffic than passenger cars). For a specific vehicle type, the associated fire frequency $F_{f,veh}$ (see Eq. 47) can be calculated by inserting vehicle-specific variables for average fire rate and traffic density into Eq. 46. The vehicle-specific fire rate $R_{f,veh}$ is calculated per Eq. 48 by multiplying R_f with the associated w_{veh}. Vehicle-specific traffic density D_{veh} can be estimated based on publicly available data.

$$F_f = R_f * D * L \tag{46}$$

$$F_{f,veh} = R_{f,veh} * D_{veh} * L \tag{47}$$

$$R_{f,veh} = w_{veh} * R_f \tag{48}$$

Besides the fire frequency (which indicates the likelihood of a vehicle fire), the uncertainty associated with the intensity of potential vehicle fires must also be addressed. The peak HRR of a vehicle fire and its corresponding time history are used to represent the fire intensity. Previous experiments have measured peak HRR for varying vehicle sizes ranging from 1-5 MW for a motorcycle to 200+ MW for an HGV (*4*, *5*). The wide variation in HRRs make it necessary to specify fire intensity and fire frequency for each vehicle type. Table 13 shows a summary of peak

HRR and weighted fire rate for a variety of common vehicle types. The ranges of peak HRR for each vehicle are obtained from NFPA 502 (NFPA 2017) as well as previous experimental studies (Ingason 2009; Ingason et al. 2015c).

Table 13 Peak HRR and weighted fire rates (per Eq. 48) for common vehicle types in tunnels

Vehicle Types	Peak HRR (MW)	Distribution	Mean	Standard Deviation	Overall Fire Rate (per mil. veh-km)	Relative Factor	Weighted Fire Rate (per mil. veh-km)
Motorcycle	1-5	Normal	3	2	0.041	0.6	0.025
Car	5-10	Normal	7.5	2.5	0.041	0.8	0.033
Pickup/Van	10-20	Normal	15	5	0.041	1.2	0.049
Bus	20-30	Normal	25	5	0.041	1.2	0.049
HGV	30-200	Normal	115	85	0.041	1.6	0.066

The HRR for specific vehicle types varies based on size, fuel quantity, and cargo as well as other physical and environmental conditions within the tunnel (Ingason 2009). Relative factors were only provided for HGV and passenger cars in the DARTS report due to the lack of fire rate data for other types of vehicles. Relative factors for other typical vehicles are assumed based on vehicle sizes (i.e. a higher relative factor is interpolated for heavier vehicles). The uncertainty associated with peak HRR for each vehicle type is quantified using a normal distribution within the ranges specified in Table 13. The mean value is set equal to the average of the maximum and minimum peak HRR values, which are assumed to be one standard deviations from the mean value (thus bounding 68.2% of randomly selected HRR within the stated range while realistically allowing extreme values outside the range at much lower probability).

Using these distributions, the random input variables for the peak HRR of each vehicle fire scenario can be generated to encompass possible tunnel fire intensity scenarios as input for tunnel fire models for consequence evaluation. Latin Hypercube Sampling (LHS) is used in this paper for its computational efficiency – compared to Monte Carlo sampling where the random variables are chaotically dispersed, LHS stratifies the distribution interval into a number of layers to generate random values within each layer. The combination of stratified sampling and random sampling enables the LHS method to represent the stochastic distribution more comprehensively with less computational effort. LHS works for both one-dimensional sampling (single random variable) and

multi-dimensional sampling (multiple random variables). Previous research efforts improved the LHS approach to control correlation between different random variables (Olsson and Sandberg 2002). Only fire HRR is evaluated as the random variable herein. Uncertainties in other aspects (*e.g.* fire location, ambient temperature and wind speed) need to be assessed in future work.

Table 14 Input proportion based on fire frequencies of different vehicle types

Vehicle Types	**Peak HRR (MW)**	**Fire Frequency per Year $F_{f,veh}$**	**Percentage of Total Fire Frequency per Year**
Motorcycle	1-5	$F_{f,motor}$	$F_{f,motor} / F_{f,total}$*100%
Car	5-10	$F_{f,car}$	$F_{f,car} / F_{f,total}$*100%
Pickup/Van	10-20	$F_{f,vans}$	$F_{f,vans} / F_{f,total}$*100%
Bus	20-30	$F_{f,bus}$	$F_{f,bus} / F_{f,total}$*100%
HGV	30-200	$F_{f,HGV}$	$F_{f,HGV} / F_{f,total}$*100%
Total		$F_{f,total}=\Sigma F_{f,veh}$	100%

To ensure adequate representation of the sampled variables, the selected number of samples should be divided according to the proportion of total fire frequency for each vehicle type (as shown in Table 14), due to the independence among vehicle types of the HRR distribution. For example, if the sampling size is 1,000 and the HGV fire frequency occupies 10% of the sum of fire frequencies of all vehicle types, there would be a requirement of 100 random HGV fire samples of HRR ranging 30 MW to 200 MW under a normal distribution. With the completion of fire intensity input variable generation, the next step is to use these inputs to model the fire hazard and evaluate structural consequences. The damage probability produced by the LHS simulation, which can be considered a conditional probability, can then be combined with fire frequencies for application to tunnel design or retrofit options.

8.2 Case Study: Fort Pitt Tunnel

The Fort Pitt Tunnel, which opened in 1960, passes under Mount Washington near Pittsburgh, PA and carries traffic from I-376 and US Routes 22, 30, and 19-Truck ("Fort Pitt Tunnel" 2019) via two bores, each with two lanes. The tunnel has a horseshoe-shaped cross section with a width of 8.94 m, maximum height of 6.58 m, total length of 1102 m, and a longitudinal grade of 2.5%. The average daily traffic for the five typical vehicle types (provided by the Pennsylvania Department of Transportation) with calculated annual fire frequencies per Eq. 47 is summarized in Table 15. The total fire frequencies per year is 1.582. For each vehicle type, the percentage of total fire frequency per year shows the conditional probability of fire based on the specific vehicle

type given that a vehicle fire accident occurs. The percentage is also used for sampling generation for each vehicle type.

Table 15 Average daily traffic and fire input for the Fort Pitt Tunnel

Vehicle Types	Peak HRR (MW)	Fire Rate (per mil. veh-km)	Relative Factor	Avg. Daily Traffic in 2019	Fire Frequency per Year	% Total Fire Frequency per Year
Motorcycle	1-5	0.041	0.6	363	0.004	0.23%
Car	5-10	0.041	0.8	81799	1.079	69.64%
Pickup/Van	10-20	0.041	1.2	13455	0.266	17.18%
Bus	20-30	0.041	1.2	1024	0.020	1.31%
HGV	30-200	0.041	1.6	6832	0.180	11.63%
			Totals:	**103473**	**1.550**	**100%**

A sampling size of 100,000 was used to develop the frequency distributions in Figure 62a-e for each vehicle type passing through the Fort Pitt Tunnel. For each vehicle type, the distribution parameters of the generated fire sizes are consistent with those shown previously in Table 13. Figure 62f shows the frequency distribution of the complete sample for all vehicle types. When combining all fire sizes, the frequency distribution implies two clusters of fire size, with one around 10 MW and the other around 115 MW. The high frequency of fire sizes around 10 MW is caused by the higher frequency of car traffic versus other vehicle types in the average daily traffic data.

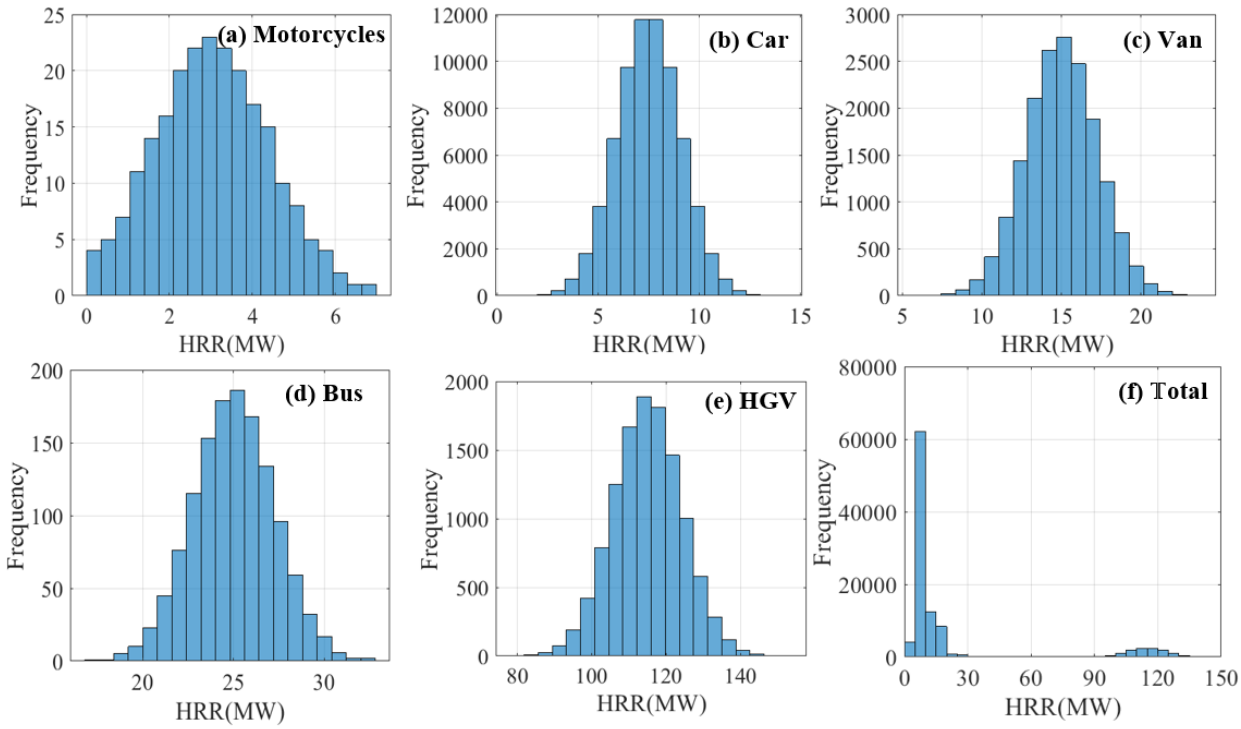

Figure 62 Frequency distribution of fire HRR (in MW) for (a-e) each vehicle type and (f) in total

8.3 Results and Discussion

The complete set of fire size samples generated from the traffic information for the Fort Pitt Tunnel are iteratively input into the CDSF model. Each iteration generates an incident heat flux map for the tunnel liner. The maximum heat flux at the fire location is selected to represent the peak thermal demand of the fire hazard. Figure 63 shows the frequency distribution and normalized cumulative frequency distribution for the HRR and the maximum heat flux. The two plots exhibit a similar trend, due to positive correlation between HRR and maximum heat flux at ceiling. As shown in Figure 63, approximately 88% of fire scenarios result in a HRR below 25 MW and a maximum heat flux on the tunnel liner below 60 kW/m^2. As the fire size increases, the cumulative frequency of the maximum heat flux stays nearly constant until approximately HRR of 105 MW and heat flux of 460 kW/m^2, when the cumulative frequency continues to increase. The cumulative frequency exceeds 99% at approximately 135 MW and 560 kW/m^2. Although the probability of generating a high heat flux (> 400 kW/m^2) is much lower than a 60 kW/m^2 event, the damage to both structural and non-structural components could range from substantial to catastrophic if the low probability event is not addressed appropriately.

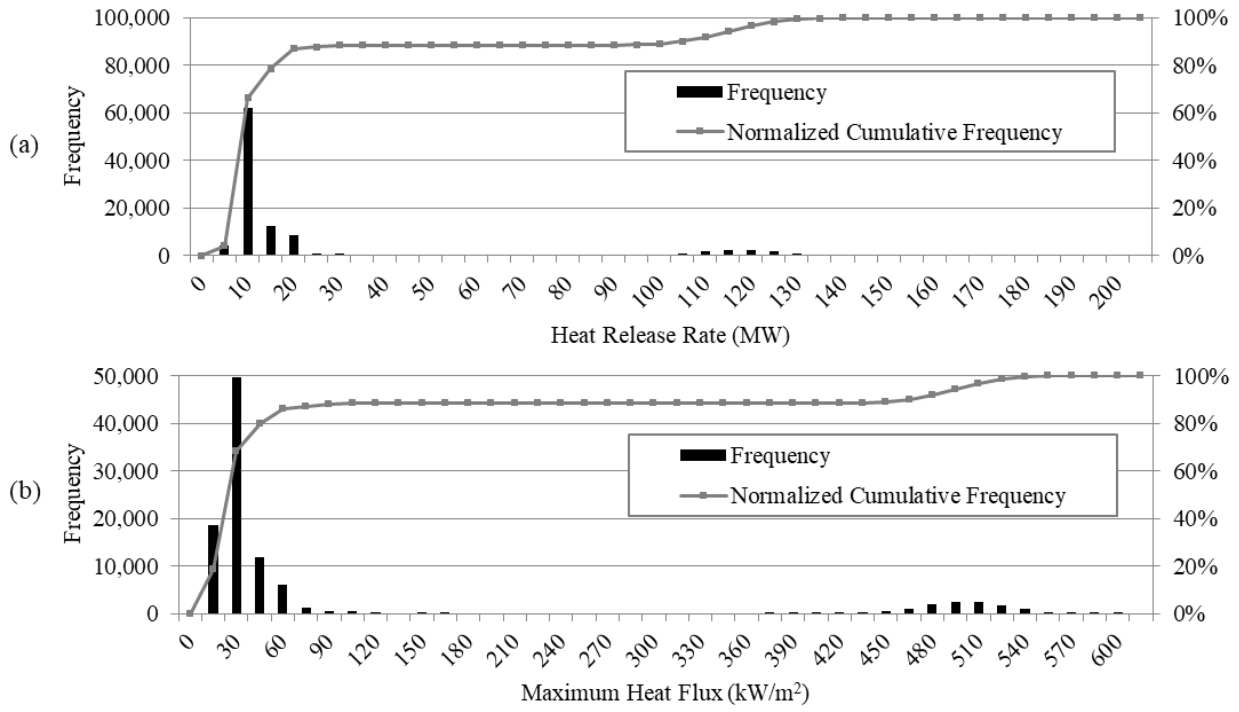

Figure 63 Frequency distribution for (a) HRR and (b) maximum heat flux at the fire location

To simulate realistic tunnel fire events, the steady-state heat flux generated from the CDSF model is used to construct a time history (i.e. design fire curve) which includes both a growth and decay phase. A design fire curve proposed by Ingason (Ingason 2009) with quadratic growth, a constant steady-state, and exponential decay is adopted in this paper. The associated equations are outlined in Eqs. 49-51, and Table 16 shows the input parameters needed to generate fire curves from steady state HRR of typical vehicle types (shown previously in Table 13). Values for the total calorific content, E_{tot} (kJ), quadratic growth rate, $\alpha_{g,q}$ (kW/s^2), and quadratic decay rate, $\alpha_{D,q}$ (s^{-1}) are taken according to the literature for bus, light HGV, and heavy HGV design vehicles (Ingason 2009). Combustion efficiency, χ, was conservatively taken as 80% (Yi et al. 2006). The same time histories can be used for total heat flux at every target by substituting the heat flux from the CDSF model for $\dot{Q}_{max}$.

$$\dot{Q}(t) = \begin{cases} \alpha_{g,q}\, t^2 & , \quad t \le t_{max} \\ \dot{Q}_{max} & , \quad t_{max} < t < t_D \\ \dot{Q}_{max} e^{-\alpha_{D,q}(t-t_D)} & , \quad t \ge t_D \end{cases} \tag{49}$$

$$t_{max} = \sqrt{\dot{Q}_{max} / \alpha_{g,q}} \tag{50}$$

$$t_D = \frac{\chi E_{tot}}{\dot{Q}_{max}} + \frac{2}{3} t_{max} - \frac{1}{\alpha_{D,q}} \tag{51}$$

Table 16 Summary of input parameters for fire curve generation per (Ingason 2009)

$\dot{Q}_{max}$ (MW)	E_{tot} (GJ)	χ	$\alpha_{g,q}$ (kW/s^2)	$\alpha_{D,q}$ (s^{-1})	t_{max} (min)	t_D (min)
5	10	0.8	0.178	0.001	3	12
10	30	0.8	0.178	0.001	4	26
20	80	0.8	0.178	0.001	6	40
30	130	0.8	0.178	0.001	7	46
200	1000	0.8	0.178	0.001	18	62

Two levels of peak heat flux (60 and 560 kW/m^2) are selected from the results in Figure 63b as milestones of cumulative frequency to benchmark thermally induced concrete degradation. Heat flux time histories for both milestone values are generated using Eqs. 49-51. In this paper, structural damage to the tunnel liner is quantified by concrete strength reduction resulting from fire exposure. Numerous experimental studies (Abrams 1971; Bingöl and Gül 2009; Chan et al. 1999) and design standards (American Concrete Institute 2014; CEN 2008) have addressed the reduction of concrete strength at high temperature as well as its residual strength after cooling down. Figure 64 plots the ACI 216-14 (American Concrete Institute 2014 p. 216) relationship between concrete compressive strength reduction and temperature for unstressed normal strength concrete ($f'c$ = 27 MPa [3.9 ksi]) with calcareous aggregate. The unstressed condition is conservative for strength reduction evaluation since concrete with mechanical stress will experience less strength loss at elevated temperature (American Concrete Institute 2014).

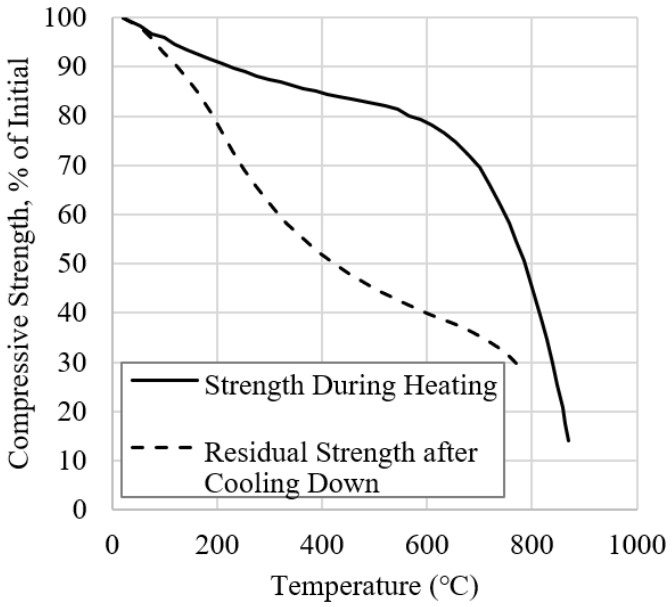

Figure 64 Concrete strength reduction at high temperature and residual after cooling for unstressed calcareous normal weight concrete per (American Concrete Institute 2014 p. 216)

The reinforced concrete liner in the Fort Pitt Tunnel is approximately 0.53-m thick. When one face of the panel is exposed to fire, a non-linear thermal gradient develops through the liner thickness due to the low thermal conductivity of the concrete. In order to analyze the thru-thickness temperature gradient, 1-D heat transfer analyses of the concrete liner can be performed using fire curves obtained from the selected heat flux inputs. The analyses are completed using SAFIR 2016 (Franssen and Gernay 2017b), a computer program developed at the University of Liege to model the behavior of structures subjected to fire. The material is defined as calcareous concrete with thermal conductivity and specific heat at room temperature assumed to be 2.0 W/m-K and 900 J/kg-K. These values are temperature dependent per the Eurocode 2 constitutive model for normal weight concrete (CEN 2008). The density of the concrete is assumed to be 2300 kg/m^3 and moisture content of 46 kg/m^3. The 0.53-m thickness is discretized into 100 equal layers, which preliminary analyses indicated to be sufficiently small to capture the thru-thickness thermal gradient. The heat flux time history generated from Eqs. 6-8 is applied uniformly on the fire-exposed side of the panel, and ambient temperature is applied as a separate boundary condition to both the exposed and unexposed surfaces to allow cooling. Surface emissivity is conservatively assumed to be 0.85 based on the published literature (Carvill 1993; Kim et al. 2014), and a convective cooling coefficient of 4 W/m^2-K is assumed per Eurocode 1 (EUROPEAN COMMITTEE FOR STANDARDIZATION 2002 p. 1). Following the end of the fire, the liner is

subjected to ambient temperature (20°C) and the analysis is continued to reach a total heat transfer duration of 12 hrs until the liner is fully cooled.

The maximum temperature reached in each discretized layer is used to evaluate compressive strength reduction per the reduction curves in Figure 64. Figure 65 plots the maximum reductions in concrete strength through the thickness both during and after exposure to the two milestone heat fluxes. When the maximum temperature is higher than the investigated range (up to about 850°C) the strength is assumed to stay at the lowest level (30% for the strength during heating and 15% for the residual strength) because extrapolation is not practical without a curve-fitting equation. For the approximate two-hour duration of heat flux exposure, the compressive strength loses less than 10% of initial strength at locations deeper than 0.05 m and 0.1 m from the exposed surface for the 60 and 560 kW/m^2 heat fluxes, respectively. Though the heat flux increases by nearly an order of magnitude, the depth of significant concrete degradation (assumed as more than 10% reduction of strength in this case) only doubles. The concrete liner with 560 kW/m^2 has a much steeper strength gradient within 0.1 m from the heated surface, for which the lowest strength during heating and after cooling is about 50% and 28% respectively. For the 60 kW/m^2 panel, the strength during heating reduces to around 88% of the initial strength while the residual strength reduced to 60%. The reduction of strength during heating can be used for other structural damage of concrete under heat exposure such as spalling. The residual strength prediction can provide information for post-fire inspection and repair.

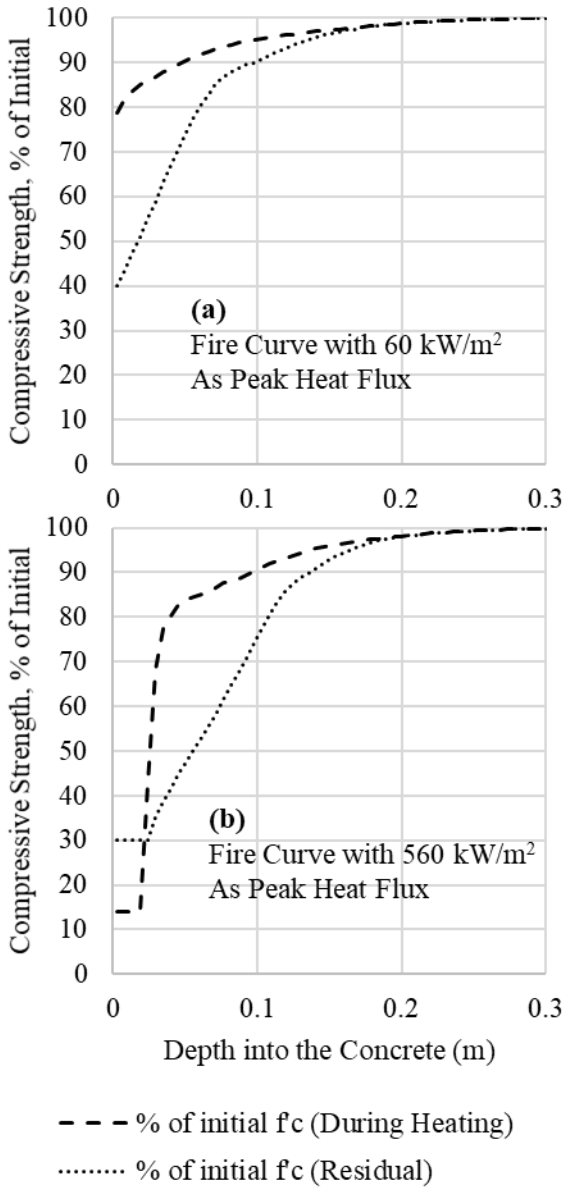

Figure 65 Thru-thickness gradients of compressive strength during and after heating for exposure to the two milestone heat flux time histories (a) 60 and (b) 560 kW/m^2

As mentioned previously, current design practice typically uses standard fire curves such the RWS (TNO-IBBC 1979) and ASTM E1529 (ASTM International 2016b) temperature time histories to develop relative hourly ratings of fire resistance for structural assemblies and other nonstructural components within a tunnel. To frame the results of the proposed approach in the context of current practice, the 0.53-m thick Fort Pitt tunnel liner is also analyzed for exposure to the RWS and E1529 fire curves, and the resulting temperature penetration and associated loss of residual concrete compressive strength is compared to that induced by the 60 and 560 kW/m^2

milestone time histories. For each standard fire, thermal analysis in SAFIR 2016 is performed using that curve's surface temperature exposure rather than a heat flux exposure as the fire's thermal boundary condition. Per Eurocode 1 (EUROPEAN COMMITTEE FOR STANDARDIZATION 2002), a semi-empirical convection coefficient of 50 W/m^2-K is applied to the surface exposed to the standard fire temperatures, which represent a high-intensity hydrocarbon fire. All other modeling parameters discussed previously are unchanged. For the RWS curve, the liner is subjected to the full 2-hr duration, and the fire is subsequently shut down with no decay phase. For the E1529 curve, several iterations are performed in which the undamaged liner is subjected to an increment of the standard fire (ranging from 30 min to 2 hrs), again followed by immediate shutdown. As before, the maximum temperature in each layer due to the full exposure of each standard fire scenario and subsequent cooling is used to calculate an associated loss of residual compressive strength according to Figure 64. The net residual compressive strength of the liner's total thickness is then calculated as an area-weighted average. A similar calculation is performed for the heat flux time histories using the residual strength gradients shown in Figure 65.

The residual compressive concrete strength due to the standard fire curves and the two milestones heat flux time histories are plotted in Figure 66. Exposure to the 560 kW/m^2 scenario produces almost the same residual compressive strength (86%) as a 2-hr exposure to both the RWS and E1529 standard fire curves, with the RWS slightly more conservative. Exposure to the 60 kW/m^2 scenario is approximately equivalent to a 40-min rating per the E1529 standard fire approach and results in approximately 93% residual compressive strength. For this particular tunnel (with the given geometry, natural ventilation, and no fixed firefighting systems), these results suggest that designing the liner for a 2-hr exposure to the RWS or E1529 fire curves could effectively address the maximum effects of potential fire hazards at the 99th intensity percentile. Designing for a 1-hr exposure to the E1529 curve would address nearly 90% of possible intensities (slightly above the probabilistic frequency of the 60 kW/m^2 milestone scenario as shown previously in Figure 63b). These comparisons can aid the selection and implementation of active (i.e. forced ventilation or sprinklers) or passive (i.e. fire-resistant paneling or coatings) fire protection systems since most of those systems are rated for deployment using standard fire tests.

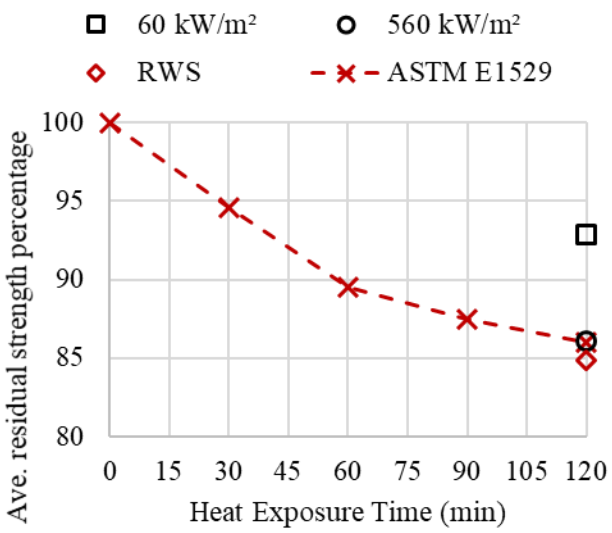

Figure 66 Comparison of average residual compressive strength due to the milestone heat flux time histories and standard fire curve exposures

CHAPTER 9 – CONCLUSION AND FUTURE WORK

9.1 Conclusion

Vehicle and cargo fires are some of the most severe and likely hazards that a roadway tunnel can experience over its service life. An approach is developed to determine a quantitative resilience measurement for tunnel structures subject to fire events. The approach directly accounts for variations in tunnel geometry, traffic composition, concrete and reinforcement materials used, and fire conditions. The functionality loss, which is directly related to the post-fire tunnel liner repair procedure (i.e., functionality disruption), is used as the indicator of resilience. The uncertainties associated with concrete thermal properties, tunnel vehicle fire characterization, tunnel ventilation and FFFS facilities, and traffic composition were included in the probabilistic functionality loss assessment. With this approach, recommendations on supplemental fire suppression systems, tunnel geometry optimization, and the impact of changes in traffic on future fire intensities and resulting repair and downtime can be quantified providing guidance for increasing tunnel structural resilience. The conclusions of this study are as follows:

- The MATLAB-SAFIR method was shown to efficiently model tunnel fire hazard including concrete spalling phenomena, and can be used to perform stochastic analysis which accounts for the associated uncertainties in the thermal properties of concrete.
- The concrete damage mapping classified concrete damage according to the post-fire repair procedure. It provides a straightforward probabilistic-based damage assessment tool that can be used to quantify the tunnel functionality through operational disruption time of the tunnel after fire hazard.
- The confined discretized solid flame (CDSF) model efficiently calculated the thermal impact to the concrete tunnel liner in both natural and longitudinally ventilated conditions. Its computational efficiency enables the stochastic analysis, including uncertainties, for tunnel resilience quantification.
- For the case study conducted on a two and three lane tunnel it was found that reductions in functionality loss and increased resilience can be achieved at the design stage by choosing larger tunnel geometries, during operation through restriction of high intensity fire capable vehicles (e.g., fuel tankers and HGV), and installing active fire mitigation systems. Among them, the FFFS provides a notable means of reducing the functionality loss from fire, and should be recommended

for installation. Longitudinal ventilation systems, though widely accepted as a life-safety fire mitigation method, did not provide a significant improvement in structural resilience.

A new approach to stochastically determine a tunnel-specific design fire exposure which considers the probability of fire-inducing accidents in a tunnel and the uncertainty of fire sizes based on tunnel traffic data. A case study on the Fort Pitt Tunnel in Pennsylvania, USA is used to illustrate the application of the stochastic framework. The results of the study are as follows:

- A probabilistic evaluation is conducted by calculating the frequency of vehicle fires in tunnels and the probability distribution of fire sizes per vehicle type (represented as heat release rate). Latin Hypercube Sampling is used to assess the possible tunnel fire intensity scenarios with improved computational efficiency versus Monte Carlo simulation.
- A confined discretized solid flame (CDSF) model (previously developed by the authors) is used as the fast-running thermal load evaluation tool in the stochastic framework. Given an HRR and tunnel geometry, the CDSF model produces steady-state incident heat flux mapping over the interior surface of the tunnel liners with little computational effort.
- The Fort Pitt Tunnel has a calculated fire frequency per year of about 1.53 fires per year, in which passenger car fires are the biggest segment (70%). The cumulative frequency distribution for the total traffic in the tunnel therefore shows a concentration around HRR of 10 MW, which corresponds to a single car fire. If a vehicle fire occurs, there is 88% of probability that the HRR is lower than 25 MW.
- A cumulative frequency distribution for the maximum heat flux on the tunnel liner is generated by running iterative CDSF analyses with stochastic fire scenario input. Design heat flux levels can be selected according to the changes in the slope of the cumulative frequency plot. Two heat flux milestones (60 and 560 kW/m^2) are selected where the cumulative frequency reaches 86.1% and 99.9%, between which the curve is mostly flat.

The compressive strength reduction of concrete both during and after the fire is used to represent structural consequences of tunnel liner exposure to these fire scenarios. In particular, the loss of residual compressive strength through the thickness of the tunnel liner is calculated for the two milestone heat flux time histories as well as for exposure to two "standard fire" curves. Residual strength loss due to the 560 kW/m^2 fire scenario was nearly equivalent to a 2-hr exposure for either the RWS or ASTM E1529 standard fires, while the 60 kW/m^2 scenario produced similar residual strength as a 40-min E1529 exposure. The levels of potential damage and probability of occurrence

associated with the two milestone scenarios, combined with their standard fire exposure equivalents, can aid decision making about fire protection design, renovation, and post-fire inspection for tunnels.

9.2 Future Work

The resilience analysis of the tunnel subject to fire hazard is on the objective level. However, it could be expanded to the network level by accounting for the importance of the tunnel in a roadway network.

The tunnel fire mitigation plan includes both the active protection (i.e., the detection device, ventilation system and FFFS) and passive fire protection (i.e., the fire protection board, Spray Fire Resistance Material, additive fibers which make the tunnel liner more fire resistance). For specific tunnel, the mitigation plan varies according to the tunnel dimension, the relative specifications, the traffic situation, tunnel importance in a roadway network, and the budget. An optimization method could be proposed to help the decision-making process for the engineers.

The numerical method could be proposed to understand the stability of the tunnel liner subjected to fire hazard and the residual stress remain afterward.

REFERENCE

Abdul Kreem, O. M. 2012. "Influence of Concrete Mix Proportions and Curing Regimes on Density, Absorption, and Voids in Hardened Concrete." *Al-Fafadain Engineering Journal*, 20 (4): 102–117.

Abrams, M. 1971. *Compressive Strength of Concrete at Temperatures to 1600F*. Research and Development Bulletin. Portland Cement Association. Skokie, USA: Portland Cement Association.

American Association of State Highway and Transportation Officials (Ed.). 2001. *A policy on geometric design of highways and streets, 2001*. Washington, D.C: American Association of State Highway and Transportation Officials.

American Concrete Institute. 2014. *(ACI 216.1-14) Code Requirements for Determining Fire Resistance of Concrete and Masonry Construction Assemblies*. Farmington Hills, MI: American Concrete Institute.

American Society of Civil Engineers. 2007. *ASCE/SEI 41-06 Seismic Rehabilitation of Existing Buildings*. *Asce/Sei 41-06*.

ASTM International. 2013. *ASTM C642 Standard Test Method for Density, Absorption, and Voids in Hardened Concrete*. 1–3.

ASTM International. 2016a. "ASTM E1529 Standard Test Methods for Determining Effects of Large Hydrocarbon Pool Fires on Structural Members and Assemblies." https://doi.org/10.1520/E1529-16.

ASTM International. 2016b. *Test Methods for Determining Effects of Large Hydrocarbon Pool Fires on Structural Members and Assemblies*. West Conshohocken, PA: American Society of Testing and Materials International.

Atllah, S., and P. K. Raj. 1974. *Radiation from LNG fires, in: LNG Safety Program,Interim Report on Phase II Work, Project IS-3-1*. Batelle Columbus Laboratories: American Gas Association.

Babrauskas, V. 2016. "Heat Release Rates." *SFPE handbook of fire protection engineering*, 799–904. Springer.

Barry, K. 2010. "Mont Blanc Tunnel Opens." *Wired*, July 16, 2010.

Bazant, Z. k P., J. Chern, and W. Thonguthai. 1981. "North-Holland Pubfishing Company FINITE ELEMENT PROGRAM FOR MOISTURE AND HEAT TRANSFER IN HEATED CONCRETE."

Bažant, Z. P., and W. Thonguthai. 1979. "Pore pressure in heated concrete walls: theoretical prediction." *Magazine of Concrete Research*, 31 (107): 67–76. https://doi.org/10.1680/macr.1979.31.107.67.

Beard, A., and R. Carvel (Eds.). 2005. *The handbook of tunnel fire safety*. London, UK: Thomas Telford.

BEA-TT, and RAIB. 2010. *Technical investigation report concerning the fire on eurotunnel freight shuttle 7412 on 11 september 2008*. Bureau d'enquêtes sur les Accidents de transport terrestre (France), Rail Accident Investigation Branch (UK).

Bechtel/Parsons Brinckerhoff., and Bechtel/Parsons Brinckerhoff. 1995. *Memorial Tunnel Fire Ventilation Test Program: Test Report*. Boston, MA: Massachusetts Highway Department, FHWA.

Bergeson, W., and S. Ernst. 2015. *Tunnel Operations, Maintenance, Inspection, and Evaluation (TOMIE) Manual*. 263. Washington DC 20590.

Bingöl, A. F., and R. Gül. 2009. "Effect of elevated temperatures and cooling regimes on normal strength concrete." *Fire and Materials*, 33 (2): 79–88.

Bruneau, M., S. E. Chang, R. T. Eguchi, G. C. Lee, T. D. O'Rourke, A. M. Reinhorn, M. Shinozuka, K. Tierney, W. A. Wallace, and D. von Winterfeldt. 2003. "A Framework to Quantitatively Assess and Enhance the Seismic Resilience of Communities." *Earthquake Spectra*, 19 (4): 733–752. https://doi.org/10.1193/1.1623497.

Buchlin, J.-M. 2005. "Thermal shielding by water spray curtain." *Journal of Loss Prevention in the Process Industries*, 18 (4–6): 423–432. https://doi.org/10.1016/j.jlp.2005.06.039.

Carlton, A., Q. Guo, S. E. Quiel, and C. J. Naito. 2022. "Experimental Assessment of Explosive Spalling in Normal Weight Concrete Panels under High Intensity Thermal Exposure." *Fire Safety Journal*, ((in review)).

Carvel, R., and H. Ingason. 2016. "Chapter 88: Fires in Vehicle Tunnels." *SFPE Handbook of Fire Protection Engineering*, Morgan J. Hurley, ed., 3303–3325. New York, NY: Society of Fire Protection Engineering.

Carvill, J. 1993. "Chapter 3 - Thermodynamics and heat transfer." *Mechanical Engineer's Data Handbook*, J. Carvill, ed., 102–145. Oxford: Butterworth-Heinemann.

CEN. 2002. *Eurocode 1: Actions on structures -Part 1-5: General actions - Actions on structures exposed to fire*. Brussels, Belgium: European Committee for Standardization.

CEN. 2008. *EN 1992-1-2: Eurocode 2: Design of concrete structures - Part 1-2: General rules - Structural fire design*. Brussels, Belgium: European Commission for Standardization.

Chan, Y. N., G. F. Peng, and M. Anson. 1999. "Residual strength and pore structure of high-strength concrete and normal strength concrete after exposure to high temperatures." *Cement and Concrete Composites*, 21 (1): 23–27.

Chávez-Galán, J., R. Almanza, and N. R. Cuevas. 2014. "Convective heat transfer coefficients: experimental estimation and its impact on thermal building design for walls made of different Mexican building materials." *Concreto y Cemento. Investigación y Desarrollo*, 5 (2): 13.

Chen, C. J., M. J. Tsai, B. C. Ji, C. W. Wu, J. Y. Pu, and T. H. Lin. 2005. "Burning Analysis Of Motor Scooters." *Fire Safety Science*, 8: 671–680.

Choe, G., G. Kim, M. Yoon, E. Hwang, J. Nam, and N. Guncunski. 2019. "Effect of moisture migration and water vapor pressure build-up with the heating rate on concrete spalling type." *Cement and Concrete Research*, 116: 1–10. https://doi.org/10.1016/j.cemconres.2018.10.021.

Cimellaro, G. P., A. M. Reinhorn, and M. Bruneau. 2010. "Seismic resilience of a hospital system." *Structure and Infrastructure Engineering*, 6 (1–2): 127–144. https://doi.org/10.1080/15732470802663847.

Commonwealth of Pennsylvania. 2016. *PennDOT Specifications*. Publication 408.

Cortes, C., and V. Vapnik. 1995. "Support-Vector Networks." *Machine Learning*, 20 (3): 273–297. https://doi.org/10.1007/BF00994018.

Crude Logistics. 2012. *MATERIAL SAFETY DATA SHEET NO. 2 DIESEL FUEL, LOW SULFUR, ALL GRADES*.

Davie, C. T., C. J. Pearce, and N. Bićanić. 2012. "Aspects of Permeability in Modelling of Concrete Exposed to High Temperatures." *Transp Porous Med*, 95 (3): 627–646. https://doi.org/10.1007/s11242-012-0066-1.

Department of Defense (DoD). 2014. *UFC 3-340-02 Unified Facilities Criteria: Structures to Resist the Effects of Accidental Explosions*. Washington, D.C.

Dwaikat, M. B., and V. K. R. Kodur. 2009. "Hydrothermal model for predicting fire-induced spalling in concrete structural systems." *Fire Safety Journal*, 44 (3): 425–434. https://doi.org/10.1016/j.firesaf.2008.09.001.

Eurocode 1 1991-1-1. n.d. *Eurocode 1: Actions on structures - Part 1-1: General actions - Densities, self-weight, imposed loads for buildings*.

EUROPEAN COMMITTEE FOR STANDARDIZATION. 2002. *EN 1991-1-2 Eurocode 1: Actions on structures - Part 1-2: General actions -Actions on structures exposed to fire*.

European Committee for Standardization. 2004. *Eurocode 2: Design of Concrete Structures - Part 1-2: General Rules - Structural Fire Design*.

FHWA. 2020. *Fixed Fire Fighting and Emergency Ventilation Systems for Highway Tunnels Literature Survey and Synthesis (FHWA-HIF-20-016)*. Washington, D.C.: US Department of Transportation, Federal Highway Administration.

"Fort Pitt Tunnel." 2019. *Wikipedia*.

Franssen, J.-M. 2005. "SAFIR: A thermal/structural program for modeling structures under fire." *Engineering Journal-American Institute of Steel Construction Inc*, 42 (3): 143–158.

Franssen, J.-M., and T. Gernay. 2017a. "Modeling structures in fire with SAFIR®: Theoretical background and capabilities." *Journal of Structural Fire Engineering*, 8 (3): 300–323.

Franssen, J.-M., and T. Gernay. 2017b. "Modeling structures in fire with SAFIR ®: theoretical background and capabilities." *Journal of Structural Fire Engineering*, 8 (3): 300–323.

Freyssinet Corporation. 2021. *Concrete Repair & Tunnel Strengthening: Channel Tunnel Fire Damage Repair*. United Kingdom.

Gawin, D., F. Pesavento, and B. A. Schrefler. 2006. "Towards prediction of the thermal spalling risk through a multi-phase porous media model of concrete." *Computer Methods in Applied Mechanics and Engineering*, John H. Argyris Memorial Issue. Part II, 195 (41): 5707–5729.

Gerasimidis, S., and S. Civjan. n.d. *Post-Fire Damage Inspection of Concrete Structures*. University of Massachusetts Amherst;UMass Transportation Center.

Guo, Q., S. E. Quiel, and C. J. Naito. 2021. "Traffic-Based Quantitative Risk Analysis of Structural Fire Damage to 2 Roadway Tunnel Linings." *Structure and Infrastructure Engineering*, Manuscript NSIE-2021-0109: 59.

Guo, Q., K. J. Root, A. Carlton, S. E. Quiel, and C. J. Naito. 2019. "Framework for rapid prediction of fire-induced heat flux on concrete tunnel liners with curved ceilings." *Fire Safety Journal*, 109: 102866.

Harmathy, T. Z. 1965. "Effect of Moisture on the Fire Endurance of Building Elements." *ASTM STP 385*, American Society for Testing and Materials-Special Technical Publication No. 385: 74–95. https://doi.org/978-0-8031-5970-9.

Hertz, K. D. 2003. "Limits of spalling of fire-exposed concrete." *Fire Safety Journal*, 38 (2): 103–116. https://doi.org/10.1016/S0379-7112(02)00051-6.

Hertz, K. D., and L. S. Sørensen. 2005. "Test method for spalling of fire exposed concrete." *Fire Safety Journal*, 40 (5): 466–476. https://doi.org/10.1016/j.firesaf.2005.04.001.

Heskestad, G. 1983. "Luminous heights of turbulent diffusion flames." *Fire Safety Journal*, 5 (2): 103–108.

Holter, K. G., and S. Geving. 2016. "Moisture Transport Through Sprayed Concrete Tunnel Linings." *Rock Mech Rock Eng*, 49 (1): 243–272. https://doi.org/10.1007/s00603-015-0730-1.

Hostikka, S., K. Mcgrattan, and A. Hamins. 2003. "Numerical Modeling Of Pool Fires Using Les And Finite Volume Method For Radiation." *Fire Safety Science*, 7: 383–394. https://doi.org/10.3801/IAFSS.FSS.7-383.

Hua, N., A. Tessari, and N. Elhami Khorasani. 2021. "Characterizing damage to a concrete liner during a tunnel fire." *Tunnelling and Underground Space Technology*, 109: 103761. https://doi.org/10.1016/j.tust.2020.103761.

Hurley, M. J. (Ed.). 2016a. *SFPE Handbook of Fire Protection Engineering*. New York, NY: Springer New York.

Hurley, M. J. (Ed.). 2016b. "Appendix 3: Fuel Properties and Combustion Data." *SFPE Handbook of Fire Protection Engineering*, 3437–3475. New York, NY: Society of Fire Protection Engineering.

Hwang, C. C., and J. C. Edwards. 2005. "The critical ventilation velocity in tunnel fires - A computer simulation." *Fire Safety Journal*, 40 (3): 213–244. https://doi.org/10.1016/j.firesaf.2004.11.001.

Ichikawa, Y., and G. L. England. 2004. "Prediction of moisture migration and pore pressure build-up in concrete at high temperatures." *Nuclear Engineering and Design*, SMiRT 16. Selected and Updated Papers from the 16th International Conference on Structural Mechanics in Reactor Technology, Washington DC, 228 (1): 245–259. https://doi.org/10.1016/j.nucengdes.2003.06.011.

Ingason, H. 2009. "Design fire curves for tunnels." *Fire Safety Journal*, 44 (2): 259–265.

Ingason, H., Y. Z. Li, and A. Lönnermark. 2011. *Runehamar tunnel fire tests (SP Report 2011:55)*. Boras, Sweden: SP Technical Research Institute of Sweden.

Ingason, H., Y. Z. Li, and A. Lönnermark. 2015a. *Tunnel Fire Dynamics*. New York, NY: Springer New York.

Ingason, H., Y. Z. Li, and A. Lönnermark. 2015b. "Runehamar tunnel fire tests." *Fire Safety Journal*, 71: 134–149. https://doi.org/10.1016/j.firesaf.2014.11.015.

Ingason, H., Y. Z. Li, and A. Lönnermark. 2015c. "Runehamar tunnel fire tests." *Fire Safety Journal*, 71: 134–149.

Ingham, J. 2009. "Forensic engineering of fire-damaged structures." *Proceedings of the Institution of Civil Engineers - Civil Engineering*, 162 (5): 12–17. https://doi.org/10.1680/cien.2009.162.5.12.

Jansson, R. 2013. "Fire Spalling of Concrete: Theoretical and Experimental Studies." Stockholm, Sweden: KTH Architecture and The Built Environment.

Jansson, R., and L. Boström. 2010. "The Influence of Pressure in the Pore System on Fire Spalling of Concrete." *Fire Technology*, 46 (1): 217–230. https://doi.org/10.1007/s10694-009-0093-9.

Jia, F., Z. Wang, and E. R. Galea. 2010. "MODELLING FACTORS THAT INFLUENCE CFD FIRE SIMULATIONS OF LARGE TUNNEL FIRES." *12th International Fire Science & Engineering Conference*, 1091–1102. University of Nottingham, UK.

Joint ACI/TMS Committee 216, and Masonry Society (U.S.) (Eds.). 2007. *Code requirements for determining fire resistance of concrete and masonry construction assemblies (ACI 216.1-07, TMS-216-07): an ACI/TMS Standard*. Farmington Hills, MI: American Concrete Institute.

Jovanović, B., N. E. Khorasani, T. Thienpont, R. K. Chaudhary, and R. Van Coile. 2020. "Probabilistic models for thermal properties of concrete." *Proceedings of the 11th*

International Conference on Structures in Fire (SiF2020). Online: The University of Queensland.

Kalifa, P., G. Chéné, and C. Gallé. 2001. "High-temperature behaviour of HPC with polypropylene fibres: From spalling to microstructure." *Cement and Concrete Research*, 31 (10): 1487–1499. https://doi.org/10.1016/S0008-8846(01)00596-8.

KBwiki. 2017. "Test Data AC4-04." Accessed December 8, 2021. https://www.kbwiki.ercoftac.org/w/index.php/Test_Data_AC4-04.

Kennedy, W. D., and J. F. L. Lowndes. 1996. "Critical velocity: Past, present and future." *Smoke and critical velocity in tunnels, Seminar, Smoke and critical velocity in tunnels*. ITC.

Kim, E., J. P. Woycheese, and N. A. Dembsey. 2008a. "Fire Dynamics Simulator (Version 4.0) Simulation for Tunnel Fire Scenarios with Forced, Transient, Longitudinal Ventilation Flows." *Fire Technology*, 44 (2): 137–166. https://doi.org/10.1007/s10694-007-0028-2.

Kim, E., J. P. Woycheese, and N. A. Dembsey. 2008b. "Fire Dynamics Simulator (Version 4.0) Simulation for Tunnel Fire Scenarios with Forced, Transient, Longitudinal Ventilation Flows." *Fire Technol*, 44 (2): 137–166. https://doi.org/10.1007/s10694-007-0028-2.

Kim, J. J., K.-S. Youm, and M. M. Reda Taha. 2014. "Extracting Concrete Thermal Characteristics from Temperature Time History of RC Column Exposed to Standard Fire." *ScientificWorldJournal*, 2014.

Kodur, V. K. R., and s. Banerji. 2021. "Modeling the fire-induced spalling in concrete structures incorporating hydro-thermo-mechanical stresses." *Cement And Concrete Composites*, 117. https://doi.org/10.1016/j.cemconcomp.2020.103902.

Kolymbas, D. 2005. "Earthquake effects on tunnels." *Tunnelling and Tunnel Mechanics: A Rational Approach to Tunnelling*, 337–339. Berlin, Heidelberg: Springer.

Lam, C. S., and E. J. Weckman. 2015. "Wind-blown pool fire, Part II: Comparison of measured flame geometry with semi-empirical correlations." *Fire Safety Journal*, 78: 130–141. https://doi.org/10.1016/j.firesaf.2015.08.004.

Lautkaski, R. 1992. "Validation of flame drag correlations with data from large pool fires." *Journal of Loss Prevention in the Process Industries*, 5 (3): 175–180. https://doi.org/10.1016/0950-4230(92)80021-Y.

Le, Q. X., V. T. N. Dao, C. Maluk, J. Torero, and L. Bisby. 2016. "An investigation into temperature gradient effects on concrete performance at elevated temperatures." *The 24th Australasian Conference on the Mechanics of Structures and Materials (ACMSM24)*.

LEE, C. K., R. F. CHAIKEN, and J. M. SINGER. 1979. "Interaction Between Duct Fires and Ventilation Flow: An Experimental Study." *Combustion Science and Technology*, 20 (1–2): 59–72. Taylor & Francis. https://doi.org/10.1080/00102207908946897.

Lee, Y., M.-S. Choi, S.-T. Yi, and J.-K. Kim. 2009. "Experimental study on the convective heat transfer coefficient of early-age concrete." *Cement and Concrete Composites*, 31 (1): 60–71. https://doi.org/10.1016/j.cemconcomp.2008.09.009.

Li, J. 2017. "Key Technologies and Applications of the Design and Manufacturing of Non-Circular TBMs." *Engineering*, 3 (6): 905–914.

Li, M., Z. Wu, H. Kao, C. Qian, and W. Sun. 2010. "Calculation and analysis of pore vapor pressure of concrete exposed to fire." *Int. J. Phys. Sci.*, 5 (8): 1315–1323.

Li, Y. Z., and H. Ingason. 2014. "Position of Maximum Ceiling Temperature in a Tunnel Fire." *Fire Technol*, 50 (4): 889–905. https://doi.org/10.1007/s10694-012-0309-2.

Li, Y. Z., and H. Ingason. 2015. *Fire-induced ceiling jet characteristics in tunnels under different ventilation conditions*. 77. Borås, Sweden: SP Technical Research Institute of Sweden.

Lu, F. 2015. "On the prediction of concrete spalling under fire." Switzerland: ETH Zurich.
Maevski, I. 2011. *NCHRP Synthesis 415: Design Fires in Road Tunnels–A Synthesis of Highway Practice*. Washington, D.C: Transportation Research Board.
Majorana, C. E., V. Salomoni, and B. A. Schrefler. 1998. "Hygrothermal and mechanical model of concrete at high temperature." *Materials and Structures*, 31 (6): 378–386. https://doi.org/10.1007/BF02480710.
MathWorks. 2014. "MATLAB." Natick, MA.
McGrattan, K. B., H. R. Baum, and A. Hamins. 2000. *Thermal radiation from large pool fires*. Gaithersburg, MD: National Institute of Standards and Technology.
McGrattan, K. B., and A. Hamins. 2002. *Numerical Simulation of the Howard Street Tunnel Fire, Baltimore, Maryland, July 2001*. 41. U.S. Department of Commerce, National Institute of Standards and Technology.
McGrattan, K. B., R. J. McDermott, C. G. Weinschenk, and G. P. Forney. 2013a. "Fire Dynamics Simulator, Technical Reference Guide, Sixth Edition." *Special Publication (NIST SP) - 1018*.
McGrattan, K., J. Floyd, G. Forney, H. Baum, and S. Hostikka. 2003. "Improved Radiation And Combustion Routines For A Large Eddy Simulation Fire Model." *Fire Safety Science*, 7: 827–838. https://doi.org/10.3801/IAFSS.FSS.7-827.
McGrattan, K., R. McDermott, S. Hostikka, and J. Floyd. 2013b. *Fire Dynamics Simulator Users Guide, Sixth Edition*. Gaithersburg, MD: National Institute of Standards and Technology.
Meng, N., L. Hu, S. Liu, L. Wu, L. Chen, and B. Liu. 2012. "Full-scale experimental study on fire suppression performance of a designed water mist system for rescue station of long railway tunnel." *Journal of Fire Sciences*, 30 (2): 138–157. https://doi.org/10.1177/0734904111428898.
Moorhouse, J. 1982. *Scaling criteria for pool fires derived from large scale experiments*. United Kingdom: British Gas Corporation,Solihull, England.
Muñoz, M., J. Arnaldos, J. Casal, and E. Planas. 2004. "Analysis of the geometric and radiative characteristics of hydrocarbon pool fires." *Combustion and Flame*, 139 (3): 263–277. https://doi.org/10.1016/j.combustflame.2004.09.001.
Muñoz, M., E. Planas, F. Ferrero, and J. Casal. 2007. "Predicting the emissive power of hydrocarbon pool fires." *Journal of Hazardous Materials*, 144 (3): 725–729.
Muntasir Billah, A. H. M., and M. Shahria Alam. 2015. "Seismic fragility assessment of highway bridges: a state-of-the-art review." *Structure and Infrastructure Engineering*, 11 (6): 804–832. https://doi.org/10.1080/15732479.2014.912243.
NFPA. 2017. *NFPA 502: Standard for road tunnels, bridges, and other limited access highways*. Quincy, MA: National Fire Protection Association.
NFPA. 2020. *NFPA 502: Standard for road tunnels, bridges, and other limited access highways*. Quincy, MA: National Fire Protection Association.
NFPA 502, Standard for road tunnels, bridges, and other limited access highways. 2011. National Fire Protection Association.
NLB Corp. 2021. "Hydrodemolition Production Rate." http://www.industrycortex.com/datasheets/profile/3144638.
Oka, Y., and G. T. Atkinson. 1995. "Control of smoke flow in tunnel fires." *Fire Safety Journal*, 25 (4): 305–322. https://doi.org/10.1016/0379-7112(96)00007-0.
Olsson, A. M. J., and G. E. Sandberg. 2002. "Latin Hypercube Sampling for Stochastic Finite Element Analysis." *Journal of Engineering Mechanics*, 128 (1): 121–125.

Ouyang, Z., A. Carlton, Q. Guo, C. Naito, and S. Quiel. 2020. "Blast Vulnerability of Drop Ceilings in Roadway Tunnels." *Journal of Performance of Constructed Facilities*. https://doi.org/10.1061/(ASCE)CF.1943-5509.0001526.

Pearlman, J., and N. Meltzer. 2012. *Risk of Commercial Truck Fires in the United States: An Exploratory Data Analysis*. Cambridge, MA: John A. Volpe National Transportation Systems Center, U.S. Department of Transportation Research and Innovative Technology Administration.

Phan, L. T., J. R. Lawson, and F. L. Davis. 2001. "Effects of elevated temperature exposure on heating characteristics, spalling, and residual properties of high performance concrete." *Materials and Structures*, 34.

PIARC Technical Committee C.4. 2021. *Improving road tunnel resilience, considering safety and availability (PIARC literature review)*.

Quiel, S. E., S. M. Marjanishvili, and B. P. Katz. 2016. "Performance-Based Framework for Quantifying Structural Resilience to Blast-Induced Damage." *Journal of Structural Engineering*, 142 (8): C4015004. https://doi.org/10.1061/(ASCE)ST.1943-541X.0001310.

Quiel, S. E., T. Yokoyama, L. S. Bregman, K. A. Mueller, and S. M. Marjanishvili. 2015. "A streamlined framework for calculating the response of steel-supported bridges to open-air tanker truck fires." *Fire Safety Journal*, 73: 63–75.

Rafiei, M. 2015. "Numerical Simulation of a Full Scaled Fire Test of the Tunnel with Natural Ventilation." *International Journal of Computer Applications*, 115 (1).

Raj, P. K. 2010. "A Physical Model and Improved Experimental Data Correlation for Wind Induced Flame Drag in Pool Fires." *Fire Technol*, 46 (3): 579–609. https://doi.org/10.1007/s10694-009-0107-7.

Shinozuka, M., M. Q. Feng, J. Lee, and T. Naganuma. 2000. "Statistical Analysis of Fragility Curves." *Journal of Engineering Mechanics*, 126 (12): 1224–1231. https://doi.org/10.1061/(ASCE)0733-9399(2000)126:12(1224).

Shorter, G. W., and T. Z. Harmathy. 1961. "Discussion on the fire resistance of prestressed concrete beams." *Proceedings of the Institution of Civil Engineers*, 20 (2): 313–315.

Shumway, J. 2014. "PennDOT To Remove Fort Pitt Tunnel Ceiling." *CBS Pittsburgh*. Accessed November 24, 2018. https://pittsburgh.cbslocal.com/2014/05/15/penndot-to-remove-fort-pitt-tunnel-roof/.

Siddapureddy, S. 2013. "Characterization of Open Pool Fires and Study of Heat Transfer in Bodies Engulfed in Pool Fires." Indian Institute of Technology Dharwad.

StoneAge. n.d. *CONCRETE HYDRO-DEMOLITION REMOVAL RATES*.

Sturm, P., M. Beyer, and M. Rafiei. 2017. "On the problem of ventilation control in case of a tunnel fire event." *Case Studies in Fire Safety*, 7: 36–43. https://doi.org/10.1016/j.csfs.2015.11.001.

Sudheer, S. 2013. "Characterization of Open Pool Fires and Study of Heat Transfer in Bodies Engulfed in Pool Fires." PhD Dissertation. Bombay, India: Indian Institute of Technology Bombay.

Sudheer, S., and S. V. Prabhu. 2012. "Measurement of Flame Emissivity of Hydrocarbon Pool Fires." *Fire Technology*, 48 (2): 183–217. https://doi.org/10.1007/s10694-010-0206-5.

Tatnall, P. C. 2002. "Shotcrete in Fires: Effects of Fibers on Explosive Spalling." *Shotcrete*, 2002.

Tenchev, R., and P. Purnell. 2005. "An application of a damage constitutive model to concrete at high temperature and prediction of spalling." *International Journal of Solids and Structures*, 42 (26): 6550–6565. https://doi.org/10.1016/j.ijsolstr.2005.06.016.

Thomas, P. H. 1958. *THE MOVEMENT OF BUOYANT FLUID AGAINST A STREAM AND THE VENTING OF UNDERGROUND FIRES*. Fire Research Note. Fire Research Note 351.

Thomas, P. H. 1968. *THE MOVEMENT OF SMOKE IN HORIZONTAL PASSAGES AGAINST AN AIR FLOW*. Fire Research Note. Fire Research Note 723.

TNO-IBBC. 1979. *Beproeving van het gedrag bij verhitting van twee isolatie materialen ter bescherming van tunnels bij brand*. Delft, the Netherlands: Instituut TNO voor Bouwmaterialen en Bouwconstructies.

Tunnel (digital). 2020. "Consequential Costs and Cost-Effectiveness of Fire Protection Boards Used in Tunnels." *Tunnel-Online*. Digital Magazine. Accessed August 13, 2021. https://www.tunnel-online.info/en/artikel/tunnel_Consequential_Costs_and_Cost-Effectiveness_of_Fire_Protection_Boards_Used_3526191.html.

US Army Corps of Engineers. 1993. *Standard Practice for Shotcrete*. DEPARTMENT OF THE ARMY.

U.S. Army Corps of Engineers. 2008. *User's Guide for the Single-Degree-of-Freedom Blast Effects Design Spreadsheets (SBEDS): PDC TR-06-02 Rev 1*. Washington, D.C.

USDOT. 2015. *Specifications for the National Tunnel Inventory*. Washington, DC: U.S. Department of Transportation; Federal Highway Administration.

VALERO. 2014. *Safety Data Sheet: Diesel Fuels*. 11. 3E Company.

Vega, M. G., K. M. Argüelles Díaz, J. M. Fernández Oro, R. B. Tajadura, and C. Santolaria Morros. 2008. "Numerical 3D simulation of a longitudinal ventilation system: Memorial Tunnel case." *Tunnelling and Underground Space Technology*, 23 (5): 539–551. https://doi.org/10.1016/j.tust.2007.10.001.

Vrouwenvelder, T., A. Breunesse, M. Nelisse, M. Ohlin, N. P. Høj, J. Hoeksma, and H. Derks. 2004. *D.A.R.T.S Durable and Reliable Tunnel Structure: Identification and Quantification of Hazards - Fire and Smoke*. Delft, the Netherland: Netherlands Organisation for Applied Scientific Research, COWI A/S, Rijkswaterstaat.

Wang, F., M. Wang, and J. Huo. 2017. "The effects of the passive fire protection layer on the behavior of concrete tunnel linings: A field fire testing study." *Tunnelling and Underground Space Technology*, 69: 162–170. https://doi.org/10.1016/j.tust.2017.06.021.

Weber. 2017. "Repair of damage with exposed steel reinforcement." Accessed August 17, 2021. https://www.middleeast.weber/concrete-repair-anchoring-and-grouting/repair-damage-exposed-steel-reinforcement.

Welker, J. R., and C. M. Sliepcevich. 1966. "Bending of wind-blown flames from liquid pools." *Fire Technol*, 2 (2): 127–135. https://doi.org/10.1007/BF02588541.

Yan, Z., Y. Shen, H. Zhu, and Y. Lu. 2016. "Experimental study of tunnel segmental joints subjected to elevated temperature." *Tunnelling and Underground Space Technology*, 53: 46–60. https://doi.org/10.1016/j.tust.2016.01.005.

Yi, L., R. Huo, J. Zhang, Y. LI, and H. ZHANG. 2006. "Characteristics of heat release rate of diesel oil pool fire." *Journal of Combustion Science and Technology*, 2: 015.

Zhou, K., N. Liu, L. Zhang, and K. Satoh. 2014. "Thermal Radiation from Fire Whirls: Revised Solid Flame Model." *Fire Technology*, 50 (6): 1573–1587.

Zhu, P., X. Wang, Z. Wang, H. Cong, and X. Ni. 2015. "Experimental and numerical study on attenuation of thermal radiation from large-scale pool fires by water mist curtain." *Journal of Fire Sciences*, 33 (4): 269–289. https://doi.org/10.1177/0734904115585796.

Zhukov, V. 1976. "Reasons of Explosive Spalling of Concrete by Fire." *Beton Zhelezobeton (Concrete and Reinforcement Concrete)*, (No. 3).

APPENDIX A – TECHNOLOGY TRANSFER ACTIVITIES

1. Accomplishments

1.1 What was done? What was learned?

- Methodologies were developed for numerical modeling of vehicle fire in tunnels under natural ventilation and forced ventilation conditions.
- A fast-running and conservatively accurate semi-empirical fire model was proposed to predict tunnel-specific fire-induced heat flux on tunnel liners which is simple to use and practical for parametric and stochastic analyses.
- The resilience of the tunnel subjected to fire hazard could be quantified as the functionality loss.
- A quantitative risk assessment framework was established for tunnel fire safety which links the results of fire analysis and tunnel damage to explicit consequences for tunnel owners.
- Quantitative recommendations were provided for tunnel fire database development, fire design, tunnel renovation and post-fire inspection.
- The tool enables decision making in terms of tunnel design and renovation for fire as well as post-fire inspection by quantifying the risk of capacity reduction in the concrete liner due to a realistic range of fire hazard intensities.
- The tool runs on MATLAB and includes visualization with Rhino and Grasshopper.

1.2 How have the results been disseminated?

- The results were presented at *Tunneling Fundamentals, Practice and Innovations Short Course*, Colorado School of Mines, Golden, 2019.
- The results were presented at *Transportation Research Board (TRB) 99th Annual Meeting*, Washington DC, 2020.
- The results were presented at *Engineering Mechanics Institute Conference*. John Hopkins University, *Baltimore, 2022*

2. Participants and Collaborating Organizations

Name: Lehigh University

Location: Bethlehem, PA

Contribution: (1) A semi-empirical solid flame model (CDSF model) was developed for rapid and accurate prediction of steady-state incident heat flux received by the tunnel linings due to vehicle fire. (2) Numerical modeling approach in FDS for the tunnel fire analyses was validated against full-scale tunnel fire tests with various tunnel geometry and fire sizes. (3) quantification method of assessing the tunnel resilience by considering the tunnel structure damage subjected to fire hazard, the tunnel traffic, and the repairing procedure. (4) A quantitative fire risk assessment tool considering both probability of the vehicle fire with various HRR and the structural consequences in terms of concrete strength reduction was established to help decision making during the process of design, renovation, inspection and repair of tunnel fire safety systems. The tool generates fire risk results based on the specific tunnel geometry and traffic data.

3. Outputs

Journal publications

- Guo, Q., Root, K. J., Carlton, A., Quiel, S. E., and Naito, C. J. (2019). "Framework for rapid prediction of fire-induced heat flux on concrete tunnel liners with curved ceilings." *Fire Safety Journal*, 109, 102866.
- Guo, Q., Quiel, S. E., & Naito, C. J. (2021). Traffic-based quantitative risk analysis of structural fire damage to roadway tunnel linings. *Structure and Infrastructure Engineering*, 1-17.
- Zhu, Z., Guo, Q., Quiel, S. E., & Naito, C. J. (2022). Rapid prediction of fire-induced heat flux on the liners of horseshoe and circular tunnels with longitudinal ventilation at critical velocity. *Fire Safety Journal*, 130, 103590.
- Zhu, Z., & Carlton, A., Quiel, S. E., & Naito, C. J., (under review). Tunnel fire structural resilience assessment and improvement.

Presentations

- Qi Guo "Streamlined Calculation of Fire-Induced Heat Flux and Resulting Spalling Damage for Concrete Tunnel Liners" at *Transportation Research Board (TRB) 98th Annual Meeting*, Washington DC, Jan 2019
- Qi Guo "Stochastic Thermal Demand and Resulting Capacity Loss of Concrete Tunnel Liners Subjected to Vehicle Fires" at *ADSC International Association of Foundation Drilling Northeast Chapter Fall Meeting*, Bethlehem, PA, Nov 2019
- Qi Guo "Stochastic Thermal Demand and Resulting Capacity Loss of Concrete Tunnel Liners Subjected to Vehicle Fires" at *Transportation Research Board (TRB) 99th Annual Meeting*, Washington DC, 2020

Workshops

- Qi Guo, Kyle Root "Tunnel Liner Damage due to Fire and Blast: Fast-Running Predictions and Upcoming Test Programs" at *Tunneling Fundamentals, Practice and Innovations Short Course*, Colorado School of Mines, Golden, 2018
- Qi Guo "Stochastic Thermal Demand and Resulting Capacity Loss of Concrete Tunnel Liners Subjected to Vehicle Fires" at *Tunneling Fundamentals, Practice and Innovations Short Course*, Colorado School of Mines, Golden, 2019

4. Outcomes

- The confined discretized solid flame (CDSF) model is developed for rapid and reliable predictions of the total heat flux (radiation and convection) imparted to tunnel liners from a range of typical vehicle fires. The fast-running CDSF model provides compatibility for stochastic and parametric study and capability to accurately predict tunnel-specific fire-induced heat flux on tunnel liners.
- The MATLAB-SAFIR method was shown to efficiently model tunnel fire hazard including concrete spalling phenomena, and can be used to perform stochastic analysis which accounts for the associated uncertainties in the thermal properties of concrete.
- The concrete damage mapping classified concrete damage according to the post-fire repair procedure. It provides a straightforward probabilistic-based damage assessment tool that can be used to quantify the tunnel functionality through operational disruption time of the tunnel after fire hazard.
- that reductions in functionality loss and increased resilience can be achieved at the design stage by choosing larger tunnel geometries, during operation through restriction of high intensity fire capable vehicles (e.g., fuel tankers and HGV), and installing active fire mitigation systems. Among them, the FFFS provides a notable means of reducing the functionality loss from fire, and should be recommended for installation. Longitudinal ventilation systems, though widely accepted as a life-safety fire mitigation method, did not provide a significant improvement in structural resilience.
- The quantitative fire risk assessment tool for tunnel structure includes the levels of potential damage and probability of occurrence associated with the two milestone scenarios, combined with their standard fire exposure equivalents, which can aid decision making about fire protection design, renovation, and post-fire inspection for tunnels.

5. Impacts

- The determination of fire demand which includes the HRR and the thermal exposure on the tunnel linings is a significant part of the tunnel fire safety design. Although the current practice uses a relatively conservative method as the criteria of fire protection design, many tunnels built 50 or more years ago might not be able to meet the criteria. There has been cases generating thermal demand much higher than that required by the current practice. This risk assessment tool can provide information of the probability of each levels of heat exposure to help the decision-making process such as the method for fire protection or the level of fire protection.
- The high-fidelity computational fluid dynamics software FDS has been dominant when there is a need for a tunnel heat transfer analysis to generate thermal exposure inside a tunnel and on tunnel linings caused by fire hazards. The CDSF model can work as a preliminary tool which enriches the ways to determine fire-induced thermal demand on tunnel structures.
- The tunnel resilience quantification method lay a foundation of the tunnel fire mitigation optimization method development, which is the next phase of the study.

APPENDIX B - DATA FROM THE PROJECT

B.1 Time History of Heat Flux (kW/m^2) measured in the Runehamar Tunnel Fire test and FDS (Figure 11)

Time (min)	TEST Heat Flux 0m	Time (min)	TEST Heat Flux 10m	Time (min)	TEST Heat Flux 20m	Time (min)	TEST Heat Flux 40m
0.0	0.0	0.0	0.4	0.2	0.5	0.2	0.5
0.7	12.6	0.4	0.7	0.4	0.7	0.4	0.5
1.2	14.4	0.5	1.1	0.8	0.9	0.8	0.9
1.7	6.2	0.6	1.3	1.0	1.0	1.0	0.8
2.2	6.8	0.9	1.5	1.2	1.0	1.2	0.8
2.8	8.3	1.1	1.6	1.5	1.0	1.4	0.9
3.2	6.2	1.3	1.7	1.7	1.1	1.7	1.0
3.6	7.3	1.6	1.7	2.1	1.0	1.9	0.9
4.2	5.4	1.8	1.7	2.4	1.0	2.1	0.8
4.9	5.5	2.0	1.7	2.6	0.9	2.3	0.8
5.2	6.1	2.2	1.7	2.8	1.0	2.5	0.8
5.7	6.6	2.4	1.5	3.0	0.9	2.7	0.8
6.2	6.1	2.6	1.5	3.0	0.8	2.9	0.8
6.6	6.4	2.9	1.4	3.3	0.8	3.2	0.7
6.9	6.6	3.1	1.3	3.5	0.9	3.4	0.7
7.3	6.9	3.4	1.4	3.7	0.8	3.6	0.7
7.6	7.1	3.6	1.4	3.9	0.8	3.8	0.7
7.9	6.9	3.8	1.4	4.1	0.7	4.0	0.7
8.4	6.8	4.0	1.2	4.4	0.7	4.3	0.6
8.8	6.9	4.2	1.2	4.6	0.8	4.5	0.6
9.1	6.9	4.4	1.4	4.8	0.7	4.7	0.6
9.5	6.6	4.7	1.3	5.0	0.8	5.0	0.5
9.7	6.5	4.9	1.4	5.2	0.8	5.2	0.5
10.0	6.5	5.1	1.5	5.4	0.8	5.5	0.5
10.7	7.3	5.4	1.5	5.6	0.8	5.7	0.5
11.1	7.6	5.6	1.4	5.8	0.7	5.9	0.6
11.3	7.7	5.9	1.6	6.0	1.0	6.1	0.6
11.6	7.5	6.2	1.5	6.2	1.0	6.3	0.6
12.0	7.4	6.5	1.5	6.4	1.0	6.5	0.6
12.3	7.4	6.7	1.4	6.6	0.9	6.7	0.6
12.7	7.4	6.9	1.5	6.8	0.8	6.9	0.7
13.0	7.4	7.1	1.7	7.1	0.8	7.2	0.7
13.3	7.7	7.4	1.7	7.3	0.9	7.4	0.6
13.6	8.0	7.7	1.7	7.5	0.9	7.7	0.6

14.4	9.9	7.9	1.7	7.7	0.8	7.9	0.6
14.8	5.3	8.1	1.6	7.9	0.8	8.1	0.6
15.3	6.4	8.3	1.5	8.1	0.8	8.3	0.6
15.7	8.9	8.7	1.5	8.3	0.9	8.5	0.6
16.0	7.9	9.0	1.4	8.5	0.8	8.7	0.6
16.9	6.8	9.3	1.6	8.8	0.9	8.9	0.6
17.4	10.0	9.5	1.7	9.0	0.8	9.2	0.7
17.7	6.8	9.7	1.5	9.2	0.9	9.5	0.7
18.4	8.7	9.9	1.4	9.4	1.0	9.7	0.6
19.2	6.6	10.1	1.6	9.6	1.0	10.0	0.7
19.5	6.2	10.3	1.6	9.9	0.9	10.2	0.7
19.9	5.2	10.5	1.5	10.1	1.0	10.4	0.7
20.1	5.2	10.8	1.4	10.4	1.0	10.6	0.7
20.6	3.5	10.9	1.4	10.6	1.0	10.9	0.6
21.0	2.4	11.3	1.5	10.8	1.0	11.1	0.6
21.7	0.9	11.6	1.5	11.0	0.9	11.3	0.6

Time (min)	FDS Heat Flux 0m	FDS Heat Flux 10m	FDS Heat Flux 20m	FDS Heat Flux 40m
-5.00E-01	3.69E-01	3.69E-01	3.69E-01	3.70E-01
-4.83E-01	3.70E-01	3.70E-01	3.70E-01	3.70E-01
-4.66E-01	3.83E-01	3.70E-01	3.70E-01	3.70E-01
-4.50E-01	4.27E-01	3.70E-01	3.70E-01	3.70E-01
-4.33E-01	4.99E-01	3.73E-01	3.70E-01	3.70E-01
-4.16E-01	6.08E-01	3.76E-01	3.70E-01	3.70E-01
-3.99E-01	7.01E-01	3.80E-01	3.70E-01	3.70E-01
-3.83E-01	7.73E-01	3.83E-01	3.70E-01	3.70E-01
-3.66E-01	8.27E-01	3.86E-01	3.70E-01	3.70E-01
-3.50E-01	8.19E-01	3.87E-01	3.70E-01	3.70E-01
-3.33E-01	8.00E-01	3.88E-01	3.70E-01	3.70E-01
-3.16E-01	8.03E-01	3.88E-01	3.70E-01	3.70E-01
-3.00E-01	7.89E-01	3.87E-01	3.71E-01	3.70E-01

-2.83E-01	7.92E-01	3.88E-01	3.72E-01	3.70E-01
-2.66E-01	7.93E-01	3.89E-01	3.73E-01	3.70E-01
-2.50E-01	7.63E-01	3.89E-01	3.73E-01	3.70E-01
-2.33E-01	7.34E-01	3.90E-01	3.74E-01	3.70E-01
-2.17E-01	7.24E-01	3.87E-01	3.74E-01	3.70E-01
-2.00E-01	7.16E-01	3.86E-01	3.75E-01	3.70E-01
-1.83E-01	7.00E-01	3.85E-01	3.75E-01	3.70E-01
-1.67E-01	6.73E-01	3.84E-01	3.75E-01	3.70E-01
-1.49E-01	6.08E-01	3.83E-01	3.75E-01	3.71E-01
-1.32E-01	5.38E-01	3.80E-01	3.74E-01	3.72E-01
-1.16E-01	4.83E-01	3.78E-01	3.74E-01	3.72E-01
-9.94E-02	4.32E-01	3.75E-01	3.74E-01	3.72E-01
-8.28E-02	3.86E-01	3.73E-01	3.75E-01	3.72E-01
-6.63E-02	3.74E-01	3.72E-01	3.75E-01	3.73E-01
-4.92E-02	3.73E-01	3.72E-01	3.74E-01	3.74E-01
-3.30E-02	3.73E-01	3.71E-01	3.73E-01	3.74E-01
-1.59E-02	3.73E-01	3.71E-01	3.72E-01	3.73E-01
2.79E-04	3.73E-01	3.70E-01	3.72E-01	3.72E-01
1.73E-02	3.72E-01	3.70E-01	3.71E-01	3.72E-01
3.36E-02	3.75E-01	3.70E-01	3.71E-01	3.72E-01
5.06E-02	3.97E-01	3.71E-01	3.70E-01	3.72E-01
6.68E-02	4.19E-01	3.71E-01	3.70E-01	3.72E-01
8.39E-02	4.44E-01	3.72E-01	3.70E-01	3.72E-01
1.00E-01	4.71E-01	3.73E-01	3.70E-01	3.71E-01
1.17E-01	5.07E-01	3.75E-01	3.70E-01	3.71E-01
1.33E-01	5.44E-01	3.76E-01	3.70E-01	3.71E-01
1.50E-01	5.61E-01	3.78E-01	3.70E-01	3.71E-01
1.68E-01	5.76E-01	3.79E-01	3.70E-01	3.70E-01
1.84E-01	5.87E-01	3.80E-01	3.71E-01	3.70E-01
2.01E-01	6.07E-01	3.81E-01	3.71E-01	3.70E-01

2.17E-01	6.16E-01	3.82E-01	3.71E-01	3.70E-01
2.34E-01	6.55E-01	3.83E-01	3.72E-01	3.70E-01
2.50E-01	7.27E-01	3.85E-01	3.72E-01	3.70E-01
2.67E-01	7.91E-01	3.88E-01	3.73E-01	3.70E-01
2.84E-01	8.43E-01	3.90E-01	3.74E-01	3.70E-01
3.01E-01	8.98E-01	3.92E-01	3.74E-01	3.70E-01
3.17E-01	9.47E-01	3.95E-01	3.73E-01	3.71E-01
3.34E-01	1.03E+00	4.00E-01	3.73E-01	3.71E-01
3.50E-01	1.13E+00	4.06E-01	3.75E-01	3.71E-01
3.67E-01	1.26E+00	4.09E-01	3.76E-01	3.71E-01
3.83E-01	1.36E+00	4.10E-01	3.77E-01	3.72E-01
4.00E-01	1.54E+00	4.14E-01	3.77E-01	3.72E-01
4.17E-01	1.59E+00	4.20E-01	3.78E-01	3.72E-01
4.34E-01	1.77E+00	4.21E-01	3.75E-01	3.72E-01
4.50E-01	1.90E+00	4.19E-01	3.77E-01	3.73E-01
4.67E-01	2.04E+00	4.23E-01	3.82E-01	3.73E-01
4.84E-01	2.30E+00	4.28E-01	3.83E-01	3.73E-01
5.01E-01	2.35E+00	4.39E-01	3.81E-01	3.73E-01
5.17E-01	2.60E+00	4.36E-01	3.81E-01	3.74E-01
5.33E-01	2.49E+00	4.35E-01	3.86E-01	3.74E-01
5.50E-01	2.72E+00	4.32E-01	3.87E-01	3.74E-01
5.67E-01	3.25E+00	4.49E-01	3.86E-01	3.75E-01
5.84E-01	3.38E+00	4.61E-01	3.85E-01	3.77E-01
6.00E-01	3.42E+00	4.50E-01	3.84E-01	3.77E-01
6.17E-01	3.55E+00	4.46E-01	3.88E-01	3.76E-01
6.34E-01	3.57E+00	4.60E-01	3.90E-01	3.77E-01
6.50E-01	3.61E+00	4.68E-01	3.92E-01	3.81E-01
6.67E-01	3.48E+00	4.61E-01	3.93E-01	3.83E-01
6.84E-01	3.35E+00	4.73E-01	3.94E-01	3.83E-01
7.00E-01	3.50E+00	4.83E-01	3.96E-01	3.81E-01
7.17E-01	3.97E+00	4.85E-01	3.96E-01	3.83E-01
7.34E-01	3.69E+00	4.74E-01	4.00E-01	3.90E-01
7.50E-01	4.11E+00	4.79E-01	4.01E-01	3.95E-01
7.67E-01	3.78E+00	4.81E-01	4.02E-01	3.94E-01
7.83E-01	3.85E+00	4.91E-01	4.02E-01	3.95E-01
8.00E-01	3.90E+00	4.81E-01	4.03E-01	4.01E-01
8.17E-01	3.87E+00	4.90E-01	4.02E-01	4.00E-01
8.33E-01	4.02E+00	4.98E-01	4.00E-01	4.01E-01
8.50E-01	4.20E+00	5.12E-01	4.04E-01	4.06E-01
8.67E-01	4.33E+00	5.04E-01	4.10E-01	4.05E-01
8.84E-01	4.08E+00	5.26E-01	4.13E-01	4.09E-01

9.00E-01	4.11E+00	5.24E-01	4.13E-01	4.13E-01
9.17E-01	4.35E+00	5.00E-01	4.19E-01	4.14E-01
9.33E-01	4.62E+00	4.97E-01	4.13E-01	4.11E-01
9.50E-01	4.80E+00	5.07E-01	4.18E-01	4.17E-01
9.67E-01	5.11E+00	5.36E-01	4.11E-01	4.22E-01
9.83E-01	5.33E+00	5.25E-01	4.13E-01	4.18E-01
1.00E+00	5.29E+00	5.16E-01	4.15E-01	4.19E-01
1.02E+00	5.71E+00	5.83E-01	4.22E-01	4.23E-01
1.03E+00	5.91E+00	5.98E-01	4.20E-01	4.19E-01
1.05E+00	5.84E+00	5.58E-01	4.32E-01	4.12E-01
1.07E+00	5.53E+00	5.44E-01	4.32E-01	4.12E-01
1.08E+00	6.06E+00	5.78E-01	4.32E-01	4.16E-01
1.10E+00	6.09E+00	6.35E-01	4.40E-01	4.23E-01
1.12E+00	6.17E+00	5.95E-01	4.43E-01	4.19E-01
1.13E+00	6.04E+00	5.88E-01	4.49E-01	4.16E-01
1.15E+00	6.31E+00	5.97E-01	4.58E-01	4.26E-01
1.17E+00	6.33E+00	6.20E-01	4.63E-01	4.29E-01
1.18E+00	6.27E+00	6.23E-01	4.50E-01	4.31E-01
1.20E+00	6.24E+00	6.30E-01	4.49E-01	4.30E-01
1.22E+00	6.70E+00	6.31E-01	4.69E-01	4.42E-01
1.23E+00	6.67E+00	6.29E-01	4.75E-01	4.51E-01
1.25E+00	6.32E+00	5.92E-01	4.63E-01	4.50E-01
1.27E+00	6.41E+00	6.21E-01	4.63E-01	4.58E-01
1.28E+00	6.79E+00	6.87E-01	4.64E-01	4.56E-01
1.30E+00	6.43E+00	6.68E-01	4.62E-01	4.60E-01
1.32E+00	6.63E+00	6.81E-01	4.74E-01	4.64E-01
1.33E+00	7.04E+00	6.99E-01	4.76E-01	4.59E-01

1.35E+00	6.97E+00	6.75E-01	4.84E-01	4.59E-01
1.37E+00	6.87E+00	6.50E-01	4.72E-01	4.64E-01
1.38E+00	6.86E+00	6.68E-01	4.69E-01	4.64E-01
1.40E+00	6.79E+00	7.07E-01	4.73E-01	4.64E-01
1.42E+00	6.99E+00	7.15E-01	4.81E-01	4.73E-01
1.43E+00	7.07E+00	7.07E-01	4.80E-01	4.64E-01
1.45E+00	7.13E+00	6.76E-01	4.77E-01	4.63E-01
1.47E+00	7.02E+00	7.02E-01	4.64E-01	4.77E-01
1.48E+00	7.19E+00	7.08E-01	4.63E-01	4.68E-01
1.50E+00	7.31E+00	7.52E-01	4.68E-01	4.64E-01
1.52E+00	7.00E+00	6.59E-01	4.77E-01	4.71E-01
1.53E+00	7.00E+00	6.33E-01	4.93E-01	4.76E-01
1.55E+00	7.31E+00	6.69E-01	4.75E-01	4.71E-01
1.57E+00	7.35E+00	7.40E-01	4.86E-01	4.63E-01
1.58E+00	7.39E+00	7.30E-01	4.90E-01	4.56E-01
1.60E+00	7.05E+00	7.13E-01	5.02E-01	4.61E-01
1.62E+00	7.66E+00	7.07E-01	5.08E-01	4.74E-01
1.63E+00	7.56E+00	7.75E-01	5.27E-01	4.79E-01
1.65E+00	7.68E+00	7.69E-01	5.10E-01	4.79E-01
1.67E+00	7.76E+00	7.73E-01	5.38E-01	4.74E-01
1.68E+00	7.43E+00	7.71E-01	5.42E-01	4.77E-01
1.70E+00	7.54E+00	7.49E-01	5.13E-01	5.02E-01
1.72E+00	7.44E+00	8.45E-01	5.19E-01	5.04E-01
1.73E+00	7.53E+00	8.07E-01	5.26E-01	4.89E-01
1.75E+00	7.93E+00	7.88E-01	5.21E-01	4.96E-01

1.77E+00	8.19E+00	7.97E-01	5.08E-01	5.20E-01
1.78E+00	8.20E+00	8.32E-01	4.99E-01	5.10E-01
1.80E+00	8.42E+00	7.69E-01	5.00E-01	5.13E-01
1.82E+00	7.96E+00	7.34E-01	5.04E-01	5.17E-01
1.83E+00	8.00E+00	8.34E-01	4.99E-01	5.05E-01
1.85E+00	8.16E+00	8.30E-01	5.21E-01	5.02E-01
1.87E+00	8.49E+00	7.93E-01	5.37E-01	4.98E-01
1.88E+00	8.34E+00	7.76E-01	5.33E-01	4.93E-01
1.90E+00	7.88E+00	7.66E-01	5.30E-01	4.97E-01
1.92E+00	7.75E+00	7.49E-01	5.25E-01	5.03E-01
1.93E+00	7.62E+00	8.98E-01	5.42E-01	4.98E-01
1.95E+00	8.19E+00	8.16E-01	5.43E-01	5.05E-01
1.97E+00	8.37E+00	8.64E-01	5.46E-01	5.19E-01
1.98E+00	7.69E+00	7.67E-01	5.63E-01	5.20E-01
2.00E+00	7.87E+00	8.14E-01	5.91E-01	5.18E-01
2.02E+00	7.93E+00	8.44E-01	5.61E-01	5.14E-01
2.03E+00	8.33E+00	8.74E-01	5.43E-01	5.06E-01
2.05E+00	8.12E+00	8.60E-01	5.78E-01	5.21E-01
2.07E+00	8.19E+00	8.14E-01	5.77E-01	5.32E-01
2.08E+00	8.15E+00	8.51E-01	5.74E-01	5.30E-01
2.10E+00	7.88E+00	7.79E-01	5.51E-01	5.21E-01
2.12E+00	8.33E+00	8.03E-01	5.80E-01	5.26E-01
2.13E+00	8.41E+00	8.52E-01	5.56E-01	5.36E-01
2.15E+00	8.42E+00	8.79E-01	5.43E-01	5.36E-01
2.17E+00	8.03E+00	8.37E-01	5.38E-01	5.36E-01

2.18E+00	8.07E+00	8.36E-01	5.61E-01	5.37E-01
2.20E+00	7.82E+00	7.78E-01	5.64E-01	5.36E-01
2.22E+00	7.50E+00	7.25E-01	5.70E-01	5.28E-01
2.23E+00	7.68E+00	7.13E-01	5.60E-01	5.36E-01
2.25E+00	7.95E+00	7.51E-01	5.19E-01	5.34E-01
2.27E+00	8.04E+00	7.52E-01	5.12E-01	5.25E-01
2.28E+00	7.70E+00	7.38E-01	5.37E-01	5.25E-01
2.30E+00	8.16E+00	7.37E-01	5.22E-01	5.20E-01
2.32E+00	8.24E+00	7.50E-01	5.32E-01	5.24E-01
2.33E+00	8.24E+00	7.74E-01	5.20E-01	5.22E-01
2.35E+00	8.44E+00	7.86E-01	5.00E-01	5.15E-01
2.37E+00	8.45E+00	7.50E-01	5.39E-01	5.12E-01
2.38E+00	8.34E+00	7.91E-01	5.60E-01	5.21E-01
2.40E+00	8.56E+00	8.29E-01	5.27E-01	5.11E-01
2.42E+00	8.40E+00	8.56E-01	5.22E-01	5.13E-01
2.43E+00	8.15E+00	8.80E-01	5.36E-01	5.04E-01
2.45E+00	8.42E+00	7.90E-01	5.48E-01	5.06E-01
2.47E+00	8.57E+00	8.37E-01	5.64E-01	5.16E-01
2.48E+00	8.19E+00	7.63E-01	5.57E-01	5.17E-01
2.50E+00	8.22E+00	7.68E-01	5.38E-01	5.18E-01
2.52E+00	8.42E+00	8.06E-01	5.55E-01	5.32E-01
2.53E+00	8.09E+00	7.56E-01	5.38E-01	5.45E-01
2.55E+00	7.73E+00	7.88E-01	5.34E-01	5.33E-01
2.57E+00	7.95E+00	7.66E-01	5.40E-01	5.36E-01
2.58E+00	8.74E+00	8.25E-01	5.40E-01	5.34E-01

2.60E+00	8.77E+00	7.61E-01	5.13E-01	5.42E-01
2.62E+00	8.29E+00	7.63E-01	5.35E-01	5.28E-01
2.63E+00	8.29E+00	8.55E-01	5.10E-01	5.28E-01
2.65E+00	8.71E+00	8.09E-01	5.20E-01	5.28E-01
2.67E+00	8.47E+00	8.05E-01	5.22E-01	5.33E-01
2.68E+00	8.66E+00	8.27E-01	5.18E-01	5.25E-01
2.70E+00	8.85E+00	8.43E-01	5.25E-01	5.20E-01
2.72E+00	8.67E+00	7.97E-01	5.23E-01	5.07E-01
2.73E+00	8.59E+00	7.83E-01	5.52E-01	5.02E-01
2.75E+00	8.32E+00	8.04E-01	5.27E-01	5.22E-01
2.77E+00	8.27E+00	7.43E-01	5.18E-01	5.20E-01
2.78E+00	8.36E+00	7.63E-01	5.37E-01	5.09E-01
2.80E+00	8.31E+00	7.60E-01	5.15E-01	5.23E-01
2.82E+00	8.23E+00	8.08E-01	5.40E-01	5.29E-01
2.83E+00	8.35E+00	7.91E-01	5.31E-01	5.25E-01
2.85E+00	8.09E+00	7.42E-01	5.17E-01	5.28E-01
2.87E+00	8.15E+00	7.22E-01	5.44E-01	5.11E-01
2.88E+00	8.22E+00	7.44E-01	5.57E-01	5.04E-01
2.90E+00	8.33E+00	7.60E-01	5.35E-01	5.09E-01
2.92E+00	8.49E+00	6.97E-01	5.33E-01	5.22E-01
2.93E+00	8.01E+00	7.07E-01	5.16E-01	5.27E-01
2.95E+00	8.53E+00	7.15E-01	5.05E-01	5.25E-01
2.97E+00	8.57E+00	7.46E-01	5.13E-01	5.08E-01
2.98E+00	8.48E+00	7.34E-01	5.18E-01	5.13E-01
3.00E+00	8.73E+00	7.36E-01	5.02E-01	5.15E-01

3.02E+00	8.57E+00	7.57E-01	5.15E-01	5.15E-01
3.03E+00	8.41E+00	7.87E-01	5.33E-01	5.04E-01
3.05E+00	8.55E+00	7.78E-01	5.63E-01	4.92E-01
3.07E+00	8.74E+00	7.91E-01	5.67E-01	4.89E-01
3.08E+00	8.41E+00	8.21E-01	5.55E-01	4.94E-01
3.10E+00	8.32E+00	7.90E-01	5.47E-01	5.04E-01
3.12E+00	8.84E+00	8.55E-01	5.48E-01	5.03E-01
3.13E+00	8.84E+00	7.87E-01	5.58E-01	5.13E-01
3.15E+00	8.20E+00	7.62E-01	5.31E-01	5.13E-01
3.17E+00	8.50E+00	7.71E-01	5.42E-01	5.12E-01
3.18E+00	8.49E+00	8.07E-01	5.34E-01	5.26E-01
3.20E+00	8.93E+00	8.25E-01	5.32E-01	5.45E-01
3.22E+00	8.66E+00	8.17E-01	5.35E-01	5.35E-01
3.23E+00	8.57E+00	7.72E-01	5.83E-01	5.22E-01
3.25E+00	8.74E+00	7.89E-01	5.61E-01	5.28E-01
3.27E+00	8.80E+00	8.27E-01	5.48E-01	5.14E-01
3.28E+00	9.18E+00	8.05E-01	5.41E-01	5.14E-01
3.30E+00	9.35E+00	8.03E-01	5.45E-01	5.27E-01
3.32E+00	9.27E+00	8.84E-01	5.38E-01	5.27E-01
3.33E+00	8.99E+00	8.37E-01	5.32E-01	5.27E-01
3.35E+00	9.01E+00	9.16E-01	5.60E-01	5.39E-01
3.37E+00	9.30E+00	9.41E-01	5.70E-01	5.25E-01
3.38E+00	8.80E+00	8.76E-01	6.00E-01	5.31E-01
3.40E+00	9.31E+00	8.17E-01	5.89E-01	5.25E-01
3.42E+00	8.80E+00	8.38E-01	5.62E-01	5.23E-01

3.43E+00	8.41E+00	8.50E-01	5.80E-01	5.43E-01
3.45E+00	8.67E+00	9.03E-01	5.72E-01	5.41E-01
3.47E+00	9.11E+00	8.72E-01	5.58E-01	5.46E-01
3.48E+00	8.71E+00	8.95E-01	5.63E-01	5.41E-01
3.50E+00	8.80E+00	8.30E-01	5.61E-01	5.62E-01
3.52E+00	8.75E+00	9.29E-01	5.94E-01	5.58E-01
3.53E+00	8.87E+00	8.80E-01	5.40E-01	5.37E-01
3.55E+00	8.88E+00	8.58E-01	5.92E-01	5.37E-01
3.57E+00	8.86E+00	8.32E-01	6.05E-01	5.45E-01
3.58E+00	9.17E+00	8.75E-01	5.63E-01	5.57E-01
3.60E+00	9.44E+00	9.32E-01	5.52E-01	5.48E-01
3.62E+00	9.40E+00	9.24E-01	5.98E-01	5.26E-01
3.63E+00	8.95E+00	9.94E-01	6.17E-01	5.51E-01
3.65E+00	8.96E+00	8.45E-01	5.74E-01	5.61E-01
3.67E+00	8.42E+00	8.87E-01	6.11E-01	5.57E-01
3.68E+00	8.47E+00	8.44E-01	5.96E-01	5.33E-01
3.70E+00	8.65E+00	8.75E-01	6.31E-01	5.47E-01
3.72E+00	8.33E+00	8.10E-01	5.75E-01	5.67E-01
3.73E+00	8.46E+00	7.87E-01	5.57E-01	5.40E-01
3.75E+00	8.62E+00	7.96E-01	5.52E-01	5.51E-01
3.77E+00	8.85E+00	7.75E-01	5.48E-01	5.57E-01
3.78E+00	8.87E+00	7.72E-01	5.49E-01	5.65E-01
3.80E+00	9.02E+00	8.22E-01	5.43E-01	5.73E-01
3.82E+00	9.10E+00	9.04E-01	5.30E-01	5.48E-01
3.83E+00	9.08E+00	8.23E-01	5.42E-01	5.30E-01

3.85E+00	8.70E+00	8.16E-01	5.76E-01	5.27E-01
3.87E+00	8.58E+00	8.06E-01	5.67E-01	5.39E-01
3.88E+00	8.96E+00	8.34E-01	5.69E-01	5.37E-01
3.90E+00	8.72E+00	8.41E-01	5.62E-01	5.32E-01
3.92E+00	8.67E+00	7.99E-01	5.69E-01	5.31E-01
3.93E+00	8.60E+00	7.68E-01	5.72E-01	5.46E-01
3.95E+00	8.79E+00	8.27E-01	5.79E-01	5.33E-01
3.97E+00	8.53E+00	8.26E-01	5.42E-01	5.25E-01
3.98E+00	8.88E+00	8.26E-01	5.40E-01	5.20E-01
4.00E+00	8.86E+00	8.16E-01	5.69E-01	5.34E-01
4.02E+00	8.64E+00	8.10E-01	5.45E-01	5.39E-01
4.03E+00	8.57E+00	7.79E-01	5.36E-01	5.27E-01
4.05E+00	8.45E+00	7.74E-01	5.65E-01	5.18E-01
4.07E+00	8.71E+00	7.79E-01	5.81E-01	5.18E-01
4.08E+00	8.49E+00	7.77E-01	5.70E-01	5.33E-01
4.10E+00	8.77E+00	7.63E-01	5.41E-01	5.27E-01
4.12E+00	9.08E+00	8.14E-01	5.30E-01	5.15E-01
4.13E+00	8.76E+00	8.26E-01	5.52E-01	5.17E-01
4.15E+00	9.00E+00	7.93E-01	5.42E-01	5.33E-01
4.17E+00	8.95E+00	8.45E-01	5.59E-01	5.33E-01
4.18E+00	8.78E+00	8.40E-01	5.57E-01	5.36E-01
4.20E+00	8.94E+00	8.84E-01	5.75E-01	5.31E-01
4.22E+00	8.77E+00	8.71E-01	5.76E-01	5.21E-01
4.23E+00	8.61E+00	7.91E-01	5.72E-01	5.32E-01
4.25E+00	8.52E+00	8.51E-01	5.62E-01	5.41E-01

4.27E+00	8.72E+00	8.18E-01	5.62E-01	5.40E-01
4.28E+00	8.67E+00	8.05E-01	5.76E-01	5.33E-01
4.30E+00	8.38E+00	7.82E-01	5.67E-01	5.43E-01
4.32E+00	8.03E+00	7.99E-01	5.43E-01	5.40E-01
4.33E+00	8.63E+00	8.06E-01	5.56E-01	5.48E-01
4.35E+00	8.74E+00	8.84E-01	5.62E-01	5.43E-01
4.37E+00	8.45E+00	8.04E-01	5.62E-01	5.42E-01
4.38E+00	8.51E+00	7.93E-01	5.42E-01	5.44E-01
4.40E+00	8.99E+00	7.75E-01	5.69E-01	5.34E-01
4.42E+00	9.16E+00	8.38E-01	5.42E-01	5.24E-01
4.43E+00	8.78E+00	8.15E-01	5.37E-01	5.33E-01
4.45E+00	8.98E+00	8.51E-01	5.61E-01	5.33E-01
4.47E+00	8.76E+00	8.49E-01	5.58E-01	5.30E-01
4.48E+00	8.84E+00	8.14E-01	5.30E-01	5.35E-01
4.50E+00	8.54E+00	8.25E-01	5.53E-01	5.31E-01
4.52E+00	8.39E+00	8.06E-01	5.48E-01	5.27E-01
4.53E+00	8.57E+00	8.22E-01	6.00E-01	5.28E-01
4.55E+00	8.69E+00	8.16E-01	5.76E-01	5.26E-01
4.57E+00	8.70E+00	8.36E-01	5.89E-01	5.23E-01
4.58E+00	8.43E+00	8.02E-01	5.42E-01	5.16E-01
4.60E+00	8.78E+00	7.90E-01	5.95E-01	5.22E-01
4.62E+00	9.10E+00	8.03E-01	5.51E-01	5.35E-01
4.63E+00	9.22E+00	8.25E-01	5.75E-01	5.48E-01
4.65E+00	8.66E+00	8.15E-01	5.53E-01	5.48E-01
4.67E+00	9.38E+00	8.59E-01	5.97E-01	5.42E-01

4.68E+00	9.19E+00	8.35E-01	5.64E-01	5.40E-01
4.70E+00	9.30E+00	8.43E-01	5.89E-01	5.20E-01
4.72E+00	9.47E+00	8.60E-01	5.47E-01	5.19E-01
4.73E+00	9.60E+00	8.72E-01	5.73E-01	5.29E-01
4.75E+00	9.48E+00	8.90E-01	5.58E-01	5.37E-01
4.77E+00	9.43E+00	9.36E-01	5.47E-01	5.32E-01
4.78E+00	9.12E+00	8.68E-01	5.67E-01	5.52E-01
4.80E+00	9.11E+00	8.41E-01	5.65E-01	5.37E-01
4.82E+00	8.97E+00	9.23E-01	5.59E-01	5.45E-01
4.83E+00	9.28E+00	8.78E-01	5.66E-01	5.50E-01
4.85E+00	9.15E+00	8.69E-01	6.08E-01	5.45E-01
4.87E+00	9.05E+00	8.04E-01	5.79E-01	5.39E-01
4.88E+00	9.18E+00	8.36E-01	5.82E-01	5.41E-01
4.90E+00	9.04E+00	8.59E-01	5.62E-01	5.47E-01
4.92E+00	9.25E+00	8.60E-01	5.65E-01	5.43E-01
4.93E+00	8.91E+00	8.12E-01	5.59E-01	5.63E-01
4.95E+00	8.58E+00	7.98E-01	5.66E-01	5.57E-01
4.97E+00	8.66E+00	8.45E-01	5.49E-01	5.49E-01
4.98E+00	8.90E+00	8.47E-01	5.33E-01	5.46E-01
5.00E+00	8.66E+00	8.37E-01	5.63E-01	5.48E-01
5.02E+00	8.93E+00	7.92E-01	5.47E-01	5.49E-01
5.03E+00	8.80E+00	7.71E-01	5.58E-01	5.43E-01
5.05E+00	8.80E+00	7.85E-01	5.42E-01	5.32E-01
5.07E+00	8.82E+00	8.20E-01	5.28E-01	5.14E-01
5.08E+00	8.91E+00	8.35E-01	5.53E-01	5.15E-01

5.10E+00	9.14E+00	8.50E-01	5.52E-01	5.44E-01
5.12E+00	9.06E+00	8.47E-01	5.55E-01	5.50E-01
5.13E+00	8.56E+00	8.31E-01	5.55E-01	5.32E-01
5.15E+00	9.01E+00	8.02E-01	5.51E-01	5.13E-01
5.17E+00	8.81E+00	8.83E-01	5.66E-01	5.30E-01
5.18E+00	8.67E+00	8.63E-01	5.53E-01	5.38E-01
5.20E+00	8.45E+00	8.01E-01	5.88E-01	5.29E-01
5.22E+00	8.27E+00	8.03E-01	5.73E-01	5.33E-01
5.23E+00	8.11E+00	7.98E-01	5.61E-01	5.26E-01
5.25E+00	8.26E+00	7.42E-01	5.67E-01	5.27E-01
5.27E+00	8.77E+00	7.85E-01	5.49E-01	5.29E-01
5.28E+00	8.60E+00	8.05E-01	5.58E-01	5.43E-01
5.30E+00	8.84E+00	8.31E-01	5.35E-01	5.38E-01
5.32E+00	9.04E+00	7.95E-01	5.59E-01	5.28E-01
5.33E+00	9.15E+00	8.19E-01	5.80E-01	5.25E-01
5.35E+00	8.67E+00	7.74E-01	5.77E-01	5.34E-01
5.37E+00	8.83E+00	7.97E-01	5.48E-01	5.30E-01
5.38E+00	8.59E+00	8.05E-01	5.45E-01	5.25E-01
5.40E+00	8.70E+00	7.79E-01	5.83E-01	5.36E-01
5.42E+00	8.57E+00	8.36E-01	5.71E-01	5.25E-01
5.43E+00	9.08E+00	7.84E-01	5.59E-01	5.34E-01
5.45E+00	8.86E+00	7.68E-01	5.59E-01	5.40E-01
5.47E+00	8.67E+00	7.74E-01	5.44E-01	5.35E-01
5.48E+00	9.18E+00	8.18E-01	5.40E-01	5.38E-01
5.50E+00	9.16E+00	7.72E-01	5.52E-01	5.56E-01

5.52E+00	8.55E+00	7.92E-01	5.76E-01	5.30E-01
5.53E+00	8.61E+00	8.13E-01	5.49E-01	5.18E-01
5.55E+00	8.69E+00	8.88E-01	5.43E-01	5.46E-01
5.57E+00	8.92E+00	7.97E-01	5.62E-01	5.45E-01
5.58E+00	8.83E+00	8.45E-01	5.82E-01	5.20E-01
5.60E+00	8.70E+00	8.00E-01	5.61E-01	5.25E-01
5.62E+00	9.31E+00	8.07E-01	5.60E-01	5.29E-01
5.63E+00	9.05E+00	7.83E-01	5.47E-01	5.29E-01
5.65E+00	8.95E+00	8.12E-01	5.48E-01	5.33E-01
5.67E+00	8.71E+00	8.04E-01	5.50E-01	5.37E-01
5.68E+00	8.63E+00	8.94E-01	5.64E-01	5.32E-01
5.70E+00	8.72E+00	7.60E-01	5.41E-01	5.39E-01
5.72E+00	9.06E+00	8.20E-01	5.46E-01	5.46E-01
5.73E+00	9.22E+00	8.32E-01	5.21E-01	5.34E-01
5.75E+00	9.02E+00	8.15E-01	5.62E-01	5.18E-01
5.77E+00	9.15E+00	8.14E-01	5.60E-01	5.30E-01
5.78E+00	8.91E+00	8.05E-01	5.48E-01	5.33E-01
5.80E+00	9.08E+00	7.89E-01	5.55E-01	5.27E-01
5.82E+00	9.10E+00	8.52E-01	5.44E-01	5.13E-01
5.83E+00	9.05E+00	8.81E-01	5.41E-01	5.23E-01
5.85E+00	8.94E+00	8.35E-01	5.60E-01	5.28E-01
5.87E+00	8.91E+00	8.40E-01	5.67E-01	5.30E-01
5.88E+00	9.05E+00	8.47E-01	5.84E-01	5.14E-01
5.90E+00	9.07E+00	7.99E-01	5.75E-01	5.21E-01
5.92E+00	9.37E+00	8.14E-01	5.74E-01	5.18E-01

5.93E+00	9.42E+00	8.71E-01	5.61E-01	5.26E-01
5.95E+00	9.22E+00	8.37E-01	5.55E-01	5.52E-01
5.97E+00	9.22E+00	8.37E-01	5.77E-01	5.38E-01
5.98E+00	9.27E+00	8.13E-01	5.86E-01	5.27E-01
6.00E+00	9.00E+00	8.00E-01	5.60E-01	5.44E-01
6.02E+00	9.34E+00	8.79E-01	5.55E-01	5.47E-01
6.03E+00	9.00E+00	8.63E-01	5.52E-01	5.27E-01
6.05E+00	8.63E+00	7.88E-01	5.51E-01	5.31E-01
6.07E+00	9.13E+00	8.16E-01	5.68E-01	5.43E-01
6.08E+00	8.92E+00	8.15E-01	5.53E-01	5.50E-01
6.10E+00	9.02E+00	8.13E-01	5.50E-01	5.42E-01
6.12E+00	8.82E+00	7.73E-01	5.52E-01	5.35E-01
6.13E+00	9.08E+00	8.11E-01	5.50E-01	5.26E-01
6.15E+00	8.63E+00	7.84E-01	5.34E-01	5.28E-01
6.17E+00	8.75E+00	8.38E-01	5.37E-01	5.33E-01
6.18E+00	8.49E+00	7.89E-01	5.51E-01	5.23E-01
6.20E+00	8.57E+00	8.07E-01	5.79E-01	5.22E-01
6.22E+00	8.78E+00	8.12E-01	5.44E-01	5.32E-01
6.23E+00	9.06E+00	8.09E-01	5.29E-01	5.19E-01
6.25E+00	8.65E+00	7.96E-01	5.47E-01	5.10E-01
6.27E+00	9.07E+00	8.19E-01	5.46E-01	5.21E-01
6.28E+00	8.75E+00	8.46E-01	5.68E-01	5.28E-01
6.30E+00	8.68E+00	8.19E-01	5.61E-01	5.17E-01
6.32E+00	9.22E+00	8.22E-01	5.76E-01	5.13E-01
6.33E+00	8.83E+00	7.95E-01	5.53E-01	5.15E-01

6.35E+00	9.03E+00	7.78E-01	5.71E-01	5.13E-01
6.37E+00	8.85E+00	8.05E-01	5.53E-01	5.18E-01
6.38E+00	8.94E+00	8.32E-01	5.37E-01	5.33E-01
6.40E+00	9.08E+00	8.52E-01	5.29E-01	5.46E-01
6.42E+00	8.73E+00	7.83E-01	5.56E-01	5.28E-01
6.43E+00	8.86E+00	8.26E-01	5.71E-01	5.29E-01
6.45E+00	8.70E+00	8.15E-01	5.61E-01	5.31E-01
6.47E+00	8.79E+00	8.04E-01	5.66E-01	5.28E-01
6.48E+00	8.51E+00	7.77E-01	5.77E-01	5.22E-01
6.50E+00	8.59E+00	7.75E-01	5.61E-01	5.16E-01
6.52E+00	8.51E+00	8.37E-01	5.62E-01	5.37E-01
6.53E+00	8.56E+00	8.35E-01	5.57E-01	5.29E-01
6.55E+00	8.45E+00	8.18E-01	5.63E-01	5.30E-01
6.57E+00	8.42E+00	7.84E-01	5.54E-01	5.43E-01
6.58E+00	9.19E+00	8.48E-01	5.37E-01	5.43E-01
6.60E+00	8.99E+00	8.44E-01	5.42E-01	5.24E-01
6.62E+00	8.65E+00	7.80E-01	5.81E-01	5.27E-01
6.63E+00	8.65E+00	7.93E-01	5.56E-01	5.29E-01
6.65E+00	8.63E+00	8.32E-01	5.49E-01	5.27E-01
6.67E+00	8.86E+00	8.07E-01	5.46E-01	5.22E-01
6.68E+00	8.69E+00	8.40E-01	5.51E-01	5.14E-01
6.70E+00	8.72E+00	8.10E-01	5.38E-01	5.23E-01
6.72E+00	8.36E+00	7.77E-01	5.52E-01	5.31E-01
6.73E+00	8.54E+00	7.56E-01	5.47E-01	5.29E-01
6.75E+00	8.48E+00	8.22E-01	5.64E-01	5.17E-01

6.77E+00	8.76E+00	7.86E-01	5.48E-01	5.24E-01
6.78E+00	8.82E+00	8.01E-01	5.71E-01	5.36E-01
6.80E+00	8.47E+00	7.90E-01	5.29E-01	5.45E-01
6.82E+00	8.94E+00	8.38E-01	5.48E-01	5.48E-01
6.83E+00	8.94E+00	8.10E-01	5.48E-01	5.25E-01
6.85E+00	8.93E+00	7.98E-01	5.62E-01	5.21E-01
6.87E+00	8.63E+00	8.35E-01	5.58E-01	5.31E-01
6.88E+00	8.37E+00	7.96E-01	5.37E-01	5.30E-01
6.90E+00	8.37E+00	7.44E-01	5.61E-01	5.14E-01
6.92E+00	8.42E+00	7.77E-01	5.45E-01	5.22E-01
6.93E+00	8.81E+00	7.98E-01	5.25E-01	5.35E-01
6.95E+00	8.58E+00	7.96E-01	5.36E-01	5.16E-01
6.97E+00	8.63E+00	7.66E-01	5.34E-01	5.09E-01
6.98E+00	8.47E+00	7.93E-01	5.41E-01	5.27E-01
7.00E+00	8.89E+00	7.72E-01	5.31E-01	5.40E-01
7.02E+00	8.55E+00	8.28E-01	5.31E-01	5.25E-01
7.03E+00	8.98E+00	7.97E-01	5.30E-01	5.05E-01
7.05E+00	8.89E+00	7.89E-01	5.55E-01	5.09E-01
7.07E+00	9.08E+00	8.23E-01	5.50E-01	5.16E-01
7.08E+00	9.02E+00	8.08E-01	5.36E-01	4.95E-01
7.10E+00	8.98E+00	8.32E-01	5.43E-01	5.05E-01
7.12E+00	9.05E+00	8.14E-01	5.32E-01	5.08E-01
7.13E+00	9.07E+00	7.76E-01	5.45E-01	5.16E-01
7.15E+00	9.08E+00	8.15E-01	5.57E-01	5.15E-01
7.17E+00	8.78E+00	8.01E-01	5.42E-01	5.18E-01

7.18E+00	8.99E+00	8.07E-01	5.35E-01	5.21E-01
7.20E+00	9.25E+00	8.22E-01	5.39E-01	5.13E-01
7.22E+00	9.12E+00	8.21E-01	5.47E-01	5.05E-01
7.23E+00	9.23E+00	8.30E-01	5.53E-01	5.07E-01
7.25E+00	8.82E+00	8.14E-01	5.37E-01	5.12E-01
7.27E+00	9.08E+00	8.04E-01	5.45E-01	5.12E-01
7.28E+00	8.74E+00	7.76E-01	5.43E-01	5.11E-01
7.30E+00	8.76E+00	7.45E-01	5.50E-01	5.25E-01
7.32E+00	9.19E+00	8.13E-01	5.64E-01	5.23E-01
7.33E+00	8.83E+00	8.37E-01	5.31E-01	5.16E-01
7.35E+00	9.05E+00	8.57E-01	5.46E-01	5.21E-01
7.37E+00	8.94E+00	8.00E-01	5.98E-01	5.23E-01
7.38E+00	9.01E+00	7.97E-01	5.58E-01	5.26E-01
7.40E+00	9.01E+00	8.13E-01	5.55E-01	5.28E-01
7.42E+00	9.07E+00	8.04E-01	5.56E-01	5.28E-01
7.43E+00	8.89E+00	8.16E-01	5.58E-01	5.22E-01
7.45E+00	9.24E+00	8.27E-01	5.54E-01	5.35E-01
7.47E+00	9.21E+00	8.30E-01	5.47E-01	5.47E-01
7.48E+00	9.03E+00	8.37E-01	5.46E-01	5.44E-01
7.50E+00	9.18E+00	8.27E-01	5.56E-01	5.31E-01
7.52E+00	9.31E+00	8.23E-01	5.64E-01	5.22E-01
7.53E+00	9.13E+00	8.47E-01	5.65E-01	5.29E-01
7.55E+00	8.75E+00	8.15E-01	5.46E-01	5.29E-01
7.57E+00	9.04E+00	7.90E-01	5.74E-01	5.21E-01
7.58E+00	8.86E+00	8.32E-01	5.68E-01	5.21E-01

7.60E+00	9.15E+00	8.04E-01	5.43E-01	5.37E-01
7.62E+00	8.97E+00	7.99E-01	5.50E-01	5.31E-01
7.63E+00	8.35E+00	7.81E-01	5.72E-01	5.44E-01
7.65E+00	8.73E+00	8.14E-01	5.59E-01	5.47E-01
7.67E+00	8.98E+00	8.98E-01	5.60E-01	5.37E-01
7.68E+00	9.03E+00	8.05E-01	5.48E-01	5.45E-01
7.70E+00	9.07E+00	7.87E-01	5.44E-01	5.41E-01
7.72E+00	8.85E+00	8.30E-01	5.53E-01	5.34E-01
7.73E+00	8.85E+00	9.02E-01	5.54E-01	5.45E-01
7.75E+00	9.13E+00	8.32E-01	5.63E-01	5.45E-01
7.77E+00	9.04E+00	8.13E-01	5.66E-01	5.35E-01
7.78E+00	8.99E+00	7.83E-01	5.51E-01	5.39E-01
7.80E+00	9.24E+00	8.18E-01	5.54E-01	5.31E-01
7.82E+00	8.89E+00	7.73E-01	5.48E-01	5.29E-01
7.83E+00	8.93E+00	7.85E-01	5.63E-01	5.33E-01
7.85E+00	8.69E+00	8.91E-01	5.44E-01	5.45E-01
7.87E+00	9.10E+00	9.08E-01	5.49E-01	5.23E-01
7.88E+00	9.18E+00	9.04E-01	5.73E-01	5.19E-01
7.90E+00	8.69E+00	8.01E-01	5.66E-01	5.12E-01
7.92E+00	8.27E+00	7.58E-01	5.72E-01	5.24E-01
7.93E+00	8.56E+00	7.37E-01	5.66E-01	5.28E-01
7.95E+00	8.73E+00	7.47E-01	5.45E-01	5.17E-01
7.97E+00	9.06E+00	7.60E-01	5.23E-01	5.34E-01
7.98E+00	8.67E+00	7.42E-01	5.28E-01	5.28E-01
8.00E+00	8.75E+00	7.60E-01	5.21E-01	5.32E-01

8.02E+00	9.24E+00	8.10E-01	5.22E-01	5.32E-01
8.03E+00	9.01E+00	7.91E-01	5.20E-01	5.33E-01
8.05E+00	8.97E+00	8.00E-01	5.42E-01	5.26E-01
8.07E+00	8.80E+00	8.80E-01	5.92E-01	5.22E-01
8.08E+00	8.55E+00	8.13E-01	5.70E-01	5.07E-01
8.10E+00	8.59E+00	7.96E-01	5.87E-01	4.99E-01
8.12E+00	8.89E+00	7.82E-01	5.81E-01	5.01E-01
8.13E+00	8.46E+00	7.67E-01	5.61E-01	5.19E-01
8.15E+00	8.50E+00	7.56E-01	5.43E-01	5.28E-01
8.17E+00	8.80E+00	7.79E-01	5.45E-01	5.42E-01
8.18E+00	8.80E+00	7.67E-01	5.26E-01	5.38E-01
8.20E+00	8.67E+00	8.16E-01	5.40E-01	5.51E-01
8.22E+00	8.98E+00	8.04E-01	5.43E-01	5.43E-01
8.23E+00	8.99E+00	8.21E-01	5.40E-01	5.22E-01
8.25E+00	8.74E+00	7.75E-01	5.47E-01	5.18E-01
8.27E+00	8.75E+00	7.43E-01	5.35E-01	5.21E-01
8.28E+00	9.29E+00	7.83E-01	5.24E-01	5.16E-01
8.30E+00	9.23E+00	8.39E-01	5.17E-01	5.16E-01
8.32E+00	9.29E+00	8.12E-01	5.14E-01	5.21E-01
8.33E+00	9.01E+00	8.37E-01	5.42E-01	5.22E-01
8.35E+00	8.86E+00	8.42E-01	5.24E-01	5.20E-01
8.37E+00	9.01E+00	8.71E-01	5.39E-01	5.23E-01
8.38E+00	8.74E+00	8.09E-01	5.47E-01	5.08E-01
8.40E+00	8.74E+00	8.42E-01	5.65E-01	4.97E-01
8.42E+00	9.14E+00	8.49E-01	5.41E-01	5.03E-01

8.43E+00	8.94E+00	8.24E-01	5.48E-01	5.01E-01
8.45E+00	8.98E+00	8.05E-01	5.46E-01	5.08E-01
8.47E+00	8.96E+00	8.09E-01	5.84E-01	5.21E-01
8.48E+00	8.67E+00	7.92E-01	5.84E-01	5.38E-01
8.50E+00	9.34E+00	8.63E-01	5.45E-01	5.36E-01
8.52E+00	9.19E+00	8.47E-01	5.38E-01	5.15E-01
8.53E+00	9.17E+00	8.72E-01	5.50E-01	5.24E-01
8.55E+00	9.37E+00	8.49E-01	5.63E-01	5.33E-01
8.57E+00	8.88E+00	8.25E-01	5.76E-01	5.31E-01
8.58E+00	8.89E+00	8.47E-01	5.71E-01	5.30E-01
8.60E+00	9.49E+00	8.94E-01	5.80E-01	5.21E-01
8.62E+00	9.54E+00	8.58E-01	5.63E-01	5.20E-01
8.63E+00	9.34E+00	8.44E-01	5.67E-01	5.42E-01
8.65E+00	9.19E+00	8.45E-01	5.76E-01	5.50E-01
8.67E+00	9.62E+00	8.25E-01	5.98E-01	5.39E-01
8.68E+00	8.85E+00	8.03E-01	5.79E-01	5.41E-01
8.70E+00	8.76E+00	8.06E-01	5.57E-01	5.42E-01
8.72E+00	8.65E+00	8.31E-01	5.57E-01	5.37E-01
8.73E+00	8.91E+00	8.34E-01	5.82E-01	5.45E-01
8.75E+00	8.29E+00	8.02E-01	5.65E-01	5.34E-01
8.77E+00	8.65E+00	7.99E-01	5.69E-01	5.38E-01
8.78E+00	8.51E+00	7.91E-01	5.60E-01	5.43E-01
8.80E+00	8.55E+00	7.92E-01	5.68E-01	5.41E-01
8.82E+00	8.46E+00	7.89E-01	5.46E-01	5.42E-01
8.83E+00	8.51E+00	7.74E-01	5.40E-01	5.51E-01

8.85E+00	8.75E+00	7.97E-01	5.55E-01	5.55E-01
8.87E+00	8.67E+00	7.55E-01	5.43E-01	5.48E-01
8.88E+00	8.54E+00	7.61E-01	5.54E-01	5.32E-01
8.90E+00	9.23E+00	8.01E-01	5.31E-01	5.25E-01
8.92E+00	8.98E+00	8.29E-01	5.40E-01	5.26E-01
8.93E+00	9.15E+00	8.06E-01	5.25E-01	5.17E-01
8.95E+00	9.31E+00	8.17E-01	5.42E-01	5.16E-01
8.97E+00	9.46E+00	8.18E-01	5.55E-01	5.14E-01
8.98E+00	9.00E+00	8.31E-01	5.41E-01	5.16E-01
9.00E+00	8.78E+00	8.12E-01	5.61E-01	5.23E-01
9.02E+00	8.94E+00	8.05E-01	5.54E-01	5.20E-01
9.03E+00	8.90E+00	8.36E-01	5.84E-01	5.20E-01
9.05E+00	9.02E+00	8.18E-01	5.64E-01	5.14E-01
9.07E+00	8.95E+00	8.08E-01	5.83E-01	5.18E-01
9.08E+00	8.84E+00	7.81E-01	5.59E-01	5.30E-01
9.10E+00	8.80E+00	8.09E-01	5.36E-01	5.27E-01
9.12E+00	8.64E+00	8.43E-01	5.48E-01	5.35E-01
9.13E+00	8.53E+00	8.12E-01	5.63E-01	5.39E-01
9.15E+00	8.63E+00	7.86E-01	5.97E-01	5.43E-01
9.17E+00	9.05E+00	7.66E-01	5.72E-01	5.36E-01
9.18E+00	9.05E+00	7.83E-01	5.61E-01	5.21E-01
9.20E+00	8.68E+00	8.00E-01	5.41E-01	5.19E-01
9.22E+00	9.13E+00	8.16E-01	5.39E-01	5.29E-01
9.23E+00	9.31E+00	7.77E-01	5.52E-01	5.57E-01
9.25E+00	9.31E+00	7.97E-01	5.49E-01	5.34E-01

9.27E+00	9.00E+00	8.28E-01	5.53E-01	5.17E-01
9.28E+00	9.08E+00	8.82E-01	5.41E-01	5.16E-01
9.30E+00	9.00E+00	7.91E-01	5.40E-01	5.09E-01
9.32E+00	9.03E+00	8.12E-01	5.71E-01	5.21E-01
9.33E+00	9.36E+00	8.64E-01	5.56E-01	5.27E-01
9.35E+00	8.97E+00	8.70E-01	5.39E-01	5.20E-01
9.37E+00	9.02E+00	8.41E-01	5.61E-01	5.26E-01
9.38E+00	9.21E+00	8.49E-01	5.54E-01	5.30E-01
9.40E+00	9.05E+00	7.95E-01	5.73E-01	5.37E-01
9.42E+00	9.15E+00	8.04E-01	5.81E-01	5.33E-01
9.43E+00	9.15E+00	8.33E-01	5.51E-01	5.12E-01
9.45E+00	9.02E+00	8.45E-01	5.67E-01	5.31E-01
9.47E+00	9.37E+00	8.71E-01	5.47E-01	5.38E-01
9.48E+00	9.02E+00	8.19E-01	5.60E-01	5.27E-01
9.50E+00	9.47E+00	8.17E-01	5.77E-01	5.37E-01
9.52E+00	9.39E+00	8.48E-01	5.57E-01	5.44E-01
9.53E+00	9.13E+00	8.33E-01	5.55E-01	5.28E-01
9.55E+00	9.13E+00	8.72E-01	5.51E-01	5.32E-01
9.57E+00	9.20E+00	8.38E-01	5.77E-01	5.33E-01
9.58E+00	9.09E+00	8.49E-01	5.58E-01	5.40E-01
9.60E+00	8.99E+00	8.33E-01	5.60E-01	5.41E-01
9.62E+00	8.99E+00	7.95E-01	5.53E-01	5.30E-01
9.63E+00	9.21E+00	7.98E-01	5.38E-01	5.35E-01
9.65E+00	9.02E+00	8.34E-01	5.59E-01	5.52E-01
9.67E+00	8.91E+00	8.15E-01	5.44E-01	5.32E-01

9.68E+00	8.83E+00	8.00E-01	5.48E-01	5.35E-01
9.70E+00	8.63E+00	7.55E-01	5.40E-01	5.29E-01
9.72E+00	8.99E+00	7.95E-01	5.39E-01	5.22E-01
9.73E+00	8.52E+00	7.77E-01	5.32E-01	5.16E-01
9.75E+00	8.64E+00	7.98E-01	5.51E-01	5.24E-01
9.77E+00	8.96E+00	8.73E-01	5.36E-01	5.26E-01
9.78E+00	8.82E+00	8.22E-01	5.56E-01	5.17E-01
9.80E+00	8.78E+00	7.90E-01	5.30E-01	5.22E-01
9.82E+00	8.83E+00	8.10E-01	5.59E-01	5.15E-01
9.83E+00	8.91E+00	8.34E-01	5.71E-01	5.23E-01
9.85E+00	8.76E+00	8.50E-01	5.47E-01	5.17E-01
9.87E+00	8.67E+00	7.68E-01	5.76E-01	5.14E-01
9.88E+00	8.65E+00	7.90E-01	5.71E-01	5.28E-01
9.90E+00	9.07E+00	8.35E-01	5.39E-01	5.28E-01
9.92E+00	9.18E+00	9.23E-01	5.42E-01	5.22E-01
9.93E+00	9.11E+00	8.87E-01	5.51E-01	5.23E-01
9.95E+00	8.79E+00	8.39E-01	6.12E-01	5.43E-01
9.97E+00	8.94E+00	8.34E-01	5.82E-01	5.33E-01
9.98E+00	8.76E+00	8.71E-01	6.07E-01	5.34E-01
1.00E+01	8.71E+00	8.14E-01	5.69E-01	5.25E-01
1.00E+01	8.98E+00	8.56E-01	5.71E-01	5.48E-01
1.00E+01	8.99E+00	7.94E-01	5.49E-01	5.48E-01
1.01E+01	9.15E+00	7.96E-01	5.74E-01	5.21E-01
1.01E+01	8.85E+00	8.16E-01	5.44E-01	5.35E-01
1.01E+01	9.12E+00	8.05E-01	5.23E-01	5.37E-01

1.01E+01	9.19E+00	8.07E-01	5.32E-01	5.48E-01
1.01E+01	9.42E+00	7.93E-01	5.50E-01	5.30E-01
1.01E+01	9.18E+00	7.69E-01	5.63E-01	5.27E-01
1.02E+01	8.94E+00	8.20E-01	5.36E-01	5.22E-01
1.02E+01	8.96E+00	8.52E-01	5.40E-01	5.20E-01
1.02E+01	9.12E+00	7.94E-01	5.44E-01	5.12E-01
1.02E+01	8.69E+00	7.68E-01	5.76E-01	5.20E-01
1.02E+01	9.15E+00	8.44E-01	5.77E-01	5.30E-01
1.02E+01	8.98E+00	8.18E-01	5.68E-01	5.23E-01
1.03E+01	8.73E+00	8.03E-01	5.78E-01	5.16E-01
1.03E+01	8.64E+00	8.12E-01	5.59E-01	5.26E-01
1.03E+01	8.75E+00	8.66E-01	5.61E-01	5.28E-01
1.03E+01	9.57E+00	8.41E-01	5.53E-01	5.44E-01
1.03E+01	9.36E+00	8.52E-01	5.54E-01	5.31E-01
1.03E+01	8.92E+00	8.09E-01	5.57E-01	5.30E-01
1.04E+01	8.75E+00	7.94E-01	5.98E-01	5.46E-01
1.04E+01	8.51E+00	8.17E-01	5.83E-01	5.32E-01
1.04E+01	8.90E+00	8.13E-01	5.57E-01	5.20E-01
1.04E+01	8.72E+00	8.04E-01	5.88E-01	5.31E-01
1.04E+01	8.88E+00	7.72E-01	5.62E-01	5.27E-01
1.04E+01	8.89E+00	8.30E-01	5.55E-01	5.40E-01
1.05E+01	8.60E+00	7.94E-01	5.60E-01	5.34E-01
1.05E+01	8.88E+00	7.92E-01	5.60E-01	5.39E-01
1.05E+01	8.87E+00	8.08E-01	5.47E-01	5.46E-01
1.05E+01	9.05E+00	8.22E-01	5.47E-01	5.33E-01

1.05E+01	9.06E+00	7.89E-01	5.54E-01	5.30E-01
1.05E+01	9.46E+00	8.04E-01	5.61E-01	5.24E-01
1.06E+01	8.70E+00	8.17E-01	5.68E-01	5.37E-01
1.06E+01	9.15E+00	7.74E-01	5.43E-01	5.33E-01
1.06E+01	9.26E+00	8.69E-01	5.50E-01	5.11E-01
1.06E+01	8.96E+00	8.51E-01	5.47E-01	5.14E-01
1.06E+01	9.16E+00	8.16E-01	5.55E-01	5.31E-01
1.06E+01	9.03E+00	8.82E-01	5.51E-01	5.38E-01
1.07E+01	9.38E+00	8.76E-01	5.37E-01	5.25E-01
1.07E+01	9.00E+00	8.61E-01	5.61E-01	5.30E-01
1.07E+01	9.06E+00	8.06E-01	5.76E-01	5.20E-01
1.07E+01	9.02E+00	7.95E-01	5.72E-01	5.31E-01
1.07E+01	9.40E+00	8.11E-01	5.64E-01	5.22E-01
1.07E+01	9.39E+00	8.65E-01	5.36E-01	5.13E-01
1.08E+01	9.03E+00	8.67E-01	5.47E-01	5.35E-01
1.08E+01	9.17E+00	8.71E-01	5.62E-01	5.38E-01
1.08E+01	9.55E+00	8.31E-01	5.66E-01	5.43E-01
1.08E+01	9.17E+00	8.97E-01	5.76E-01	5.23E-01
1.08E+01	9.47E+00	9.05E-01	5.68E-01	5.16E-01
1.08E+01	9.43E+00	8.63E-01	6.01E-01	5.29E-01
1.09E+01	9.15E+00	8.19E-01	5.55E-01	5.29E-01
1.09E+01	8.95E+00	9.03E-01	5.60E-01	5.42E-01
1.09E+01	8.83E+00	9.13E-01	5.66E-01	5.51E-01
1.09E+01	9.07E+00	7.93E-01	6.02E-01	5.32E-01
1.09E+01	8.93E+00	8.44E-01	5.89E-01	5.45E-01

1.09E+01	8.90E+00	7.98E-01	5.58E-01	5.33E-01
1.10E+01	8.95E+00	9.01E-01	5.61E-01	5.48E-01
1.10E+01	9.22E+00	8.58E-01	5.52E-01	5.37E-01
1.10E+01	9.08E+00	7.92E-01	5.69E-01	5.40E-01
1.10E+01	9.04E+00	8.36E-01	5.48E-01	5.62E-01
1.10E+01	9.18E+00	8.29E-01	5.66E-01	5.42E-01
1.10E+01	9.11E+00	8.72E-01	5.78E-01	5.32E-01
1.11E+01	9.13E+00	8.55E-01	5.55E-01	5.42E-01
1.11E+01	9.21E+00	8.42E-01	5.82E-01	5.41E-01
1.11E+01	9.09E+00	8.47E-01	5.69E-01	5.31E-01
1.11E+01	8.78E+00	7.79E-01	5.59E-01	5.27E-01
1.11E+01	8.82E+00	7.71E-01	5.61E-01	5.17E-01
1.11E+01	8.76E+00	8.30E-01	5.46E-01	5.37E-01
1.12E+01	9.06E+00	8.46E-01	5.38E-01	5.36E-01
1.12E+01	9.18E+00	8.47E-01	5.57E-01	5.29E-01
1.12E+01	8.93E+00	8.26E-01	5.50E-01	5.33E-01
1.12E+01	9.14E+00	8.51E-01	5.58E-01	5.34E-01
1.12E+01	9.33E+00	8.09E-01	5.66E-01	5.22E-01
1.12E+01	9.54E+00	8.03E-01	5.56E-01	5.18E-01
1.13E+01	9.27E+00	8.24E-01	5.54E-01	5.38E-01
1.13E+01	9.00E+00	8.17E-01	5.40E-01	5.23E-01
1.13E+01	9.42E+00	7.69E-01	5.85E-01	5.21E-01
1.13E+01	8.99E+00	7.50E-01	5.42E-01	5.36E-01
1.13E+01	8.85E+00	7.91E-01	5.51E-01	5.37E-01
1.13E+01	9.02E+00	7.89E-01	5.34E-01	5.26E-01

1.14E+01	9.42E+00	8.10E-01	5.30E-01	5.22E-01
1.14E+01	8.92E+00	8.14E-01	5.49E-01	5.33E-01
1.14E+01	8.75E+00	7.62E-01	5.60E-01	5.32E-01
1.14E+01	9.05E+00	8.14E-01	5.49E-01	5.34E-01
1.14E+01	8.92E+00	8.02E-01	5.39E-01	5.14E-01
1.14E+01	8.83E+00	7.76E-01	5.31E-01	5.21E-01
1.15E+01	9.00E+00	7.87E-01	5.23E-01	5.16E-01
1.15E+01	8.93E+00	7.86E-01	5.27E-01	5.21E-01
1.15E+01	9.22E+00	7.80E-01	5.19E-01	5.29E-01
1.15E+01	9.04E+00	7.63E-01	5.36E-01	5.23E-01
1.15E+01	8.92E+00	7.93E-01	5.30E-01	5.20E-01
1.15E+01	8.57E+00	8.05E-01	5.37E-01	5.20E-01
1.16E+01	9.00E+00	8.01E-01	5.29E-01	5.12E-01
1.16E+01	9.20E+00	8.12E-01	5.38E-01	4.96E-01
1.16E+01	9.00E+00	8.37E-01	5.39E-01	5.02E-01
1.16E+01	8.77E+00	7.94E-01	5.36E-01	5.09E-01
1.16E+01	8.82E+00	7.89E-01	5.46E-01	5.09E-01
1.16E+01	8.62E+00	7.95E-01	5.37E-01	5.16E-01
1.17E+01	9.14E+00	7.72E-01	5.37E-01	5.19E-01
1.17E+01	9.26E+00	7.72E-01	5.34E-01	5.18E-01
1.17E+01	8.51E+00	7.68E-01	5.35E-01	5.11E-01
1.17E+01	8.68E+00	7.87E-01	5.24E-01	5.17E-01
1.17E+01	8.92E+00	8.25E-01	5.24E-01	5.18E-01
1.17E+01	9.18E+00	7.75E-01	5.35E-01	5.12E-01
1.18E+01	8.94E+00	7.74E-01	5.56E-01	5.14E-01

1.18E+01	8.83E+00	8.09E-01	5.53E-01	5.08E-01
1.18E+01	8.89E+00	8.49E-01	5.39E-01	5.01E-01
1.18E+01	8.79E+00	8.24E-01	5.51E-01	5.03E-01
1.18E+01	9.47E+00	7.93E-01	5.55E-01	5.05E-01
1.18E+01	9.13E+00	8.05E-01	5.44E-01	5.13E-01
1.19E+01	9.24E+00	8.26E-01	5.38E-01	5.26E-01
1.19E+01	8.76E+00	8.01E-01	5.40E-01	5.17E-01
1.19E+01	9.06E+00	7.84E-01	5.50E-01	5.22E-01
1.19E+01	8.70E+00	7.78E-01	5.34E-01	5.25E-01
1.19E+01	8.38E+00	7.25E-01	5.42E-01	5.21E-01
1.19E+01	8.33E+00	7.36E-01	5.36E-01	5.17E-01
1.20E+01	8.49E+00	7.57E-01	5.17E-01	5.13E-01
1.20E+01	8.77E+00	7.53E-01	5.10E-01	5.18E-01
1.20E+01	9.12E+00	7.90E-01	5.34E-01	5.13E-01
1.20E+01	9.05E+00	8.12E-01	5.28E-01	5.17E-01
1.20E+01	9.54E+00	7.95E-01	5.30E-01	5.19E-01
1.20E+01	9.33E+00	8.20E-01	5.23E-01	5.15E-01
1.21E+01	9.22E+00	8.09E-01	5.37E-01	5.05E-01
1.21E+01	9.07E+00	8.24E-01	5.49E-01	5.07E-01
1.21E+01	9.39E+00	8.54E-01	5.34E-01	5.09E-01
1.21E+01	9.02E+00	8.19E-01	5.60E-01	5.08E-01
1.21E+01	9.17E+00	8.22E-01	5.72E-01	5.15E-01
1.21E+01	9.05E+00	8.50E-01	5.82E-01	5.12E-01
1.22E+01	9.06E+00	8.42E-01	5.76E-01	5.12E-01
1.22E+01	8.91E+00	8.06E-01	5.65E-01	5.17E-01

1.22E+01	9.11E+00	7.85E-01	5.68E-01	5.41E-01
1.22E+01	9.24E+00	8.39E-01	5.41E-01	5.32E-01
1.22E+01	9.21E+00	8.28E-01	5.32E-01	5.33E-01
1.22E+01	9.11E+00	8.07E-01	5.62E-01	5.29E-01
1.23E+01	9.07E+00	8.12E-01	5.56E-01	5.35E-01
1.23E+01	9.02E+00	8.17E-01	5.47E-01	5.37E-01
1.23E+01	9.01E+00	7.95E-01	5.50E-01	5.23E-01
1.23E+01	9.02E+00	7.87E-01	5.62E-01	5.16E-01
1.23E+01	9.12E+00	7.93E-01	5.48E-01	5.20E-01
1.23E+01	8.82E+00	7.86E-01	5.35E-01	5.28E-01
1.24E+01	9.05E+00	8.26E-01	5.35E-01	5.20E-01
1.24E+01	9.01E+00	7.98E-01	5.27E-01	5.23E-01
1.24E+01	8.87E+00	7.55E-01	5.42E-01	5.39E-01
1.24E+01	8.54E+00	7.52E-01	5.59E-01	5.28E-01
1.24E+01	8.84E+00	7.71E-01	5.39E-01	5.17E-01
1.24E+01	8.89E+00	8.23E-01	5.35E-01	5.17E-01
1.25E+01	8.77E+00	8.30E-01	5.31E-01	5.08E-01
1.25E+01	8.63E+00	7.69E-01	5.47E-01	5.05E-01
1.25E+01	8.95E+00	8.01E-01	5.56E-01	5.23E-01
1.25E+01	9.22E+00	8.33E-01	5.79E-01	5.29E-01
1.25E+01	8.88E+00	7.93E-01	5.59E-01	5.17E-01
1.25E+01	8.66E+00	8.01E-01	5.58E-01	5.16E-01
1.26E+01	8.74E+00	8.31E-01	5.43E-01	5.23E-01
1.26E+01	8.77E+00	7.78E-01	5.54E-01	5.13E-01
1.26E+01	8.48E+00	7.86E-01	5.29E-01	5.29E-01

1.26E+01	8.84E+00	7.80E-01	5.40E-01	5.28E-01
1.26E+01	8.90E+00	8.30E-01	5.35E-01	5.35E-01
1.26E+01	8.78E+00	7.83E-01	5.44E-01	5.22E-01
1.27E+01	8.44E+00	8.03E-01	5.45E-01	5.14E-01
1.27E+01	8.62E+00	7.74E-01	5.46E-01	5.19E-01
1.27E+01	8.71E+00	7.68E-01	5.35E-01	5.27E-01
1.27E+01	8.76E+00	7.95E-01	5.29E-01	5.16E-01
1.27E+01	8.99E+00	7.89E-01	5.35E-01	5.09E-01
1.27E+01	8.88E+00	7.95E-01	5.40E-01	5.17E-01
1.28E+01	8.39E+00	8.16E-01	5.69E-01	5.12E-01
1.28E+01	8.79E+00	7.95E-01	5.55E-01	5.03E-01
1.28E+01	9.36E+00	8.24E-01	5.46E-01	4.99E-01
1.28E+01	9.57E+00	8.43E-01	5.32E-01	5.07E-01
1.28E+01	9.61E+00	7.96E-01	5.48E-01	5.20E-01
1.28E+01	9.33E+00	8.02E-01	5.49E-01	5.18E-01
1.29E+01	9.27E+00	8.85E-01	5.49E-01	5.17E-01
1.29E+01	9.39E+00	8.21E-01	5.61E-01	5.15E-01
1.29E+01	9.35E+00	8.76E-01	5.74E-01	5.21E-01
1.29E+01	9.31E+00	8.84E-01	5.76E-01	5.12E-01
1.29E+01	9.06E+00	8.29E-01	5.79E-01	5.11E-01
1.29E+01	9.39E+00	8.47E-01	6.03E-01	5.14E-01
1.30E+01	8.87E+00	8.15E-01	5.71E-01	5.28E-01
1.30E+01	8.87E+00	7.81E-01	5.64E-01	5.43E-01
1.30E+01	9.00E+00	8.00E-01	5.62E-01	5.38E-01
1.30E+01	9.19E+00	8.26E-01	5.58E-01	5.42E-01

1.30E+01	8.98E+00	8.12E-01	5.37E-01	5.36E-01
1.30E+01	9.19E+00	7.94E-01	5.62E-01	5.43E-01
1.31E+01	9.32E+00	8.26E-01	5.43E-01	5.48E-01
1.31E+01	9.15E+00	8.33E-01	5.36E-01	5.39E-01
1.31E+01	9.14E+00	8.42E-01	5.70E-01	5.28E-01
1.31E+01	9.43E+00	7.80E-01	5.78E-01	5.26E-01
1.31E+01	9.85E+00	8.48E-01	5.58E-01	5.30E-01
1.31E+01	9.46E+00	8.79E-01	5.70E-01	5.16E-01
1.32E+01	9.06E+00	8.14E-01	5.53E-01	5.19E-01
1.32E+01	9.05E+00	7.89E-01	5.67E-01	5.39E-01
1.32E+01	8.89E+00	7.93E-01	5.71E-01	5.42E-01
1.32E+01	9.01E+00	8.08E-01	5.67E-01	5.27E-01
1.32E+01	8.80E+00	7.89E-01	5.50E-01	5.20E-01
1.32E+01	8.50E+00	7.57E-01	5.61E-01	5.23E-01
1.33E+01	8.39E+00	7.35E-01	5.46E-01	5.29E-01
1.33E+01	8.74E+00	7.64E-01	5.50E-01	5.30E-01
1.33E+01	8.89E+00	7.97E-01	5.30E-01	5.31E-01
1.33E+01	9.33E+00	8.36E-01	5.28E-01	5.25E-01
1.33E+01	9.69E+00	8.06E-01	5.40E-01	5.12E-01
1.33E+01	9.51E+00	7.80E-01	5.55E-01	5.12E-01
1.34E+01	9.08E+00	8.15E-01	5.52E-01	5.06E-01
1.34E+01	8.79E+00	8.20E-01	5.38E-01	5.18E-01
1.34E+01	8.69E+00	8.11E-01	5.80E-01	5.13E-01
1.34E+01	8.71E+00	7.67E-01	5.54E-01	5.12E-01
1.34E+01	8.39E+00	7.61E-01	5.62E-01	5.23E-01

1.34E+01	8.14E+00	8.17E-01	5.47E-01	5.20E-01
1.35E+01	8.05E+00	7.44E-01	5.44E-01	5.16E-01
1.35E+01	8.43E+00	7.40E-01	5.37E-01	5.25E-01
1.35E+01	8.62E+00	7.73E-01	5.38E-01	5.38E-01
1.35E+01	8.61E+00	7.51E-01	5.41E-01	5.33E-01
1.35E+01	9.12E+00	7.58E-01	5.28E-01	5.19E-01
1.35E+01	9.18E+00	7.72E-01	5.08E-01	5.23E-01
1.36E+01	9.18E+00	7.72E-01	5.26E-01	5.32E-01
1.36E+01	9.32E+00	7.46E-01	5.30E-01	5.14E-01
1.36E+01	9.30E+00	7.72E-01	5.30E-01	5.17E-01
1.36E+01	9.48E+00	8.52E-01	5.36E-01	5.12E-01
1.36E+01	9.67E+00	8.35E-01	5.35E-01	5.08E-01
1.36E+01	9.34E+00	8.27E-01	5.69E-01	4.94E-01
1.37E+01	8.85E+00	8.37E-01	5.62E-01	5.01E-01
1.37E+01	8.98E+00	8.43E-01	5.53E-01	4.97E-01
1.37E+01	8.79E+00	7.98E-01	5.78E-01	5.02E-01
1.37E+01	8.85E+00	7.53E-01	5.74E-01	5.22E-01
1.37E+01	8.24E+00	7.72E-01	5.72E-01	5.27E-01
1.37E+01	8.09E+00	7.85E-01	5.71E-01	5.31E-01
1.38E+01	8.37E+00	7.63E-01	5.51E-01	5.23E-01
1.38E+01	8.51E+00	8.05E-01	5.43E-01	5.29E-01
1.38E+01	9.14E+00	7.89E-01	5.49E-01	5.35E-01
1.38E+01	9.44E+00	7.97E-01	5.43E-01	5.35E-01
1.38E+01	9.24E+00	8.00E-01	5.47E-01	5.30E-01
1.38E+01	9.45E+00	8.50E-01	5.57E-01	5.30E-01

1.39E+01	9.55E+00	8.75E-01	5.54E-01	5.24E-01
1.39E+01	9.08E+00	8.04E-01	5.91E-01	5.21E-01
1.39E+01	9.18E+00	7.84E-01	5.71E-01	5.17E-01
1.39E+01	9.21E+00	8.05E-01	5.47E-01	5.16E-01
1.39E+01	9.00E+00	8.20E-01	5.43E-01	5.14E-01
1.39E+01	9.02E+00	8.12E-01	5.58E-01	5.26E-01
1.40E+01	8.97E+00	8.07E-01	5.63E-01	5.33E-01
1.40E+01	8.79E+00	7.93E-01	5.52E-01	5.31E-01
1.40E+01	8.56E+00	7.66E-01	5.34E-01	5.27E-01
1.40E+01	8.27E+00	7.95E-01	5.46E-01	5.19E-01
1.40E+01	8.63E+00	7.89E-01	5.42E-01	5.12E-01
1.40E+01	9.09E+00	8.11E-01	5.53E-01	5.28E-01
1.41E+01	9.00E+00	7.68E-01	5.48E-01	5.28E-01
1.41E+01	8.98E+00	8.10E-01	5.66E-01	5.22E-01
1.41E+01	9.00E+00	7.88E-01	5.41E-01	5.15E-01
1.41E+01	9.22E+00	7.87E-01	5.49E-01	5.16E-01
1.41E+01	9.57E+00	7.69E-01	5.38E-01	5.24E-01
1.41E+01	9.42E+00	8.38E-01	5.31E-01	5.28E-01
1.42E+01	9.14E+00	8.39E-01	5.28E-01	5.21E-01
1.42E+01	8.97E+00	8.36E-01	5.69E-01	5.15E-01
1.42E+01	9.05E+00	8.07E-01	5.70E-01	5.12E-01
1.42E+01	8.42E+00	8.19E-01	5.76E-01	5.18E-01
1.42E+01	8.98E+00	8.02E-01	5.57E-01	5.13E-01
1.42E+01	8.80E+00	8.29E-01	5.57E-01	5.06E-01
1.43E+01	8.77E+00	8.04E-01	5.91E-01	5.22E-01

1.43E+01	8.82E+00	7.61E-01	5.67E-01	5.38E-01
1.43E+01	8.72E+00	7.60E-01	5.78E-01	5.31E-01
1.43E+01	9.21E+00	8.24E-01	5.49E-01	5.29E-01
1.43E+01	9.11E+00	7.94E-01	5.35E-01	5.30E-01
1.43E+01	8.93E+00	8.14E-01	5.30E-01	5.41E-01
1.44E+01	8.57E+00	8.15E-01	5.50E-01	5.32E-01
1.44E+01	8.47E+00	8.04E-01	5.63E-01	5.29E-01
1.44E+01	8.30E+00	8.50E-01	5.54E-01	5.32E-01
1.44E+01	7.96E+00	7.75E-01	5.58E-01	5.29E-01
1.44E+01	7.55E+00	7.46E-01	5.51E-01	5.26E-01
1.44E+01	7.92E+00	7.58E-01	5.50E-01	5.21E-01
1.45E+01	8.09E+00	7.13E-01	5.34E-01	5.20E-01
1.45E+01	8.12E+00	7.39E-01	5.29E-01	5.29E-01
1.45E+01	8.27E+00	7.58E-01	5.30E-01	5.31E-01
1.45E+01	8.54E+00	7.82E-01	5.31E-01	5.22E-01
1.45E+01	8.88E+00	8.09E-01	5.19E-01	5.14E-01
1.45E+01	8.76E+00	7.93E-01	5.31E-01	5.11E-01
1.46E+01	8.66E+00	7.68E-01	5.42E-01	5.12E-01
1.46E+01	8.36E+00	8.61E-01	5.48E-01	5.13E-01
1.46E+01	8.47E+00	7.76E-01	5.46E-01	5.07E-01
1.46E+01	8.26E+00	7.67E-01	5.56E-01	5.12E-01
1.46E+01	8.47E+00	7.55E-01	5.35E-01	5.11E-01
1.46E+01	8.24E+00	7.71E-01	5.26E-01	5.12E-01
1.47E+01	7.98E+00	7.47E-01	5.28E-01	5.02E-01
1.47E+01	7.89E+00	7.57E-01	5.26E-01	5.10E-01

1.47E+01	7.99E+00	7.64E-01	5.40E-01	5.19E-01
1.47E+01	8.00E+00	7.28E-01	5.36E-01	5.13E-01
1.47E+01	7.90E+00	7.12E-01	5.35E-01	5.01E-01
1.47E+01	7.52E+00	7.13E-01	5.21E-01	5.03E-01
1.48E+01	7.59E+00	7.19E-01	5.28E-01	5.03E-01
1.48E+01	7.58E+00	7.14E-01	5.17E-01	5.19E-01
1.48E+01	7.99E+00	7.15E-01	5.08E-01	5.07E-01
1.48E+01	8.31E+00	7.32E-01	5.27E-01	4.96E-01
1.48E+01	7.94E+00	7.55E-01	5.13E-01	5.01E-01
1.48E+01	7.71E+00	7.08E-01	5.12E-01	4.87E-01
1.49E+01	7.78E+00	7.43E-01	5.21E-01	4.93E-01
1.49E+01	7.87E+00	7.46E-01	4.95E-01	4.99E-01
1.49E+01	8.01E+00	7.55E-01	5.15E-01	4.93E-01
1.49E+01	7.90E+00	7.46E-01	5.29E-01	4.91E-01
1.49E+01	7.64E+00	7.17E-01	5.43E-01	4.88E-01
1.49E+01	7.98E+00	7.66E-01	5.36E-01	4.88E-01
1.50E+01	7.80E+00	7.21E-01	5.21E-01	4.81E-01
1.50E+01	7.57E+00	7.03E-01	5.17E-01	4.83E-01
1.50E+01	7.44E+00	7.06E-01	5.17E-01	4.96E-01
1.50E+01	7.16E+00	7.40E-01	5.12E-01	5.02E-01
1.50E+01	7.07E+00	7.20E-01	5.18E-01	5.11E-01
1.50E+01	7.68E+00	7.06E-01	5.16E-01	4.97E-01
1.51E+01	6.72E+00	7.19E-01	5.12E-01	4.83E-01
1.51E+01	6.52E+00	6.78E-01	4.99E-01	4.83E-01
1.51E+01	6.75E+00	6.68E-01	4.99E-01	4.85E-01

1.51E+01	6.83E+00	6.78E-01	5.05E-01	4.80E-01
1.51E+01	7.16E+00	6.83E-01	4.96E-01	4.86E-01
1.51E+01	6.67E+00	7.06E-01	4.94E-01	4.83E-01
1.52E+01	6.74E+00	6.52E-01	4.99E-01	4.77E-01
1.52E+01	6.90E+00	6.62E-01	5.02E-01	4.74E-01
1.52E+01	6.64E+00	6.58E-01	4.91E-01	4.77E-01
1.52E+01	7.16E+00	6.58E-01	4.88E-01	4.77E-01
1.52E+01	6.14E+00	6.67E-01	4.91E-01	4.73E-01
1.52E+01	5.59E+00	6.41E-01	4.90E-01	4.76E-01
1.53E+01	6.60E+00	6.40E-01	4.86E-01	4.70E-01
1.53E+01	6.56E+00	6.55E-01	4.82E-01	4.71E-01
1.53E+01	5.81E+00	6.72E-01	4.84E-01	4.64E-01
1.53E+01	6.20E+00	6.55E-01	4.91E-01	4.64E-01
1.53E+01	6.20E+00	6.65E-01	4.92E-01	4.63E-01
1.53E+01	6.12E+00	6.52E-01	4.91E-01	4.60E-01
1.54E+01	6.24E+00	6.56E-01	4.88E-01	4.63E-01
1.54E+01	5.71E+00	6.63E-01	4.88E-01	4.61E-01
1.54E+01	5.91E+00	6.72E-01	4.86E-01	4.63E-01
1.54E+01	5.74E+00	6.56E-01	4.87E-01	4.65E-01
1.54E+01	6.23E+00	6.48E-01	4.87E-01	4.60E-01
1.54E+01	5.87E+00	6.53E-01	4.79E-01	4.66E-01
1.55E+01	5.72E+00	6.35E-01	4.83E-01	4.64E-01
1.55E+01	5.83E+00	6.41E-01	4.81E-01	4.63E-01
1.55E+01	5.57E+00	6.55E-01	4.81E-01	4.62E-01
1.55E+01	5.46E+00	6.45E-01	4.88E-01	4.62E-01

1.55E+01	5.15E+00	6.41E-01	4.80E-01	4.62E-01
1.55E+01	5.38E+00	6.18E-01	4.81E-01	4.54E-01
1.56E+01	5.68E+00	6.23E-01	4.87E-01	4.56E-01
1.56E+01	5.73E+00	6.46E-01	4.80E-01	4.59E-01
1.56E+01	5.90E+00	6.21E-01	4.76E-01	4.59E-01
1.56E+01	6.19E+00	6.24E-01	4.76E-01	4.56E-01
1.56E+01	5.69E+00	6.37E-01	4.68E-01	4.59E-01
1.56E+01	5.66E+00	6.24E-01	4.66E-01	4.53E-01
1.57E+01	5.80E+00	6.35E-01	4.68E-01	4.53E-01
1.57E+01	5.56E+00	6.33E-01	4.71E-01	4.56E-01
1.57E+01	5.26E+00	6.19E-01	4.73E-01	4.55E-01
1.57E+01	5.20E+00	6.02E-01	4.72E-01	4.51E-01
1.57E+01	5.04E+00	6.02E-01	4.73E-01	4.43E-01
1.57E+01	5.12E+00	5.96E-01	4.67E-01	4.42E-01
1.58E+01	5.09E+00	6.01E-01	4.62E-01	4.45E-01
1.58E+01	5.11E+00	6.04E-01	4.66E-01	4.45E-01
1.58E+01	5.36E+00	6.17E-01	4.61E-01	4.48E-01
1.58E+01	5.42E+00	5.94E-01	4.64E-01	4.50E-01
1.58E+01	5.39E+00	5.93E-01	4.64E-01	4.49E-01
1.58E+01	5.15E+00	5.96E-01	4.58E-01	4.45E-01
1.59E+01	4.88E+00	5.99E-01	4.57E-01	4.41E-01
1.59E+01	5.25E+00	5.90E-01	4.57E-01	4.38E-01
1.59E+01	5.15E+00	5.94E-01	4.66E-01	4.36E-01
1.59E+01	4.91E+00	6.03E-01	4.64E-01	4.37E-01
1.59E+01	4.92E+00	6.00E-01	4.59E-01	4.36E-01

1.59E+01	5.16E+00	6.04E-01	4.61E-01	4.29E-01
1.60E+01	5.11E+00	5.97E-01	4.60E-01	4.29E-01
1.60E+01	4.93E+00	6.11E-01	4.60E-01	4.33E-01
1.60E+01	4.59E+00	5.99E-01	4.64E-01	4.38E-01
1.60E+01	4.78E+00	5.93E-01	4.63E-01	4.36E-01
1.60E+01	4.71E+00	5.92E-01	4.62E-01	4.38E-01
1.60E+01	4.69E+00	5.89E-01	4.61E-01	4.39E-01
1.61E+01	4.53E+00	5.83E-01	4.58E-01	4.37E-01
1.61E+01	4.68E+00	5.92E-01	4.63E-01	4.38E-01
1.61E+01	4.52E+00	5.86E-01	4.58E-01	4.45E-01
1.61E+01	4.32E+00	5.98E-01	4.59E-01	4.43E-01
1.61E+01	4.20E+00	5.94E-01	4.57E-01	4.38E-01
1.61E+01	4.23E+00	5.87E-01	4.56E-01	4.40E-01
1.62E+01	4.12E+00	5.98E-01	4.55E-01	4.36E-01
1.62E+01	4.45E+00	5.93E-01	4.55E-01	4.37E-01
1.62E+01	4.64E+00	5.93E-01	4.55E-01	4.36E-01
1.62E+01	4.37E+00	6.06E-01	4.58E-01	4.36E-01
1.62E+01	4.59E+00	6.06E-01	4.57E-01	4.34E-01
1.62E+01	4.79E+00	5.99E-01	4.55E-01	4.34E-01
1.63E+01	4.62E+00	5.84E-01	4.55E-01	4.30E-01
1.63E+01	4.87E+00	5.85E-01	4.56E-01	4.30E-01
1.63E+01	4.67E+00	5.90E-01	4.56E-01	4.29E-01
1.63E+01	4.57E+00	5.90E-01	4.53E-01	4.30E-01
1.63E+01	4.72E+00	5.90E-01	4.53E-01	4.30E-01
1.63E+01	4.83E+00	5.97E-01	4.51E-01	4.29E-01

1.64E+01	4.62E+00	5.89E-01	4.53E-01	4.29E-01
1.64E+01	4.42E+00	5.90E-01	4.56E-01	4.31E-01
1.64E+01	4.23E+00	5.81E-01	4.57E-01	4.30E-01
1.64E+01	3.90E+00	6.06E-01	4.57E-01	4.31E-01
1.64E+01	3.76E+00	5.85E-01	4.53E-01	4.31E-01
1.64E+01	4.35E+00	5.88E-01	4.58E-01	4.35E-01
1.65E+01	4.19E+00	5.81E-01	4.53E-01	4.35E-01
1.65E+01	4.29E+00	5.70E-01	4.56E-01	4.35E-01
1.65E+01	4.40E+00	5.73E-01	4.53E-01	4.37E-01
1.65E+01	4.53E+00	5.77E-01	4.52E-01	4.32E-01
1.65E+01	4.57E+00	5.79E-01	4.48E-01	4.32E-01
1.65E+01	4.66E+00	5.78E-01	4.45E-01	4.31E-01
1.66E+01	4.64E+00	5.96E-01	4.49E-01	4.33E-01
1.66E+01	4.47E+00	5.91E-01	4.51E-01	4.34E-01
1.66E+01	4.27E+00	5.92E-01	4.50E-01	4.31E-01
1.66E+01	4.32E+00	5.86E-01	4.50E-01	4.27E-01
1.66E+01	4.14E+00	5.74E-01	4.52E-01	4.22E-01
1.66E+01	4.56E+00	5.73E-01	4.55E-01	4.21E-01
1.67E+01	4.80E+00	5.89E-01	4.54E-01	4.23E-01
1.67E+01	4.78E+00	5.77E-01	4.50E-01	4.25E-01
1.67E+01	4.83E+00	5.79E-01	4.49E-01	4.24E-01
1.67E+01	4.97E+00	5.92E-01	4.53E-01	4.26E-01
1.67E+01	4.90E+00	6.02E-01	4.50E-01	4.27E-01
1.67E+01	5.21E+00	6.07E-01	4.50E-01	4.29E-01
1.68E+01	4.94E+00	5.89E-01	4.53E-01	4.29E-01

1.68E+01	5.05E+00	6.01E-01	4.56E-01	4.27E-01
1.68E+01	5.23E+00	6.03E-01	4.55E-01	4.26E-01
1.68E+01	5.05E+00	6.02E-01	4.61E-01	4.27E-01
1.68E+01	5.12E+00	6.22E-01	4.57E-01	4.26E-01
1.68E+01	5.06E+00	6.08E-01	4.59E-01	4.30E-01
1.69E+01	5.00E+00	6.12E-01	4.58E-01	4.33E-01
1.69E+01	5.16E+00	6.10E-01	4.63E-01	4.36E-01
1.69E+01	5.16E+00	6.01E-01	4.61E-01	4.37E-01
1.69E+01	5.09E+00	5.80E-01	4.62E-01	4.39E-01
1.69E+01	5.01E+00	5.85E-01	4.61E-01	4.44E-01
1.69E+01	4.80E+00	6.00E-01	4.58E-01	4.43E-01
1.70E+01	4.73E+00	5.82E-01	4.51E-01	4.40E-01
1.70E+01	4.94E+00	5.80E-01	4.55E-01	4.42E-01
1.70E+01	4.95E+00	5.89E-01	4.57E-01	4.44E-01
1.70E+01	5.18E+00	5.85E-01	4.54E-01	4.47E-01
1.70E+01	5.17E+00	6.00E-01	4.59E-01	4.44E-01
1.70E+01	4.76E+00	6.01E-01	4.53E-01	4.38E-01
1.71E+01	4.46E+00	5.84E-01	4.54E-01	4.32E-01
1.71E+01	4.62E+00	6.12E-01	4.60E-01	4.31E-01
1.71E+01	4.78E+00	5.98E-01	4.58E-01	4.31E-01
1.71E+01	4.87E+00	5.97E-01	4.55E-01	4.29E-01
1.71E+01	4.91E+00	5.90E-01	4.57E-01	4.33E-01
1.71E+01	5.10E+00	5.86E-01	4.58E-01	4.30E-01
1.72E+01	5.18E+00	5.86E-01	4.56E-01	4.29E-01
1.72E+01	5.44E+00	5.92E-01	4.60E-01	4.36E-01

1.72E+01	5.41E+00	5.95E-01	4.58E-01	4.32E-01
1.72E+01	5.50E+00	5.92E-01	4.54E-01	4.32E-01
1.72E+01	5.75E+00	5.96E-01	4.61E-01	4.28E-01
1.72E+01	5.66E+00	6.08E-01	4.54E-01	4.35E-01
1.73E+01	5.72E+00	6.07E-01	4.56E-01	4.40E-01
1.73E+01	5.73E+00	6.03E-01	4.60E-01	4.38E-01
1.73E+01	5.76E+00	5.94E-01	4.63E-01	4.41E-01
1.73E+01	5.81E+00	5.97E-01	4.65E-01	4.37E-01
1.73E+01	5.37E+00	5.91E-01	4.60E-01	4.35E-01
1.73E+01	5.58E+00	6.12E-01	4.62E-01	4.31E-01
1.74E+01	6.02E+00	6.24E-01	4.59E-01	4.36E-01
1.74E+01	6.19E+00	6.14E-01	4.67E-01	4.42E-01
1.74E+01	6.13E+00	6.17E-01	4.69E-01	4.45E-01
1.74E+01	6.25E+00	6.34E-01	4.65E-01	4.43E-01
1.74E+01	6.35E+00	6.20E-01	4.66E-01	4.46E-01
1.74E+01	6.59E+00	6.22E-01	4.66E-01	4.43E-01
1.75E+01	6.17E+00	6.48E-01	4.66E-01	4.43E-01
1.75E+01	5.90E+00	6.38E-01	4.63E-01	4.43E-01
1.75E+01	5.97E+00	6.19E-01	4.65E-01	4.42E-01
1.75E+01	6.01E+00	6.25E-01	4.68E-01	4.46E-01
1.75E+01	5.90E+00	6.25E-01	4.70E-01	4.50E-01
1.75E+01	6.22E+00	6.41E-01	4.69E-01	4.47E-01
1.76E+01	5.78E+00	6.04E-01	4.73E-01	4.43E-01
1.76E+01	5.87E+00	6.14E-01	4.70E-01	4.43E-01
1.76E+01	6.43E+00	6.18E-01	4.71E-01	4.45E-01

1.76E+01	6.04E+00	6.28E-01	4.63E-01	4.51E-01
1.76E+01	6.40E+00	6.20E-01	4.64E-01	4.53E-01
1.76E+01	6.62E+00	6.44E-01	4.77E-01	4.57E-01
1.77E+01	6.52E+00	6.51E-01	4.76E-01	4.51E-01
1.77E+01	6.83E+00	6.53E-01	4.76E-01	4.50E-01
1.77E+01	6.95E+00	6.76E-01	4.79E-01	4.50E-01
1.77E+01	7.27E+00	6.80E-01	4.83E-01	4.47E-01
1.77E+01	7.25E+00	6.62E-01	4.87E-01	4.48E-01
1.77E+01	7.15E+00	6.60E-01	4.88E-01	4.57E-01
1.78E+01	6.96E+00	6.92E-01	4.81E-01	4.62E-01
1.78E+01	7.23E+00	7.20E-01	4.83E-01	4.65E-01
1.78E+01	6.84E+00	6.53E-01	4.87E-01	4.60E-01
1.78E+01	7.07E+00	6.76E-01	4.98E-01	4.59E-01
1.78E+01	6.12E+00	6.78E-01	4.98E-01	4.62E-01
1.78E+01	6.42E+00	6.92E-01	5.00E-01	4.59E-01
1.79E+01	7.13E+00	6.72E-01	4.96E-01	4.55E-01
1.79E+01	7.15E+00	6.81E-01	4.97E-01	4.61E-01
1.79E+01	7.02E+00	6.90E-01	5.06E-01	4.77E-01
1.79E+01	7.19E+00	6.79E-01	4.96E-01	4.80E-01
1.79E+01	7.29E+00	6.70E-01	4.93E-01	4.74E-01
1.79E+01	7.46E+00	6.61E-01	4.91E-01	4.77E-01
1.80E+01	7.62E+00	7.21E-01	4.84E-01	4.79E-01
1.80E+01	7.84E+00	7.10E-01	4.82E-01	4.76E-01
1.80E+01	7.15E+00	6.90E-01	4.92E-01	4.76E-01
1.80E+01	7.43E+00	6.93E-01	4.95E-01	4.72E-01

1.80E+01	7.44E+00	7.23E-01	4.99E-01	4.73E-01
1.80E+01	7.95E+00	7.22E-01	5.05E-01	4.75E-01
1.81E+01	7.96E+00	7.74E-01	5.06E-01	4.71E-01
1.81E+01	7.94E+00	7.41E-01	5.27E-01	4.70E-01
1.81E+01	8.09E+00	7.07E-01	5.45E-01	4.75E-01
1.81E+01	7.87E+00	6.94E-01	5.32E-01	4.77E-01
1.81E+01	8.14E+00	7.46E-01	5.15E-01	4.72E-01
1.81E+01	8.13E+00	7.77E-01	5.05E-01	4.82E-01
1.82E+01	8.12E+00	7.37E-01	5.19E-01	5.01E-01
1.82E+01	8.19E+00	7.21E-01	5.18E-01	4.98E-01
1.82E+01	7.84E+00	7.42E-01	5.21E-01	5.04E-01
1.82E+01	8.05E+00	7.30E-01	5.25E-01	5.00E-01
1.82E+01	8.24E+00	7.40E-01	5.20E-01	5.01E-01
1.82E+01	8.18E+00	7.24E-01	5.17E-01	4.96E-01
1.83E+01	8.08E+00	6.96E-01	5.19E-01	5.00E-01
1.83E+01	7.89E+00	7.45E-01	5.14E-01	4.96E-01
1.83E+01	8.14E+00	7.35E-01	5.22E-01	4.91E-01
1.83E+01	8.37E+00	7.45E-01	5.49E-01	4.90E-01
1.83E+01	7.97E+00	7.92E-01	5.23E-01	4.95E-01
1.83E+01	8.26E+00	7.85E-01	5.26E-01	4.97E-01
1.84E+01	8.62E+00	7.98E-01	5.50E-01	4.88E-01
1.84E+01	8.47E+00	7.68E-01	5.44E-01	4.97E-01
1.84E+01	8.24E+00	7.30E-01	5.41E-01	5.06E-01
1.84E+01	8.46E+00	7.76E-01	5.31E-01	5.02E-01
1.84E+01	8.42E+00	7.75E-01	5.38E-01	5.15E-01

1.84E+01	8.38E+00	7.72E-01	5.38E-01	5.14E-01
1.85E+01	8.10E+00	7.46E-01	5.45E-01	5.23E-01
1.85E+01	8.52E+00	7.62E-01	5.35E-01	5.23E-01
1.85E+01	8.30E+00	7.41E-01	5.34E-01	5.03E-01
1.85E+01	8.25E+00	7.44E-01	5.32E-01	5.10E-01
1.85E+01	7.75E+00	7.64E-01	5.28E-01	5.27E-01
1.85E+01	8.11E+00	7.40E-01	5.31E-01	5.27E-01
1.86E+01	8.31E+00	7.51E-01	5.33E-01	5.15E-01
1.86E+01	8.22E+00	7.30E-01	5.17E-01	5.06E-01
1.86E+01	8.23E+00	7.29E-01	5.34E-01	5.11E-01
1.86E+01	8.44E+00	7.26E-01	5.19E-01	5.05E-01
1.86E+01	8.23E+00	7.45E-01	5.14E-01	4.95E-01
1.86E+01	8.39E+00	7.68E-01	5.18E-01	4.95E-01
1.87E+01	8.52E+00	8.10E-01	5.12E-01	5.01E-01
1.87E+01	8.87E+00	8.12E-01	5.12E-01	4.96E-01
1.87E+01	8.36E+00	7.37E-01	5.24E-01	5.04E-01
1.87E+01	8.80E+00	7.81E-01	5.32E-01	5.09E-01
1.87E+01	8.89E+00	8.28E-01	5.22E-01	4.98E-01
1.87E+01	9.10E+00	8.47E-01	5.34E-01	4.92E-01
1.88E+01	8.87E+00	8.42E-01	5.47E-01	4.86E-01
1.88E+01	8.77E+00	7.67E-01	5.45E-01	4.91E-01
1.88E+01	8.88E+00	8.13E-01	5.42E-01	5.01E-01
1.88E+01	8.93E+00	8.17E-01	5.44E-01	5.04E-01
1.88E+01	9.47E+00	7.84E-01	5.68E-01	5.04E-01
1.88E+01	9.12E+00	8.20E-01	5.68E-01	5.17E-01

1.89E+01	9.01E+00	8.11E-01	5.29E-01	5.16E-01
1.89E+01	8.36E+00	8.05E-01	5.48E-01	5.10E-01
1.89E+01	9.01E+00	8.06E-01	5.34E-01	5.07E-01
1.89E+01	8.84E+00	8.00E-01	5.42E-01	5.17E-01
1.89E+01	8.82E+00	7.67E-01	5.36E-01	5.31E-01
1.89E+01	8.57E+00	7.72E-01	5.42E-01	5.17E-01
1.90E+01	8.46E+00	8.15E-01	5.52E-01	5.15E-01
1.90E+01	8.69E+00	7.62E-01	5.40E-01	5.20E-01
1.90E+01	8.66E+00	7.69E-01	5.45E-01	5.15E-01
1.90E+01	8.53E+00	7.63E-01	5.40E-01	5.10E-01
1.90E+01	8.48E+00	7.73E-01	5.54E-01	5.21E-01
1.90E+01	8.36E+00	7.59E-01	5.30E-01	5.21E-01
1.91E+01	8.50E+00	7.69E-01	5.19E-01	5.15E-01
1.91E+01	8.64E+00	7.59E-01	5.38E-01	5.13E-01
1.91E+01	8.47E+00	7.67E-01	5.31E-01	5.15E-01
1.91E+01	8.37E+00	7.40E-01	5.20E-01	5.05E-01
1.91E+01	8.08E+00	7.43E-01	5.26E-01	5.06E-01
1.91E+01	8.26E+00	7.27E-01	5.17E-01	5.09E-01
1.92E+01	8.45E+00	7.31E-01	5.21E-01	5.04E-01
1.92E+01	8.58E+00	7.38E-01	5.24E-01	5.05E-01
1.92E+01	8.07E+00	7.44E-01	5.08E-01	5.02E-01
1.92E+01	8.67E+00	8.05E-01	5.09E-01	5.04E-01
1.92E+01	8.34E+00	7.70E-01	5.37E-01	5.00E-01
1.92E+01	8.18E+00	7.43E-01	5.10E-01	4.86E-01
1.93E+01	8.10E+00	7.25E-01	5.26E-01	4.93E-01

1.93E+01	8.38E+00	7.49E-01	5.36E-01	4.86E-01
1.93E+01	8.22E+00	7.67E-01	5.39E-01	4.85E-01
1.93E+01	8.37E+00	7.34E-01	5.25E-01	4.95E-01
1.93E+01	8.54E+00	7.70E-01	5.24E-01	4.92E-01
1.93E+01	8.20E+00	7.97E-01	5.14E-01	4.95E-01
1.94E+01	8.28E+00	7.84E-01	5.23E-01	4.94E-01
1.94E+01	8.26E+00	7.47E-01	5.26E-01	4.98E-01
1.94E+01	7.97E+00	7.20E-01	5.37E-01	5.02E-01
1.94E+01	7.92E+00	7.04E-01	5.18E-01	4.91E-01
1.94E+01	7.71E+00	7.23E-01	5.20E-01	4.90E-01
1.94E+01	7.51E+00	7.05E-01	5.07E-01	4.90E-01
1.95E+01	7.57E+00	7.26E-01	5.17E-01	4.97E-01
1.95E+01	7.46E+00	7.19E-01	5.08E-01	5.01E-01
1.95E+01	7.68E+00	6.95E-01	5.11E-01	4.97E-01
1.95E+01	7.31E+00	7.13E-01	5.05E-01	5.00E-01
1.95E+01	6.88E+00	6.82E-01	5.09E-01	5.03E-01
1.95E+01	7.00E+00	6.74E-01	5.22E-01	4.93E-01
1.96E+01	7.06E+00	6.98E-01	5.08E-01	4.91E-01
1.96E+01	7.03E+00	6.95E-01	4.96E-01	4.91E-01
1.96E+01	7.33E+00	7.03E-01	4.98E-01	4.93E-01
1.96E+01	7.58E+00	7.01E-01	4.94E-01	4.90E-01
1.96E+01	7.35E+00	6.91E-01	4.91E-01	4.85E-01
1.96E+01	7.31E+00	6.79E-01	4.93E-01	4.81E-01
1.97E+01	7.58E+00	6.81E-01	4.98E-01	4.81E-01
1.97E+01	7.11E+00	6.82E-01	5.04E-01	4.80E-01

1.97E+01	6.76E+00	6.93E-01	4.87E-01	4.78E-01
1.97E+01	6.27E+00	6.58E-01	5.07E-01	4.60E-01
1.97E+01	6.61E+00	6.36E-01	4.96E-01	4.60E-01
1.97E+01	6.69E+00	6.62E-01	4.86E-01	4.76E-01
1.98E+01	5.94E+00	6.71E-01	4.87E-01	4.70E-01
1.98E+01	5.83E+00	6.48E-01	4.82E-01	4.68E-01
1.98E+01	6.24E+00	6.32E-01	4.81E-01	4.71E-01
1.98E+01	6.31E+00	6.38E-01	4.85E-01	4.65E-01
1.98E+01	6.04E+00	6.51E-01	4.80E-01	4.65E-01
1.98E+01	6.14E+00	6.41E-01	4.73E-01	4.61E-01
1.99E+01	6.04E+00	6.33E-01	4.87E-01	4.62E-01
1.99E+01	6.30E+00	6.27E-01	4.85E-01	4.64E-01
1.99E+01	6.21E+00	6.29E-01	4.74E-01	4.62E-01
1.99E+01	6.29E+00	6.62E-01	4.78E-01	4.56E-01
1.99E+01	6.26E+00	6.41E-01	4.68E-01	4.57E-01
1.99E+01	5.74E+00	6.40E-01	4.78E-01	4.58E-01
2.00E+01	5.97E+00	6.28E-01	4.81E-01	4.60E-01
2.00E+01	6.23E+00	6.60E-01	4.81E-01	4.56E-01
2.00E+01	6.04E+00	6.32E-01	4.77E-01	4.45E-01
2.00E+01	5.72E+00	6.41E-01	4.76E-01	4.47E-01
2.00E+01	5.69E+00	6.42E-01	4.77E-01	4.48E-01
2.00E+01	5.66E+00	6.15E-01	4.78E-01	4.49E-01
2.01E+01	5.65E+00	6.12E-01	4.78E-01	4.47E-01
2.01E+01	5.62E+00	6.21E-01	4.72E-01	4.47E-01
2.01E+01	5.55E+00	6.30E-01	4.65E-01	4.53E-01

2.01E+01	5.46E+00	6.38E-01	4.69E-01	4.54E-01
2.01E+01	4.61E+00	6.18E-01	4.67E-01	4.52E-01
2.01E+01	4.81E+00	5.99E-01	4.67E-01	4.53E-01
2.02E+01	5.36E+00	6.25E-01	4.70E-01	4.54E-01
2.02E+01	5.14E+00	6.14E-01	4.69E-01	4.49E-01
2.02E+01	4.77E+00	6.13E-01	4.63E-01	4.41E-01
2.02E+01	4.76E+00	6.11E-01	4.63E-01	4.42E-01
2.02E+01	4.84E+00	6.16E-01	4.73E-01	4.41E-01
2.02E+01	4.74E+00	6.06E-01	4.67E-01	4.40E-01
2.03E+01	4.68E+00	5.97E-01	4.62E-01	4.48E-01
2.03E+01	4.80E+00	5.93E-01	4.64E-01	4.46E-01
2.03E+01	4.81E+00	5.94E-01	4.61E-01	4.40E-01
2.03E+01	4.64E+00	5.94E-01	4.62E-01	4.39E-01
2.03E+01	4.62E+00	6.01E-01	4.58E-01	4.46E-01
2.03E+01	4.79E+00	5.90E-01	4.60E-01	4.46E-01
2.04E+01	4.73E+00	5.80E-01	4.57E-01	4.41E-01
2.04E+01	4.67E+00	5.82E-01	4.56E-01	4.39E-01
2.04E+01	4.59E+00	5.91E-01	4.58E-01	4.37E-01
2.04E+01	4.35E+00	5.89E-01	4.54E-01	4.36E-01
2.04E+01	4.36E+00	5.87E-01	4.54E-01	4.33E-01
2.04E+01	4.54E+00	5.80E-01	4.57E-01	4.33E-01
2.05E+01	4.25E+00	5.76E-01	4.56E-01	4.32E-01
2.05E+01	4.19E+00	5.74E-01	4.52E-01	4.33E-01
2.05E+01	4.19E+00	5.70E-01	4.53E-01	4.34E-01
2.05E+01	3.98E+00	5.67E-01	4.50E-01	4.29E-01

2.05E+01	3.93E+00	5.57E-01	4.47E-01	4.28E-01
2.05E+01	3.97E+00	5.70E-01	4.48E-01	4.30E-01
2.06E+01	3.98E+00	5.75E-01	4.44E-01	4.32E-01
2.06E+01	3.88E+00	5.60E-01	4.47E-01	4.31E-01
2.06E+01	3.90E+00	5.67E-01	4.48E-01	4.29E-01
2.06E+01	3.79E+00	5.73E-01	4.48E-01	4.26E-01
2.06E+01	3.95E+00	5.79E-01	4.48E-01	4.21E-01
2.06E+01	4.07E+00	5.71E-01	4.45E-01	4.20E-01
2.07E+01	3.93E+00	5.68E-01	4.44E-01	4.21E-01
2.07E+01	3.58E+00	5.58E-01	4.45E-01	4.21E-01
2.07E+01	3.45E+00	5.63E-01	4.46E-01	4.23E-01
2.07E+01	3.46E+00	5.62E-01	4.48E-01	4.22E-01
2.07E+01	3.26E+00	5.61E-01	4.42E-01	4.21E-01
2.07E+01	3.12E+00	5.67E-01	4.45E-01	4.19E-01
2.08E+01	3.08E+00	5.51E-01	4.44E-01	4.17E-01
2.08E+01	3.20E+00	5.48E-01	4.44E-01	4.17E-01
2.08E+01	3.04E+00	5.52E-01	4.43E-01	4.21E-01
2.08E+01	2.93E+00	5.50E-01	4.42E-01	4.23E-01
2.08E+01	3.03E+00	5.51E-01	4.38E-01	4.17E-01
2.08E+01	3.00E+00	5.53E-01	4.39E-01	4.17E-01
2.09E+01	2.94E+00	5.46E-01	4.40E-01	4.18E-01
2.09E+01	2.67E+00	5.51E-01	4.39E-01	4.18E-01
2.09E+01	2.71E+00	5.49E-01	4.39E-01	4.16E-01
2.09E+01	2.68E+00	5.44E-01	4.37E-01	4.14E-01
2.09E+01	2.64E+00	5.51E-01	4.39E-01	4.11E-01

2.09E+01	2.53E+00	5.43E-01	4.37E-01	4.11E-01
2.10E+01	2.50E+00	5.41E-01	4.35E-01	4.12E-01
2.10E+01	2.42E+00	5.40E-01	4.37E-01	4.12E-01
2.10E+01	2.38E+00	5.37E-01	4.34E-01	4.12E-01
2.10E+01	2.32E+00	5.33E-01	4.36E-01	4.11E-01
2.10E+01	2.30E+00	5.37E-01	4.35E-01	4.12E-01
2.10E+01	2.24E+00	5.32E-01	4.33E-01	4.09E-01
2.11E+01	2.13E+00	5.28E-01	4.33E-01	4.07E-01
2.11E+01	2.15E+00	5.27E-01	4.34E-01	4.08E-01
2.11E+01	2.05E+00	5.29E-01	4.33E-01	4.08E-01
2.11E+01	1.96E+00	5.27E-01	4.32E-01	4.07E-01
2.11E+01	1.93E+00	5.25E-01	4.31E-01	4.06E-01
2.11E+01	1.89E+00	5.25E-01	4.32E-01	4.06E-01
2.12E+01	1.80E+00	5.23E-01	4.31E-01	4.06E-01
2.12E+01	1.82E+00	5.20E-01	4.31E-01	4.06E-01
2.12E+01	1.75E+00	5.18E-01	4.32E-01	4.06E-01
2.12E+01	1.72E+00	5.19E-01	4.29E-01	4.04E-01
2.12E+01	1.72E+00	5.19E-01	4.30E-01	4.03E-01
2.12E+01	1.63E+00	5.13E-01	4.29E-01	4.04E-01
2.13E+01	1.54E+00	5.12E-01	4.29E-01	4.04E-01
2.13E+01	1.51E+00	5.13E-01	4.28E-01	4.03E-01
2.13E+01	1.42E+00	5.07E-01	4.28E-01	4.03E-01
2.13E+01	1.37E+00	5.02E-01	4.29E-01	4.02E-01
2.13E+01	1.30E+00	4.99E-01	4.29E-01	4.02E-01
2.13E+01	1.21E+00	4.94E-01	4.27E-01	4.02E-01

2.14E+01	1.13E+00	4.91E-01	4.26E-01	4.02E-01
2.14E+01	1.07E+00	4.90E-01	4.26E-01	4.01E-01
2.14E+01	1.03E+00	4.87E-01	4.25E-01	4.02E-01
2.14E+01	9.95E-01	4.86E-01	4.25E-01	4.01E-01

B.2 Heat Flux Results Comparison for the Tunnel Prototypes and Fire Scenarios (Figure 21)

CDSF (Tunnel A Fire B-1)									
	CEILING			SIDEWALL			CROSS SECTION		
x (m)	TOTAL	RADI	CONV	TOTAL	RADI	CONV	TOTAL	RADI	CONV
-55	0	0	0	0	0	0	11	11	0
-50	0	0	0	0	0	0	15	15	0
-45	0	0	0	0	0	0	18	18	0
-40	0	0	0	0	0	0	21	21	0
-35	0	0	0	0	0	0	23	23	0
-30	0	0	0	0	0	0	25	25	0
-25	0	0	0	0	0	0	27	27	0
-20	0	0	0	0	0	0	30	30	0
-18	0	0	0	0	0	0	33	33	0
-16	0	0	0	0	0	0	37	37	0
-15	0	0	0	0	0	0	41	41	0
-14	1	1	0	1	1	0	46	46	0
-12	1	1	0	1	1	0	55	55	0
-10	1	1	0	2	2	0	67	67	0
-8	2	2	0	3	3	0	55	55	0
-6	5	5	0	6	6	0	46	46	0
-5	7	7	0	8	8	0	41	41	0
-4	11	11	0	11	11	0	37	37	0
-2	31	31	0	19	19	0	33	33	0
0	67	67	0	23	23	0	30	30	0
2	31	31	0	19	19	0	27	27	0
4	11	11	0	11	11	0	25	25	0
5	7	7	0	8	8	0	23	23	0
6	5	5	0	6	6	0	21	21	0

8	2	2	0	3	3	0	18	18	0
10	1	1	0	2	2	0	15	15	0
12	1	1	0	1	1	0	12	12	0
14	1	1	0	1	1	0			
15	0	0	0	0	0	0			
16	0	0	0	0	0	0			
18	0	0	0	0	0	0			
20	0	0	0	0	0	0			
25	0	0	0	0	0	0			
30	0	0	0	0	0	0			
35	0	0	0	0	0	0			
40	0	0	0	0	0	0			
45	0	0	0	0	0	0			
50	0	0	0	0	0	0			
55	0	0	0	0	0	0			

FDS (Tunnel A Fire B-1)									
	CEILING			SIDEWALL			CROSS SECTION		
x (m)	UB	MEAN	LB	UB	MEAN	LB	UB	MEAN	LB
-55	2.3	2.0	1.7	0.7	0.6	0.6	16.2	14.5	12.8
-50	2.5	2.2	1.9	0.7	0.7	0.6	22.0	19.8	17.6
-45	2.7	2.4	2.0	0.7	0.7	0.7	27.7	24.9	22.2
-40	3.0	2.6	2.2	0.8	0.7	0.7	27.2	24.1	21.0
-35	3.2	2.8	2.4	0.8	0.8	0.7	26.1	22.8	19.5
-30	3.3	2.9	2.4	0.9	0.8	0.8	27.8	23.8	19.9
-25	4.5	3.8	3.1	0.9	0.9	0.8	22.1	18.7	15.3
-20	5.1	4.2	3.3	1.0	1.0	0.9	23.1	18.7	14.4
-18	5.3	4.3	3.3	1.1	1.0	1.0	28.0	19.9	11.7
-16	5.6	4.5	3.4	1.2	1.1	1.1	24.5	16.0	7.6
-15	5.8	4.6	3.4	1.3	1.2	1.1	43.6	26.0	8.5
-14	6.0	4.7	3.4	1.5	1.4	1.3	63.6	38.6	13.7

-12	6.5	5.0	3.5	2.0	1.8	1.7	93.2	57.2	21.2
-10	7.1	5.3	3.5	2.7	2.5	2.2	102.2	63.9	25.5
-8	8.2	6.0	3.7	3.8	3.4	3.1	93.1	57.3	21.5
-6	11.3	7.7	4.1	5.9	5.3	4.6	60.2	37.5	14.8
-5	13.6	8.9	4.2	7.3	6.5	5.6	40.0	25.1	10.1
-4	20.2	12.3	4.5	10.4	9.2	8.0	22.1	15.6	9.1
-2	52.7	30.7	8.7	19.0	16.6	14.2	16.2	12.5	8.8
0	102.2	63.9	25.5	26.1	22.8	19.5	22.3	18.5	14.6
2	50.0	29.7	9.4	18.1	15.9	13.7	21.8	18.6	15.4
4	20.4	12.6	4.8	10.1	8.9	7.7	27.6	23.8	19.9
5	15.7	10.3	4.9	8.2	7.2	6.3	26.0	22.7	19.4
6	11.7	8.0	4.3	5.8	5.2	4.5	27.2	24.0	20.9
8	8.5	6.2	4.0	3.8	3.4	3.0	27.6	24.8	22.0
10	7.3	5.6	3.9	2.7	2.5	2.2	21.9	19.7	17.4
12	6.7	5.2	3.8	2.0	1.8	1.6	16.1	14.4	12.7
14	6.3	5.0	3.6	1.5	1.4	1.3			
15	6.1	4.8	3.6	1.3	1.2	1.1			
16	5.9	4.7	3.6	1.2	1.1	1.1			
18	5.6	4.5	3.5	1.1	1.0	1.0			
20	5.3	4.4	3.4	1.0	1.0	0.9			
25	4.8	4.0	3.2	0.9	0.9	0.8			
30	4.0	3.4	2.9	0.9	0.8	0.8			
35	3.4	2.9	2.4	0.8	0.8	0.7			
40	3.1	2.7	2.3	0.8	0.7	0.7			
45	2.8	2.4	2.1	0.7	0.7	0.7			
50	2.6	2.2	1.9	0.7	0.7	0.6			
55	2.4	2.1	1.8	0.7	0.6	0.6			

CDSF (Tunnel A Fire HGV-1)									
	CEILING			SIDEWALL			CROSS SECTION		
x (m)	TOTAL	RADI	CONV	TOTAL	RADI	CONV	TOTAL	RADI	CONV
-55	4	0	4	0	0	0	10	10	0
-50	5	0	5	0	0	0	15	15	0
-45	6	0	6	1	0	1	20	20	0
-40	7	0	7	1	0	1	24	24	0
-35	9	0	9	1	0	1	31	27	4
-30	10	0	10	1	0	1	38	29	9
-25	12	0	12	1	0	1	47	32	15
-20	15	0	14	2	0	1	60	40	20
-18	16	0	15	2	0	1	84	58	26
-16	17	1	17	2	1	1	127	96	31
-15	18	1	17	2	1	1	165	128	37
-14	19	1	18	2	1	1	192	150	42
-12	20	1	19	3	2	2	208	161	47
-10	23	3	20	4	3	2	220	170	50
-8	28	6	22	7	5	2	208	161	47
-6	41	18	23	11	10	2	192	150	42
-5	61	37	24	15	13	2	165	128	37
-4	101	75	26	19	17	2	127	96	31
-2	176	146	31	27	24	3	84	58	26
0	220	170	50	31	27	4	60	40	20
2	176	146	31	27	24	3	47	32	15
4	101	75	26	19	17	2	38	29	9
5	61	37	24	15	13	2	31	27	4
6	41	18	23	11	10	2	25	25	0
8	28	6	22	7	5	2	21	21	0
10	23	3	20	4	3	2	16	16	0
12	20	1	19	3	2	2	10	10	0
14	19	1	18	2	1	1			
15	18	1	17	2	1	1			
16	17	1	17	2	1	1			
18	16	0	15	2	0	1			
20	15	0	14	2	0	1			
25	12	0	12	1	0	1			
30	10	0	10	1	0	1			
35	9	0	9	1	0	1			
40	7	0	7	1	0	1			
45	6	0	6	1	0	1			

50	5	0	5	0	0	0			
55	4	0	4	0	0	0			

FDS (Tunnel A Fire HGV-1)									
	CEILING			SIDEWALL			CROSS SECTION		
x (m)	UB	MEAN	LB	UB	MEAN	LB	UB	MEAN	LB
-55	5.9	5.0	4.2	1.0	0.9	0.9	19.7	18.1	16.5
-50	6.7	5.6	4.6	1.0	1.0	0.9	31.9	29.4	26.9
-45	7.7	6.4	5.1	1.1	1.0	1.0	45.9	42.4	38.8
-40	8.9	7.3	5.8	1.2	1.1	1.1	51.6	47.6	43.5
-35	10.4	8.4	6.5	1.4	1.3	1.2	49.4	45.3	41.3
-30	11.2	8.9	6.6	1.7	1.6	1.4	55.1	49.9	44.7
-25	16.8	13.9	11.0	1.8	1.7	1.5	44.2	37.8	31.3
-20	20.8	16.9	12.9	2.2	2.0	1.8	104.9	79.6	54.2
-18	22.9	18.4	13.8	2.4	2.2	2.0	114.9	87.1	59.2
-16	25.5	20.1	14.8	2.8	2.6	2.3	114.2	84.0	53.8
-15	27.0	21.2	15.4	3.1	2.8	2.5	179.4	136.8	94.2
-14	28.8	22.3	15.9	3.5	3.1	2.8	213.8	169.5	125.2
-12	33.3	25.2	17.2	4.6	4.1	3.6	263.9	215.2	166.6
-10	39.5	29.0	18.6	6.3	5.6	5.0	272.7	223.4	174.1
-8	49.3	35.0	20.8	9.0	8.1	7.2	263.0	213.7	164.4
-6	67.5	46.1	24.8	14.1	12.8	11.6	212.2	168.2	124.3
-5	78.7	53.4	28.1	17.0	15.5	14.0	177.6	136.0	94.4
-4	108.8	74.1	39.5	23.9	21.9	19.9	114.1	84.6	55.2
-2	214.6	162.6	110.6	40.2	36.8	33.3	95.4	69.3	43.1
0	272.7	223.4	174.1	49.4	45.3	41.3	106.5	80.8	55.0
2	202.8	150.6	98.5	38.0	34.7	31.4	45.1	38.4	31.8
4	101.4	68.8	36.1	22.3	20.3	18.4	55.3	50.0	44.7

5	82.9	56.9	30.8	18.2	16.5	14.9	49.6	45.2	40.9
6	65.1	44.4	23.7	13.4	12.1	10.8	51.8	47.5	43.1
8	47.7	34.0	20.4	8.7	7.8	6.9	46.0	42.2	38.5
10	38.1	28.3	18.5	6.1	5.5	4.8	32.0	29.3	26.6
12	32.0	24.6	17.2	4.4	4.0	3.6	19.8	18.0	16.3
14	27.8	21.9	16.0	3.4	3.1	2.8			
15	26.2	20.8	15.4	3.1	2.8	2.5			
16	24.8	19.8	14.9	2.8	2.6	2.3			
18	22.5	18.2	13.8	2.4	2.2	2.0			
20	20.5	16.7	12.9	2.2	2.0	1.8			
25	16.6	13.8	11.1	1.8	1.7	1.5			
30	12.6	10.7	8.7	1.6	1.5	1.4			
35	10.2	8.3	6.4	1.4	1.3	1.2			
40	8.8	7.2	5.7	1.2	1.1	1.1			
45	7.5	6.3	5.0	1.1	1.0	1.0			
50	6.6	5.6	4.5	1.0	1.0	0.9			
55	5.8	5.0	4.1	1.0	0.9	0.9			

CDSF (Tunnel A Fire HGV-2)									
	CEILING			SIDEWALL			CROSS SECTION		
x (m)	TOTAL	RADI	CONV	TOTAL	RADI	CONV	TOTAL	RADI	CONV
-55	6	0	6	1	0	1	9	9	0
-50	7	0	7	1	0	1	16	16	0
-45	8	0	8	1	0	1	22	22	0
-40	10	0	10	1	0	1	27	27	1
-35	12	0	11	1	0	1	37	29	8
-30	14	0	14	2	0	2	45	31	14
-25	16	0	16	2	0	2	56	35	21
-20	20	0	19	3	0	2	75	47	28
-18	21	1	21	3	1	2	128	93	35
-16	23	1	22	3	1	2	202	159	43
-15	24	1	23	4	1	3	238	188	50
-14	25	1	24	4	1	3	263	207	57
-12	28	2	25	5	2	3	275	212	63
-10	32	5	27	7	4	3	290	222	67
-8	41	12	29	10	7	3	275	212	63
-6	76	45	31	16	13	4	263	207	57

-5	124	92	33	21	17	4	238	188	50
-4	180	146	34	25	21	4	202	159	43
-2	242	201	41	32	27	5	128	93	35
0	290	222	67	37	29	8	75	47	28
2	242	201	41	32	27	5	56	35	21
4	180	146	34	25	21	4	45	31	14
5	124	92	33	21	17	4	37	29	8
6	76	45	31	16	13	4	28	27	1
8	41	12	29	10	7	3	23	23	0
10	32	5	27	7	4	3	17	17	0
12	28	2	25	5	2	3	10	10	0
14	25	1	24	4	1	3			
15	24	1	23	4	1	3			
16	23	1	22	3	1	2			
18	21	1	21	3	1	2			
20	20	0	19	3	0	2			
25	16	0	16	2	0	2			
30	14	0	14	2	0	2			
35	12	0	11	1	0	1			
40	10	0	10	1	0	1			
45	8	0	8	1	0	1			
50	7	0	7	1	0	1			
55	6	0	6	1	0	1			

FDS (Tunnel A Fire HGV-2)									
	CEILING			SIDEWALL			CROSS SECTION		
x (m)	UB	MEAN	LB	UB	MEAN	LB	UB	MEAN	LB
-55	9.8	8.2	6.6	1.2	1.1	1.0	21.4	18.8	16.2
-50	11.2	9.4	7.5	1.3	1.2	1.1	37.9	33.5	29.0
-45	13.1	10.8	8.6	1.5	1.3	1.2	59.1	52.1	45.1
-40	15.5	12.6	9.8	1.6	1.5	1.4	65.6	58.4	51.3
-35	18.3	14.6	11.0	1.9	1.8	1.6	60.9	55.2	49.4
-30	19.6	15.2	10.9	2.3	2.2	2.0	66.4	59.5	52.6
-25	29.5	24.1	18.7	2.6	2.4	2.2	91.7	76.0	60.2
-20	37.8	30.2	22.7	3.3	3.1	2.8	177.6	139.9	102.2
-18	42.2	33.5	24.7	3.7	3.4	3.2	188.8	148.8	108.8
-16	47.7	37.4	27.1	4.3	4.0	3.7	188.4	147.3	106.3

-15	51.0	39.7	28.4	4.7	4.3	4.0	249.5	207.7	165.9
-14	54.8	42.4	29.9	5.2	4.8	4.4	263.5	221.3	179.1
-12	64.6	49.0	33.4	6.6	6.0	5.4	317.0	277.1	237.3
-10	78.8	58.3	37.8	8.8	7.9	7.0	326.4	286.3	246.2
-8	98.7	71.9	45.1	12.6	11.2	9.7	318.2	277.7	237.2
-6	129.1	93.6	58.1	19.6	17.2	14.9	260.3	219.4	178.5
-5	145.8	107.1	68.5	23.6	20.7	17.9	236.6	198.9	161.2
-4	186.9	142.5	98.1	32.5	28.7	25.0	172.0	136.2	100.3
-2	293.9	246.8	199.7	51.7	46.3	41.0	144.6	112.6	80.5
0	326.4	286.3	246.2	60.9	55.2	49.4	160.4	128.3	96.2
2	287.8	242.2	196.6	49.5	44.5	39.4	91.1	74.0	56.9
4	187.3	142.2	97.0	30.9	27.5	24.0	66.0	58.1	50.3
5	159.5	119.6	79.6	25.5	22.6	19.7	61.2	53.7	46.1
6	130.4	95.0	59.6	18.7	16.6	14.5	66.0	57.2	48.4
8	99.4	72.9	46.4	12.1	10.8	9.6	59.4	51.3	43.1
10	78.9	58.9	38.9	8.6	7.7	6.9	38.2	32.8	27.4
12	65.0	49.4	33.9	6.4	5.9	5.4	21.5	18.4	15.3
14	55.0	42.6	30.1	5.1	4.7	4.3			
15	51.1	39.9	28.6	4.6	4.3	3.9			
16	47.7	37.5	27.3	4.2	3.9	3.6			
18	42.0	33.5	24.9	3.7	3.4	3.1			
20	37.6	30.2	22.9	3.3	3.0	2.8			
25	29.5	24.1	18.7	2.6	2.4	2.2			
30	22.0	18.1	14.1	2.2	2.0	1.9			
35	18.1	14.5	10.8	1.9	1.8	1.6			
40	15.3	12.5	9.6	1.6	1.5	1.4			
45	13.0	10.7	8.4	1.5	1.3	1.2			
50	11.2	9.3	7.4	1.3	1.2	1.1			
55	9.8	8.2	6.6	1.2	1.1	1.0			

CDSF (Tunnel B Fire B-1)									
	CEILING			SIDEWALL			CROSS SECTION		
x (m)	TOTAL	RADI	CONV	TOTAL	RADI	CONV	TOTAL	RADI	CONV
-55	0	0	0	0	0	0	9	9	0
-50	0	0	0	0	0	0	11	11	0
-45	0	0	0	0	0	0	13	13	0
-40	0	0	0	0	0	0	15	15	0
-35	0	0	0	0	0	0	15	15	0
-30	0	0	0	0	0	0	15	15	0
-25	0	0	0	0	0	0	16	16	0
-20	0	0	0	0	0	0	16	16	0
-18	0	0	0	0	0	0	16	16	0
-16	0	0	0	1	1	0	17	17	0
-15	1	1	0	1	1	0	18	18	0
-14	1	1	0	1	1	0	20	20	0
-12	1	1	0	1	1	0	23	23	0
-10	1	1	0	2	2	0	32	32	0
-8	2	2	0	3	3	0	23	23	0
-6	3	3	0	6	6	0	20	20	0
-5	4	4	0	7	7	0	18	18	0
-4	5	5	0	9	9	0	17	17	0
-2	11	11	0	13	13	0	17	17	0
0	32	32	0	15	15	0	16	16	0
2	11	11	0	13	13	0	16	16	0
4	5	5	0	9	9	0	15	15	0
5	4	4	0	7	7	0	15	15	0
6	3	3	0	6	6	0	15	15	0
8	2	2	0	3	3	0	13	13	0
10	1	1	0	2	2	0	12	12	0
12	1	1	0	1	1	0	9	9	0
14	1	1	0	1	1	0			
15	1	1	0	1	1	0			
16	0	0	0	1	1	0			
18	0	0	0	0	0	0			
20	0	0	0	0	0	0			
25	0	0	0	0	0	0			
30	0	0	0	0	0	0			
35	0	0	0	0	0	0			
40	0	0	0	0	0	0			
45	0	0	0	0	0	0			

50	0	0	0	0	0	0			
55	0	0	0	0	0	0			

FDS (Tunnel B Fire B-1)									
	CEILING			SIDEWALL			CROSS SECTION		
x (m)	UB	MEAN	LB	UB	MEAN	LB	UB	MEAN	LB
-55	1.3	1.2	1.0	0.6	0.5	0.5	12.0	10.6	9.1
-50	1.4	1.2	1.1	0.6	0.5	0.5	16.3	14.5	12.7
-45	1.4	1.3	1.1	0.6	0.6	0.5	17.4	15.3	13.2
-40	1.5	1.3	1.2	0.6	0.6	0.5	16.6	14.3	12.0
-35	1.6	1.4	1.2	0.6	0.6	0.6	16.0	13.7	11.3
-30	1.6	1.4	1.2	0.6	0.6	0.6	13.7	11.4	9.2
-25	2.1	1.8	1.5	0.7	0.7	0.7	12.1	9.9	7.8
-20	2.2	1.9	1.6	0.8	0.8	0.7	10.2	8.4	6.5
-18	2.3	1.9	1.6	0.9	0.9	0.8	9.0	7.3	5.5
-16	2.4	2.0	1.6	1.2	1.1	1.0	7.0	5.8	4.5
-15	2.4	2.0	1.6	1.3	1.2	1.1	9.1	6.6	4.0
-14	2.5	2.1	1.6	1.5	1.4	1.3	14.6	9.4	4.2
-12	2.6	2.2	1.7	1.9	1.7	1.6	24.3	14.3	4.4
-10	2.9	2.3	1.8	2.4	2.1	1.9	31.7	18.5	5.2
-8	3.6	2.8	2.0	3.2	2.9	2.5	28.0	16.1	4.2
-6	5.0	3.6	2.3	5.1	4.5	3.9	19.2	11.3	3.4
-5	5.9	4.1	2.3	6.2	5.4	4.6	11.3	7.6	3.9
-4	8.6	5.6	2.7	8.2	7.1	6.1	7.2	5.8	4.4
-2	20.1	11.2	2.4	12.8	11.0	9.2	6.7	5.7	4.7

0	31.7	18.5	5.2	16.0	13.7	11.3	10.4	8.5	6.5
2	18.0	10.3	2.6	12.3	10.5	8.7	12.3	10.0	7.8
4	8.7	5.5	2.3	7.8	6.7	5.7	13.8	11.5	9.2
5	6.8	4.6	2.3	6.6	5.7	4.8	16.3	13.9	11.5
6	5.1	3.7	2.2	4.8	4.2	3.6	16.9	14.6	12.2
8	3.7	2.8	2.0	3.1	2.7	2.3	17.7	15.6	13.5
10	3.0	2.4	1.8	2.3	2.1	1.8	16.6	14.7	12.9
12	2.7	2.2	1.7	1.9	1.7	1.5	12.3	10.8	9.4
14	2.6	2.1	1.7	1.5	1.3	1.2			
15	2.5	2.1	1.7	1.3	1.2	1.1			
16	2.5	2.1	1.7	1.1	1.0	1.0			
18	2.4	2.0	1.6	0.9	0.8	0.8			
20	2.3	2.0	1.6	0.8	0.8	0.7			
25	2.2	1.9	1.6	0.7	0.7	0.7			
30	2.0	1.7	1.5	0.7	0.6	0.6			
35	1.6	1.4	1.2	0.6	0.6	0.6			
40	1.6	1.4	1.2	0.6	0.6	0.5			
45	1.5	1.3	1.1	0.6	0.6	0.5			
50	1.4	1.2	1.1	0.6	0.5	0.5			
55	1.4	1.2	1.0	0.6	0.5	0.5			

CDSF (Tunnel B Fire HGV-1)									
	CEILING			SIDEWALL			CROSS SECTION		
x (m)	TOTAL	RADI	CONV	TOTAL	RADI	CONV	TOTAL	RADI	CONV
-55	7	0	7	1	0	1	10	10	0

-50	8	0	8	1	0	1	14	14	0
-45	9	0	9	1	0	1	17	17	0
-40	10	0	10	1	0	1	20	20	0
-35	12	0	12	1	0	1	27	22	5
-30	14	0	13	2	0	1	34	24	10
-25	15	0	15	2	0	2	42	26	15
-20	18	0	17	2	1	2	50	30	21
-18	19	1	18	3	1	2	60	34	26
-16	20	1	19	3	1	2	71	39	32
-15	21	1	20	3	1	2	81	44	37
-14	21	1	20	4	1	2	92	50	42
-12	23	2	21	4	2	2	107	59	47
-10	25	3	22	6	4	2	121	71	50
-8	29	5	24	9	6	2	107	59	47
-6	36	11	25	13	10	3	92	50	42
-5	42	16	26	16	13	3	81	44	37
-4	51	24	28	18	16	3	71	39	32
-2	83	50	33	24	20	4	60	34	26
0	121	71	50	27	22	5	50	30	21
2	83	50	33	24	20	4	42	26	15
4	51	24	28	18	16	3	34	24	10
5	42	16	26	16	13	3	28	22	5
6	36	11	25	13	10	3	20	20	0
8	29	5	24	9	6	2	18	18	0
10	25	3	22	6	4	2	14	14	0
12	23	2	21	4	2	2	10	10	0
14	21	1	20	4	1	2			
15	21	1	20	3	1	2			
16	20	1	19	3	1	2			
18	19	1	18	3	1	2			
20	18	0	17	2	1	2			
25	15	0	15	2	0	2			
30	14	0	13	2	0	1			
35	12	0	12	1	0	1			
40	10	0	10	1	0	1			
45	9	0	9	1	0	1			
50	8	0	8	1	0	1			
55	7	0	7	1	0	1			

FDS (Tunnel B Fire HGV-1)			
	CEILING	**SIDEWALL**	**CROSS SECTION**

x (m)	UB	MEAN	LB	UB	MEAN	LB	UB	MEAN	LB
-55	3.2	2.7	2.3	0.8	0.7	0.7	16.6	15.2	13.8
-50	3.4	2.9	2.5	0.8	0.7	0.7	23.0	21.0	19.0
-45	3.7	3.2	2.7	0.8	0.8	0.7	31.8	29.1	26.5
-40	4.1	3.5	2.9	0.9	0.8	0.8	31.0	28.0	25.0
-35	4.5	3.8	3.1	0.9	0.9	0.8	31.2	27.9	24.5
-30	4.7	3.9	3.1	1.0	0.9	0.8	28.6	25.2	21.8
-25	7.2	5.9	4.5	1.3	1.2	1.1	24.9	21.5	18.1
-20	8.2	6.5	4.8	1.6	1.5	1.3	23.7	19.6	15.5
-18	8.8	6.8	4.9	1.8	1.7	1.6	28.5	20.8	13.0
-16	9.6	7.2	4.9	2.3	2.1	2.0	29.6	18.9	8.3
-15	10.1	7.5	4.9	2.6	2.4	2.2	41.8	26.0	10.2
-14	10.6	7.8	4.9	2.9	2.7	2.5	65.6	40.3	15.1
-12	11.9	8.5	5.0	3.7	3.4	3.2	105.9	66.0	26.1
-10	13.9	9.5	5.1	4.7	4.4	4.0	134.7	85.2	35.6
-8	17.6	11.4	5.3	6.7	6.1	5.6	123.8	77.9	32.1
-6	25.3	15.3	5.3	10.4	9.5	8.6	91.6	55.2	18.7
-5	30.8	18.3	5.7	12.4	11.3	10.2	58.4	34.6	10.9
-4	44.6	26.1	7.6	17.0	15.4	13.9	31.1	19.8	8.6
-2	95.0	57.0	19.1	26.0	23.3	20.7	23.7	16.1	8.4
0	134.7	85.2	35.6	31.2	27.9	24.5	25.3	20.5	15.7
2	84.2	50.2	16.3	25.0	22.4	19.7	25.8	22.3	18.8
4	41.6	24.2	6.8	16.2	14.6	13.0	29.6	26.1	22.5
5	32.5	19.6	6.7	13.3	12.0	10.7	32.2	28.8	25.4

6	24.1	14.5	4.8	9.9	9.0	8.0	31.9	28.9	25.9
8	17.2	11.0	4.7	6.4	5.8	5.2	32.6	30.0	27.3
10	13.8	9.1	4.5	4.6	4.2	3.8	23.7	21.7	19.7
12	11.7	8.1	4.5	3.6	3.3	3.0	17.3	15.8	14.4
14	10.3	7.5	4.6	2.8	2.6	2.4			
15	9.8	7.2	4.6	2.5	2.3	2.1			
16	9.4	7.0	4.7	2.2	2.1	1.9			
18	8.6	6.6	4.6	1.8	1.7	1.5			
20	8.0	6.3	4.6	1.6	1.4	1.3			
25	7.1	5.7	4.4	1.3	1.2	1.1			
30	5.7	4.8	3.9	1.1	1.1	1.0			
35	4.4	3.7	3.1	0.9	0.9	0.8			
40	4.0	3.4	2.8	0.9	0.8	0.8			
45	3.6	3.1	2.6	0.8	0.8	0.7			
50	3.3	2.9	2.4	0.8	0.7	0.7			
55	3.1	2.7	2.3	0.8	0.7	0.7			

CDSF (Tunnel B Fire HGV-2)									
	CEILING			SIDEWALL			CROSS SECTION		
x (m)	TOTAL	RADI	CONV	TOTAL	RADI	CONV	TOTAL	RADI	CONV
-55	10	0	10	1	0	1	10	10	0
-50	11	0	11	2	0	1	15	15	0
-45	12	0	12	2	0	2	19	19	0
-40	14	0	14	2	0	2	24	21	2
-35	16	0	16	2	0	2	32	23	9
-30	18	0	18	3	0	2	41	25	16
-25	21	0	20	3	0	3	49	27	22
-20	24	1	23	4	1	3	61	32	29
-18	25	1	24	4	1	3	76	39	36
-16	27	1	26	5	1	3	94	51	43
-15	27	1	26	5	1	4	112	62	50
-14	28	2	27	5	2	4	130	73	57
-12	31	3	28	7	3	4	147	83	63
-10	34	4	30	9	5	4	159	92	67
-8	40	8	31	12	8	4	147	83	63
-6	53	20	34	17	12	5	130	73	57
-5	67	32	35	20	15	5	112	62	50

-4	85	49	37	23	18	5	94	51	43
-2	122	77	45	28	22	6	76	39	36
0	159	92	67	32	23	9	61	32	29
2	122	77	45	28	22	6	50	27	22
4	85	49	37	23	18	5	41	25	16
5	67	32	35	20	15	5	33	23	9
6	53	20	34	17	12	5	24	22	2
8	40	8	31	12	8	4	19	19	0
10	34	4	30	9	5	4	15	15	0
12	31	3	28	7	3	4	11	11	0
14	28	2	27	5	2	4			
15	27	1	26	5	1	4			
16	27	1	26	5	1	3			
18	25	1	24	4	1	3			
20	24	1	23	4	1	3			
25	21	0	20	3	0	3			
30	18	0	18	3	0	2			
35	16	0	16	2	0	2			
40	14	0	14	2	0	2			
45	12	0	12	2	0	2			
50	11	0	11	2	0	1			
55	10	0	10	1	0	1			

FDS (Tunnel B Fire HGV-2)									
	CEILING			SIDEWALL			CROSS SECTION		
x (m)	UB	MEAN	LB	UB	MEAN	LB	UB	MEAN	LB
-55	4.7	4.0	3.4	0.9	0.9	0.8	20.1	18.5	16.8
-50	5.1	4.4	3.6	1.0	0.9	0.8	30.9	28.3	25.7
-45	5.6	4.8	3.9	1.0	1.0	0.9	42.2	38.7	35.2
-40	6.3	5.3	4.2	1.1	1.0	0.9	41.6	37.7	33.8
-35	7.1	5.8	4.6	1.2	1.1	1.0	41.7	37.2	32.8
-30	7.4	6.0	4.6	1.3	1.2	1.1	37.0	32.6	28.2
-25	12.0	9.8	7.5	1.9	1.7	1.5	29.3	25.5	21.7
-20	14.4	11.2	8.0	2.3	2.1	1.9	42.3	30.8	19.2

-18	15.8	12.0	8.2	2.7	2.5	2.3	46.7	31.9	17.0
-16	17.4	12.9	8.4	3.3	3.0	2.8	49.1	31.3	13.4
-15	18.3	13.4	8.5	3.7	3.4	3.1	73.8	45.3	16.7
-14	19.4	14.0	8.6	4.1	3.8	3.4	107.5	68.1	28.7
-12	22.2	15.5	8.8	5.1	4.7	4.3	147.4	97.1	46.8
-10	26.7	17.8	9.0	6.7	6.2	5.6	168.2	111.4	54.5
-8	34.2	21.7	9.2	9.8	8.9	8.0	158.1	103.5	49.0
-6	49.2	29.5	9.8	15.1	13.7	12.3	129.5	81.7	33.8
-5	58.6	35.1	11.7	18.3	16.6	14.8	93.6	57.7	21.9
-4	81.6	49.3	17.1	23.9	21.6	19.3	54.1	34.4	14.7
-2	146.0	93.2	40.4	35.8	32.1	28.4	43.7	28.4	13.1
0	168.2	111.4	54.5	41.7	37.2	32.8	45.4	32.8	20.2
2	128.7	80.4	32.1	34.6	31.1	27.6	29.9	26.0	22.0
4	68.7	41.0	13.4	22.8	20.7	18.6	37.3	32.9	28.4
5	55.2	33.7	12.2	19.5	17.7	15.9	42.1	37.6	33.1
6	41.9	25.1	8.3	14.2	13.0	11.7	42.0	38.0	34.0
8	30.3	19.0	7.7	9.2	8.4	7.6	42.6	39.0	35.3
10	24.4	15.9	7.5	6.4	5.9	5.4	31.1	28.5	25.8
12	20.8	14.1	7.4	4.9	4.5	4.1	20.3	18.6	16.9
14	18.3	12.8	7.3	3.9	3.6	3.3			
15	17.4	12.3	7.1	3.5	3.2	2.9			
16	16.7	11.8	7.0	3.2	2.9	2.6			
18	15.2	11.0	6.8	2.6	2.4	2.2			
20	13.9	10.3	6.8	2.2	2.0	1.9			
25	11.4	9.1	6.7	1.8	1.6	1.5			
30	8.5	7.1	5.7	1.5	1.4	1.3			
35	6.6	5.5	4.3	1.2	1.1	1.0			

40	5.9	5.0	4.0	1.1	1.0	0.9			
45	5.3	4.5	3.7	1.0	0.9	0.9			
50	4.8	4.1	3.5	0.9	0.9	0.8			
55	4.5	3.8	3.2	0.9	0.9	0.8			

CDSF (Tunnel B Fire HGV-3)									
	CEILING			SIDEWALL			CROSS SECTION		
x (m)	TOTAL	RADI	CONV	TOTAL	RADI	CONV	TOTAL	RADI	CONV
-55	16	0	15	3	0	3	10	10	0
-50	18	0	18	3	0	3	17	17	0
-45	20	0	20	4	0	4	22	22	0
-40	23	0	23	4	0	4	35	25	10
-35	26	0	26	5	0	5	47	27	20
-30	29	0	29	6	0	5	58	28	30
-25	34	0	33	7	0	6	71	31	40
-20	39	1	38	8	1	7	90	39	51
-18	41	1	40	9	1	7	136	74	62
-16	44	2	42	10	2	8	182	109	73
-15	45	3	43	10	2	8	208	124	83
-14	47	4	44	11	3	8	234	140	94
-12	52	6	46	13	5	9	247	144	103
-10	63	14	48	17	8	9	263	153	110
-8	91	39	51	22	13	10	247	144	103
-6	146	91	55	28	18	10	234	140	94
-5	169	112	57	31	21	11	208	124	83
-4	186	126	60	34	23	11	182	109	73
-2	214	142	73	39	26	13	136	74	62
0	263	153	110	47	27	20	90	39	51
2	214	142	73	39	26	13	71	31	40
4	186	126	60	34	23	11	58	28	30
5	169	112	57	31	21	11	47	27	20
6	146	91	55	28	18	10	36	25	10
8	91	39	51	22	13	10	23	23	0
10	63	14	48	17	8	9	18	18	0
12	52	6	46	13	5	9	11	11	0
14	47	4	44	11	3	8			
15	45	3	43	10	2	8			
16	44	2	42	10	2	8			
18	41	1	40	9	1	7			
20	39	1	38	8	1	7			

25	34	0	33	7	0	6			
30	29	0	29	6	0	5			
35	26	0	26	5	0	5			
40	23	0	23	4	0	4			
45	20	0	20	4	0	4			
50	18	0	18	3	0	3			
55	10	0	10	1	0	1			

FDS (Tunnel B Fire HGV-3)									
	CEILING			SIDEWALL			CROSS SECTION		
x (m)	UB	MEAN	LB	UB	MEAN	LB	UB	MEAN	LB
-55	11.8	10.1	8.5	1.4	1.3	1.2	26.5	24.7	22.9
-50	13.3	11.4	9.5	1.5	1.4	1.3	47.5	44.4	41.3
-45	15.3	13.0	10.7	1.6	1.5	1.5	63.3	59.1	54.9
-40	18.1	15.2	12.2	1.8	1.7	1.6	65.1	60.6	56.1
-35	21.8	17.9	14.0	2.1	2.0	1.8	63.8	58.9	53.9
-30	24.7	19.6	14.4	2.4	2.2	1.9	59.1	49.9	40.7
-25	39.2	31.9	24.5	3.8	3.4	3.1	105.3	80.0	54.8
-20	50.8	40.1	29.3	4.8	4.5	4.1	136.8	101.8	66.8
-18	57.6	44.7	31.7	5.6	5.2	4.8	142.3	107.2	72.0
-16	66.4	50.6	34.7	6.6	6.1	5.6	159.8	118.6	77.3
-15	71.8	54.1	36.5	7.3	6.7	6.2	206.4	160.5	114.5
-14	78.1	58.3	38.5	8.1	7.4	6.8	276.6	222.5	168.4
-12	94.8	69.2	43.5	10.1	9.3	8.5	330.5	274.5	218.5
-10	117.0	83.6	50.2	13.8	12.6	11.4	361.9	302.0	242.2
-8	146.7	104.3	61.9	19.8	18.1	16.3	354.8	293.7	232.7
-6	193.7	141.7	89.8	29.4	26.9	24.5	325.9	261.8	197.7
-5	221.0	165.7	110.3	33.8	30.9	28.1	265.7	205.8	145.9
-4	279.0	219.3	159.6	42.9	39.4	35.9	182.3	133.3	84.4
-2	355.3	294.3	233.2	58.3	53.7	49.2	151.5	109.3	67.0

0	361.9	302.0	242.2	63.8	58.9	53.9	155.0	114.2	73.5
2	353.6	287.6	221.6	56.0	51.7	47.4	117.4	88.1	58.8
4	266.6	206.5	146.4	40.5	37.1	33.8	64.6	53.5	42.4
5	230.2	175.6	121.0	35.1	32.2	29.3	69.0	62.4	55.8
6	185.6	135.8	86.0	28.0	25.7	23.4	69.6	63.5	57.5
8	142.6	101.4	60.2	18.8	17.2	15.6	67.0	61.4	55.9
10	114.0	81.7	49.4	13.2	12.1	10.9	50.3	46.2	42.1
12	93.2	68.1	43.0	9.9	9.1	8.3	28.5	26.0	23.5
14	77.8	57.9	38.1	8.0	7.3	6.7			
15	71.8	54.0	36.2	7.2	6.7	6.1			
16	66.6	50.6	34.5	6.6	6.1	5.6			
18	58.1	44.9	31.7	5.6	5.2	4.7			
20	51.2	40.3	29.4	4.8	4.5	4.1			
25	39.6	32.1	24.6	3.8	3.4	3.1			
30	30.0	24.7	19.3	3.1	2.8	2.4			
35	22.1	18.0	13.9	2.1	2.0	1.8			
40	18.2	15.2	12.1	1.8	1.7	1.6			
45	15.4	13.0	10.6	1.6	1.5	1.4			
50	13.3	11.4	9.4	1.5	1.4	1.3			
55	11.8	10.1	8.4	1.4	1.3	1.2			

CDSF (Tunnel C Fire B-1)									
	CEILING			SIDEWALL			CROSS SECTION		
x (m)	TOTAL	RADI	CONV	TOTAL	RADI	CONV	TOTAL	RADI	CONV
-55	0	0	0	0	0	0	9	9	0
-50	0	0	0	0	0	0	10	10	0
-45	0	0	0	0	0	0	11	11	0
-40	0	0	0	0	0	0	12	12	0
-35	0	0	0	0	0	0	13	13	0
-30	0	0	0	0	0	0	14	14	0
-25	0	0	0	0	0	0	15	15	0
-20	0	0	0	0	0	0	16	16	0
-18	0	0	0	0	0	0	17	17	0
-16	0	0	0	1	1	0	19	19	0
-15	1	1	0	1	1	0	21	21	0

-14	1	1	0	1	1	0	24	24	0
-12	1	1	0	1	1	0	29	29	0
-10	1	1	0	2	2	0	41	41	0
-8	2	2	0	3	3	0	29	29	0
-6	4	4	0	5	5	0	24	24	0
-5	5	5	0	7	7	0	21	21	0
-4	7	7	0	8	8	0	19	19	0
-2	16	16	0	11	11	0	17	17	0
0	41	41	0	13	13	0	16	16	0
2	16	16	0	11	11	0	15	15	0
4	7	7	0	8	8	0	14	14	0
5	5	5	0	7	7	0	13	13	0
6	4	4	0	5	5	0	12	12	0
8	2	2	0	3	3	0	11	11	0
10	1	1	0	2	2	0	10	10	0
12	1	1	0	1	1	0	9	9	0
14	1	1	0	1	1	0			
15	1	1	0	1	1	0			
16	0	0	0	1	1	0			
18	0	0	0	0	0	0			
20	0	0	0	0	0	0			
25	0	0	0	0	0	0			
30	0	0	0	0	0	0			
35	0	0	0	0	0	0			
40	0	0	0	0	0	0			
45	0	0	0	0	0	0			
50	0	0	0	0	0	0			
55	0	0	0	0	0	0			

FDS (Tunnel C Fire B-1)									
	CEILING			**SIDEWALL**			**CROSS SECTION**		
x (m)	**UB**	**MEAN**	**LB**	**UB**	**MEAN**	**LB**	**UB**	**MEAN**	**LB**
-55	2.0	1.7	1.4	0.6	0.5	0.5	10.3	9.0	7.7
-50	2.1	1.8	1.5	0.6	0.5	0.5	11.3	9.8	8.3
-45	2.2	1.9	1.6	0.6	0.6	0.5	13.8	12.1	10.4
-40	2.4	2.1	1.7	0.6	0.6	0.5	11.7	10.1	8.5

-35	2.6	2.2	1.8	0.6	0.6	0.6	13.4	11.4	9.4
-30	2.8	2.4	2.0	0.6	0.6	0.6	13.0	11.0	9.1
-25	3.1	2.6	2.1	0.8	0.7	0.7	13.6	11.3	9.0
-20	3.3	2.8	2.2	0.9	0.9	0.8	11.7	9.7	7.8
-18	3.4	2.8	2.3	1.1	1.0	1.0	9.2	7.4	5.6
-16	3.6	2.9	2.3	1.4	1.3	1.2	12.1	8.7	5.3
-15	3.6	3.0	2.3	1.6	1.5	1.4	19.0	12.0	4.9
-14	3.8	3.0	2.3	1.8	1.6	1.5	31.3	18.1	5.0
-12	4.0	3.2	2.3	2.1	1.9	1.7	52.0	29.5	7.1
-10	4.5	3.4	2.3	2.6	2.3	2.0	67.0	38.9	10.8
-8	5.7	4.1	2.4	3.6	3.1	2.7	58.9	33.8	8.7
-6	8.5	5.6	2.6	5.2	4.5	3.8	35.6	20.9	6.1
-5	10.5	6.6	2.6	6.1	5.2	4.4	17.5	11.7	5.9
-4	15.8	9.4	3.1	7.6	6.6	5.6	11.2	8.5	5.9
-2	41.6	22.6	3.6	11.3	9.6	8.0	8.4	7.2	6.0
0	67.0	38.9	10.8	13.4	11.4	9.4	11.3	9.6	7.9
2	36.5	19.8	3.1	10.7	9.1	7.5	13.6	11.3	9.1
4	14.3	8.6	2.8	7.1	6.1	5.2	13.0	11.1	9.2
5	10.8	6.9	2.9	6.2	5.4	4.5	13.4	11.5	9.6
6	7.8	5.2	2.5	4.8	4.2	3.6	11.7	10.2	8.6
8	5.3	3.8	2.3	3.3	2.9	2.5	13.8	12.1	10.5
10	4.4	3.3	2.2	2.4	2.2	1.9	11.3	9.9	8.5
12	4.0	3.1	2.2	2.0	1.8	1.7	10.4	9.1	7.8

14	3.7	3.0	2.2	1.7	1.6	1.4			
15	3.6	2.9	2.2	1.5	1.4	1.3			
16	3.6	2.9	2.2	1.4	1.3	1.2			
18	3.4	2.8	2.2	1.1	1.0	0.9			
20	3.3	2.7	2.1	0.9	0.8	0.8			
25	3.0	2.5	2.1	0.8	0.7	0.7			
30	2.8	2.4	2.0	0.7	0.7	0.6			
35	2.5	2.2	1.8	0.6	0.6	0.6			
40	2.3	2.0	1.7	0.6	0.6	0.5			
45	2.2	1.9	1.6	0.6	0.6	0.5			
50	2.0	1.8	1.5	0.6	0.5	0.5			
55	1.9	1.7	1.4	0.6	0.5	0.5			

CDSF (Tunnel C Fire HGV-1)									
	CEILING			SIDEWALL			CROSS SECTION		
x (m)	TOTAL	RADI	CONV	TOTAL	RADI	CONV	TOTAL	RADI	CONV
-55	6	0	6	1	0	1	10	10	0
-50	7	0	7	1	0	1	12	12	0
-45	8	0	8	1	0	1	14	14	0
-40	9	0	9	1	0	1	16	15	1
-35	11	0	11	1	0	1	23	17	6
-30	12	0	12	2	0	1	30	19	11
-25	14	0	14	2	0	2	38	22	16
-20	17	0	16	2	0	2	47	25	21
-18	18	1	17	3	1	2	57	31	27
-16	19	1	18	3	1	2	72	40	32
-15	20	1	19	3	1	2	89	52	37
-14	20	1	19	4	1	2	108	65	42
-12	22	2	20	5	2	2	129	82	47
-10	24	3	22	6	3	3	146	95	50
-8	28	5	23	8	5	3	129	82	47

-6	37	13	24	11	9	3	108	65	42
-5	47	21	25	14	10	3	89	52	37
-4	63	36	27	16	12	3	72	40	32
-2	107	75	32	20	16	4	57	31	27
0	146	95	50	23	17	6	47	25	21
2	107	75	32	20	16	4	38	22	16
4	63	36	27	16	12	3	31	19	11
5	47	21	25	14	10	3	23	17	6
6	37	13	24	11	9	3	16	16	1
8	28	5	23	8	5	3	14	14	0
10	24	3	22	6	3	3	12	12	0
12	22	2	20	5	2	2	11	11	0
14	20	1	19	4	1	2			
15	20	1	19	3	1	2			
16	19	1	18	3	1	2			
18	18	1	17	3	1	2			
20	17	0	16	2	0	2			
25	14	0	14	2	0	2			
30	12	0	12	2	0	1			
35	11	0	11	1	0	1			
40	9	0	9	1	0	1			
45	8	0	8	1	0	1			
50	7	0	7	1	0	1			
55	6	0	6	1	0	1			

FDS (Tunnel C Fire HGV-1)									
	CEILING			SIDEWALL			CROSS SECTION		
x (m)	UB	MEAN	LB	UB	MEAN	LB	UB	MEAN	LB
-55	4.8	4.1	3.4	0.7	0.7	0.6	17.5	16.1	14.8
-50	5.2	4.5	3.8	0.8	0.7	0.7	19.1	17.5	15.9
-45	5.7	4.9	4.1	0.8	0.8	0.7	25.7	23.7	21.8
-40	6.4	5.5	4.6	0.8	0.8	0.7	22.3	20.5	18.7
-35	7.2	6.1	5.1	0.9	0.9	0.8	26.2	23.8	21.5
-30	8.1	6.8	5.5	1.0	0.9	0.8	25.0	22.7	20.3
-25	9.7	8.0	6.3	1.4	1.3	1.2	27.7	23.9	20.2

-20	11.3	9.1	6.8	1.7	1.6	1.5	36.3	28.0	19.6
-18	12.2	9.6	7.0	2.0	1.9	1.8	40.2	27.4	14.6
-16	13.2	10.2	7.3	2.5	2.4	2.2	55.0	36.8	18.5
-15	13.8	10.6	7.4	2.9	2.7	2.5	82.4	54.8	27.3
-14	14.6	11.0	7.5	3.2	3.0	2.8	126.9	84.7	42.5
-12	16.4	12.0	7.7	4.1	3.8	3.5	171.1	120.1	69.0
-10	19.5	13.7	7.8	5.3	4.9	4.5	196.8	141.6	86.3
-8	25.7	17.0	8.3	7.2	6.7	6.2	179.6	127.5	75.3
-6	37.7	23.4	9.2	10.6	9.8	9.0	134.6	90.4	46.2
-5	45.2	27.9	10.6	12.2	11.3	10.3	78.2	51.9	25.7
-4	64.7	40.3	15.9	15.8	14.5	13.2	52.3	34.7	17.1
-2	143.3	96.1	48.8	22.4	20.5	18.5	38.2	26.0	13.9
0	196.8	141.6	86.3	26.2	23.8	21.5	35.2	27.1	19.1
2	130.7	86.6	42.6	21.7	19.8	17.9	27.6	23.6	19.7
4	61.5	37.9	14.4	15.0	13.8	12.6	24.7	22.4	20.1
5	48.5	30.4	12.3	12.9	11.9	10.8	25.8	23.5	21.3
6	36.0	22.5	9.1	10.1	9.3	8.5	22.0	20.3	18.6
8	24.5	16.4	8.3	7.0	6.4	5.9	25.4	23.5	21.7
10	18.8	13.3	7.9	5.1	4.7	4.4	18.8	17.3	15.8
12	15.8	11.8	7.8	3.9	3.7	3.4	17.2	16.0	14.7
14	14.0	10.8	7.5	3.1	2.9	2.7			
15	13.3	10.4	7.4	2.8	2.6	2.4			
16	12.7	10.0	7.3	2.5	2.3	2.2			
18	11.7	9.4	7.1	2.0	1.8	1.7			
20	10.9	8.9	6.9	1.6	1.5	1.4			
25	9.3	7.8	6.4	1.3	1.2	1.2			

30	8.2	7.0	5.8	1.2	1.1	1.0			
35	7.0	6.0	5.0	0.9	0.8	0.8			
40	6.2	5.4	4.5	0.8	0.8	0.7			
45	5.6	4.9	4.1	0.8	0.7	0.7			
50	5.1	4.4	3.7	0.8	0.7	0.7			
55	4.7	4.1	3.4	0.7	0.7	0.6			

CDSF (Tunnel C Fire HGV-2)									
	CEILING			SIDEWALL			CROSS SECTION		
x (m)	TOTAL	RADI	CONV	TOTAL	RADI	CONV	TOTAL	RADI	CONV
-55	8	0	8	1	0	1	11	11	0
-50	9	0	9	1	0	1	13	13	0
-45	11	0	11	2	0	2	15	15	0
-40	12	0	12	2	0	2	20	17	3
-35	14	0	14	2	0	2	29	19	10
-30	16	0	16	3	0	2	38	21	17
-25	19	0	19	3	0	3	47	24	23
-20	22	0	22	4	1	3	58	28	30
-18	24	1	23	4	1	3	73	36	36
-16	25	1	24	5	1	4	97	54	43
-15	26	1	25	5	1	4	127	77	50
-14	27	1	26	5	2	4	156	100	57
-12	30	2	27	7	3	4	178	115	63
-10	33	4	29	8	4	4	192	125	67
-8	40	9	31	11	7	4	178	115	63
-6	59	26	33	15	10	5	156	100	57
-5	82	48	34	17	12	5	127	77	50
-4	111	75	36	20	14	5	97	54	43
-2	153	110	43	24	18	6	73	37	36
0	192	125	67	29	19	10	58	28	30
2	153	110	43	24	18	6	47	24	23
4	111	75	36	20	14	5	38	21	17
5	82	48	34	17	12	5	29	19	10
6	59	26	33	15	10	5	20	17	3
8	40	9	31	11	7	4	15	15	0
10	33	4	29	8	4	4	13	13	0
12	30	2	27	7	3	4	11	11	0
14	27	1	26	5	2	4			
15	26	1	25	5	1	4			
16	25	1	24	5	1	4			

18	24	1	23	4	1	3			
20	22	0	22	4	1	3			
25	19	0	19	3	0	3			
30	16	0	16	3	0	2			
35	14	0	14	2	0	2			
40	12	0	12	2	0	2			
45	11	0	11	2	0	2			
50	9	0	9	1	0	1			
55	8	0	8	1	0	1			

FDS (Tunnel C Fire HGV-2)									
	CEILING			SIDEWALL			CROSS SECTION		
x (m)	UB	MEAN	LB	UB	MEAN	LB	UB	MEAN	LB
-55	7.1	6.2	5.2	0.8	0.8	0.7	21.0	19.8	18.5
-50	7.8	6.8	5.8	0.9	0.8	0.8	24.4	22.9	21.4
-45	8.6	7.5	6.4	0.9	0.9	0.8	33.0	31.0	29.1
-40	9.7	8.4	7.2	1.0	1.0	0.9	28.2	26.4	24.7
-35	11.0	9.5	8.1	1.1	1.1	1.0	33.4	31.0	28.7
-30	12.5	10.8	9.0	1.2	1.1	1.1	29.4	26.5	23.5
-25	15.3	12.9	10.6	1.8	1.7	1.5	52.5	40.9	29.2
-20	18.6	15.3	12.0	2.3	2.2	2.0	63.4	46.4	29.5
-18	20.4	16.6	12.7	2.7	2.6	2.5	68.6	47.6	26.6
-16	22.7	18.1	13.5	3.4	3.2	3.0	87.8	61.9	36.1
-15	24.1	19.0	13.8	3.8	3.6	3.4	130.2	92.9	55.6
-14	25.9	20.0	14.2	4.3	4.0	3.7	185.9	135.2	84.5
-12	30.9	22.9	15.0	5.5	5.1	4.7	233.9	177.9	121.8
-10	38.6	27.4	16.2	7.2	6.7	6.2	262.1	201.9	141.7
-8	50.7	34.6	18.4	9.9	9.2	8.5	245.7	189.0	132.4
-6	71.8	47.3	22.7	14.3	13.4	12.4	203.7	150.8	98.0
-5	85.2	56.2	27.2	16.7	15.6	14.4	129.2	93.6	57.9
-4	118.4	79.8	41.1	21.1	19.6	18.1	88.1	62.4	36.7
-2	213.0	156.9	100.8	29.3	27.2	25.2	69.8	48.5	27.2

0	262.1	201.9	141.7	33.4	31.0	28.7	65.2	47.7	30.2
2	204.6	149.9	95.2	28.5	26.5	24.5	54.2	41.4	28.5
4	110.3	74.1	38.0	20.3	18.9	17.5	29.2	26.3	23.3
5	88.7	60.1	31.5	17.7	16.5	15.3	33.4	30.9	28.5
6	68.3	45.1	21.9	13.9	12.9	11.9	28.2	26.3	24.5
8	48.3	33.4	18.5	9.6	9.0	8.3	33.0	30.9	28.9
10	36.6	26.5	16.5	7.0	6.6	6.1	24.5	22.8	21.2
12	29.8	22.6	15.3	5.3	5.0	4.7	21.1	19.8	18.4
14	25.6	20.0	14.3	4.2	3.9	3.7			
15	24.1	19.0	13.9	3.8	3.5	3.3			
16	22.8	18.2	13.6	3.4	3.2	3.0			
18	20.7	16.8	12.8	2.7	2.6	2.4			
20	18.9	15.6	12.2	2.3	2.1	2.0			
25	15.7	13.2	10.7	1.8	1.7	1.6			
30	13.5	11.6	9.6	1.5	1.4	1.3			
35	11.3	9.7	8.2	1.1	1.1	1.0			
40	9.9	8.6	7.3	1.0	1.0	0.9			
45	8.8	7.7	6.5	1.0	0.9	0.8			
50	7.9	6.9	5.9	0.9	0.8	0.8			
55	7.2	6.3	5.3	0.9	0.8	0.7			

CDSF (Tunnel C Fire HGV-3)									
	CEILING			SIDEWALL			CROSS SECTION		
x (m)	TOTAL	RADI	CONV	TOTAL	RADI	CONV	TOTAL	RADI	CONV
-55	13	0	13	3	0	3	12	12	0
-50	15	0	15	3	0	3	15	15	0
-45	18	0	17	3	0	3	18	18	0
-40	20	0	20	4	0	4	31	21	10
-35	23	0	23	5	0	4	44	23	21
-30	27	0	27	5	0	5	58	26	31
-25	31	0	31	6	1	6	73	31	42
-20	36	1	35	8	1	7	96	45	52
-18	39	1	37	9	1	7	149	87	62
-16	42	2	40	10	2	8	215	143	72
-15	44	3	41	10	2	8	253	170	83
-14	46	4	42	11	3	8	283	189	93

-12	51	7	44	13	5	9	298	195	103
-10	64	17	47	16	7	9	317	208	109
-8	103	53	50	21	11	10	298	195	103
-6	183	130	53	26	16	10	283	189	93
-5	213	158	55	29	18	11	253	170	83
-4	233	175	58	31	20	11	215	143	72
-2	264	194	70	36	23	14	149	87	62
0	317	208	109	44	23	21	96	45	52
2	264	194	70	36	23	14	73	31	42
4	233	175	58	31	20	11	58	26	31
5	213	158	55	29	18	11	44	23	21
6	183	130	53	26	16	10	32	21	10
8	103	53	50	21	11	10	19	19	0
10	64	17	47	16	7	9	16	16	0
12	51	7	44	13	5	9	12	12	0
14	46	4	42	11	3	8			
15	44	3	41	10	2	8			
16	42	2	40	10	2	8			
18	39	1	37	9	1	7			
20	36	1	35	8	1	7			
25	31	0	31	6	1	6			
30	27	0	27	5	0	5			
35	23	0	23	5	0	4			
40	20	0	20	4	0	4			
45	18	0	17	3	0	3			
50	15	0	15	3	0	3			
55	13	0	13	3	0	3			

FDS (Tunnel C Fire HGV-3)									
	CEILING			SIDEWALL			CROSS SECTION		
x (m)	UB	MEAN	LB	UB	MEAN	LB	UB	MEAN	LB
-55	18.9	15.7	12.6	1.4	1.2	1.1	32.3	26.7	21.2
-50	21.5	17.8	14.1	1.5	1.3	1.2	41.1	33.8	26.4
-45	24.7	20.3	15.9	1.6	1.5	1.3	53.8	44.2	34.5
-40	28.9	23.6	18.3	1.8	1.6	1.5	45.0	37.2	29.4
-35	34.3	27.7	21.0	2.0	1.9	1.7	51.0	43.2	35.3
-30	40.4	32.3	24.3	2.3	2.1	1.9	73.8	59.9	46.1
-25	51.9	40.8	29.8	3.9	3.5	3.1	158.4	129.6	100.8

-20	68.5	52.5	36.6	4.9	4.5	4.0	157.5	130.0	102.4
-18	78.4	59.4	40.3	5.7	5.1	4.6	170.3	139.3	108.3
-16	91.6	68.2	44.9	6.7	6.0	5.3	204.1	170.2	136.2
-15	99.7	73.7	47.6	7.4	6.5	5.7	259.6	218.8	178.1
-14	109.1	80.0	50.8	8.1	7.1	6.2	314.3	270.8	227.3
-12	132.4	95.9	59.4	10.2	8.8	7.5	357.2	309.0	260.7
-10	161.0	116.5	71.9	13.4	11.5	9.6	387.9	334.2	280.5
-8	194.3	142.6	90.8	18.6	15.8	12.9	370.9	318.2	265.6
-6	242.9	185.1	127.2	26.3	22.3	18.3	335.2	283.6	231.9
-5	269.5	210.5	151.5	29.7	25.3	20.8	260.6	213.2	165.9
-4	319.4	264.2	209.1	36.6	31.3	25.9	204.6	163.7	122.8
-2	375.3	331.7	288.2	47.3	40.2	33.1	172.7	136.4	100.1
0	387.9	334.2	280.5	51.0	43.2	35.3	160.6	127.8	95.0
2	372.4	326.9	281.5	46.1	39.4	32.6	160.3	128.0	95.8
4	317.2	256.9	196.5	35.0	30.2	25.4	73.1	58.7	44.4
5	287.2	225.5	163.7	30.9	26.7	22.5	50.1	43.0	36.0
6	245.7	185.2	124.7	25.3	21.8	18.2	44.4	36.7	29.1
8	203.0	148.0	92.9	17.9	15.4	13.0	53.1	43.7	34.2
10	168.2	121.6	75.0	13.0	11.3	9.6	40.5	33.3	26.1
12	137.4	100.0	62.6	10.0	8.8	7.6	31.9	26.4	20.8
14	112.6	82.9	53.2	8.0	7.1	6.2			
15	102.5	76.1	49.7	7.3	6.5	5.7			
16	94.0	70.3	46.5	6.6	6.0	5.3			
18	80.4	60.9	41.4	5.6	5.1	4.6			

20	69.8	53.7	37.5	4.9	4.5	4.0			
25	52.3	41.3	30.3	3.9	3.5	3.1			
30	42.1	33.7	25.4	3.0	2.7	2.3			
35	34.3	27.7	21.1	2.1	1.9	1.7			
40	28.8	23.5	18.3	1.8	1.6	1.5			
45	24.5	20.3	16.0	1.6	1.5	1.3			
50	21.3	17.7	14.1	1.5	1.3	1.2			
55	18.8	15.7	12.6	1.4	1.2	1.1			